An investigation of the structure of disordered materials by using neutron diffraction

Petri, Ingrid

Award date:
1999

Awarding institution:
University of Bath

AN INVESTIGATION OF THE STRUCTURE OF DISORDERED MATERIALS BY USING NEUTRON DIFFRACTION

submitted by Ingrid Petri

for the degree of Doctor of Philosophy

of the University of Bath

1999

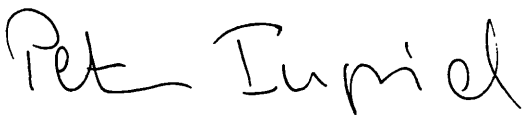

ProQuest LLC
789 East Eisenhower Parkway
P.O. Box 1346
Ann Arbor, MI 48106-1346

Abstract

The structure of several semiconducting, metallic and ionic disordered materials was investigated using neutron diffraction and the results were compared with those obtained from recent *ab initio* molecular dynamics methods.

The method of isotopic substitution was applied to measure the full set of partial structure factors, $S_{\alpha\beta}(Q)$, for the liquid semiconductor GeSe and the covalent network glass $GeSe_2$. Their short range ordering and for $GeSe_2$ also the intermediate range ordering were identified and a substantial number of 'defects' such as homopolar bonds were detected in both systems. Further, the structure of liquid $GeSe_2$ with increasing temperature was studied at the total structure factor level. Also, changes in the topology of Ge_xSe_{1-x} glasses in the range $0 \leq x \leq 0.4$ were observed and investigated by measuring the total structure factors. As far as possible our results were compared with those from molecular dynamics studies. The Ge-Se system was found to serve as a sensitive test-system for these studies, giving an insight into the strengths and limitations of them. For instance, problems are found in the region of the homopolar bonds for $g_{GeGe}(r)$ and for the first sharp diffraction peak in the Bhatia-Thornton concentration-concentration structure factor that could not be reproduced.

The structure of liquid lithium was measured and particular attention was paid to the inelasticity and resolution function corrections. The ion-ion and ion-valence electron partial structure factors were obtained and found to be in good agreement with *ab initio* molecular dynamics studies.

The method of first order difference functions in neutron diffraction in combination with H/D substitution was applied to 2 molal solutions of $Cu(ClO_4)_2$ in perchloric acid to measure the Cu-H and, to a first order approximation, the Cu-O partial structure factor. A $(4+1)$ distortion of the hydration shell around the Cu^{2+} ion was measured.

Gewidmet meinen Eltern, Egon und Christine,
und meinen Großeltern,
für all ihre Liebe, Ermutigung, und Unterstützung.

Acknowledgements

There are many people who helped me during my PhD studies and I am indebted to all of them.

I would particularly like to thank my supervisor Dr Phil Salmon for motivating and advising the work in this thesis and for always keeping me going. A big thank you also goes to the former UEA members of staff, Dr Kai Gilkes, Dr Ray Wood and Dr David Champeney, and especially to Dr Moises Silbert for always reminding me that 'Germans are supposed to work hard'. I also would like to acknowledge the help of Prof Paul Coleman regarding our move to the University of Bath, the kindliness of Dr Dan Wolverson in helping me out with both equipment and good advice and Dr Alison Walker-Jensen for letting me use the facilities her group.

Of course my work would not have been possible without the great help and assistance of Dr Spencer Howells, Dr Chris Benmore and Prof Alan Soper at the Rutherford Appleton Laboratory, and Dr Henry Fischer at the ILL. Additionally thanks goes to all the staff and technicians at both institutes, especially to John Dreyer, Chris Goodway and Pierre Palleau.

A thank you goes to all the simulation and calculation people such as Prof Paul Madden, Drs Juan Anta, Alfredo Pasquarello, Luis Enrique González, and Manel Canales. Over the years they provided results and fruitful discussions, which were very helpful to my research. Thanks to Prof Merbachs research group in Lausanne, especially to Eva Toth for preparing some of my samples. Thanks also goes to Dr Peter Verkerk for providing the lithium data, which proved a challenge to analyse, and to Dr Chris Anson for providing crystallography data.

Thanks to all the technicians and workshop staff at UEA, especially to Harry Bone, Dennis Woodcock and Dick Fuller, not only for the good work they did, but also for reminding me that I am not only a Physicist but a woman! Also thanks to John Preston, the legendary UEA Glassblower, and Bob Draper and Dr Peter Ford at the University of Bath.

Lots of thanks to the previous members of the group, Shuqin Xin and Jonathan Wasse for sharing their knowledge with me, and especially to Jonathan for giving me a big insight into a typical English way o life including birdwatching, eating

pies and supporting a football team (Sheffield Wednesday) that will never make its way to the top (I hope you forgive me Jonathan!).

There are many other people who deserve thanks in the Physics departments at UEA and Bath. This includes Peter Briggs, Jeremy Watling, Catherine Orange, who have already managed to escape, and Oleg Karimov, Faz Malik (long live my car!), Ivan Griffin, who always managed to shorten long afternoons with interesting stories, especially his 'theories of life', and Chris Blades, whose help with all computing matters will never be forgotten and who, whenever I was feeling bad commented that he was having it much worse. PS: Don't experiment too much with my hamsters! Thanks to all the Bath PhD students and postdocs who made the move to Bath easier, particularly to Diego Oriato, who I never could 'convince enough' to go for coffee with us, Claire Blay for sharing my moaning and adding some girl power, Brian Mangan, for teaching me English words you are not supposed to say, and Graeme Moore and Jim Partridge for not letting me sleep on the streets and showing me the delights of Sam Wellers.

There are many friends outside my PhD who I would not like to forget to thank. This includes Farah Rahimi, who always with a big bottle of wine managed to help me forget about Physics at least for an evening, Alexandrine Cerfontaine, Edith Wegener, who always reminded me about the important things outside Physics and Stephan Winnerl, who was a very good companion and friend during my whole Physics career.

All my love and thanks goes to my parents and grandparents for their constant support, understanding and Bavarian food parcels reminding me about what I was missing at home.

But the main thanks goes to Steve Woods for listening to all my moaning, helping me through bad times and making me happy, and also to his parents and granddad for welcoming me with such friendliness to their family.

Danksagung - Kurzfassung

Eine Menge Leute haben mir während meiner Doktorarbeit geholfen, und ich bin allen zu Dank verpflichtet.

Besonders danken möchte ich meinem Betreuer, Dr Phil Salmon, für die Motivation und Hilfe während der Doktorarbeit, und dafür daß er mich immer beschäftigt gehalten hat.

Vielen Dank den ehemaligen Mitarbeitern der Arbeitsgruppe, Shuqin Xin und Jonathan Wasse, dafür daß sie ihr Wissen mit mir geteilt haben, und besonders Jonathan, der mir einen guten Einblick in den typisch englischen Lebensstil gegeben hat, Vogelbeobachtung, Essen von Pies und Unterstützen eines Fußballteams, das nie den Weg nach oben schaffen wird. (Ich hoffe, du vergibst mir für das Jonathan!)

Viele andere Mitglieder der Physik Departments der University of East Anglia und Bath verdienen eine Menge Dank. Da sind Peter Briggs, Jeremy Watling und Catherine Orange, die es schon geschafft haben zu entkommen. Außerdem Oleg Karimov, Faz Malik, Ivan Griffin, der lange Nachmittage immer mit interessanten Geschichten und 'Lebensweisheiten' verkürzen konnte, und Chris Blades, dessen Hilfe bei allen Computer-Angelegenheiten ich nie vergessen werde, und der mich, wenn es mir nicht sehr gut ging, immer daran erinnert hat, daß es ihm viel schlechter ginge, PS. keine Experimente mit meinen Hamstern! Vielen Dank auch allen Bath Doktoranten und Postdocs, die uns den Umzug nach Bath erleichtert haben, v.a. Diego Oriato, den ich niemals 'genug überzeugen' konnte, uns zum Kaffeetrinken zu begleiten, Claire Blay, die mich immer im Beklagen und mit Frauen-Power unterstützt hat, Brian Mangan, der mir all die englischen Ausdrücke beigebracht hat, die man niemals verwenden sollte, und schließlich Graeme Moore und Jim Partridge, die mich davor bewahrt haben in meinen letzten zwei Wochen in Bath auf der Straße zu übernachten und die mich in all die Genüsse von Sam Wellers eingeweiht haben.

Auch einer Menge von Freunden außerhalb meiner Doktorarbeit möchte ich nicht vergessen zu danken. Da ist Farah Rahimi, der es mit einer Flasche Wein immer gelungen ist, mich Physik wenigstens für einen Abend vergessen zu lassen, Alexandrine Cerfontaine, Edith Wegener, die mir die wichtigen Dinge außerhalb

von Physik immer ins Gedächtnis rief, und Stephan Winnerl, der mir während meiner gesamten 'Physik-Karriere' ein guter Begleiter und Freund war.

All meine Liebe und mein Dank geht an meine Eltern und Großeltern für ihre fortwährende Unterstützung, ihr Verständnis und die Essens-Pakete, die mich immer daran erinnerten, was ich von daheim vermisse.

Am meisten aber möchte ich mich bei Steve Woods bedanken, der all meinen Klagen mit großer Geduld zugehört hat, der mir durch schlechte Zeiten geholfen hat und der mich sehr glücklich macht. Vielen Dank auch seinen Eltern und seinem Großvater, dafür daß sie mich so herzlich in ihrer Familie aufgenommen haben.

Contents

Chapter 1

Introduction

1.1 Disordered materials

Disordered materials are of particular interest from both the scientific and technological points of view. They have substantial technological applications, ranging from the use of chalcogenide and halide glasses as fibre optical materials, to the use of amorphous semiconductors in xerography and solar cells. The extensive field of research that has developed is reviewed in several textbooks, see for example Elliott[1], Zallen[2], Feltz[3] and Cusack[4].

In order to explain the physical properties and characteristics of liquids and glasses knowledge is required on their structure. These materials exhibit, in general, a well-defined short range atomic ordering (SRO) on a scale of 0 to ≈ 5 Å due to chemical constraints, and possibly an intermediate range ordering (IRO) on a length scale of $\approx 5 - 20$ Å as a consequence of the packing of the structural units which are defined by the short range order in the system (Elliott[1]). However, liquids and glasses do not possess any long range ordering that characterises their crystalline counterparts.

1.2 Structural probes: experimental techniques

The structure of disordered materials can be investigated using a variety of experimental techniques which include diffraction, using neutrons, x-rays or electrons, extended x-ray absorption fine structure (EXAFS) spectroscopy, differential

anomalous x-ray scattering (DAS), Mössbauer spectroscopy, and vibrational spectroscopy (e.g. Raman spectroscopy and infra-red absorption).

In this thesis neutron diffraction was applied to several liquid and glassy systems. The method is preferred to x-ray or electron diffraction because elements located next to each other in the periodic table are more readily distinguishable. Also, in contrast to the use of x-rays, the intensity in a neutron diffraction experiment does not (neglecting magnetic scattering) decrease with increasing scattering vector Q. In electron diffraction there are also problems arising from multiple scattering effects within the sample and the heating-up of the sample by the electron beam. Furthermore, for the study of multicomponent systems neutron diffraction offers the important advantage of the method of isotopic substitution to extract individual pair correlation functions from the data, and therefore structural information concerning one specific species may be obtained (see e.g. Enderby et al.[5], Penfold & Salmon[6], and Salmon et al.[7]). In the absence of suitable isotopes and for structurally similar disordered materials the method of isomorphic substitution may be used to remove some of the contributions to the total structure factors (e.g. Skipper et al.[8], Wasse[9]). Also the use of x-ray diffraction complementary to neutron diffraction, for example if individual correlations have a weak weighting for neutrons but a high weighting for x-rays, may be helpful in the study of multicomponent systems (see e.g. Barnes et al.[10]).

The EXAFS method yields information on the local structure of individual atomic species within multicomponent systems (e.g. Zhou et al.[11]). However, information is restricted to the nearest and in some cases next nearest neighbour correlations, and a model system is required to determine the x-ray phase shift, which may lead to erroneous results for complex structures. DAS is a developing technique that benefits from the development of synchrotron radiation sources. It can provide information on the SRO as well as on the IRO (Fischer-Colbrie & Fuoss[12]). However, it covers a limited range of scattering vectors and the 'dispersion corrections', $f'(Q,\omega)$ and $f''(Q,\omega)$, to the scattering factor must be known with considerable accuracy. Mössbauer spectroscopy is a qualitative technique to obtain information about the structural environment of individual atomic species (see e.g. Bresser et al.[13] and Boolchand et al.[14]).

The main aim of this thesis is to investigate the effect of differences in bonding

mechanisms on the structure of several liquid and glassy materials. Particularly, in the binary Ge_xSe_{1-x} ($0 \leq x \leq 0.4$) system the evolution in the bonding mechanism from semiconducting to metallic with both increasing temperature and changing composition is studied. This leads to the investigation of the structure of lithium, a liquid metal comprising positive ions in a 'sea' of conduction electrons. Further, the solvation of Cu^{2+} cations in aqueous solution is studied.

The common theme is to understand the nature of the SRO and IRO in these disordered materials and thereby to find quantitative information to test models for the systems. Often, these models have been provided by very recent and ongoing work involving so called *ab initio* molecular dynamics calculations.

1.3 Outline of the present work

In chapter 2 the theory of the neutron diffraction method is summarised and the method of isotopic substitution is introduced. In chapter 3 details are given about the neutron diffraction instruments used, and the data analysis procedures necessary to extract a total structure factor from the measured data are outlined.

In chapter 4 the method of isotopic substitution is applied to the liquid semiconductor GeSe. Its structure is compared with the high and low temperature forms of crystalline GeSe and, at the partial structure factor level, with the structures of molten CuSe, CuBr and $GeSe_2$.

In chapter 5 the structure of liquid $GeSe_2$ is studied as a function of increasing temperature at the total structure factor level. This gives, to a first approximation, the Bhatia Thornton number-number partial structure factor which describes the topology of the system. The temperature development of the structure is compared with the change in structure that occurs when the composition is altered from $GeSe_2$ to GeSe.

In chapter 6 the structure of the proto-typical network glass $GeSe_2$ is studied by using the method of isotopic substitution in neutron diffraction. The effect of truncation of the measured structure factors on the real-space data is considered and corrected for. The results are discussed with reference to the structures of crystalline $GeSe_2$ and liquid $GeSe_2$, and are compared with *ab initio* molecular dynamics studies. Particular interest is taken in the identification of the 'defects',

i.e. structural motifs that do not exist in the high-temperature crystalline phase, inherent in the disordered structure of glassy $GeSe_2$.

In chapter 7 the system under study is glassy Ge_xSe_{1-x} ($0 \leq x \leq 0.4$), and the development of the Bhatia Thornton number-number partial structure factor and the corresponding pair distribution function are measured as a function of the germanium content x.

In chapter 8 the structure of the liquid metal lithium is studied at different temperatures. Special care is taken to account for the effects caused by the detector integration path, the inelastic scattering of the neutrons by the light lithium nuclei and the instrumental resolution function. In addition to the ion-ion structure factor the ion-valence electron structure factor for liquid lithium is derived by combining our measured static structure factor from neutron diffraction with the x-ray structure factor measured by Olbrich et al.[15].

In chapter 9 a 2 molal solution of $Cu(ClO_4)_2$ in perchloric acid is studied using the method of neutron first-order difference functions in combination with H/D substitution to directly measure the Cu-H and, to a first order approximation, the Cu-O coordination environments. The results are compared with those from recent *ab initio* molecular dynamics simulations.

Finally, in chapter 10, a summary of the results obtained in this work is given and ideas for future work arising from this thesis are discussed.

Bibliography

[1] Elliott S R, *Physics of Amorphous Materials*, 2nd Ed., Longman Group UK Limited: Essex (1990).

[2] Zallen R, *The Physics of Amorphous Solids*, Wiley: New York (1983).

[3] Feltz A, *Amorphous Inorganic Materials and Glasses*, VCH: Weinheim (1993).

[4] Cusack N E, *The Physics of Structurally Disordered Matter*, Hilger: Bristol (1987).

[5] Enderby J E, North D M and Egelstaff P A, *Phil. Mag.* **14** (1966) 961.

[6] Penfold I T and Salmon P S, *Phys. Rev. Lett.* **67** (1991) 97.

[7] Salmon P S, Xin S and Fischer H E, *Phys. Rev. B* **58** (1999) 6115.

[8] Skipper N T, Cummings N, Neilson G W and Enderby J E, *Nature* **321** (1986) 52.

[9] Wasse J C, *Ph.D. Thesis, University of East Anglia* (1998).

[10] Barnes A C, Lague S B, Hamilton M A, Fischer H E, Fitch A N and Dooryhee E, *J. Phys.: Cond. Mat.* **10** (1998) L645.

[11] Zhou W, Paesler M and Sayers D E, *Phys. Rev. B* **43** (1991) 2315.

[12] Fischer-Colbrie A and Fuoss P H, *J. Non-Cryst. Sol.* **126** (1990) 1.

[13] Bresser W J, Boolchand P, Suranyi P and de Neufville J P, *Phys. Rev. Lett.* **46** (1981) 1689.

[14] Boolchand P, Grothaus J, Bresser W J and Suranyi P, *Phys. Rev. B* **25** (1982) 2975.

[15] Olbrich H, Ruppersberg H and Steeb S, *Z. Naturforsch.* **38a** (1983) 1328.

Chapter 2

Theory of thermal neutron scattering

2.1 Introduction

In this chapter the basic principles of the theory of neutron scattering concerning the present work will be described. A full and detailed description can be found in many textbooks (e.g. Squires[1], Lovesey[2]).

2.2 Basic properties of the neutron

The neutron is an uncharged particle that belongs to the family of fermions (spin $\frac{1}{2}$). It has a mass m = $1.625 \cdot 10^{-27}$ kg and its magnetic dipole moment μ_n is -1.913μ_N where μ_N is the nuclear magneton. The de Broglie wavelength of a neutron with mass m and velocity v is $\lambda = \frac{h}{mv}$, where h is the Planck constant. The wavevector $\underline{k}$ has the magnitude $k = \frac{2\pi}{\lambda}$ in the same direction as $\underline{v}$. With the momentum $\underline{p}$ of the neutron being $\underline{p} = \hbar\underline{k} = \frac{h\underline{k}}{2\pi}$, its energy is conventionally taken to be $E = k_B T = \frac{1}{2}mv^2 = \frac{h^2}{2m\lambda^2} = \frac{\hbar^2 k^2}{2m}$, where k_B is the Boltzmann constant and T the absolute temperature.

Thermal neutrons are much used in the investigation of condensed matter. Conventionally, thermal neutrons are characterised by a standard velocity $v = 2.20\,km\,s^{-1}$. This corresponds to an energy E = 25.3 meV, an absolute temperature T = 293 K, a de Broglie wavelength λ = 1.798 Å, and a wavevector $\underline{k}$

with a magnitude $k = 3.49 \cdot 10^{10}\ m^{-1}$.

The usefulness of thermal neutrons arises from their basic properties:

- The de Broglie wavelength λ is in the order of typical interatomic distances in solids and liquids. Interference effects therefore occur that comprise information about the scattering system.

- Because the neutron is uncharged it penetrates deeply into the investigated matter, allowing the measurement of its bulk properties. Also, as there is no Coulomb barrier to be overcome, it is scattered only by nuclear forces (dipole-dipole interactions neglected). This results in an advantage over using X-rays and electrons as the scattering power for neutrons does not scale with the atomic number (e.g. hydrogen can be detected). Also the scattering powers of two isotopes of the same element can be notable different. This allows use of the powerful method of isotopic substitution in neutron scattering (see chapters 2.11 and 2.12).

- The energy of thermal neutrons is comparable to that of many excitations in condensed matter (e.g. phonons). The amount of energy neutrons loose or gain by the creation or annihilation of an excitation thus corresponds to a large fraction of their initial energy. So by measuring the energy of inelastically scattered neutrons it is possible to obtain accurate information about the energies of the excitations and therefore the interatomic forces connected with these excitations.

- Because of their magnetic moment neutrons interact with the unpaired electrons in magnetic atoms, via dipole-dipole interactions, and can therefore be used to investigate the magnetic properties of matter on a microscopic length scale. By using elastic scattering it is possible to examine the arrangement of the electron spins and the density distribution of unpaired spins. Inelastic neutron scattering offers the possibility to measure the energies of magnetic excitations (e.g. spin waves) and to study time-dependent spin correlations.

Generally thermal neutrons are produced using a reactor or spallation source. In a reactor they are created by nuclear fission, whereas in a spallation source they are created by the splitting of the nuclei in a heavy-metal target when they are hit by

high energy particles (e.g. protons). The neutrons emerge, however, with too high energy and need to be 'cooled down' before being used for scattering experiments. This is achieved by the use of moderators. Usually materials consisting of light atoms are used (e.g. methane) as the energy transfer is largest between particles of the same mass. The thermalised neutrons are emitted from the moderator with a Maxwellian velocity distribution and an average temperature that is determined by the moderator temperature.

2.3 The scattering cross-section

Consider a beam of neutrons, characterised by a wavevector $\underline{k}$, an energy E and of uniform flux Φ, incident on a target. Because of the basic properties of the neutron, mainly because it is uncharged, the interaction probability is rather small (see Price[3]). Only a minor percentage of neutrons will be scattered and these can be measured by a detector placed in the direction θ, ϕ from the direction of the transmitted neutrons (see figure 2.1).

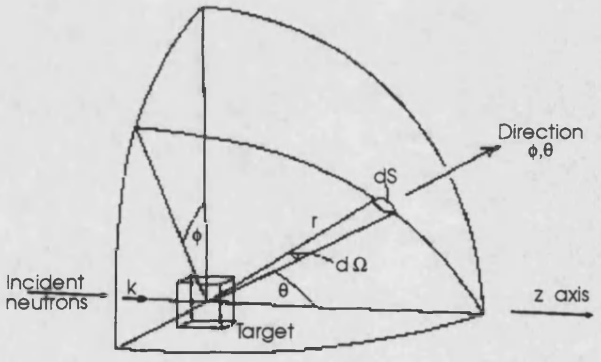

Figure 2.1: Geometry for the scattering cross-sections (Reproduced from Squires[1].)

It is assumed the target or sample consists of N identical atoms and the detector covers a solid angle $d\Omega$. Various measurements can be made on the neutrons after they have interacted with the target, and the results of these measurements are expressed by cross-sections. If the number of neutrons scattered in a given direction is measured as a function of their energy E', the *double differential scattering cross-*

section, $\frac{d^2\sigma}{d\Omega dE'}$, is obtained and is defined by the following equation

$$\frac{d^2\sigma}{d\Omega dE'} = \frac{(number\ of\ neutrons\ scattered\ per\ sec.\ into\ the\ solid\ angle\ d\Omega\ in\ the\ direction\ \theta, \phi\ with\ final\ energies\ between\ E'\ and\ E'+dE')}{N\Phi\, d\Omega\, dE'}. \tag{2.1}$$

In an experiment where the energy of the scattered neutrons is not analysed, but all neutrons that are scattered into dΩ in the direction θ, ϕ are measured, the *differential scattering cross-section*, $\frac{d\sigma}{d\Omega}$, is obtained:

$$\frac{d\sigma}{d\Omega} = \frac{number\ of\ neutrons\ scattered\ per\ sec.\ into\ d\Omega\ in\ direction\ \theta, \phi}{N\Phi\, d\Omega}. \tag{2.2}$$

The *total scattering cross-section*, σ_{tot}, where 'total' means the number of neutrons scattered into all directions, is defined by the equation

$$\sigma_{tot} = \frac{total\ number\ of\ neutrons\ scattered\ per\ sec.}{N\Phi}. \tag{2.3}$$

The cross-sections are the quantities that are actually measured in a scattering experiment and they contain information about the interaction of the neutrons with the sample.

The scattering vector is illustrated in figure 2.2. It is defined by $\underline{Q} = \underline{k} - \underline{k}'$ and corresponds to the momentum transfer during the scattering process ($\underline{k}'$ denotes the wavevector of the scattered neutrons). The energy transfer is given by $\hbar\omega = E - E'$ and is equal to zero for the case of elastic scattering.

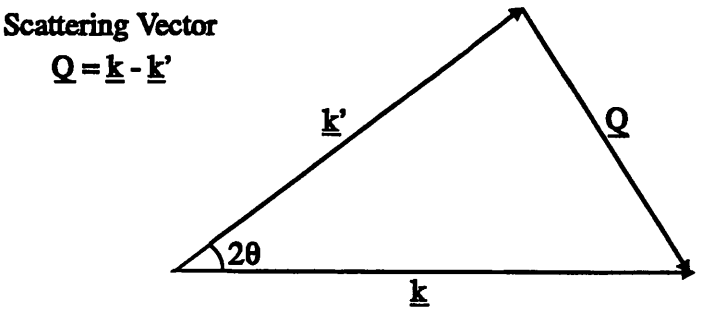

Figure 2.2: Definition of the scattering vector

2.4 Scattering of a neutron by a single fixed nucleus

In this section the simple case of nuclear scattering by a single nucleus at a fixed position is discussed. The incident neutrons can be described by a normalised plane wave in the z-direction, which is along the direction of $\underline{k}$, and can therefore be represented by the wavefunction

$$\Psi_{inc}(z) = e^{ikz}. \tag{2.4}$$

If the wavelength of the neutrons is 10^{-10} m, which is large compared to the range of the nuclear forces ($10^{-14} - 10^{-15}$ m) that cause the scattering, the scattered wave is spherically symmetric (S-wave scattering only) and at a point $\underline{r}$ it can be written as,

$$\Psi_{sc}(r) = -\frac{b}{r}e^{ik'r}. \tag{2.5}$$

The quantity b is known as the *scattering length* and it characterises the strength of the neutron-nucleus interaction. b can be complex and either positive or negative (positive corresponds to a repulsive scattering potential) depending on the energy of the incident neutrons and the particular nucleus in the sample. The imaginary part of b corresponds to absorption of the neutron by a nucleus to form compound nuclei with energies close to those of excited nuclear states. For most nuclei this imaginary part is small at thermal neutron energies. The value of b changes not only from element to element, but also from isotope to isotope of a single element and it depends on the relative orientation of the neutron and nucleus spins.

The differential cross-section $\frac{d\sigma}{d\Omega}$ for the scattering from a fixed nucleus can be calculated as follows. The flux of scattered neutrons with final velocity $v' = v$ through the area $dS = r^2 d\Omega$ (see figure 2.1) is given by

$$v \cdot |\Psi_{sc}|^2 \cdot dS = v \cdot \frac{b^2}{r^2} \cdot dS. \tag{2.6}$$

The flux of incident neutrons is

$$\Phi = v \cdot |\Psi_{inc}|^2 = v. \tag{2.7}$$

Therefore from the definition of the differential scattering cross-section (equation 2.2) it follows that

$$\frac{d\sigma}{d\Omega} = \frac{v \cdot \frac{b^2}{r^2} \cdot dS}{v \cdot d\Omega} = b^2 \tag{2.8}$$

such that

$$\sigma_{tot} = 4\pi b^2. \tag{2.9}$$

2.5 Scattering by a generalised scattering system

The result for the scattering from one nucleus is generalised now to the scattering from a scattering system containing N nuclei, at the positions $\underline{R}_j$ (j=1,...,N) from the origin (see fig. 2.3).

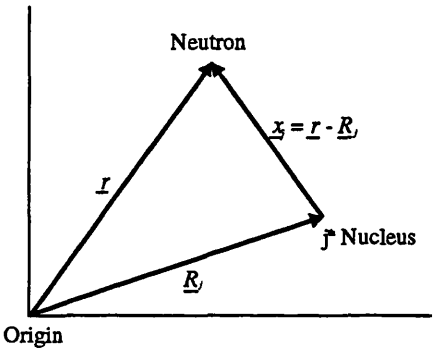

Figure 2.3: Scattering coordinates

Assume that a neutron at position $\underline{r}$ with wavevector $\underline{k}$ and described by the wavefunction $\Psi_{\underline{k}}$ is incident on this scattering system. If the neutron interacts with the system via a potential V its wavevector changes to $\underline{k}'$. As a result of the interaction the system changes from a state λ to λ'.

The differential scattering cross-section $(\frac{d\sigma}{d\Omega})_{\lambda\to\lambda'}$, for all the processes in which the state of the scattering system changes from λ to λ' can be expressed as

$$\left(\frac{d\sigma}{d\Omega}\right)_{\lambda\to\lambda'} = \frac{1}{\Phi \cdot d\Omega} \sum_{k' \, in \, d\Omega} W_{\underline{k},\lambda\to\underline{k}',\lambda'} \tag{2.10}$$

where $W_{\underline{k},\lambda\to\underline{k}',\lambda'}$ is the probability of transitions per second from the state $\underline{k}$,λ to the state $\underline{k}'$,λ'. Φ is the flux of incoming neutrons and the sum is taken over all values of k' that lie in the solid angle dΩ. The sum over all these probabilities is given as a fundamental result in quantum mechanics by *Fermi's Golden Rule* (see e.g. Schwabl[4]):

$$\sum_{k' \, in \, d\Omega} W_{\underline{k},\lambda\to\underline{k}',\lambda'} = \frac{2\pi}{\hbar} \rho_{\underline{k}'} \mid \langle \underline{k}', \lambda' | V | \underline{k}, \lambda \rangle \mid^2 \tag{2.11}$$

where $\rho_{\underline{k}'} = \frac{Y}{(2\pi)^3}\frac{m}{\hbar^2}k'd\Omega$ is the number of momentum states in $d\Omega$ per unit energy range for neutrons in the state $\underline{k}'$ (see Squires[1]). Here box normalisation is used. This assumes that the neutron and scattering system are in a large box of volume Y.

Writing the matrix element in terms of integrals, gives

$$\langle \underline{k}', \lambda' | V | \underline{k}, \lambda \rangle = \int \Psi^*_{\underline{k}'} \chi^*_{\lambda'} V \Psi_{\underline{k}} \chi_{\lambda} \, d\underline{R} \, d\underline{r} \tag{2.12}$$

where $d\underline{R} = d\underline{R}_1 d\underline{R}_2 \cdots d\underline{R}_{N-1} d\underline{R}_N$. $d\underline{R}_j$ is an element of volume for the j^{th} nucleus and $d\underline{r}$ is an element of volume for the neutron. The integral has to be taken over all space for each of the N+1 variables. The wavefunctions $\Psi_{\underline{k}}$ and $\Psi_{\underline{k}'}$ are described by plane waves and their normalisation factor is $\frac{1}{\sqrt{Y}}$ as there is one neutron in the box of volume Y. Therefore they are given by

$$\Psi_{\underline{k}} = \frac{1}{\sqrt{Y}} e^{i\underline{k}\cdot\underline{r}} \tag{2.13}$$

and

$$\Psi_{\underline{k}'} = \frac{1}{\sqrt{Y}} e^{i\underline{k}'\cdot\underline{r}}. \tag{2.14}$$

Using this, the matrix element in equation 2.12 becomes

$$\langle \underline{k}', \lambda' | V | \underline{k}, \lambda \rangle = \frac{1}{Y} \int e^{-i\underline{k}'\cdot\underline{r}} \chi^*_{\lambda'} V \, e^{i\underline{k}\cdot\underline{r}} \chi_{\lambda} \, d\underline{R} \, d\underline{r}. \tag{2.15}$$

The flux Φ of neutrons is given as the product of their density $(\frac{1}{Y})$ and velocity:

$$\Phi = \frac{1}{Y}\frac{\hbar k}{m}. \tag{2.16}$$

In order to evaluate the transition probability an expression for the interaction potential V is required. The effective Fermi pseudopotential $V_j(\underline{r} - \underline{R}_j)$ is used to describe the interaction between a neutron at position $\underline{r}$ and a bound nucleus at $\underline{R}_j$:

$$V_j(\underline{r} - \underline{R}_j) = \frac{2\pi\hbar^2}{m} b_j \cdot \delta(\underline{r} - \underline{R}_j) \tag{2.17}$$

where b_j is the *bound scattering length*, which describes the strength of the interaction between the neutron and the bound nucleus.

This potential is extremely short ranged and very strong, and therefore contains a delta-function. At first it might seem contradictory to describe the weak interaction between the neutron and scattering system using this strong pseudopotential.

However combined with Fermi's Golden Rule it describes the scattering of thermal neutrons correctly, and gives the required result for the case of isotropic scattering for a single fixed nucleus (see Squires[1]).

In the case that the nucleus is free, the scattering has to be treated in the centre of mass system. The formulation is the same as if the nucleus was fixed, but the mass of the neutron m has to be replaced by the reduced mass μ of the neutron-nucleus system,

$$\mu = \frac{mM}{m+M} \tag{2.18}$$

where M is the mass of the free nucleus. Therefore the bound scattering length b is going to be replaced by the *free scattering length* b_f, which is related to its bound equivalent by

$$b_f = \frac{M}{M+m} \cdot b. \tag{2.19}$$

The potential V for the whole scattering system is given by the sum over all V_j's:

$$V = \sum_j V_j(\underline{r} - \underline{R}_j) = \frac{2\pi\hbar^2}{m} \sum_j b_j \cdot \delta(\underline{r} - \underline{R}_j) \tag{2.20}$$

2.6 Expression for $\frac{d^2\sigma}{d\Omega dE'}$

An equation for the double differential scattering cross-section can be derived by first inserting equations 2.11 and 2.16 into equation 2.10 to give the differential cross-section,

$$\left(\frac{d\sigma}{d\Omega}\right)_{\lambda\to\lambda'} = \frac{k'}{k}\left(\frac{m}{2\pi\hbar^2}\right)^2 \cdot |\langle \underline{k}', \lambda' | V | \underline{k}, \lambda \rangle|^2 . \tag{2.21}$$

The energy conservation condition can be expressed by $E + E_\lambda = E' + E_{\lambda'}$, where E and E' are the initial and final energies of the neutron, E_λ and $E_{\lambda'}$ the initial and final energies of the scattering system. This energy conservation condition can be incorporated as a delta-function, with

$$\int \delta(E_\lambda - E_{\lambda'} + E + E')\, dE' = 1. \tag{2.22}$$

Then the double differential cross-section can be written as

$$\left(\frac{d^2\sigma}{d\Omega dE'}\right) = \frac{k'}{k}\left(\frac{m}{2\pi\hbar^2}\right)^2 \cdot |\langle \underline{k}', \lambda' | V | \underline{k}, \lambda \rangle|^2 \cdot \delta(E_\lambda - E_{\lambda'} + E + E'). \tag{2.23}$$

By inserting the Fermi pseudopotential in the above equation, replacing the delta-function by an integral over time, writing the operators in terms of their Heisenberg time-dependent representation, and taking a thermal average over the system (for more details see Price[3]), we finally obtain

$$\left(\frac{d^2\sigma}{d\Omega dE'}\right) = \frac{k'}{k}\frac{1}{2\pi\hbar}\sum_{jj'}\overline{b_j b_{j'}}\int_{-\infty}^{\infty}\left\langle e^{-i\underline{Q}\cdot\underline{R}_{j'}(0)}\, e^{-i\underline{Q}\cdot\underline{R}_j(t)}\right\rangle e^{-i\omega t}\, dt \tag{2.24}$$

where

$$\underline{R}_j(t) = e^{\frac{iHt}{\hbar}}\,\underline{R}_j\, e^{\frac{-iHt}{\hbar}}, \tag{2.25}$$

$$e^{i\underline{Q}\cdot\underline{R}_j(t)} = e^{\frac{iHt}{\hbar}}\, e^{i\underline{Q}\cdot\underline{R}_j}\, e^{\frac{-iHt}{\hbar}} \tag{2.26}$$

and

$$\omega = \frac{(E - E')}{\hbar}. \tag{2.27}$$

H is the Hamiltonian of the scattering system, the triangular brackets indicate a thermal average and $\overline{b_j b_{j'}}$ denotes an average over the isotope and spin distributions of the nuclei.

Equation 2.24 is the basic equation for the double differential scattering cross-section used for the description of nuclear scattering.

2.7 Coherent and incoherent scattering

A scattering system containing only one single element is considered, where the scattering length varies from one nucleus to another due to their nuclear spins or due to the presence of isotopes or due to both. If a value of the scattering length, b_i, occurs with the relative frequency f_i, where $\sum_i f_i = 1$, then the average value of the scattering length, $\overline{b}$, for the scattering system is given by,

$$\overline{b} = \sum_i f_i b_i \tag{2.28}$$

and the mean square value, $\overline{b^2}$, is given by

$$\overline{b^2} = \sum_i f_i {b_i}^2. \tag{2.29}$$

Here uncorrelated sites are assumed, that is to say whatever the value b_j for one

nucleus is, the probability for another nucleus to have the value b_i is f_i.

For the case that the scattering system contains a large number of nuclei (usually fulfilled in an experiment) the measured cross-section is a good approximation of the average over a whole ensemble of scattering systems and equation 2.24 can be written as,

$$\left(\frac{d^2\sigma}{d\Omega dE'}\right) = \frac{k'}{k}\sum_{jj'}\overline{b_j b_{j'}}\,A(\underline{Q},\omega) \tag{2.30}$$

where

$$A(\underline{Q},\omega) = \frac{1}{2\pi\hbar}\int_{-\infty}^{\infty}\left\langle e^{-i\underline{Q}\cdot\underline{R}_{j'}(0)}\,e^{-i\underline{Q}\cdot\underline{R}_j(t)}\right\rangle e^{-i\omega t}dt. \tag{2.31}$$

From the assumption of no correlation between the values of b_i for different nuclei it follows that

$$\overline{b_j b_{j'}} = \begin{cases} \overline{b_j b_{j'}} = (\overline{b})^2 & \text{if j} \neq \text{j}' \\ \overline{b_j^2} = \overline{b^2} & \text{if j} = \text{j}'. \end{cases} \tag{2.32}$$

This gives the possibility to separate the double differential cross-section into a coherent and an incoherent part:

$$\begin{aligned}\left(\frac{d^2\sigma}{d\Omega dE'}\right) &= \frac{k'}{k}\overline{b}^2\sum_{jj'\,j'\neq j}A(\underline{Q},\omega) + \frac{k'}{k}\overline{b^2}\sum_j A(\underline{Q},\omega) \\ &= \frac{k'}{k}\overline{b}^2\sum_{jj'}A(\underline{Q},\omega) + \frac{k'}{k}\left(\overline{b^2}-\overline{b}^2\right)\sum_j A(\underline{Q},\omega) \\ &= \frac{\sigma_{coh}}{4\pi}\frac{k'}{k}\sum_{jj'}A(\underline{Q},\omega) + \frac{\sigma_{inc}}{4\pi}\frac{k'}{k}\sum_j A(\underline{Q},\omega) \\ &= \left(\frac{d^2\sigma}{d\Omega dE'}\right)_{coh} + \left(\frac{d^2\sigma}{d\Omega dE'}\right)_{inc}\end{aligned} \tag{2.33}$$

where $\sigma_{coh} = 4\pi\overline{b}^2$ and $\sigma_{inc} = 4\pi\left(\overline{b^2}-\overline{b}^2\right)$ are called the *coherent* and *incoherent cross-section* respectively.

The coherent scattering describes the correlations between the positions of the same nucleus at different times and the correlations between different nuclei at different times. It therefore gives rise to interference effects. The incoherent scattering only depends, however, on correlations of the same nucleus at different times, and does not give rise to interference effects. Physically it arises from the random distribution of the scattering lengths from their mean value.

The expressions for $\overline{\text{b}}$ and $\overline{\text{b}^2}$ will now be derived for a scattering system consisting of a single isotope with nuclear spin I. Then the spin of the nucleus-neutron

system has the value I + $\frac{1}{2}$ or I - $\frac{1}{2}$. The scattering lengths for these two spin states are denoted by b^+ and b^- respectively. The number of states with spin I + $\frac{1}{2}$ is given by

$$2(I+\frac{1}{2})+1 = 2I+2 \tag{2.34}$$

and the number of states with spin I - $\frac{1}{2}$ is given by

$$2(I-\frac{1}{2})+1 = 2I. \tag{2.35}$$

Assuming each spin has the same probability, i.e. unpolarised neutrons are used and the nuclear spins are randomly oriented, then the scattering length b^+ occurs with the frequency

$$f^+ = \frac{2I+2}{4I+2} = \frac{I+1}{2I+1} \tag{2.36}$$

and b^- occurs with the frequency

$$f^- = \frac{2I}{4I+2} = \frac{I}{2I+1}. \tag{2.37}$$

Thus

$$\overline{b} = \frac{1}{2I+1}\left[(I+1)b^+ + Ib^-\right]. \tag{2.38}$$

In the case of several isotopes contained in the scattering system, both frequencies have to be multiplied by the relative abundance of each isotope. Therefore in general the average values of $\overline{b}$ and $\overline{b^2}$ are given by

$$\overline{b} = \sum_\xi \frac{c_\xi}{2I_\xi+1}\left[(I_\xi+1)b_\xi^+ + I_\xi b_\xi^-\right] \tag{2.39}$$

and

$$\overline{b^2} = \sum_\xi \frac{c_\xi}{2I_\xi+1}\left[(I_\xi+1)(b_\xi^+)^2 + I_\xi(b_\xi^-)^2\right] \tag{2.40}$$

where c_ξ is the relative abundance of the ξ^{th} isotope, I_ξ its nuclear spin and b_ξ^+ and b_ξ^- its scattering lengths.

2.8 Definition of Correlation Functions

For a system comprising N particles an *intermediate scattering function* $I(\underline{Q},t)$ can be defined,

$$I(\underline{Q},t) = \frac{1}{N}\sum_{jj'}\left\langle e^{-i\underline{Q}\cdot\underline{R}_{j'}(0)}\, e^{-i\underline{Q}\cdot\underline{R}_j(t)}\right\rangle \tag{2.41}$$

that is used to express the thermal averages in equation 2.24. Using this the functions G($\underline{r}$, t) and S($\underline{Q}, \omega$) can be defined as

$$G(\underline{r},t) = \frac{1}{(2\pi)^3} \int I(\underline{Q},t)\, e^{-i\underline{Q}\cdot\underline{r}}\, d\underline{Q} \tag{2.42}$$

$$S(\underline{Q},\omega) = \frac{1}{2\pi\hbar} \int I(\underline{Q},t)\, e^{-i\omega t}\, dt. \tag{2.43}$$

From inverse Fourier transform relations it follows that I($\underline{Q}$, t) is the Fourier transform of G($\underline{r}$, t) in position and the Fourier transform of S($\underline{Q}, \omega$) in energy,

$$I(\underline{Q},t) = \int G(\underline{r},t)\, e^{i\underline{Q}\cdot\underline{r}}\, d\underline{r} \tag{2.44}$$

$$I(\underline{Q},t) = \hbar \int S(\underline{Q},\omega)\, e^{i\omega t}\, d\omega \tag{2.45}$$

$G(\underline{r},t)$ is called the *time-dependent correlation function* or the *van Hove correlation function* of the scattering system, and $S(\underline{Q},\omega)$ the *scattering law* or the *dynamical structure factor*. Both are connected to each other via a Fourier transform,

$$G(\underline{r},t) = \frac{\hbar}{(2\pi)^3} \int S(\underline{Q},\omega)\, e^{-i(\underline{Q}\cdot\underline{r}-\omega t)}\, d\underline{Q}\, d\omega, \tag{2.46}$$

$$S(\underline{Q},\omega) = \frac{1}{2\pi\hbar} \int G(\underline{r},t)\, e^{i(\underline{Q}\cdot\underline{r}-\omega t)}\, d\underline{r}\, dt \tag{2.47}$$

and are used to describe the coherent part of the double differential cross-section. Similarly a *self intermediate scattering function* can be defined by,

$$I_s(\underline{Q},t) = \frac{1}{N} \sum_j \left\langle e^{-i\underline{Q}\cdot\underline{R}_j(0)}\, e^{-i\underline{Q}\cdot\underline{R}_j(t)} \right\rangle \tag{2.48}$$

and gives rise to a corresponding *self time-dependent pair correlation function* $G_s(\underline{r},t)$ and to the *incoherent dynamical structure factor* $S_i(\underline{Q},\omega)$. Using equations 2.33 and 2.31 the double differential cross-section can now be written in terms of the dynamical structure factors:

$$\left(\frac{d^2\sigma}{d\Omega dE'}\right) = \frac{\sigma_{coh}}{4\pi}\frac{k'}{k} N\, S(\underline{Q},\omega) + \frac{\sigma_{inc}}{4\pi}\frac{k'}{k} N\, S_i(\underline{Q},\omega) \tag{2.49}$$

This equation contains terms that only depend on the nature of the neutron-nucleus interaction, $\sigma_{\mathrm{coh}}\,\frac{k'}{k}$ and $\sigma_{\mathrm{inc}}\,\frac{k'}{k}$, and terms that describe the properties of the scattering system at thermal equilibrium, S($\underline{Q}, \omega$) and $S_i(\underline{Q},\omega)$. These dynamical structure factors are real functions, describing observable quantities.

If one is exclusively interested in the structure of the system, this means the relative positions of the different nuclei, but not the dynamics, then the time dependence can be omitted. Therefore a system at a particular time t = 0 is considered and the particle positions are assumed to be 'frozen'. In this case the position operators $\underline{R}_j(0)$ and $\underline{R}_{j'}(0)$ commute, thus with using equation 2.41, equation 2.42 can be written as,

$$\begin{aligned} G(\underline{r},0) &= \frac{1}{N}\sum_{jj'}\left\langle \delta(\underline{r}-\underline{R}_j(0)-\underline{R}_{j'}(0))\right\rangle \\ &= \frac{1}{N}\sum_{jj'\,j\neq j'}\left\langle \delta(\underline{r}-\underline{R}_j(0)-\underline{R}_{j'}(0))\right\rangle + \delta(\underline{r}) \\ &= n_0\, g(\underline{r}) + \delta(\underline{r}) \end{aligned} \tag{2.50}$$

where $n_0 = \frac{N}{V}$ is the number density of the system and $g(\underline{r})$ is called the *pair distribution function.* $g(\underline{r})$ describes the probability of finding an atom in a volume element $d\underline{r}$ at a distance $\underline{r}$ from the origin of the coordinates.

In the case of isotropic scattering systems, like liquids and glasses, the vectors $\underline{r}$ and $\underline{Q}$ in the above equations can be replaced by their moduli r and Q. Then the pair distribution function is connected with the structure factor via a sine Fourier transform and reads as

$$g(r) = 1 + \frac{1}{2\pi^2 r n_0}\int_0^\infty Q\,[S(Q)-1]\,sin(Qr)\,dQ \tag{2.51}$$

where *S(Q)* is called the *static structure factor.*

2.9 The static approximation and Placzek correction

In a real diffraction experiment an effective differential cross-section is measured:

$$\left(\frac{d\sigma}{d\Omega}\right)_{coh}^{eff} = N\frac{\sigma_{coh}}{4\pi}\int_{-\infty}^{E_0/\hbar}\frac{k'}{k}\,\eta(k')\,S(\underline{Q},\omega)\,d\omega \tag{2.52}$$

where E_0 is the energy of the incident neutrons. For a reactor experiment, the detector, characterised by an efficiency $\eta(k')$, integrates over the whole energy range of the scattered neutrons, but the integration is carried out at constant angle θ instead of constant values of $\underline{Q}$. Both are connected via

$$Q^2 = k'^2 + k^2 - 2kk'\,cos(2\theta), \tag{2.53}$$

see the scattering triangle (figure 2.2). To perform the data analysis of a real experiment it is necessary to use the static approximation, which holds if the energy of the incident neutrons is large compared to the energy transfer involved in the neutron-nucleus interaction, i.e. $E_0 \gg (\hbar\omega)$ such that $k' \cong k$ and therefore equation 2.53 reduces to $Q^2 = 2k^2\,[1 - \cos(2\theta)]$ or $Q = \frac{4\pi}{\lambda}\sin\theta$. This requirement is problematical for nuclei of low mass and incoming neutrons with low energies. It also has to be ensured that the main area of the dynamical structure factor $S(\underline{Q},\omega)$ (e.g. the Rayleigh and Brillouin modes at low-Q) lie within the integration path of the detector.

By using the static approximation the effective differential cross-section simplifies to

$$\left(\frac{d\sigma}{d\Omega}\right)_{coh}^{eff} = N\,\frac{\sigma_{coh}}{4\pi}\,\eta_0\,S(\underline{Q}) \tag{2.54}$$

where η_0 is the detector efficiency for elastically scattered neutrons. Small deviations from the static approximation, i.e. the difference between the quantity measured with $\frac{\hbar\omega}{E_0} \neq 0$ and the ideal result for $\frac{\hbar\omega}{E_0} \to 0$, can be corrected following a procedure invented by Placzek[5], that takes the recoil energy of the scattering nucleus and the detector efficiency into account. In the approach of Yarnell et al.[6] the integrand in equation 2.52 is expanded about $\hbar\omega = 0$, i.e. $k = k_0$, and is written in terms of a series in frequency moments of $S(Q,\omega)$ with Q constant, defined by

$$\langle\omega^n\rangle_{coh(inc)} = \int_{-\infty}^{\infty} \omega^n\,S_{(i)}(Q,\omega)\,d\omega\,. \tag{2.55}$$

This gives for the zeroth moments $<\omega^0>_{coh} = S(Q)$ and $<\omega^0>_{inc} = 1$,
for the 1st moments $\hbar <\omega^1>_{coh} = \hbar <\omega^1>_{inc} = E_{rec}$ and
for the 2nd moments $\hbar^2 <\omega^2>_{coh} = \hbar^2 <\omega^2>_{inc} = E_{rec}^2 + 2k_B T E_{rec}$, where $E_{rec} = \frac{\hbar^2 Q^2}{2M}$ is the recoil energy of the scattering nucleus. A detailed discussion can be found in Yarnell et al.[6].

Using this correction the effective coherent cross-section $\left(\frac{d\sigma}{d\Omega}\right)_{coh}^{eff}$ becomes

$$\begin{aligned}\left(\frac{d\sigma}{d\Omega}\right)_{coh}^{eff} &= \eta_0\frac{\sigma_{coh}}{4\pi}\left[S(Q) - c_1\frac{E_{rec}}{E_0} + c_2\left(\frac{E_{rec}}{E_0}\right)^2 - c_3\frac{E_{rec}}{E_0}\frac{k_BT}{E_0}\right.\\ &\quad\left. + \frac{m}{2M}\left(\frac{E_{rec}}{E_0} + \frac{k_BT}{E_0}\right)\right]\end{aligned} \tag{2.56}$$

where m is the mass of the neutron, M the mass of an atom in the scattering system and c_1, c_2 and c_3 are constants depending on the detector efficiency. The detector efficiency $\eta(k')$ is usually given as

$$\eta(k') = \frac{1 - e^{-\frac{\gamma}{k'}}}{\eta_0} \tag{2.57}$$

where η_0 is the detector efficiency for neutrons having the incident energy E_0, k' is given by $k' = \frac{2\pi}{\lambda}$ and for a ^{3}He gas detector, the parameter γ is proportional to the number of gas particles in the detector.

A different approach to Placzek[5] is given by Wick[7], and is used by Egelstaff & Soper[8] to obtain a general correction for inelasticity effects. It is an approximate method, which is based on the expansion of $S(Q,\omega)$ about the recoil energy E_{rec}. Wick's method may therefore provide for a better correction for scattering systems comprising light elements (Egelstaff[9]), assuming that the corrections are carried out to the same order.

The corrections to deviations from the static approximation for time-of-flight experiments are discussed in Powles[10],[11] and Howe et al.[12]

2.10 Multicomponent systems

In this chapter the equations for the scattering cross-sections will be generalised to the case of multicomponent systems.

A system of volume V comprising ξ chemical species labeled α, where $\alpha = 1, 2, \cdots, \xi$ is considered. Then the total number N of atoms in the system is given by $N = \sum_{\alpha=1}^{\xi} N_\alpha$, with N_α being the number of atoms of type α. The atomic fraction c_α of each species is $c_\alpha = \frac{N_\alpha}{N}$ and the atomic number density $\rho_\alpha = \frac{N_\alpha}{V}$. The total number density is defined by $n_0 = \frac{N}{V}$ like that of a single component system. Using the above definitions, equation 2.24 for the double differential cross-section

$$\begin{aligned}\left(\frac{d^2\sigma}{d\Omega dE'}\right) &= \frac{k'}{k}\sum_{\alpha=1}^{\xi}\sum_{\beta=1}^{\xi}\overline{b_\alpha}\,\overline{b_\beta}\sqrt{N_\alpha N_\beta}\,S_{\alpha\beta}(Q,\omega) + \frac{k'}{k}\sum_{\alpha=1}^{\xi} b_{\alpha,inc}^2\,N_\alpha\,S_{\alpha,inc}(Q,\omega)\,,\\ \left(\overline{\frac{d^2\sigma}{d\Omega dE'}}\right) &= \frac{}{k}\sum_{\alpha=1}^{}\sum_{\beta=1}^{} b_\alpha\,b_\beta\,\sqrt{N_\alpha N_\beta}\,S_{\alpha\beta}(Q,\omega) + \frac{}{k}\sum_{\alpha=1}^{} b_{\alpha,inc}^{2}\,N_\alpha\,S_{\alpha,inc}(Q,\omega)\,,\end{aligned} \tag{2.58}$$

where $S_{\alpha\beta}(Q,\omega)$ is called the *partial dynamical structure factor* and $S_{\alpha,inc}(Q,\omega)$ the *self partial dynamical structure factor*. The differential scattering cross-section

is obtained by integrating equation 2.58 with respect to energy transfers,

$$\frac{d\sigma}{d\Omega} = \sum_{\alpha=1}^{\xi} \sum_{\beta=1}^{\xi} \overline{b_\alpha}\,\overline{b_\beta} \sqrt{N_\alpha N_\beta}\, S_{\alpha\beta}^{AL}(Q) + N \sum_{\alpha=1}^{\xi} c_\alpha b_{\alpha,inc}^2, \tag{2.59}$$

where $S_{\alpha\beta}^{AL}(Q)$ is known as an *Ashcroft-Langreth partial structure factor* (Ashcroft & Langreth[14]) and is related to the *partial pair distribution function* $g_{\alpha\beta}(r)$ via

$$S_{\alpha\beta}^{AL}(Q) = \sqrt{\rho_\alpha \rho_\beta} \int_{-\infty}^{\infty} e^{i\underline{Q}\cdot\underline{r}} \left[g_{\alpha\beta}(\boldsymbol{r}) - 1\right] dr + \delta_{\alpha\beta}. \tag{2.60}$$

More frequently used by experimentalists is the description using the so-called *Faber-Ziman*[13] *partial structure factors* $S_{\alpha\beta}(Q)$, which are defined by

$$S_{\alpha\beta}(Q) = 1 + n_0 \int_{-\infty}^{\infty} e^{i\underline{Q}\cdot\underline{r}} \left[g_{\alpha\beta}(r) - 1\right] dr\,. \tag{2.61}$$

Therefore they are connected with the $S_{\alpha\beta}^{AL}(Q)$'s by

$$S_{\alpha\beta}^{AL}(Q) = \left[S_{\alpha\beta}(Q) - 1\right] \sqrt{c_\alpha c_\beta} + \delta_{\alpha\beta}. \tag{2.62}$$

At high values of Q, $S_{\alpha\beta}(Q)$ tends to unity, hence using equation 2.62 and substituting it into equation 2.59 gives for the differential cross-section

$$\frac{d\sigma}{d\Omega} = N \left[F(Q) + \sum_{\alpha=1}^{\xi} c_\alpha \left(\overline{b_\alpha^2} + b_{\alpha,inc}^2\right)\right], \tag{2.63}$$

where $\sum_{\alpha=1}^{\xi} c_\alpha \left(\overline{b_\alpha^2} + b_{\alpha,inc}^2\right)$ is called the *self scattering term* and *F(Q)* is known as the *total structure factor*,

$$F(Q) = \sum_{\alpha=1}^{\xi} \sum_{\beta=1}^{\xi} \overline{b_\alpha}\,\overline{b_\beta}\, c_\alpha c_\beta \left[S_{\alpha\beta}(Q) - 1\right]. \tag{2.64}$$

F(Q) is defined as a linear combination of all the Faber-Ziman partial structure factors $S_{\alpha\beta}(Q)$ for the system, that are weighted by the product of the atomic fractions $c_\alpha c_\beta$ with the scattering lengths $\overline{b_\alpha}\,\overline{b_\beta}$. F(Q) therefore contains information about all of the neutron-weighted atomic pair-correlations in the system.

In the case of an isotropic scattering system the Faber-Ziman partial structure factors $S_{\alpha\beta}(Q)$ are related to the partial pair-distribution functions $g_{\alpha\beta}(r)$ via a sine Fourier transform

$$g_{\alpha\beta}(r) = 1 + \frac{1}{2\pi^2 r n_0} \int_0^{\infty} Q \left[S_{\alpha\beta}(Q) - 1\right] sin(Qr)\, dQ. \tag{2.65}$$

Therefore the real-space function, G(r), measured in a single diffraction experiment on a multicomponent system is given by

$$\begin{aligned} G(r) &= \frac{1}{2\pi^2 r n_0}\int_0^\infty Q\,F(Q)\,sin(Qr)\,dQ \\ &= \sum_{\alpha=1}^{\xi}\sum_{\beta=1}^{\xi}\overline{b_\alpha}\,\overline{b_\beta}\,c_\alpha c_\beta\,[g_{\alpha\beta}(r)-1]. \end{aligned} \tag{2.66}$$

From equation 2.65 it follows that for the low-r limit $r \to 0$, $g_{\alpha\beta}(r) = 0$, hence

$$G(0) = -\sum_{\alpha=1}^{\xi}\sum_{\beta=1}^{\xi}\overline{b_\alpha}\,\overline{b_\beta}\,c_\alpha c_\beta\,. \tag{2.67}$$

Assuming the special case of a binary system A_xB_{1-x} $(0 \le x \le 1)$, a further method of defining the partial structure factors, following the work of Bhatia & Thornton[15], is very useful. The total structure factor F(Q) describing the coherent scattering can be written as,

$$\begin{aligned} F(Q) &= <b>^2\,[S_{NN}(Q)-1] + x(1-x)(b_A-b_B)^2\left[\frac{S_{CC}(Q)}{x(1-x)}-1\right] \\ &\quad + 2<b>(b_A-b_B)S_{NC}(Q) \end{aligned} \tag{2.68}$$

where $<b> = xb_A + (1-x)b_B$ and b_A, b_B are the coherent scattering lengths of the chemical species A or B. $S_{NN}(Q)$, $S_{NC}(Q)$ and $S_{CC}(Q)$ are called the *Bhatia-Thornton (BT) number-number, number-concentration* and *concentration-concentration partial structure factor* respectively. The Bhatia-Thornton partial structure factors can also be written as linear combinations of the Faber-Ziman partial structure factors,

$$\begin{aligned} S_{NN}(Q) &= x^2 S_{AA}(Q) + (1-x)^2 S_{BB}(Q) + 2x(1-x)S_{AB}(Q) \\ S_{NC}(Q) &= x(1-x)\,[x(S_{AA}(Q)-S_{AB}(Q)) - (1-x)(S_{BB}(Q)-S_{AB}(Q))] \\ S_{CC}(Q) &= x(1-x)\,[1 + x(1-x)(S_{AA}(Q)+S_{BB}(Q)-2S_{AB}(Q))]\,. \end{aligned} \tag{2.69}$$

The representation in real-space is given by the Fourier transform of F(Q),

$$\begin{aligned} G(r) &= \frac{1}{2\pi^2 r n_0}\int_0^\infty Q\,F(Q)\,sin(Qr)\,dQ \\ &= <b>^2\,[g_{NN}(r)-1] + x(1-x)(b_A-b_B)^2 g_{CC}(r) \\ &\quad + 2x(1-x)<b>(b_A-b_B)g_{NC}(r), \end{aligned} \tag{2.70}$$

where $g_{\alpha\beta}(r)$ are called the *Bhatia-Thornton partial pair-distribution functions.* They are defined by

$$\begin{aligned} g_{NN}(r) &= x^2 g_{AA}(r) + (1-x)^2 g_{BB}(r) + 2x(1-x)g_{AB}(r) \\ g_{NC}(r) &= [x(g_{AA}(r) - g_{AB}(r)) - (1-x)(g_{BB}(r) - g_{AB}(r))] \\ g_{CC}(r) &= x(1-x)\left[g_{AA}(r) + g_{BB}(r) - 2g_{AB}(r)\right] \end{aligned} \tag{2.71}$$

The Fourier transform of $S_{NN}(Q)$, $g_{NN}(r)$, describes the topology of the binary scattering system, i.e. the sites of the scattering nuclei irrespective of the chemical species occupying those sites. For a binary system with $b_A \approx b_B$ the measured total structure factor F(Q) is approximately identical to $S_{NN}(Q)$. $S_{NC}(Q)$ describes the number-concentration fluctuations in the scattering system. If $S_{NC}(Q) = 0$ for all Q the system can be considered as a random substitutional alloy, i.e. the probability of a particle exchanging is independent of the species type. $S_{CC}(Q)$ and its Fourier transform $g_{CC}(r)$ represent the fluctuations in concentration in the scattering system. Deviations of $S_{CC}(Q)$ from the product of the concentrations x and $(1-x)$ indicate that the distribution of atoms is not random. $S_{CC}(Q)$ is measured directly for a binary system where $< b >= 0$, such systems are called 'zero alloys'.

2.11 Method of isotopic substitution

The method of isotopic substitution is a very powerful method that can be used in neutron diffraction to help tackle the problem of resolving the structure of multi-component systems.

This method is based on varying the isotopic composition of the scattering system in a way such that two or more samples are produced that are identical in every respect except for the isotopic enrichment of a one or more of the chemical species. As the scattering length $\overline{b}$ varies for different isotopes, the weighting factors for individual $S_{\alpha\beta}(Q)$ in the measured total structure factors (see equation 2.64) are changed. Thus the total structure factors for the different enriched samples can show measurable differences. In this case it is possible to extract some or even all of the partial structure factors $S_{\alpha\beta}(Q)$ and hence the partial pair-distribution functions $g_{\alpha\beta}(r)$. This procedure was first considered by Keating[16] in 1963 and

actually implemented for the first time by Enderby, North and Egelstaff[17] in 1966 for the investigation of Cu_6Sn_5. A real limiting factor to the method of isotopic substitution is the availability of suitable isotopes. This means that the difference in the scattering lengths has to be large enough to allow for a measurable difference between the F(Q)'s of the individual samples. Elements that fulfil this requirement include H, Li, Cl, Ag, Ni, Cu, Ge and Se. In these elements the contrast in the $\overline{b}$ values $\Delta\overline{b} \geq 2\,\mathrm{fm}$.

2.12 Difference Functions

The total structure factor measured in a single diffraction experiment on a multi-component system comprising ξ chemical species contains $\frac{\xi(\xi+1)}{2}$ independent partial structure factors $S_{\alpha\beta}(Q)$. Consider a binary system A_xB_{1-x}, with $x = c_A$ and $1 - x = c_B$ being the atomic fractions of the species A and B respectively. To obtain all three partial structure factors $S_{AA}(Q)$, $S_{AB}(Q)$ and $S_{BB}(Q)$ three diffraction measurements on different enriched samples have to be performed.

Let the three total structure factors be called F(Q), 'F(Q) and ''F(Q), where

$$\begin{aligned} F(Q) &= c_A^2 b_A^2 [S_{AA}(Q) - 1] + 2c_A c_B b_A b_B [S_{AB} - 1] + c_B^2 b_B^2 [S_{BB}(Q) - 1], \\ {}'F(Q) &= c_A^2 b_A'^2 [S_{AA}(Q) - 1] + 2c_A c_B b_A' b_B [S_{AB} - 1] + c_B^2 b_B^2 [S_{BB}(Q) - 1], \\ {}''F(Q) &= c_A^2 b_A''^2 [S_{AA}(Q) - 1] + 2c_A c_B b_A'' b_B' [S_{AB} - 1] + c_B^2 b_B'^2 [S_{BB}(Q) - 1]. \end{aligned} \tag{2.72}$$

Here b_A, b_A', b_A'' and b_B, b_B' are the coherent scattering lengths corresponding to the different enriched isotopes of A and B respectively. The problem can then be solved using the matrix representation for linear equations,

$$[F] = [A]\,[S] \tag{2.73}$$

where

$$[F] = \begin{vmatrix} F(Q) \\ {}'F(Q) \\ {}''F(Q) \end{vmatrix}, \quad [S] = \begin{vmatrix} S_{AA}(Q) - 1 \\ S_{AB}(Q) - 1 \\ S_{BB}(Q) - 1 \end{vmatrix} \tag{2.74}$$

and

$$[A] = \begin{vmatrix} c_A^2 b_A^2 & 2c_A c_B b_A b_B & c_B^2 b_B^2 \\ c_A^2 b_A'^2 & 2c_A c_B b_A' b_B & c_B^2 b_B^2 \\ c_A^2 b_A''^2 & 2c_A c_B b_A'' b_B' & c_B^2 b_B'^2 \end{vmatrix} \tag{2.75}$$

The solution of equation 2.73 is given by $[S] = [A]^{-1}[F]$. A measure of the reliability (conditioning) with which the $S_{\alpha\beta}$ are obtained, is given by the normalised determinant of the matrix [A], $|A_n|$ (Edwards et al.[18]); ideally $|A_n| = \pm 1$. However, the partial structure factors can be separated in a case where $|A_n| = -0.011$ (see Penfold[19]). In cases where this procedure cannot be used, e.g. when the matrix is strongly ill-conditioned or when the system comprises too many components, the method of difference functions is a powerful tool to reduce the number of unknown partial structure factors describing the multicomponent system.

Consider now a ternary system of type M-A-X, where M denotes a metal such as Cu or Ag, A a pnictogen like for example P or As and X a chalcogen such as S, Se or Te. By isotopically substituting the metal M, the weighting factors of the $S_{M\beta}(Q)$ correlations can be changed. Therefore on measuring the total structure factors, denoted by ${}^{M}F(Q)$ and ${}^{M'}F(Q)$ and assuming $b_M > b_{M'}$ the *first order difference function* $\Delta_M(Q)$ can be obtained,

$$\begin{aligned} \Delta_M(Q) &= {}^{M}F(Q) - {}^{M'}F(Q) \\ &= c_M^2(b_M^2 - b_{M'}^2)\,[S_{MM}(Q) - 1] + 2c_M c_X b_X (b_M - b_{M'})\,[S_{MX}(Q) - 1] \\ &\quad + 2c_M c_A b_A (b_M - b_{M'})\,[S_{MA}(Q) - 1]\,. \end{aligned} \tag{2.76}$$

Here the subscript M indicates that the first order difference function contains only those correlations involving the metal atom. Additionally a function known as the *total minus weighted difference function* $\Delta F(Q)$ can be defined,

$$\begin{aligned} \Delta F(Q) &= {}^{M}F(Q) - \frac{b_M}{b_M - b_{M'}}\Delta_M(Q) \\ &= -c_M^2 b_M b_M' [S_{MM}(Q) - 1] + c_A^2 b_A^2 [S_{AA}(Q) - 1] \\ &\quad + c_X^2 b_X^2 [S_{XX}(Q) - 1] + 2c_X c_A b_X b_A [S_{AX}(Q) - 1] \end{aligned} \tag{2.77}$$

In this equation the metal-A and metal-X correlations are eliminated and in the case of all $b > 0$ the metal-metal correlations are the only ones with a negative weighting. If in a certain region in real-space the A-A, A-X and X-X contributions

are small, then the metal-metal correlations reveal themselves in a negative going peak in $\Delta G(r)$ (see Penfold & Salmon[20]), the real-space representation of $\Delta F(Q)$.

The method of isotopic substitution and with it the method of difference functions meets one of its major challenges in measuring a *second order difference function*. Assume that a system comprises four components, where two can be isotopically substituted, e.g. one being a metal like Cu and one being hydrogen H, that can be substituted for D. Let the other two components be for example Cl and O. Then four samples are required that contain the different combinations of the isotopically enriched $'$Cu and $''$Cu, where $b_{'Cu} > b_{''Cu}$, with H and D to measure the partial structure factor $S_{CuH}(Q)$. Two first order difference functions, substituting for the metal, are measured for the H and D samples respectively,

$$\begin{aligned}\Delta^{(H)}_{Cu}(Q) &= c^2_{Cu}(b^2_{'Cu} - b^2_{''Cu})[S_{CuCu}(Q) - 1] + 2c_{Cu}c_{Cl}(b_{'Cu} - b_{''Cu})b_{Cl}[S_{CuCl}(Q) - 1] \quad (2.78)\\ &\quad + 2c_{Cu}c_O(b_{'Cu} - b_{''Cu})b_O[S_{CuO}(Q) - 1] + 2c_{Cu}c_H(b_{'Cu} - b_{''Cu})b_H[S_{CuH}(Q) - 1]\\ \Delta^{(D)}_{Cu}(Q) &= c^2_{Cu}(b^2_{'Cu} - b^2_{''Cu})[S_{CuCu}(Q) - 1] + 2c_{Cu}c_{Cl}(b_{'Cu} - b_{''Cu})b_{Cl}[S_{CuCl}(Q) - 1] \quad (2.79)\\ &\quad + 2c_{Cu}c_O(b_{'Cu} - b_{''Cu})b_O[S_{CuO}(Q) - 1] + 2c_{Cu}c_H(b_{'Cu} - b_{''Cu})b_D[S_{CuH}(Q) - 1]\end{aligned}$$

In these two functions only the Cu-H and Cu-D correlations have a different weighting. Hence subtracting them will directly reveal the Cu-hydrogen partial structure factor,

$$S_{CuH}(Q) - 1 = \frac{\Delta^{(D)}_M(Q) - \Delta^{(H)}_M(Q)}{2c_{Cu}c_H(b_{'Cu} - b_{''Cu})(b_D - b_H)}. \quad (2.80)$$

It is also possible to obtain a *first order difference function minus weighted second order difference function* from the above described method, e.g. the Cu-oxygen correlations can be measured, to a first order approximation,

$$\begin{aligned}\Delta^{\Delta}_{Cu}(Q) &= \frac{\Delta^{(D)}_{Cu}(Q) - 2c_{Cu}c_Hb_D(b_{'Cu} - b_{''Cu})[S_{CuH}(Q) - 1]}{2c_{Cu}c_O(b_{'Cu} - b_{''Cu})b_O} \quad (2.81)\\ &= [S_{CuO}(Q) - 1] + \frac{c_{Cu}(b_{'Cu} + b_{''Cu})}{2c_Ob_O}[S_{CuCu}(Q) - 1] + \frac{c_{Cl}b_{Cl}}{c_Ob_O}[S_{CuCl}(Q) - 1]\end{aligned}$$

Bibliography

[1] Squires G L, *Introduction to the theory of thermal neutron scattering*, University Press: Cambridge (1978).

[2] Lovesey S W, *Theory of neutron scattering from condensed matter*, Claredon Press (1984).

[3] Price D L, *Introduction in neutron scattering* in *Methods of Experimental Physics* Vol.23-Part A, eds. Sköld K and Price D L, Academic Press: Orlando (1986).

[4] Schwabl F, *Quantenmechanik*, Springer: New York (1990).

[5] Placzek G, *Phys. Rev.* **86** (1952) 377.

[6] Yarnell J L, Katz M J, Wentzel R G and Koenig S H, *Phys. Rev. A* **7(6)** (1973) 2130.

[7] Wick G C, *Phys. Rev.* **94** (1954) 1228.

[8] Egelstaff P A and Soper A K, *Molec. Phys.* **40** (1980) 553.

[9] Egelstaff P A, *Classical fluids* in *Methods of Experimental Physics* Vol.23-Part A, eds. Sköld K and Price D L, Academic Press: Orlando (1986).

[10] Powles J G, *Molec. Phys.* **26** (1973) 1235.

[11] Powles J G, *Molec. Phys.* **36** (1978) 1181.

[12] Howe M A, McGreevy R L and Howells W S, *J. Phys.: Cond Mat.* **1** (1989) 3433.

[13] Faber T E and Ziman J M, *Phil. Mag.* **11** (1965) 153.

[14] Ashcroft N W and Langreth D C, *Phys. Rev.* **156** (1967) 685.

[15] Bhatia A B and Thornton D E, *Phys. Rev. B* **2(8)** (1970) 3004.

[16] Keating D T *J. Appl. Phys.* **34** (1963) 923.

[17] Enderby J E, North D M and Egelstaff P A, *Phil. Mag.* **14** (1966) 961.

[18] Edwards F G, Enderby J E, Howe R A and Page D I, *J. Phys. C* **8** (1975) 3483.

[19] Penfold I T, *Ph.D. Thesis University of East Anglia* (1990).

[20] Penfold I T and Salmon P S, *J. Phys.: Condens. Matter* **2** (1990) SA233.

Chapter 3

Diffraction experiments and data treatment

In this chapter the instruments used to obtain the presented neutron diffraction data are described. Furthermore, the data analysis procedures and self consistency checks on the data are explained and the concept of coordination numbers is introduced.

The neutron diffraction experiments discussed in this thesis were carried out on the D4B instrument at the reactor source of the Institut Laue Langevin (ILL), Grenoble, and on the SANDALS (**S**mall **A**ngle **N**eutron **D**iffractometer for **A**morphous and **L**iquid **S**amples) and LAD (**L**iquids and **A**morphous Materials **D**iffractometer) instruments at the ISIS spallation source facility at the Rutherford Appleton Laboratory.

3.1 Neutron sources

In a diffraction experiment the transmitted intensity I(Q) is measured as a function of momentum transfer Q, where $Q = 4\pi\frac{\sin\theta}{\lambda}$. A variation in Q can be achieved in two different ways. Firstly by changing the scattering angle 2θ, i.e. changing the position of the detector that records I(Q) and keeping the wavelength of the incident neutrons fixed. This is the procedure implemented in reactor experiments. Secondly by fixing the scattering angle and using neutrons with different wavelengths. This is done in time-of-flight experiments.

The high-flux reactor at the ILL operates at a power of 58 MW. Neutrons are produced by nuclear fission using a 93 % enriched ^{235}U fuel element.
The spallation source at the ISIS facility is the most powerful source of pulsed neutrons in the world [1]. Neutrons are produced by bombarding a heavy metal target (depleted U or Ta) 50-times a second with highly energetic protons of energy 800 MeV.

3.2 Employed instruments

3.2.1 The D4B diffractometer

The D4B diffractometer, shown in figure 3.1, is especially adapted for the investigation of liquids, amorphous materials and gases. It offers a choice of wavelengths for the incident neutrons, 0.7 Å, 0.5 Å and 0.3 Å. The standard operation is at $\lambda = 0.7$ Å. At this wavelength the range of momentum transfers is $0.2\,\text{Å}^{-1} \leq Q \leq 16\,\text{Å}^{-1}$, with an optimum resolution of $\Delta Q/Q = 2\%$ and a maximum neutron flux of $4 \cdot 10^7\,\text{n}\,\text{cm}^{-1}\text{s}^{-1}$.

The instrument employs a hot source graphite moderator, which is kept at a temperature of 2400 K to enhance the neutron intensity in the wavelength range $0.4\,\text{Å} < \lambda < 0.8\,\text{Å}$. The (220) planes of a Cu single crystal are used as monochromators for $\lambda = 0.7\,\text{Å}$ neutrons, and $\lambda/2$ Ir filters are employed to suppress higher order scattering. Most of the beam path and the sample chamber are kept under vacuum to reduce the background scattering. In normal operation, the instrument is placed on a Tanzboden. It has two independent 2θ arms that cover the low and high angle scattering respectively. At the end of each of these spectrometer arms a 64-cell ^3He multidetector is positioned. The He pressure is 15 bar to allow for a reasonable detection efficiency even at low wavelengths. The sample to detector distances are 1.5 m and 0.75 m for the low angle and high angle detectors respectively.

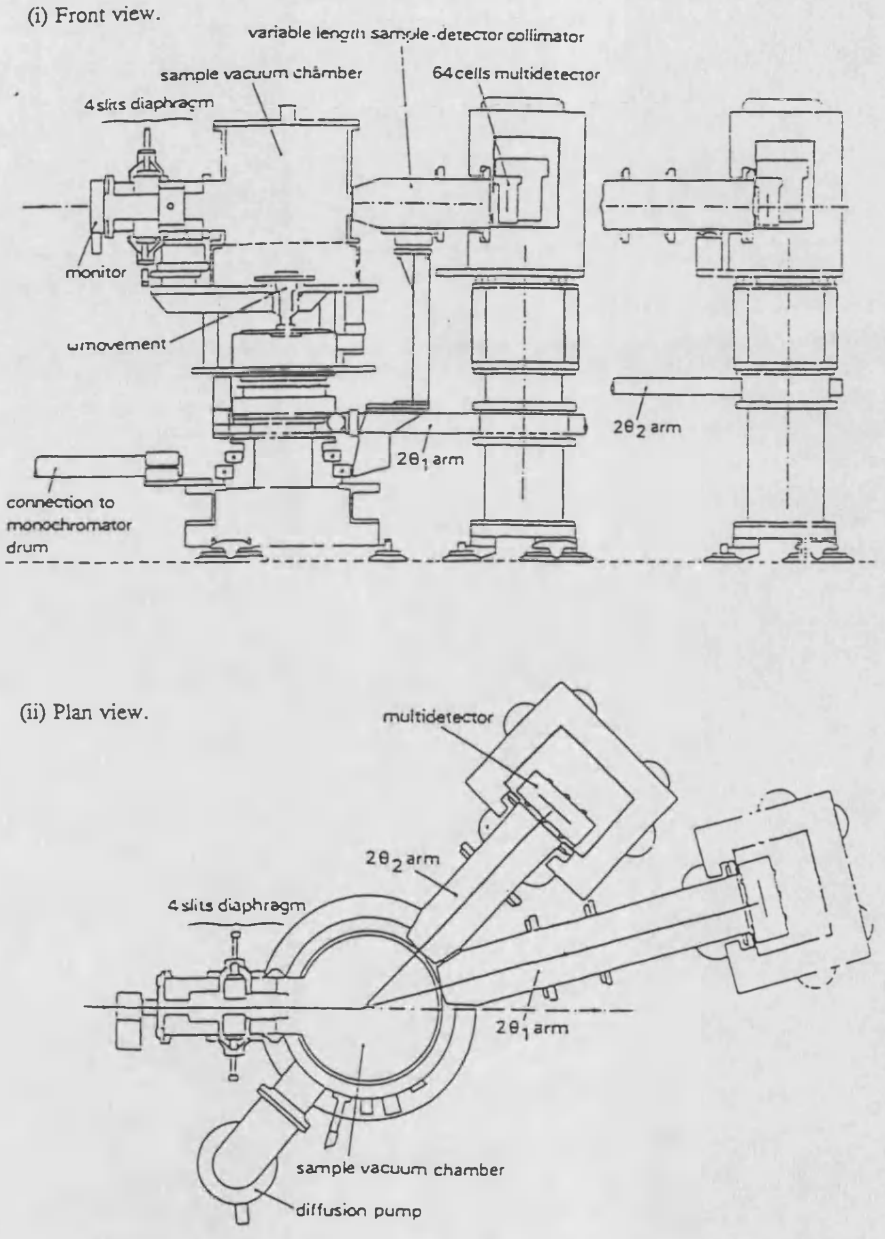

Figure 3.1: Schematic view of the D4B two-axis diffractometer.

3.2.2 The SANDALS diffractometer

SANDALS is a small angle diffractometer built for the investigation of liquids and amorphous solids (see figure 3.2). Using this second generation total scattering instrument the static structure factor S(Q) of a disordered material can be measured over a wide range of momentum transfers ($0.05\,\text{Å}^{-1} \leq Q \leq 50\,\text{Å}^{-1}$). Its high stability in combination with an intense pulsed neutron source allows the powerful technique of isotopic substitution to be employed. Inelasticity corrections are minimised by using an extensive low angle bank of detectors in connection with high energy neutrons (Soper[2]). SANDALS is therefore particularly useful for the measurement of structure factors of samples containing light atoms, such as hydrogen.

The incident neutron beam used on SANDALS originates in a methane moderator that is kept at a constant temperature of 100 K. A 32 mm diameter beam is then defined by a boron collimator. The incident neutron flight path is 11 m, the incident neutron wavelengths are in the range of 0.05 Å to 4.5 Å and the sample to detector distance varies between 0.75 m and 4.0 m depending on the particular detector bank. Currently there are 1180 zinc sulphide detectors installed on SANDALS that give a continuous angular coverage for 2θ of 3.8° to 39°[3]. The detectors are arranged in four banks and each bank is divided into modules of 20 detectors. The detectors, 10 mm wide x 20 mm deep x 200 mm tall, are arranged into 18 groups for the analysis procedure.

The following table summarises the specifications of all the detector banks.

Range in 2θ [°]	Number of Detectors	Groups	Resolution $\Delta Q/Q$ [%]
3-11	300	7-10	3-16
11-21	360	1-6	3
19-31	300	11-14	3
29-41	220	15-18	2

Table 3.1 : Specifications of the SANDALS detector banks

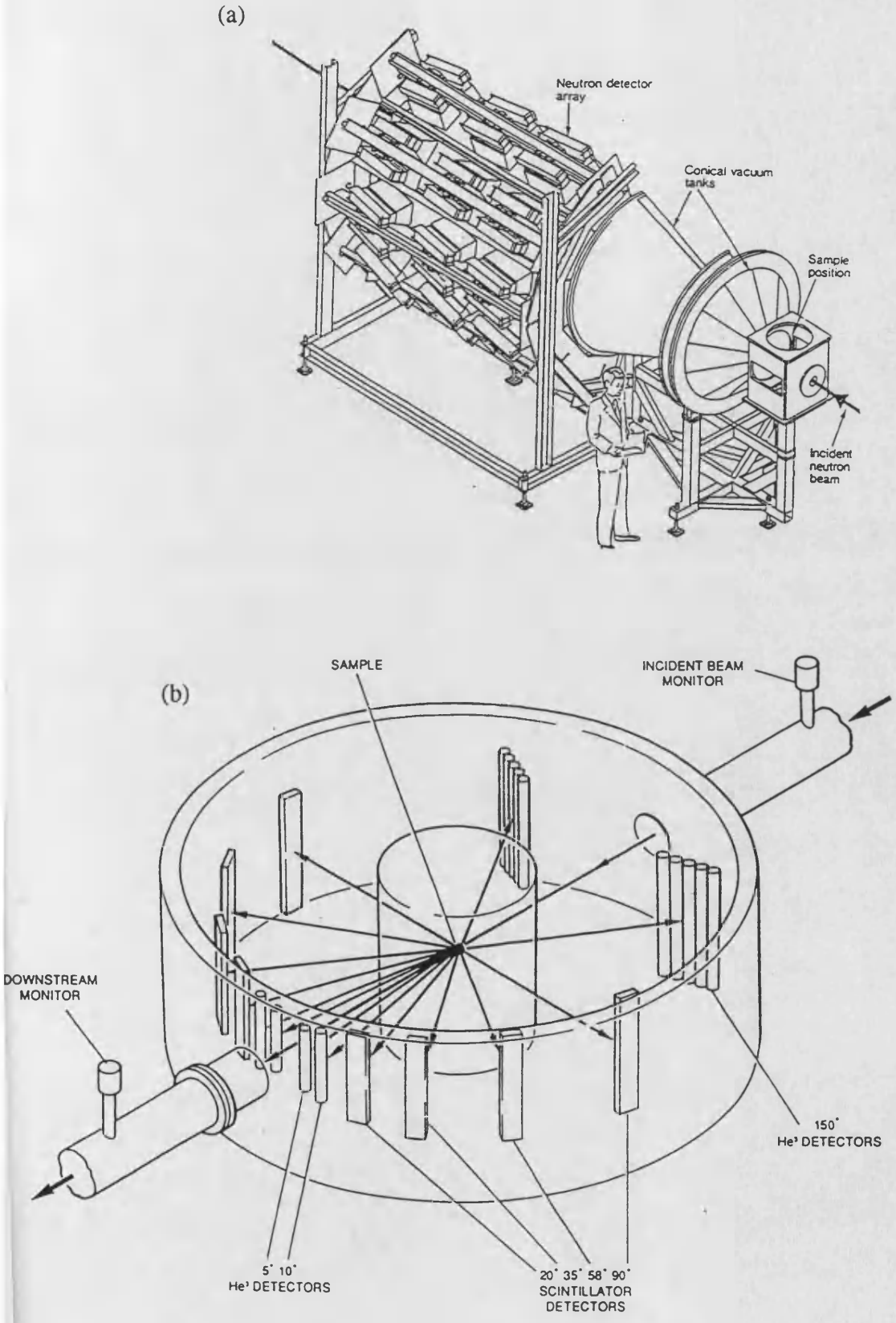

Figure 3.2: (a) The SANDALS instrument and (b) the LAD instrument.

3.2.3 The LAD diffractometer

LAD is a total scattering instrument optimised for the study of liquids and amorphous solids. It can also be used as a moderate resolution powder diffractometer [4].

The detector banks are positioned in a horizontal plane on either side of the instrument at scattering angles between 5° and 150°. Thus the static structure factor can be measured over a wide range of momentum transfers (0.25 $Å^{-1}$ to 50 $Å^{-1}$). Additional to a monitor, recording the incident neutron flux, LAD is equipped with a transmission monitor, enabling the total sample cross-sections to be measured.

Before entering the instrument, the high energy neutrons are slowed down to incident wavelengths between 0.25 Å and 6.5 Å in the same 100 K methane moderator as used by SANDALS. At the position of the sample (10 m away from the moderator) the rectangular beam is 40 mm high and 20 mm wide, but these dimensions can be reduced by inserting appropriate apertures. The flight path of the scattered neutrons to the detectors is about 1 m. Two types of detectors are implemented on LAD. For the 5°, 10° and 150° banks ^{3}He gas detectors are used, while all other banks are equipped with lithium glass scintillator detectors. The resolution $\Delta Q/Q$ of these detectors varies from 0.5 % (150°) to 11 % (5°).
Table 3.2 shows the LAD detector bank parameters.

Bank	Range in 2θ [°]	Resolution $\Delta Q/Q$ [%]	Detector Type
1	5	11	10 atm ^{3}He
2	10	6	10 atm ^{3}He
3	20	2.8	Li-glass scintillator
4	35	1.7	Li-glass scintillator
5	60	1.2	Li-glass scintillator
6	90	0.8	Li-glass scintillator
7	150	0.5	10 atm ^{3}He

Table 3.2 : Specifications of the LAD detector banks.

3.3 Data correction procedures

3.3.1 Reactor based experiments

The observed intensity in a reactor based experiment for a single component system, assuming a small sample, is proportional to the effective differential cross-section,

$$I_S^E(\theta) \propto \left(\frac{d\sigma}{d\Omega}\right)_{coh}^{eff}, \tag{3.1}$$

where $\left(\frac{d\sigma}{d\Omega}\right)_{coh}^{eff}$ is defined in equation 2.52. The sample is considered to be sufficiently small to neglect attenuation and multiple scattering effects and it is without a container. However in a real experiment the finite size of the sample, even if not placed in a container, gives rise to an attenuation of the neutron beam and multiple scattering events that have to be taken into account. Furthermore, for the purpose of data normalisation the diffraction pattern of a vanadium standard of similar dimensions to that of the sample has to be measured. All of the measured intensities include an additional contribution from the scattering due to the background, which also has to be corrected for.

The background corrected intensity for a single component, finite sized sample (without container), taking into account the attenuation and multiple scattering corrections, is given by,

$$\begin{aligned} I_S'^E(\theta) &= I_S^E(\theta) - I_B^E(\theta) \\ &= a(\theta) N_S A_{S,S}(\theta) \left[J(Q) + \frac{\sigma_S \Delta_S}{4\pi}\right] \\ &\equiv a(\theta) \left[I_S'(\theta) + M_S(\theta)\right] \end{aligned} \tag{3.2}$$

where

$$J(Q) = \overline{b}^2 \left[S(Q) - 1\right] + (\overline{b}^2 + b_{inc}^2) \left[1 + P(Q)\right], \tag{3.3}$$

$$M_S(\theta) = N_S A_{S,S}(\theta) \frac{\sigma_S \Delta_S}{4\pi} \tag{3.4}$$

and

$$Q = 4\pi \frac{sin\theta}{\lambda} \tag{3.5}$$

$M_S(\theta)$ is called the multiple scattering cross-section and is defined by Soper & Egelstaff[5]. $I_B^E(\theta)$ is the background scattering, $P(Q)$ the Placzek correction (see section 2.9) and $a(\theta)$ a normalisation factor, obtained from the measurement of the

vanadium diffraction pattern. σ_S is the scattering cross-section of the sample and Δ_S is the fraction of multiple to single scattered neutrons, calculated following the method of Blech & Averbach[6]. Finally $I'_S(\theta) = N_S A_{S,S}(\theta) J(Q)$, where $A_{S,S}(\theta)$ is the attenuation correction, i.e. the factor by which the incident and transmitted neutron beams are attenuated due to the presence of the sample. The method used to calculate $A_{S,S}(\theta)$ is described by Paalman & Pings[7].

To obtain an absolute normalisation of the measured diffraction patterns, vanadium is used as a standard. The coherent scattering cross-section for vanadium is negligible, and it can be considered as a fully isotropic elastic scatterer for thermal neutrons (Mayers[8]). The background corrected intensity for a vanadium rod $I'^E_V(\theta)$ is given by,

$$\begin{aligned} I'^E_V(\theta) &= I^E_V(\theta) - I^E_B(\theta) \\ &= a(\theta) N_V A_{V,V}(\theta) \left[b^2_{V,inc}(1 + P_V(Q)) + \frac{\sigma_V \Delta_V}{4\pi} \right] \end{aligned} \tag{3.6}$$

where $P_V(Q)$ is the Placzek correction for vanadium. From the above equation it follows for the normalisation factor $a(\theta)$ that

$$a(\theta) = \frac{I'^E_V(\theta)}{N_V A_{V,V}(\theta) b^2_{V,inc}[1 + P_V(Q)] + M_V(\theta)} \tag{3.7}$$

where $\mathrm{M_V}(\theta) = \mathrm{N_V A_{V,V}}(\theta) \frac{\sigma_V \Delta_V}{4\pi}$.

Usually the sample is placed in a container during an experiment and a furnace might be present. To perform the necessary corrections for the extraction of the real scattered intensity of the sample, $I_S(\theta)$, a series of further diffraction patterns have to be measured:

- The sample placed in its container in the furnace, $I^E_{SCH}(\theta)$
- The empty container in the furnace, $I^E_{CH}(\theta)$
- The empty furnace, $I^E_H(\theta)$
- A vanadium rod of dimensions similar to the sample, $I^E_V(\theta)$
- Background with nothing in the beam, $I^E_0(\theta)$
- A cadmium rod of dimensions close to those of the sample, $I^E_{Cd}(\theta)$

The measured diffraction pattern can be very sensitive to the positioning of the container (with and without the sample). It has therefore to be ensured that it is placed in exactly the same position (within to 0.1 mm) during each measurement.

The geometrical arrangement for the case of a cylindrical sample in a container and a furnace is illustrated in figure 3.3.

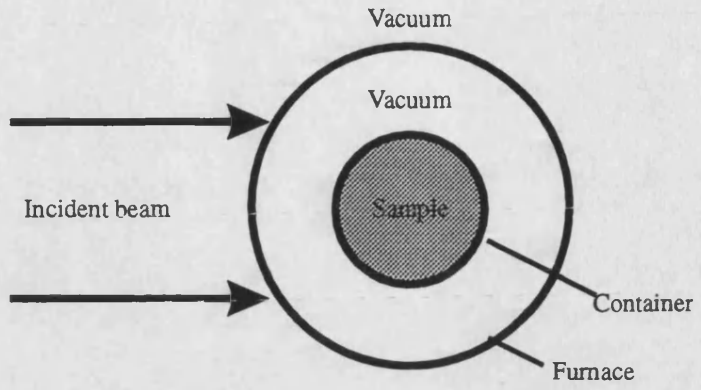

Figure 3.3: Plan view of the experimental geometry

Whenever the experimental conditions permit (exceptions are e.g. corrosive samples and high temperature experiments), the sample containers are made from materials having negligible coherent cross-sections, like vanadium and zirconium-titanium 'zero'-alloys. All of the furnaces used for the experiments described in this thesis were cylindrical vanadium foil furnaces that worked via resistive heating.

The measured background corrected intensities, $I'^{E}_{SCH}(\theta)$, $I'^{E}_{CH}(\theta)$ and $I'^{E}_{H}(\theta)$, are related to the intensities for single scattering from the sample, $I_S(\theta)$, the container, $I_C(\theta)$, and the heater, $I_H(\theta)$, via (see Poncet[9])

$$\begin{aligned} I'^{E}_{SCH}(\theta) &= A_{S,SCH}(\theta)I_S(\theta) + A_{C,SCH}(\theta)I_C(\theta) + A_{H,SCH}(\theta)I_H(\theta) + a(\theta)M_{SCH}(\theta) \\ I'^{E}_{CH}(\theta) &= A_{C,CH}(\theta)I_C(\theta) + A_{H,CH}(\theta)I_H(\theta) + a(\theta)M_{CH}(\theta) \\ I'^{E}_{H}(\theta) &= A_{H,H}(\theta)I_H(\theta) + a(\theta)M_H(\theta)\,. \end{aligned} \tag{3.8}$$

The $A_{i,j}(\theta)$ are the attenuation factors that describe attenuation (via absorption and scattering) of the intensity scattered in material i (S, C or H) by the presence of material j, see Poncet[9]. The $M_i(\theta)$ are the multiple scattering cross-sections.

The above equations can be used to express the single scattering from the sample, $I_S(\theta)$, and therefore $J(Q)$ (equation 3.3), see Salmon[10],

$$J(Q) = \frac{1}{Q_1}\left[\left[\frac{I^{E}_{SCH}(\theta)}{a(\theta)} - M_{SCH}(\theta)\right] - Q_2\left[\frac{I^{E}_{CH}(\theta)}{a(\theta)} - M_{CH}(\theta)\right] - Q_3\left[\frac{I^{E}_{H}(\theta)}{a(\theta)} - M_H(\theta)\right]\right] \tag{3.9}$$

where

$$Q_1 = N_S A_{S,SCH}(\theta)\,, \tag{3.10}$$

$$Q_2 = \frac{A_{C,SCH}(\theta)}{A_{C,CH}(\theta)} \tag{3.11}$$

and

$$Q_3 = \frac{1}{A_{H,H}(\theta)} \left[A_{H,SCH}(\theta) - A_{C,SCH}(\theta) \frac{A_{H,CH}(\theta)}{A_{C,CH}(\theta)} \right] . \tag{3.12}$$

For experiments with no furnace present, $Q_3 = 0$ and the subscript H can be omitted in equations 3.9 - 3.12.

Therefore when $J(Q)$ is known, the total structure factor for a single component system, S(Q), can be extracted using equation 3.3. For a multicomponent system J(Q) is written as,

$$J(Q) = F(Q) + \sum_{\alpha} c_{\alpha} (\overline{b_{\alpha}}^2 + b_{\alpha,inc}^2) [1 + P_{\alpha}(Q)] \tag{3.13}$$

where $F(Q)$ is the total structure factor that is defined by equation 2.64 and $P_{\alpha}(Q)$ is the Placzek correction for chemical species α. Hence $F(Q)$ can be extracted from $J(Q)$ by using equation 3.13.

At low values of θ ($\theta \leq 15°$) the background correction is performed by considering the intensity observed for a pure absorber of neutrons (cadmium), of the same size as the sample, placed at the sample position (Bertagnolli et al.[11]). Hence the effect of the sample on the background scattering is taken into account. In this low θ region $I_B^E(\theta)$ becomes,

$$I_B^E(\theta) = A_{H,H}(\theta) I_{Cd}^E(\theta) + A_{S,SCH}(\theta) [I_0^E(\theta) - I_{Cd}^E(\theta)] . \tag{3.14}$$

At higher θ values a straight forward subtraction of the background measured with nothing in the beam is made.

Figure 3.4 shows a flowchart of the procedures and programs used to extract G(r) from experimental data taken on D4B.

3.3.2 Time-of-flight experiments

For the analysis of data measured in time-of-flight experiments, the intensity measured as a function of time-of-flight first has to be rescaled to a function of the scattering vector Q. Then the detectors have to be corrected for deadtime and the intensity normalised to the incident flux shape. As the differential cross-section is measured at several different scattering angles, all the correction procedures have to be applied to each angle separately, before the individual data sets are merged.

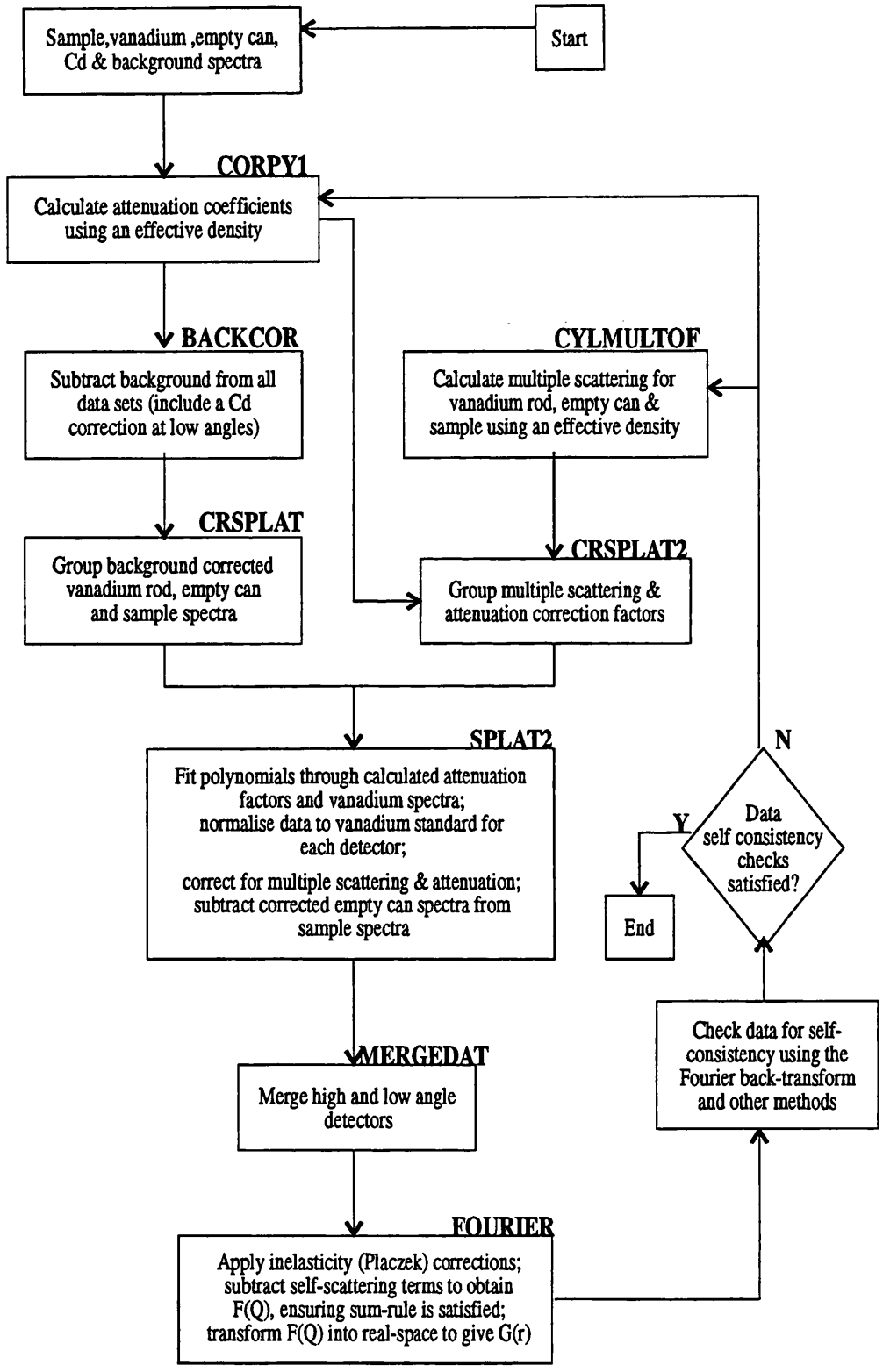

Figure 3.4: Data analysis programs used to extract G(r) from a diffraction experiment on a liquid or amorphous sample on a reactor source (D4B).

In the case of a nuclear resonance (at a fixed energy), the affected region can be left out, if the remaining detector banks still provide enough angular coverage, and provided that the scattering length does not change markedly through the resonance region, such that the levels of the data before and after the resonance region are the same.

Apart from the above, the same correction procedures as described in 3.3.1 are used to obtain the total structure factor F(Q) from SANDALS and LAD data (Soper et al.[2]). However, the cadmium correction cannot be applied at low angles as the Cd absorption resonance has a finite width and the material is not, therefore, a perfect absorber for all of the incident neutron energies. Also the incident wavelength changes, so the full wavelength dependence of the total scattering cross-section has to be used in the correction procedures (see Hannon et al.[12]). A flowchart of the correction programs for time-of-flight experiments is shown in fig 3.5

3.4 Difference functions

First and second order difference functions (section 2.12) have the important property that the coefficients of the total structure factors sum to zero, see equation 2.76. The inelasticity corrections $P_\alpha(Q)$ for chemical species that are not isotopically substituted will therefore cancel (equation 3.13), and the inelasticity corrections for the substituted species are often considerably reduced (see Soper et al.[13]). Furthermore, provided that the same container is used for all the sample measurements and that the total absorption and scattering cross-sections of the samples are similar, the multiple scattering and container corrections in equation 3.9 will themselves be similar for all samples. Hence, in the first order difference function, to a first order approximation, any systematic errors that may arise from these corrections will cancel.

3.5 Data transformation

The scattered intensity is measured in reciprocal-space (Q-space), and to obtain the real-space representation a sine Fourier transform (see e.g. Champeney[14]) of the

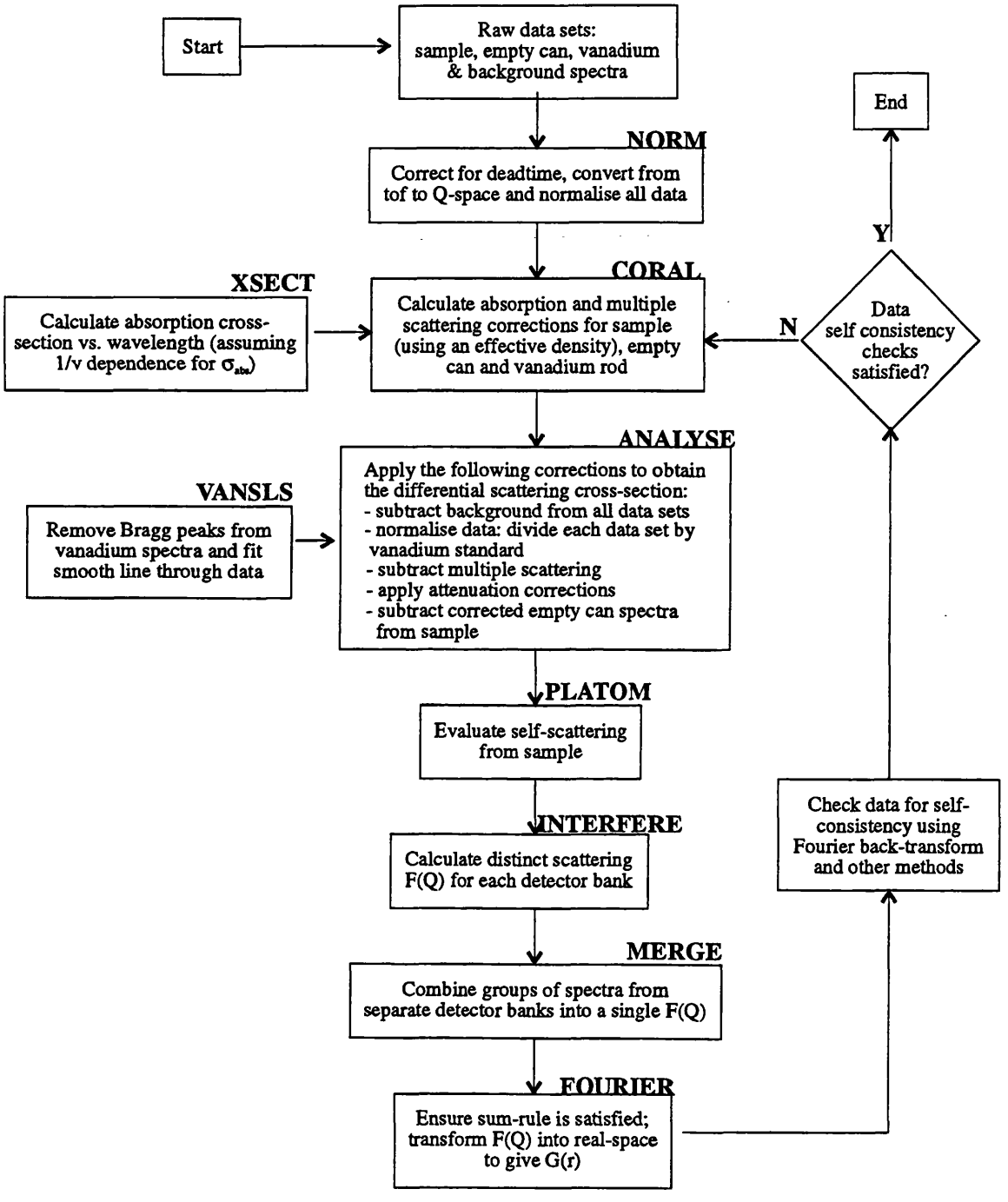

Figure 3.5: Data analysis procedures used to obtain G(r) for a liquid or amorphous sample on a time-of-flight instrument (SANDALS & LAD).

data is carried out as given by equation 2.66. A main problem with the transform arises from the absence of measured diffraction data for scattering angles greater than a limiting angle Q_{max}. Therefore, what is actually transformed, can be described as Q times the measured Q-space function multiplied by a step function, which is unity where data is measured and zero for values of $Q > Q_{max}$. From the convolution theorem (e.g. Waser & Schomaker[15]) it follows that the Fourier transform of a product of two functions corresponds to the folding or convolution of the Fourier transforms of those functions. Therefore in real-space, $r \cdot g(r)$ or $r \cdot G(r)$ will be convoluted with a sinc-function due to the step-function in Q-space, and hence unphysical oscillations will appear around each peak in real-space. The sharper the peaks the more pronounced the oscillations will be. Additionally, spurious real-space features (most notable before the first real-space physical peak) can appear, owing to random and systematic errors in the measured Q-space functions.

Different methods are used to overcome the problems arising from the finite Q-range and from noise in the data.

- The effect in real-space of the finite Q-range can be changed by a multiplication of the Q-space function with a suitable factor or modification function instead of the step function (Waser & Schomaker[15]). A function that is, according to Waser & Schomaker[15], often used is $exp(-aQ^2)$ with a chosen such that the integrand has a negligible value beyond Q_{max}. Since the Fourier transform of this function is $\propto exp(-ar^2/4a)$ it will only broaden the real-space features but not introduce unphysical oscillations around them.

- A special procedure can be used to overcome truncation effects. In the case of partial structure factors, the real-space functions are given by

$$t'_{\alpha\beta}(r) = \frac{2}{\pi}\int_0^\infty [S_{\alpha\beta}(Q) - 1]\, M(Q)\, Q\, sin(Qr)\, dQ \qquad (3.15)$$

  where $t'_{\alpha\beta}(r) = t_{\alpha\beta}(r) \otimes M(r)$, $t_{\alpha\beta}(r) = 4\pi n_0 r[g_{\alpha\beta}(r) - 1]$, $M(r)$ is the Fourier transform of the step function due to the finite range of measured Q-space data, and $\otimes$ is a one-dimensional convolution operator. To enable those features that are artefacts of the step function to be distinguished from the remainder the $t'_{\alpha\beta}(r)$ are fitted by using a least squares algorithm to a sum

of Gaussians (since this is how $t_{\alpha\beta}$ can be expressed in a solid where the atoms are assumed to be executing simple harmonic motion around equilibrium positions, see Susman et al.[16]) representing the individual pair correlations convoluted with $M(r)$. The final $t_{\alpha\beta}(r)$ are obtained by smoothly merging the Gaussian representation of $t_{\alpha\beta}(r)$ in the region where the effect of $M(r)$ is measurable with the $t'_{\alpha\beta}(r)$ obtained by direct Fourier transform of the Q-space data, and by setting the unphysical low-r oscillations to $-4\pi n_0 r$. To check the validity of the obtained $g_{\alpha\beta}(r)$ their back Fourier transforms have to agree well with the measured partial structure factors $S_{\alpha\beta}(Q)$.

- A different approach to overcome truncation effects, the finite resolution of the measuring instrument, statistical noise or other systematic errors is given by the Minimum Noise (MIN) Reconstruction method (e.g. Root et al.[17], Soper[18] and Soper et al.[19]).

  It is a Monte Carlo method that uses a restraining function based on minimising the noise in the data. The degree of smoothness is judged by the square of the second derivative of the estimated function. The main goal is to find solutions that minimise the quality factor Q_f, where

$$Q_f = \chi^2 + \lambda S \ . \tag{3.16}$$

  χ^2 is defined as,

$$\chi^2 = \sum_i \frac{(D_i - M_i)^2}{\sigma_i^2} \ , \tag{3.17}$$

  where M_i is an estimate of the i^{th} data point D_i in Q-space and σ_i represents the statistical error on D_i. M_i is obtained from a trial distribution N_j in r-space via the transformation matrix T_{ij},

$$M_i = \sum_j T_{ij} N_j \ . \tag{3.18}$$

  In equation 3.16, S represents the noise in the distribution and is given by $S = \sum_j S_j$, where

$$S_j = \begin{cases} \Delta_j^2 / R_j & -\frac{1}{2}R_j < \Delta_j < \frac{1}{2}R_j \\ |\Delta_j| & -\frac{1}{2}R_j > \Delta_j > \frac{1}{2}R_j \end{cases} \tag{3.19}$$

R_j and Δ_j are defined by the following equations,

$$R_j = \frac{1}{2}|N_{j+1} - N_{j-1}| \,, \tag{3.20}$$

$$\Delta_j = N_j - P_j \tag{3.21}$$

with

$$P_j = \frac{1}{4}[N_{j-1} + 2N_j + N_{j+1}] \,. \tag{3.22}$$

P_j can be thought of as a prior distribution, which is always smoother than the distribution from which it was derived.

In summary, minimising the quality factor can be considered as a compromise between obtaining the best χ^2 fit to the data and forcing the distribution to be smooth, where the extent of smoothness can be controlled by the weighting factor λ.

3.6 Self consistency checks

The efficacy of the performed data correction procedures and therefore the reliability of the measured structure factors can be tested by applying the following checks (Salmon & Benmore[20]):

- The total structure factors F(Q) must tend to their right high-Q limit of zero. Hence the $S_{\alpha\beta}(Q)$ must tend to unity.
- The low-Q limits for systems in thermodynamic equilibrium are related to measurable macroscopic quantities, such as for example the isothermal compressibility (see e.g. Beeby[21]).
- The sum-rule relations derived by Enderby et al.[22] must be satisfied:

$$\int_0^\infty [S_{\alpha\beta}(Q) - 1]Q^2 \, dQ = -2\pi^2 n_0 \tag{3.23}$$

The above equation holds for the Faber-Ziman partial structure factors; for the Bhatia-Thornton partial structure factors the sum-rule equations are,

$$\int_0^\infty [S_{NN}(Q) - 1]Q^2 \, dQ = -2\pi^2 n_0$$

$$\int_0^\infty [S_{CC}(Q) - c_1c_2]Q^2\,dQ = 0 \qquad (3.24)$$

$$\int_0^\infty S_{NC}(Q)Q^2\,dQ = 0$$

- The measured structure factors F(Q) and the Fourier back-transforms of G(r), after the low-r oscillations have been set to their calculated limit of G(0), must be in good agreement over all values of Q.

Additive and multiplicative errors may arise when, for example an incorrect sample cross-section or density is used in the evaluation of the $A_{ij}(\theta)$ and $M_i(\theta)$ terms in equation 3.9 (see e.g. Cossy et al.[23]). Additive errors are eliminated by an appropriate shift of the Q-space data. Now consider a multiplicative error ϵ, such that $F'(Q) = (1+\epsilon)F(Q)$. Hence the Fourier transform of $F'(Q)$ is given by $G'(r) = (1+\epsilon)G(r)$. In the case of $\epsilon = 0$ and no shift of the data, $G'(r)$ should oscillate about the right G(0) limit (see equation 2.67) for $0 \leq r < r_0$, where r_0 is the closest distance between two sample nuclei. Setting $G'(0 \leq r < r_0) = G(0)$ and back Fourier transforming it, should essentially reproduce $F'(Q)$. But if $\epsilon \neq 0$ and $G'(0 \leq r < r_0)$ is again set to G(0), then a discrepancy between the back Fourier transform of $G'(r)$ and $F'(Q)$ of the following form will appear,

$$\epsilon G(0) 4\pi n_0 r_0^2 Q^{-1} j_1(Qr_0)\ , \qquad (3.25)$$

where $j_1(Qr_0)$ is a first order spherical Bessel function, which is largest at low values of Q. Therefore if all the data analysis procedures were performed correctly, the G(r)'s should oscillate around their right G(0) limits at $0 \leq r < r_0$ and the back Fourier transform and F(Q) should show a high level of agreement.

3.7 Coordination numbers: Determination and Interpretation

The coordination number or number of nearest-neighbours is defined as the average number of particles surrounding a certain atom placed at the origin of coordinates. Usually one is interested in the number of atoms of species β surrounding an atom of species α at a distance $r_1 \leq r \leq r_2$. It can be obtained from the partial pair

distribution functions $g_{\alpha\beta}(r)$ via the expression

$$\overline{n}_{\alpha}^{\beta} = 4\pi n_0 c_{\beta} \int_{r_1}^{r_2} r^2 g_{\alpha\beta}(r)\, dr \ , \tag{3.26}$$

where c_β is the atomic fraction of β atoms. The coordination number therefore contains information about the short range order in amorphous materials and hence about the chemical bonding connected with it.

If one is not interested in the particular species of atoms, an average coordination number can be defined as,

$$\begin{aligned} \overline{n} &= 4\pi n_0 \int_{r_1}^{r_2} r^2 g_{NN}(r)\, dr \\ &= c_\alpha \left(\overline{n}_{\alpha}^{\beta} + \overline{n}_{\alpha}^{\alpha}\right) + c_\beta \left(\overline{n}_{\beta}^{\alpha} + \overline{n}_{\beta}^{\beta}\right) , \end{aligned} \tag{3.27}$$

where $g_{NN}(r)$ is the Bhatia-Thornton number-number partial pair distribution function (see equation 2.71).

For a well defined peak, i.e. $g_{\alpha\beta}(r_2)$ reaches the $g_{\alpha\beta}(0)$ limit, $\overline{n}_{\alpha}^{\beta}$ can be calculated in a straight forward way. Generally, however, the minimum after the first peak does not return to this limit and problems in unambiguously determining the coordination numbers can arise. The following short summary gives an overview of commonly used approaches to deal with an ill-defined peak:

(a) symmetrical peak in $rg_{\alpha\beta}(r)$.

This method involves symmetrising the first peak in $rg_{\alpha\beta}(r)$ about the mean atomic position.

(b) symmetrical peak in $r^2 g_{\alpha\beta}(r)$.

This method assumes that the shells are symmetric in $r^2 g_{\alpha\beta}(r)$ and it requires symmetrising the first peak in $r^2 g_{\alpha\beta}(r)$ about the mean atomic position.

(c) extrapolation.

This approach assumes that the atomic shells are asymmetric in $r^2 g_{\alpha\beta}(r)$, and with the further assumption that the functions are continuous and vary smoothly in r, the trailing edge of the first shell is extrapolated to $g_{\alpha\beta}(r = 0)$.

(d) integration to first minimum in $r^2 g_{\alpha\beta}(r)$.

In this method the integration in equation 3.26 is carried out to a distance r_{min} corresponding to the minimum after the first peak in $r^2 g_{\alpha\beta}(r)$. The method is based on the assumption that the nearest neighbours are more likely to be positioned at

distances further away, than closer to the central particle.

A graphical illustration of these approaches is given in figure 3.6.

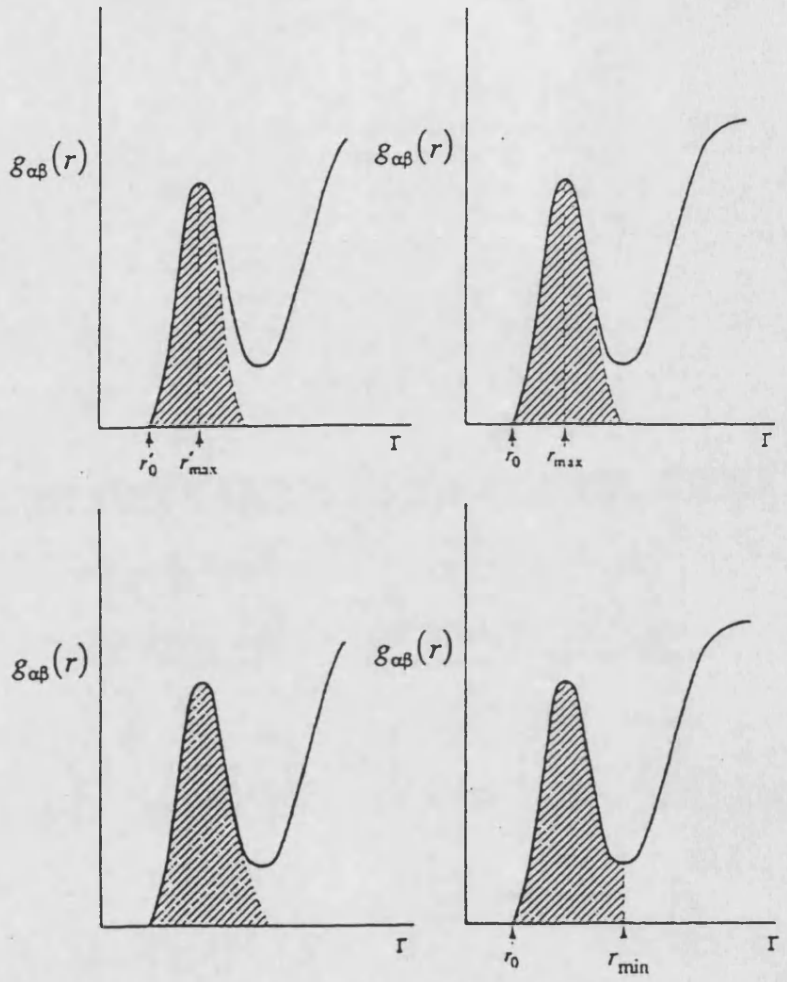

Figure 3.6: Qualitative plots of $g_{\alpha\beta}(r)$ vs. r showing the four different methods used in the determination of coordination numbers described in the text. (Reproduced from Waseda[24].)

Bibliography

[1] Correspondents' Report in *Neutron News* **1/1** (1990) 14.

[2] Soper A K, Howells W S and Hannon A C, *ATLAS - Analysis of Time-of-flight diffraction data from Liquid and Amorphous Samples* (1989).

[3] Benmore C J and Soper A K, *The Sandals Manual* Technical Report **RAL-TR-98-006** (1998).

[4] Boland B and Whapham S, *ISIS User Guide - Experimental Facilities* ISIS, Rutherford Appleton Laboratory (1992).

[5] Soper A K and Egelstaff P A, *Nucl. Inst. Meth.* **178** (1980) 415.

[6] Blech I A and Averbach B L, *Phys. Rev.* **137** (1965) (4A) A1113.

[7] Paalman H H and Pings C J, *J. Appl. Phys.* **33** (1962) 2635.

[8] Mayers J, *Nucl. Inst. and Meth.* **221** (1984) 609.

[9] Poncet P F J, Ph.D. Thesis, University of Reading (1976).

[10] Salmon P S, *J. Phys. F* **18** (1988) 2345.

[11] Bertagnolli H, Chieux P and Zeidler M D, *Mol. Phys.* **32** (1976) 759.

[12] Hannon A C, Howells W S and Soper A K, Inst. of Phys. Conf. Series No. 107 *Neutron Scattering Data Analysis* ed. by Johnson M W (IOP: Bristol) (1990) 193.

[13] Soper A K, Neilson G W, Enderby J E and Howe R A, *J. Phys. C* **10** (1977) 1793.

[14] Champeney D C, *Fourier Transforms in Physics* (Hilger: Bristol) (1985).

[15] Waser J and Schomaker V, *Rev. Mod. Phys.* **25/3** (1953) 671.

[16] Susman S, Volin K J, Montague D G and Price D L, *J. Non-Cryst. Sol.* **125** (1990) 168.

[17] Root J H, Egelstaff P A and Nickel B G, Inst. of Phys. Conf. Series No. 81 *Neutron Scattering Data Analysis* ed. by Johnson M W (IOP: Bristol) (1986) 71.

[18] Soper A K, Inst. of Phys. Conf. Series No. 107 *Neutron Scattering Data Analysis* ed. by Johnson M W (IOP: Bristol) (1990) 57.

[19] Soper A K, Andreani C and Nardone M, *Phys. Rev. E* **47/4** (1993) 2598.

[20] Salmon P S and Benmore C J, *Recent Developments in the Physics of Fluids* ed. by Howells W S and Soper A K (Hilger: Bristol) (1992) F225.

[21] Beeby J L, *Journ. Phys. C* **6** (1973) 2262.

[22] Enderby J E, North D M and Egelstaff P A, *Phil. Mag.* **14** (1966) 961.

[23] Cossy C, Barnes A C, Enderby J E and Merbach A E, *J. Chem. Phys* **90** (1989) 3254.

[24] Waseda Y, *The Structure of Disordered Materials* (McGraw-Hill: New York) (1980).

Chapter 4

The structure of the liquid semiconductor GeSe

4.1 Introduction and previous work

The binary Ge_xSe_{1-x} ($0 \leq x \leq 1$) system is a much studied proto-typical glass forming system with a wide composition range for bulk quenched glass formation, covering $0 \leq x \leq 0.42$ (see Azoulay et al.[1], Tronc et al.[2]). However, as the edge of the glass-forming region is approached, a wide range of experiments indicate that there is a significant change in the nature of the chemical bonding. For example, as the Ge concentration is increased from $x = 0.33$ to $x = 0.5$ at 750°C the electrical resistivity of the liquid decreases by approximately four orders of magnitude (Haisty & Krebs[3] and Ruska & Thurn[4]), the molar volume decreases by a factor of 1.24 [4], and the adiabatic compressibility decreases by a factor of 2.9 (Tsuchiya[5]). For the same change in composition at a temperature of 900°C, the kinematic viscosity decreases by a factor of approximately two (Glazov & Situlina[6] and Ruska & Thurn[4]). As the germanium content is increased to $x = 1$ the system becomes metallic (see e.g. Uemura et al.[8]). To understand the change in the nature of bonding in liquid Ge_xSe_{1-x} from metallic (Ge) to covalent as x is decreased from unity, maximum information on the pair distribution functions is required.

The phase diagram for the Ge_xSe_{1-x} system in figure 4.1 is reproduced from Ipser et al.[7]. It can be seen that on the Se-rich side $GeSe_2$ has the highest melting point. It melts congruently at 742(2) °C while GeSe is reported to melt

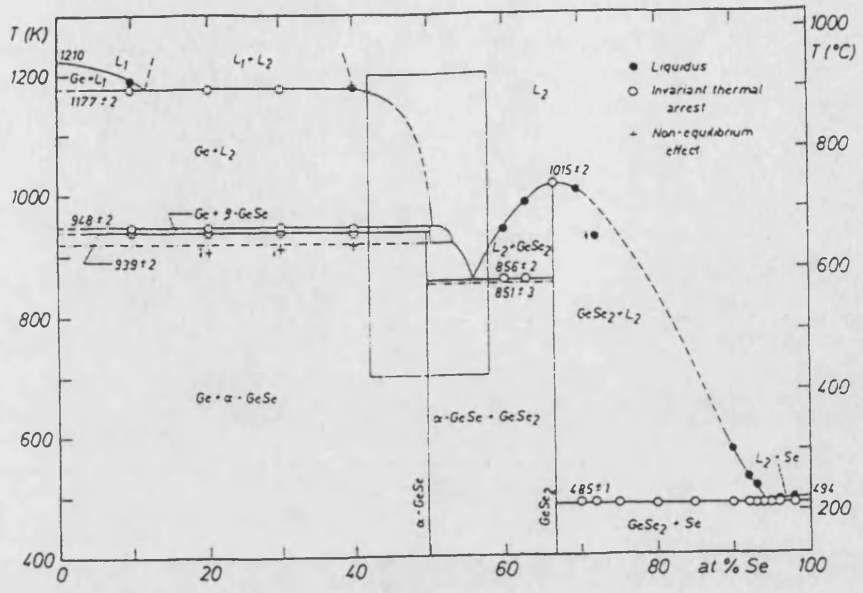

Figure 4.1: The Ge-Se phase diagram. (Reproduced from Ipser et al.[7].)

incongruently at 675(2) °C (Ipser et al.[7]). There are two crystalline compounds formed in the Ge-Se system that have substantially different structures due to differing bonding mechanisms. The structure of $GeSe_2$ is determined by $GeSe_{4/2}$ tetrahedra and the bonding is sp^3. However, in GeSe $p\sigma$ bonding yields a distorted orthorhombic NaCl-type structure at low temperatures in which each chemical species makes three strong and three weak bonds to unlike chemical species to form a double layer structure (see e.g. Dutta & Jeffrey[10]). It undergoes a structural phase transition to a normal NaCl-type structure at 651(5) °C (see Wiedemeier & Siemers[9]).

Recent neutron diffraction experiments, for example the measurement of the full set of partial structure factors for liquid $GeSe_2$ (Penfold & Salmon[11],[12]) and the investigation of the topology of molten Ge_xSe_{1-x} alloys (Salmon & Liu[13]), have initiated further studies of the Ge-Se system, which are presented in the following chapters.

The investigation of the topology of molten Ge_xSe_{1-x} alloys (Salmon & Liu[13]), by using neutron diffraction to measure the Bhatia-Thornton number-number partial structure factors (see section 2.10), has shown that there is a considerable

change in the liquid structure when x is increased from $x = 0.33$ to $x = 1$. For example the first sharp diffraction peak (FSDP) at approximately 1 $Å^{-1}$ in $GeSe_2$ is virtually eliminated in GeSe, a composition for which amorphous samples cannot be formed by bulk quenching methods. This indicates that for molten GeSe the intermediate range order associated with the FSDP does not exit and that the $GeSe_{4/2}$ tetrahedral units of molten $GeSe_2$ are broken-up. Additionally a coordination number of Se around Ge of $<< 6$ was obtained for GeSe, which is significant as GeSe melts from a normal NaCl-type crystal structure (Wiedemeier & Siemers[9]). Instead the number-number partial structure factor was found to be notably different to that for molten NaCl (Rovere & Tosi[14]) or a 1:1 liquid such as CuCl which melts from a superionic phase (Eisenberg et al.[15]), but it resembles that for liquid As (Bellisent et al.[16]). Indeed, the local structure of molten GeSe was best thought of as being described by a model in which both Ge and Se are three-fold coordinated, i.e. the structure of the melt is *not* similar to the structure of the high-temperature crystalline phase of GeSe from which it melts, but is comparable to its low temperature phase, described by Dutta & Jeffrey[10].

These recent findings for molten GeSe show the importance for a detailed investigation of the local coordination environments of Ge and Se. Since Ge and Se have close atomic numbers and sizes and for natural isotopic abundances their coherent neutron scattering lengths are similar, the use of conventional neutron or x-ray diffraction methods to measure total structure factors cannot yield detailed enough information. However the partial structure factors are accessible by using the method of isotopic substitution in neutron diffraction.

The partial pair distribution functions will allow for a detailed comparison with both the high-temperature and low-temperature phases of crystalline GeSe, so that a decision can be made about how far molten GeSe resembles the low-temperature phase. Additionally, the structure of GeSe can be discussed by reference to that of the molten AX materials CuSe (Barnes & Enderby[17]) and CuBr (Allen & Howe[18], Saito et al.[19] and Pusztai & McGreevy[20]), where A and X denote the electropositive and electronegative species respectively. These three AX systems have the same or similarly sized anions and structural information on CuSe and CuBr is also available at the partial pair distribution function level.

Using the results for the glass-forming network melt $GeSe_2$, measured by Penfold

& Salmon[11], the partial structure factors for two compositions of the same binary system, which differ in their ability to form glasses by bulk quenching methods, can be thoroughly compared. Detailed information about the structure of molten GeSe may also be helpful for solving the structure of amorphous GeSe prepared, for example, by evaporation techniques (e.g. Uemura et al.[21]). Although the short-range order of amorphous GeSe has been studied by many authors, there is still a considerable controversy about whether it has a structure with a 3(Ge):3(Se) coordination like in the low temperature crystalline structure, or if it is best described by a 4(Ge):2(Se) coordination, see Hosokawa et al.[22].

Previous investigations by Ruska & Thurn[4] and by Okada et al.[23] showed that molten GeSe is a semiconductor with an electrical conductivity $\sigma \approx 40\ \Omega^{-1}\,\mathrm{cm}^{-1}$ just above its melting point and with a positive temperature coefficient $\mathrm{d}\sigma/\mathrm{dT}$. Okada et al.[23]'s thermopower measurements are consistent with p-type conductivity, while the sign of the Hall coefficient is reported to change from positive to negative on melting (Glazov et al.[24]). However, according to Cusack[25], an interpretation of the Hall coefficient in disordered materials is problematic.

4.2 Sample preparation

The three samples used in the diffraction experiments, $^{\mathrm{N}}\mathrm{Ge}^{\mathrm{N}}\mathrm{Se}$, $^{70}\mathrm{Ge}^{\mathrm{N}}\mathrm{Se}$ and $^{73}\mathrm{Ge}^{76}\mathrm{Se}$, where N denotes a natural isotopic abundance, were made from $^{\mathrm{N}}$Ge (99.9999 %, Aldrich), $^{\mathrm{N}}$Se (99.999 %, Johnson Matthey) and highly-enriched isotopes, ^{70}Ge (99.8 % ^{70}Ge and 0.2 % ^{72}Ge), ^{73}Ge (98 % ^{73}Ge, 0.3 % ^{70}Ge, 0.8 % ^{72}Ge, 0.8 % ^{74}Ge and 0.1 % ^{76}Ge) and ^{76}Se (99.75 % ^{76}Se, 0.2 % ^{74}Se and 0.05 % ^{77}Se), supplied by Europa Scientific Limited, Crewe. The isotopes were sealed under vacuum directly after separation to minimise contamination by chemical impurities.

All of the sample handling and preparation was carried out in a high purity argon filled glove box (purity > 99.999 %, ≈ 1 ppm O_2 and $H_2O < 20$ ppm) to avoid any surface contamination with hydrogen or oxygen. The sample preparation follows the following procedure:

(a) The silica tubes used for the sample preparation (5 mm inner diameter and 1 mm wall thickness) were cleaned with a chromic acid solution and pure water

before etching for about two minutes with a 40 % solution of hydrofluoric acid and rinsing again carefully with pure water. Then the tubes were dried overnight in an oven at about 150 °C, outgassed for four hours under vacuum (approximately 10^{-5} torr at a temperature of 600 °C) and sealed using a Young's tap.

(b) The elements were crushed using a stainless steel mortar and pestle and loaded in the argon filled glovebox into a cleaned silica tube. The composition was determined by mass, with the uncertainty being less than 1 mg. The tubes were sealed again using the Young's tap, before they were removed from the glovebox, and were put in an ultrasonic bath to increase the packing fraction of the sample. Then the tubes were positioned on a vacuum-line and evacuated slowly to a vacuum of $10^{-5} - 10^{-6}$ torr using a combination of a rotary and a diffusion pump system that also incorporates a liquid nitrogen cold trap, positioned between the pumps and the silica tubes to prevent any contamination of the samples with hydrocarbon from the back-streaming oil of the diffusion pump. Subsequently the samples were flushed three times with helium to enhance outgassing and after evacuating for another 12 hours they were sealed under a vacuum better than 10^{-5} torr into double walled tubes to prevent oxygen contamination in case the inner tube containing the sample cracked during the heating or cooling processes.

(c) The sealed tubes were fixed into a rocking furnace by alumel wires on each end of the tube. The elements were mixed and heated slowly at 1 °C/min while the furnace kept rocking at 1 rpm. The exact heating procedure is as follows:
The samples are heated up at a rate of 1 °C/min to 200 °C, the approximate melting temperature of Se, and held at this temperature for 60 minutes. Then they are further heated to 690 °C, the boiling temperature of Se, and are again held at this temperature for 60 minutes before they are taken up further to 938 °C, the melting temperature of Ge, and held for 60 minutes. After this the samples are heated up to 1000 °C and kept at this temperature for 48 hours. The samples are then cooled down slowly at 1 °C/min to room-temperature, separated from the silica tubes, crushed into a coarse powder, transferred to matched silica ampoules for the experiment (nominally 5 mm internal diameter and 1 mm wall thickness) and sealed under a vacuum better than 10^{-5} torr. All of the sample handling is again carried out in the pure argon filled glove box.

4.3 Neutron diffraction parameters and experiment

The neutron diffraction experiments were carried out on the D4B instrument at the Institut Laue-Langevin. A wavelength of $\lambda = 0.7051$ Å for the incident neutrons was used. The samples (2.2 g of $^{N}Ge^{N}Se$, 1.9 g of $^{70}Ge^{N}Se$ and 1.7 g of $^{73}Ge^{76}Se$) were fully illuminated by a rectangular beam of 16 mm height and 13 mm width. The complete diffraction experiment comprised the measurement of the scattering intensities at 727(2) °C for the three samples in silica cells placed within a cylindrical vanadium heater, an empty silica cell in the heater and the empty heater. The diffraction pattern for a cadmium bar of 5 mm diameter placed in the heater was measured at room temperature for performing the low-angle background correction (section 3.3.1). The diffraction pattern of a 6.08 mm vanadium rod was used for the data normalisation. On heating, the $^{N}Ge^{N}Se$ sample and empty silica cell, diffraction patterns were measured at 617(2) °C and 662(2) °C, i.e. on either side of the reported solid-state structural phase transition (Wiedemeier & Siemers[9]).

The data analysis followed the procedure described in section 3.3.1, and the temperature at which the experiment on the liquid was carried out was the same as that chosen by Salmon & Liu[13]. At this temperature, liquid GeSe forms a single homogeneous phase: the measured diffraction patterns indicate no small angle scattering and electrical conductivity (Okada et al.[23]) and sound velocity measurements (Tsuchiya[5]) show no evidence of phase separation.

The neutron cross-sections and scattering lengths for elemental Ge and Se and for the enriched isotopes used in the experiment are summarised in table 4.1.

Element	$\overline{b}$ [fm]	$\sigma_{free,coh}$ [barn]	$\sigma_{free,inc}$ [barn]	σ_{abs} (@ 1.798 Å) [barn]
^{N}Ge	8.185(20)	8.19(4)	0.18(7)	2.20(4)
^{70}Ge	10.0(1)	12.25(29)	0	3.0(2)
^{73}Ge	5.09(4)	3.19(5)	1.46(29)	14.8(4)
^{N}Se	7.970(9)	7.78(2)	0.31(6)	11.7(2)
^{76}Se	12.2(1)	18.22(29)	0	85(7)

Table 4.1 : Neutron scattering lengths and cross-sections for the elements and isotopes, calculated for the correct isotopic enrichments (Sears[26]). The statistical errors are given in brackets.

The cross-sections of the three samples, calculated from the above parameters, are summarised in table 4.2.

Sample	$\sigma_{free,sc} = \sigma_{free,coh} + \sigma_{free,inc}$ [barn]	σ_{abs} (@ $\lambda = 1.798$ Å) [barn]	$\sigma^{total} = \sigma_{free,sc} + \sigma_{abs}$ (@λ) [barn]
^{N}Ge^{N}Se	8.23(4)	6.95(10)	2.73(4)
^{70}Ge^{N}Se	10.17(15)	7.35(14)	2.88(6)
^{73}Ge^{76}Se	11.44(20)	49.9(3.5)	19.6(1.4)

Table 4.2: Cross-sections of the samples. Here $\lambda = 0.7051$ Å is the wavelength of the incident neutrons.

The number density of the sample used in the analysis and for the calculation of the coordination numbers is 0.0387(2) Å^{-3}, taken from Ruska & Thurn[4]. It corresponds to mass density values of 4.870 gcm^{-3}, 4.784 gcm^{-3} and 4.782 gcm^{-3} for ^{N}Ge^{N}Se, ^{70}Ge^{N}Se and ^{73}Ge^{76}Se respectively.

Total structure factors :

Each total structure factor $F(Q)$ comprises three partial structure factors,

$$F(Q) = A[S_{GeGe}(Q) - 1] + B[S_{GeSe}(Q) - 1] + C[S_{SeSe}(Q) - 1] \qquad (4.1)$$

where $A = c_{Ge}^2 b_{Ge}^2$, $B = 2c_{Ge}c_{Se}b_{Ge}b_{Se}$ and $C = c_{Se}^2 b_{Se}^2$. These weighting factors together with the low-r limits and sum-rule relations of the three F(Q)'s are sum-

marised in table 4.3. The low-r limits and sum-rule relations are calculated using

$$G(0) = -(A + B + C) \tag{4.2}$$

and

$$\int_0^\infty F(Q)\, Q^2\, dQ = 2\pi^2 n_0 G(0) \tag{4.3}$$

respectively. The corresponding real-space functions, the total pair distribution functions G(r), are obtained from equation 4.1 by substituting the $S_{\alpha\beta}(Q)$ by the partial pair distribution functions $g_{\alpha\beta}(r)$.

Sample	A [barn]	B [barn]	C [barn]	G(0) [barn]	sum-rule [barn/Å^3]
^{N}Ge^{N}Se	0.1675(8)	0.3262(9)	0.1588(4)	-0.6525(13)	-0.4984(10)
^{70}Ge^{N}Se	0.250(5)	0.399(4)	0.1588(4)	-0.807(6)	-0.617(3)
^{73}Ge^{76}Se	0.0648(10)	0.311(4)	0.372(6)	-0.747(7)	-0.571(3)

Table 4.3: Weighting coefficients, low-r limits G(0), and sum-rule relations. The statistical errors are given in brackets.

First order difference function :

By forming the first order difference function, $\Delta_{Ge}(Q)$, many systematic errors can be eliminated (e.g. Salmon et al.[27] and section 3.4). Therefore it is advisable to use it as an additional criterion for checking the data self-consistency, even when the full set of partial structure factors can be obtained by solving the matrix equation (see section 2.12). By using the ${}^{N}_{N}F(Q)$ and ${}^{70}_{N}F(Q)$ total structure factors, the Se-Se correlations can be eliminated,

$$\begin{aligned} \Delta_{Ge}(Q)\,/\text{barn} &= {}^{70}_{N}F(Q) - {}^{N}_{N}F(Q) \\ &= 0.083(5)[S_{GeGe}(Q) - 1] + 0.072(4)[S_{GeSe}(Q) - 1] \end{aligned} \tag{4.4}$$

The real-space function corresponding to $\Delta_{Ge}(Q)$ is denoted by $\Delta G_{Ge}(r)$ and is obtained by replacing the $S_{\alpha\beta}(Q)$ by the partial pair distribution functions $g_{\alpha\beta}(r)$ in the above equation. The low-r limit, $\Delta G_{Ge}(0)$, is given by

$$\begin{aligned} \Delta G_{Ge}(0) &= -\left[c^2_{Ge}[b^2(^{70}Ge) - b^2(^{N}Ge)] + 2c_{Ge}c_{Se}b_{Se}[b(^{70}Ge) - b(^{N}Ge)]\right] \\ &= -0.155(7)\,\text{barn} \end{aligned} \tag{4.5}$$

and the sum-rule by

$$2\pi^2 n_0 \Delta G_{Ge}(0) = -0.118(5)\,\text{barn}/\text{Å}^3 \,. \tag{4.6}$$

Partial structure factors :

The Faber Ziman partial structure factors are obtained by inverting the system of linear equations defined by the total structure factors (see section 2.12):

$$\begin{bmatrix} S_{GeGe}(Q)-1 \\ S_{GeSe}(Q)-1 \\ S_{SeSe}(Q)-1 \end{bmatrix} = \begin{bmatrix} -45(17) & 33(12) & 5.3(2.0) \\ 38(14) & -23.8(8.8) & -6.0(2.2) \\ -23.7(8.8) & 14.1(5.2) & 6.8(2.6) \end{bmatrix} \begin{bmatrix} {}^{N}_{N}F(Q) \\ {}^{70}_{N}F(Q) \\ {}^{73}_{76}F(Q) \end{bmatrix} \tag{4.7}$$

The conditioning of these equations is given by the determinant of the normalised weighting factor matrix $|A_n| = -0.02$. Therefore the set of simultanious equations for GeSe is better conditioned than for $GeSe_2$ (section 6.1.3 and Penfold & Salmon[11]).

4.4 Results

4.4.1 Total structure factors

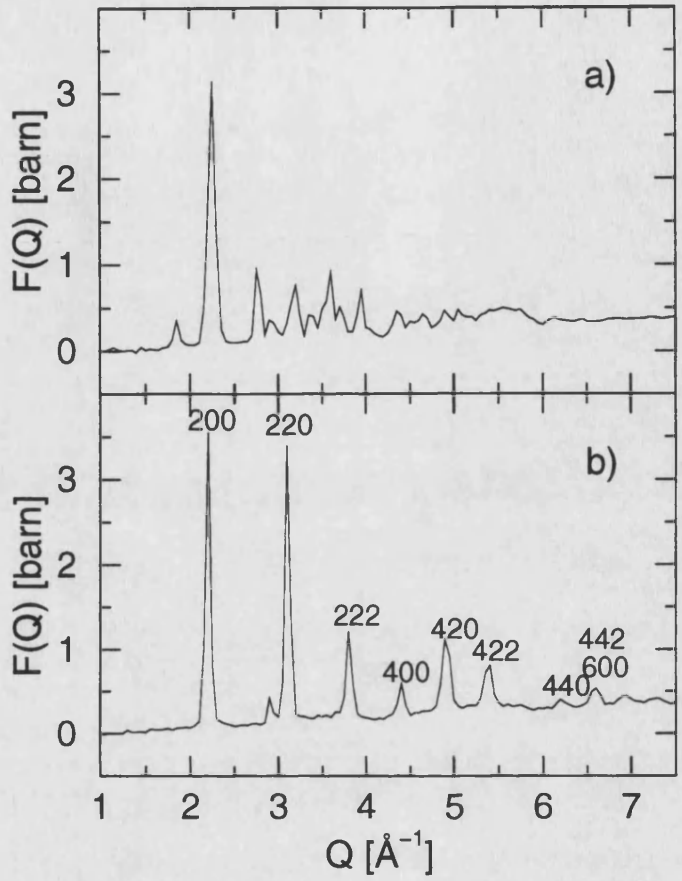

Figure 4.2: The measured total structure factors for crystalline a) LT-^{N}Ge^{N}Se at 617(2) °C and b) HT-^{N}Ge^{N}Se at 662(2) °C. Each peak in a) generally comprises reflections from several different planes and the *hkl* indices are therefore not given. The peaks in b) correspond only to reflections having even-numbered *hkl* values since b(^{N}Ge) ≈ b(^{N}Se) (see Wiedemeier & Siemers[9]). The small peak at ≈ 2.91 Å^{-1} arises from the vanadium heater.

The diffraction patterns measured for crystalline ^{N}Ge^{N}Se are shown in figure 4.2. The Bragg peaks were indexed and the structures were found to be fully consistent with those previously measured for the low temperature (LT) (Okazaki[29], Kannewurf et al.[30], Dutta & Jeffrey[10], Hulliger[31]) and high temperature (HT) (Wiedemeier & Siemers[9]) phases of GeSe. The existence of a structural phase transition to a normal NaCl-type structure prior to melting is therefore confirmed (Petri et al.[28]). The fractional volume change $(V' - V)/V$ is 0.5 % for the solid

to solid phase transition and 9 % for the melting transition (Ruska & Thurn[4], Wiedemeier & Siemers[9]), where V' and V denote the volumes for temperatures just above and below the transition of interest.

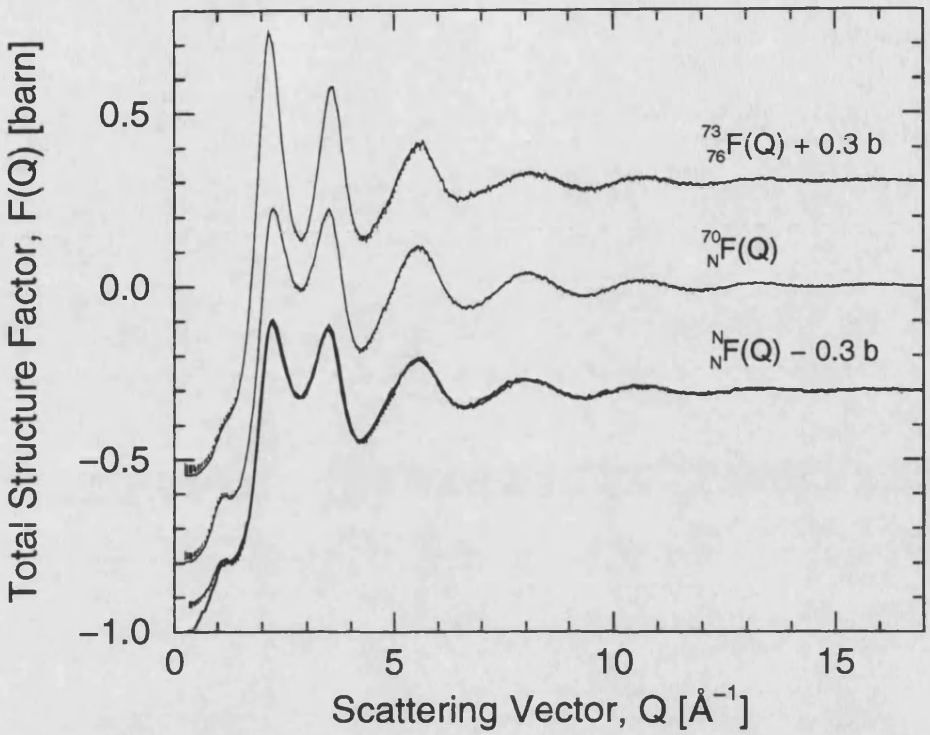

Figure 4.3: The measured total structure factors $^{N}_{N}F(Q)$, $^{70}_{N}F(Q)$ and $^{73}_{76}F(Q)$ for molten GeSe at 727(2) °C. The bars represent the statistical errors on the data points and the thin solid curves are the Fourier back transforms of the corresponding real-space functions obtained after setting the unphysical low-r oscillations to their calculated limiting value, G(0). The thick solid curve represents the previously measured $^{N}_{N}F(Q)$ by Salmon & Liu[13].

The measured total structure factors are shown in figure 4.3 together with the Fourier back transforms of the corresponding real-space functions obtained after the unphysical oscillations have been set to their calculated limiting value (see table 4.3). The good overall agreement between the data and back transform at all Q-values indicates that the data correction procedure has been properly undertaken (see Salmon & Benmore[32]). Our measured $^{N}_{N}F(Q)$ is found to be in excellent agreement for $Q > 1$ Å with that previously measured by Salmon & Liu[13] using the LAD instrument at the ISIS pulsed neutron source, shown as the thick solid curve in figure 4.3. The discrepancy at lower Q-values may be attributed to the difficulty in making the background correction at low angles to the LAD data.

If only the total structure factors are considered, the small pre-peak at $\approx 1.10\,\text{Å}^{-1}$ might be identified as a small first sharp diffraction peak (FSDP), corresponding to an intermediate range atomic ordering (IRO) in real-space. Since it is more pronounced in ${}^{70}_{N}F(Q)$ and ${}^{N}_{N}F(Q)$ than in ${}^{73}_{76}F(Q)$ it is anticipated to be associated with Ge correlations, which have a higher weighting for ${}^{70}Ge^{N}Se$ and ${}^{N}Ge^{N}Se$. This pre-peak is discussed in more detail in section 4.4.3. The oscillations in the three total structure factors are strongly damped at higher-Q, and at the maximum measured Q value of $16.75\,\text{Å}^{-1}$ they are no longer visible.

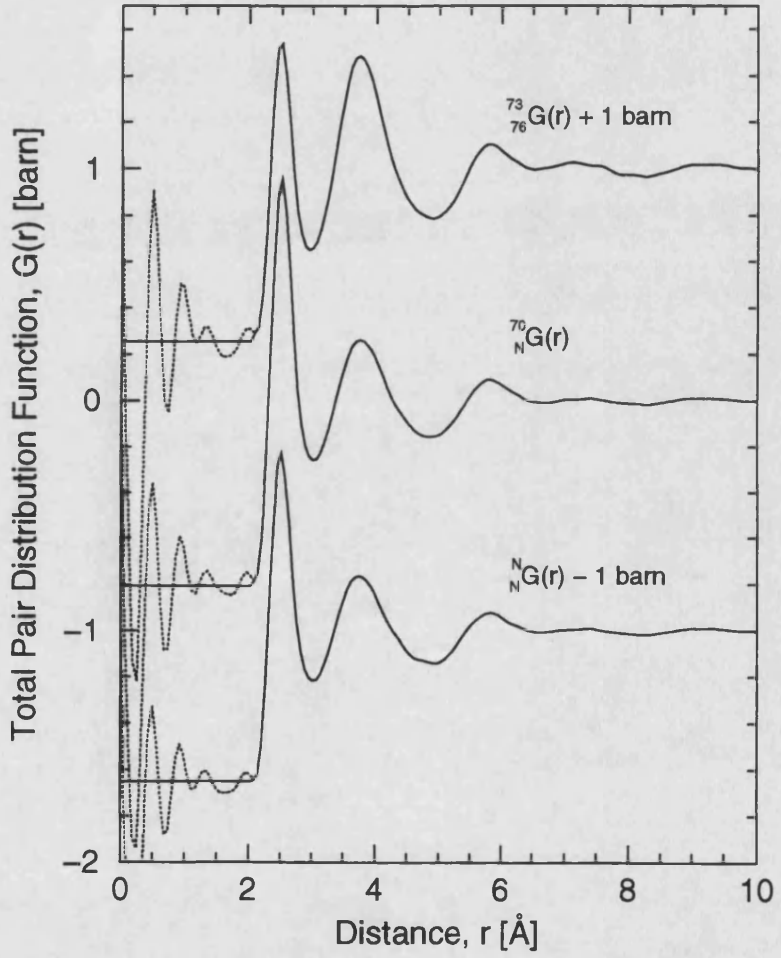

Figure 4.4: The measured total pair distribution functions ${}^{N}_{N}G(r)$, ${}^{70}_{N}G(r)$ and ${}^{73}_{76}G(r)$. The solid curves are the real-space representations of the F(Q)'s given in figure 4.3. The dotted curves for $r \leq 2.1\,\text{Å}$ show the corresponding unphysical low-r oscillations.

sample	1st peak [Å]	$\overline{n}^{Se}_{Ge}$ $2.09 \leq r\,[Å] \leq 3.04$ or 2.98	2nd peak	3rd peak
$^{N}Ge^{N}Se$	2.51(2)	3.5(3)	3.74(2)	5.84(2)
$^{70}Ge^{N}Se$	2.51(2)	3.5(3)	3.75(2)	5.81(2)
$^{73}Ge^{76}Se$	2.50(2)	3.1(3)	3.74(2)	5.82(2)

Table 4.4 : Peak positions in the total pair distribution functions. $\overline{n}^{Se}_{Ge}$ is calculated assuming only Ge-Se nearest neighbours for $r \leq 3.04$ Å in $^{N}Ge^{N}Se$ and $^{70}Ge^{N}Se$ and for $r \leq 2.98$ Å in $^{73}Ge^{76}Se$.

The corresponding total real-space functions are given in figure 4.4. Each of them has well defined first and second peaks. The first peak can be identified with Ge-Se correlations on the basis of a comparison with the crystal structures of both LT- and HT-GeSe, although the nearest neighbour distance is greater in HT-GeSe (details will be given in section 4.5). The second peak must contain a large contribution from Se-Se correlations, as it shows the highest intensity for the $^{73}Ge^{76}Se$ sample where the Se-Se correlations have their largest weighting. The peak positions in the total pair distribution functions and the nearest neighbour coordination number, $\overline{n}^{Se}_{Ge}$, obtained assuming no homopolar bonding, are summarised in table 4.4.

4.4.2 First order difference functions

The first order difference function $\Delta_{Ge}(Q) = {}^{70}_{N}F(Q) - {}^{N}_{N}F(Q)$ is illustrated by the error bars in figure 4.5 and shows that there is a significant contrast between ${}^{N}_{N}F(Q)$ and ${}^{70}_{N}F(Q)$ (Petri et al.[28]). It agrees very well over the whole measured Q-range with the Fourier back transform, given by the thin solid curve. A spline fit to $\Delta_{Ge}(Q)$ is shown by the thick solid curve. A very small pre-peak is found again at $1.10(2)\,Å^{-1}$.

The corresponding real-space function is shown as an inset in figure 4.5. The dotted curve corresponds to the Fourier transform of the error bars, the solid curve to the Fourier transform of the spline fitted data set with the unphysical oscillations set to their theoretical value (equation 4.5). $\Delta G_{Ge}(r)$ oscillates about the correct $\Delta G_{Ge}(0)$ value and integration of the first peak at 2.51(2) Å over the range $2.09 \leq r[Å] \leq 3.04$ yields $\overline{n}^{Se}_{Ge} = 3.9(2)$ which is significantly less than the

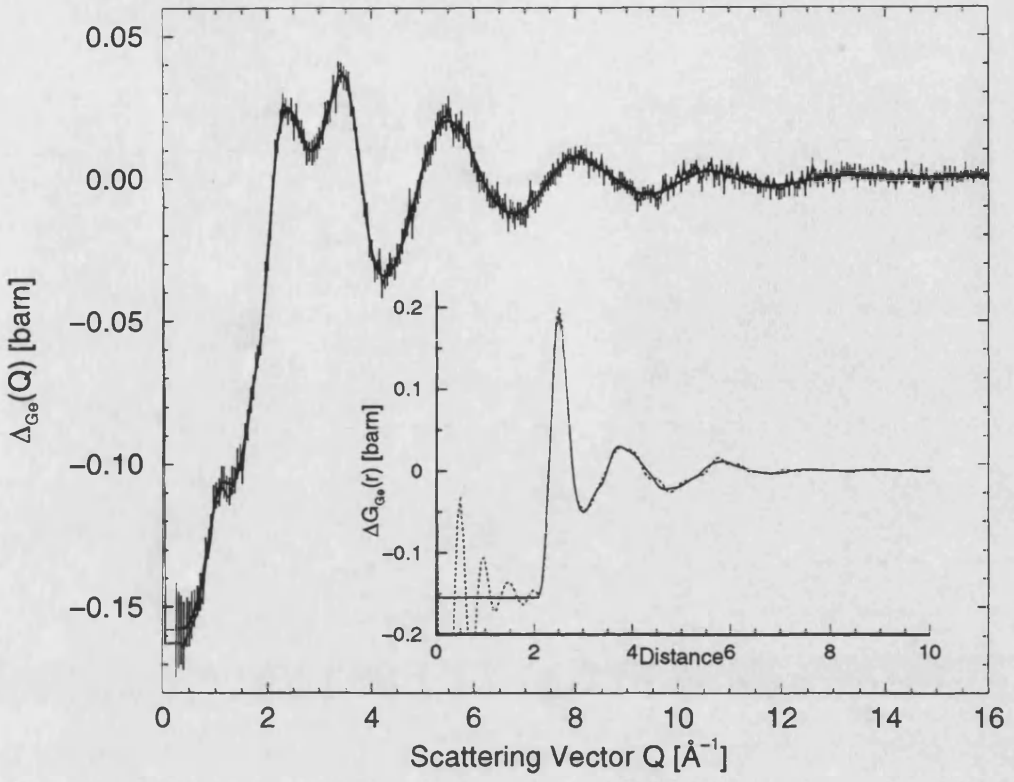

Figure 4.5: First order difference function in Q- and r-space (inset). The error bars represent $\Delta_{Ge}(Q) = {}^{70}_{N}F(Q) - {}^{N}_{N}F(Q)$, the thin solid curve is the Fourier back transform of $\Delta G_{Ge}(r)$, after the unphysical low-r oscillations have been removed, and the thick solid curve shows a spline fit to $\Delta_{Ge}(Q)$. The dotted curve illustrating $\Delta G_{Ge}(r)$ is the real-space function corresponding to the error bars and the solid curve corresponds to the spline fitted data set with the low-r oscillations set to $\Delta G_{Ge}(0)$.

value of 6 found in HT-GeSe and larger than the value of 3 found in LT-GeSe. If only Ge-Se correlations contribute to the first peak region then integration of either G(r) or $\Delta G_{Ge}(r)$ over the same range $2.09 \leq r[\text{Å}] \leq 3.04$ should give an identical coordination number. However, a larger $\overline{n}^{Se}_{Ge}$ value is obtained from $\Delta G_{Ge}(r)$ than from G(r), i.e. 3.9(2) cf. 3.5(3) (see table 4.4). This discrepancy can be rationalised by assuming the existence of Ge-Ge homopolar bonds. The Ge-Ge correlations have a higher weighting in $\Delta G_{Ge}(r)$ than in G(r) (equations 4.1 and 4.4), the ratio of the $g_{GeGe(r)} : g_{GeSe(r)}$ coefficients is 1.152 for $\Delta G_{Ge}(r)$, 0.513 for ${}^{N}_{N}G(r)$ and 0.627 for ${}^{70}_{N}G(r)$. Hence if $\overline{n}^{Se}_{Ge}$ is fixed at a value of three, a coordination number $\overline{n}^{Se}_{Ge} = 0.8(2)$ is obtained from all three real-space functions (Petri et al.[28]).

4.4.3 Partial structure factors

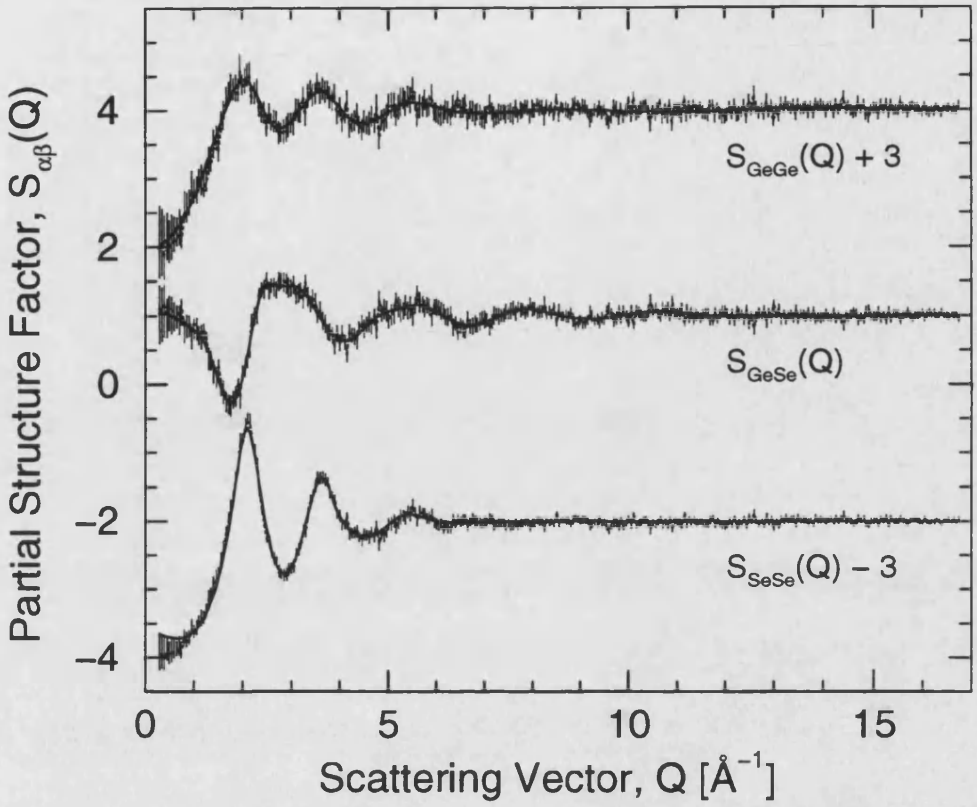

Figure 4.6: The experimental partial structure factors $S_{GeGe}(Q)$, $S_{GeSe}(Q)$ and $S_{SeSe}(Q)$ for molten GeSe. The bars represent the statistical errors on the data points, the dotted curves show the Fourier back transforms, and the solid curves are the smoothed $S_{\alpha\beta}(Q)$ (see text).

Figure 4.6 shows the Faber-Ziman partial structure factors $S_{\alpha\beta}(Q)$ by the error bars, obtained directly from equation 4.7. The $S_{\alpha\beta}(Q)$ satisfy the sum-rule and inequality relations (Edwards et al.[33]) and their agreement with the Fourier back transforms of the $g_{\alpha\beta}(r)$ after the unphysical oscillations have been set to the $g_{\alpha\beta}(0)$ value, is excellent (see the dotted curves). The cubic spline fits to $S_{GeGe}(Q)$ and $S_{GeSe}(Q)$ are also shown in figure 4.6 by the thick solid curves. The thick solid curve for $S_{SeSe}(Q)$ was obtained by making a cubic spline fit to the data, Fourier transforming to real-space, setting the unphysical negative going region between 2.64 Å and 3.01 Å to $g_{SeSe}(0)$, and back-transforming to reciprocal-space. An unphysical negative region after the first peak in $g_{SeSe}(r)$ has been found before for different samples. For example in liquid CuSe the Se-Se partial pair distribution function shows a negative peak at 2.80 Å (Barnes & Enderby[17]) and a similar peak at

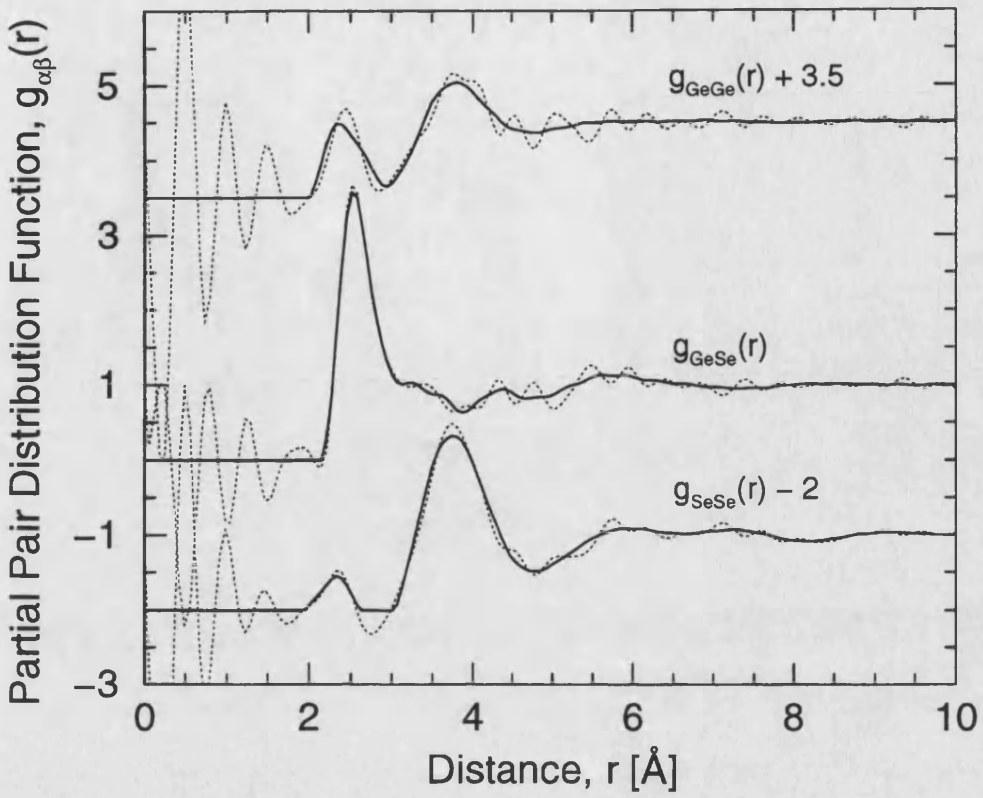

Figure 4.7: The partial pair distribution functions for molten GeSe at 727(2) °C obtained from the $S_{\alpha\beta}(Q)$ shown in figure 4.6. The broken curves are the Fourier transforms of the unsmoothed $S_{\alpha\beta}(Q)$ and the solid curves are the Fourier transforms of the smoothed $S_{\alpha\beta}(Q)$ with the low-r oscillations set to the $S_{\alpha\beta}(0)$ limit.

the same value of r has also been found for liquid $NiSe_2$, where the Se-Se partial structure factor was directly measured by the use of zero-scattering nickel (Enderby & Barnes[34]). These negative peaks could not be traced to any identifiable systematic or random errors.

Unlike the total structure factors, both the spline fitted partial structure factors and those obtained by the direct inversion of the total structure factors show no FSDP. The small pre-peak observed in the total structure factors and in the first order difference function, is therefore anticipated to originate from the interference of the partial structure factors in the 1.1 $Å^{-1}$ region, see figure 4.8. The like-atom partial structure factors show strongly damped oscillations and little structure after the third peaks.

It is seen from figure 4.7 that the $g_{\alpha\beta}(r)$ oscillate about the correct low-r limit

and there is no trace of a peak at the Si-O bond length of 1.6 Å, which would arise from an incorrect silica container correction (Barnes et al.[35]).

Homopolar Ge-Ge and Se-Se bonds occur in molten GeSe as represented by the low-r peaks in $g_{GeGe}(r)$ and $g_{SeSe}(r)$. These peaks are considered to be real since their removal, by setting them equal to the limiting value of $g_{\alpha\beta}(r) = 0$, leads to a detrimental agreement between the corresponding $S_{\alpha\beta}(Q)$ and the Fourier back transform of the resultant $g_{\alpha\beta}(r)$'s (see the χ^2 values given in table 4.5). A summary of the mean atomic distances and coordination numbers obtained from the $g_{\alpha\beta}(r)$ is given in table 4.6.

	χ^2 homopolar bonds incl.	χ^2 homopolar bonds excl.
$S_{GeGe}(Q)$	15.1	272.8
$S_{SeSe}(Q)$	36.1	94.4

Table 4.5 : Comparison of the χ^2 values for the $S_{\alpha\beta}(Q)$ and the back transform of the corresponding $g_{\alpha\beta}(r)$ after the unphysical low-r oscillations have been set to their theoretical limits when homopolar bonds are present and when they are removed. The values were obtained from the unsmoothed partial pair distribution functions and the number of data points is 331.

	1st peak position [Å]	$\overline{n}_\alpha^\beta$	integration range [Å]	2nd peak position [Å]	$\overline{n}_\alpha^\beta$	integration range [Å]
$g_{GeGe}(r)$						
a)	2.44(2)	0.7(1)	1.96 - 2.85	3.76(2)	7.4(3)	2.85 - 4.85
b)	2.36(2)	0.8(1)	1.96 - 2.91	3.81(2)	7.4(3)	2.91 - 4.85
$g_{GeSe}(r)$						
a)	2.53(2)	3.3(1)	2.15 - 3.10	$\approx 3.2^{(*)}$	$1.6(3)^{(*)}$	$3.10 - 3.80^{(*)}$
b)	2.54(2)	3.2(2)	2.15 - 3.10	$\approx 3.5^{(*)}$	$2.1(2)^{(*)}$	$3.10 - 3.93^{(*)}$
$g_{SeSe}(r)$						
a)	2.35(2)	0.23(5)	2.02 - 2.58	3.74(2)	8.6(3)	2.95 - 4.85
b)	2.34(2)	0.22(3)	1.90 - 2.64	3.76(2)	8.6(3)	3.01 - 4.85

Table 4.6 : Peak positions in $g_{\alpha\beta}(r)$, coordination numbers and integration ranges for the partial pair distribution functions. The integration ranges in $g_{SeSe}(r)$ are discontinuous because of the negative going region after the first peak. $^{(*)}$ Corresponds to the first shoulder in $g_{GeSe}(r)$. a) $g_{\alpha\beta}(r)$ unsmoothed, b) $g_{\alpha\beta}(r)$ from the spline fits.

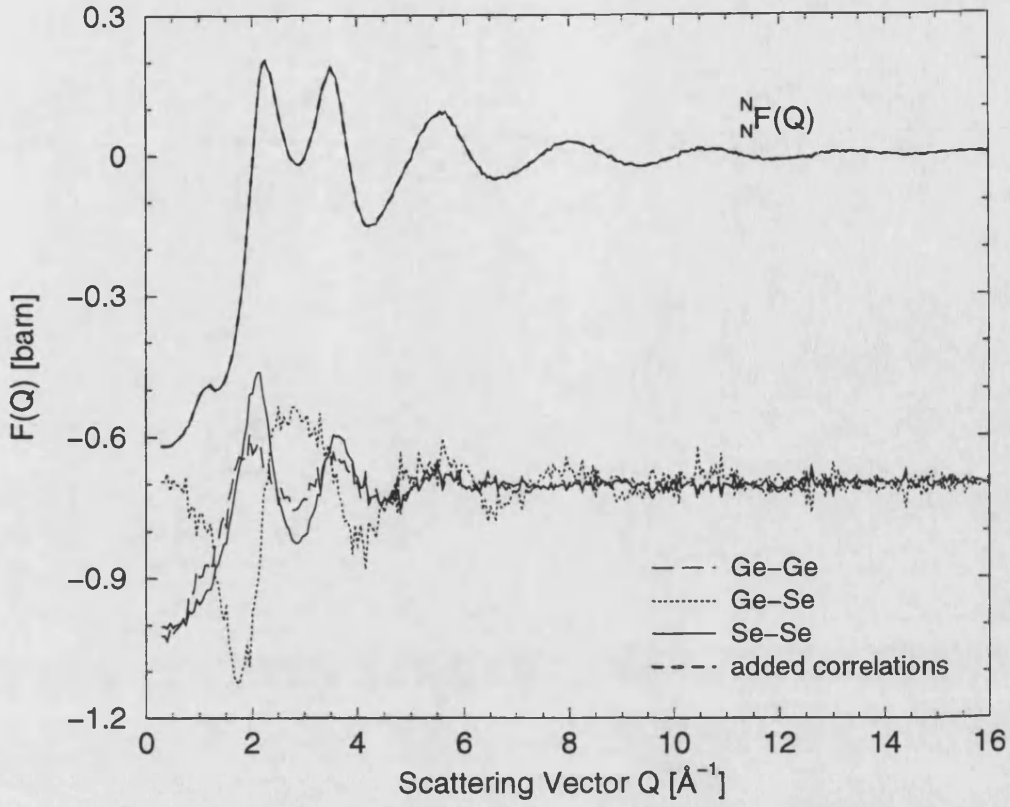

Figure 4.8: $^{N}_{N}$F(Q) together with the neutron weighted Ge-Ge, Ge-Se and Se-Se contributions (shifted by -0.7). These contributions are added up to reproduce the total structure factor (thick dashed curve). The reproduction agrees perfectly with the measured total structure factor.

The homo-polar bonding peak positions represent reasonable bonding distances. For example, the Ge-Ge bonds appear at a distance of 2.36(2) Å that is intermediate between 2.33(3) Å estimated for molten $GeSe_2$ (Penfold & Salmon[11]) and 2.45 – 2.47 Å observed in crystalline or amorphous Ge (Etherington et al.[36], Dalba et al.[37]). Also the Se-Se bond length of 2.34(2) Å is comparable to that found in liquid and amorphous Se (see e.g. Hohl & Jones[38]). $g_{GeSe}(r)$ is found to have a first peak at 2.54(2) Å and a shoulder at $\approx$ 3.5 Å. The first peak gives a Ge-Se coordination number of 3.2(2), which with the Ge-Ge homopolar bonding coordination number of 0.8(1) is consistent with the results obtained from the first order difference function, see section 4.4.2.

The total structure factor for the $^{N}Ge^{N}Se$ sample with its contributions from the individual $S_{\alpha\beta}(Q)$'s, weighted by the appropriate concentrations and scattering

lengths (see table 4.3), is shown in figure 4.8. The added up unsmoothed data sets perfectly reproduce the measured total structure factor including the small pre-peak at 1.1 $Å^{-1}$. The spline fitted $S_{\alpha\beta}(Q)$ also add-up to give the pre-peak at 1.1 $Å^{-1}$ which arises from a cancellation effect in the low-Q region from the Faber-Ziman partial structure factors rather than from a peak in any individual function. The peaks in the like-atom correlations are in phase over the entire measured Q-space region, and they both contribute towards the high second and third peaks in ${}^{N}_{N}F(Q)$. For $Q \leq 5\,Å^{-1}$ the Ge-Se correlations are in anti-phase with the like-atom correlations. The Ge-Se correlations are the only contributions showing oscillations up to $Q > 12\,Å^{-1}$, therefore the oscillations in the total structure factor at higher values of Q are due to these correlations.

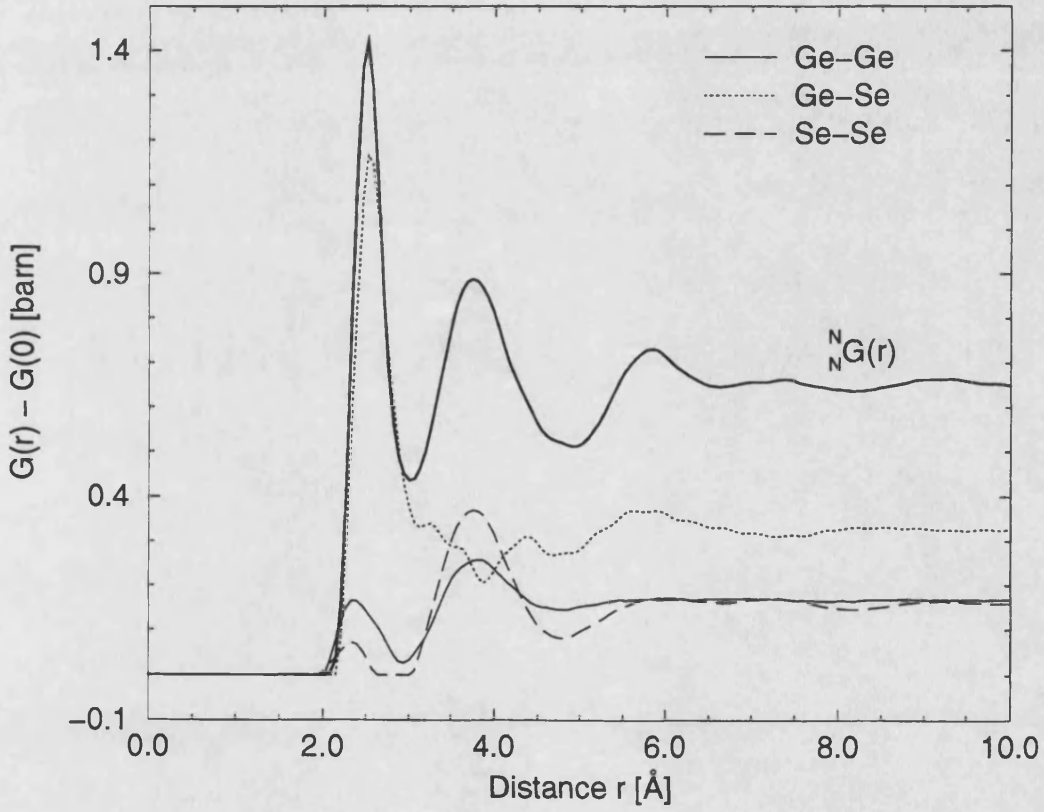

Figure 4.9: G(r) - G(0) for the ${}^{N}Ge^{N}Se$ sample (thick solid curve) drawn together with the neutron weighted Ge-Ge, Ge-Se and Se-Se correlations (spline fitted data sets).

The contributions of the partial pair distribution functions to ${}^{N}_{N}G(r)$ in real-space are shown in figure 4.9. It is seen that the $g_{\alpha\beta}(r)$ functions differ slightly in their low-r cut off values, see tables 4.4 and 4.6, an artefact of the smoothing

procedure. The first peak in the total pair distribution function is dominated by the Ge-Se correlations, but it also comprises the contributions from the Ge-Ge and Se-Se homopolar bonds. All three $g_{\alpha\beta}(r)$'s contribute to the second peak, although the Ge-Se correlations show a minimum at the position of the peak maximum. The Ge-Ge correlations do show little structure for $r > 5$ Å. However the Ge-Se and Se-Se contributions exhibit slight oscillations out to higher-r values.

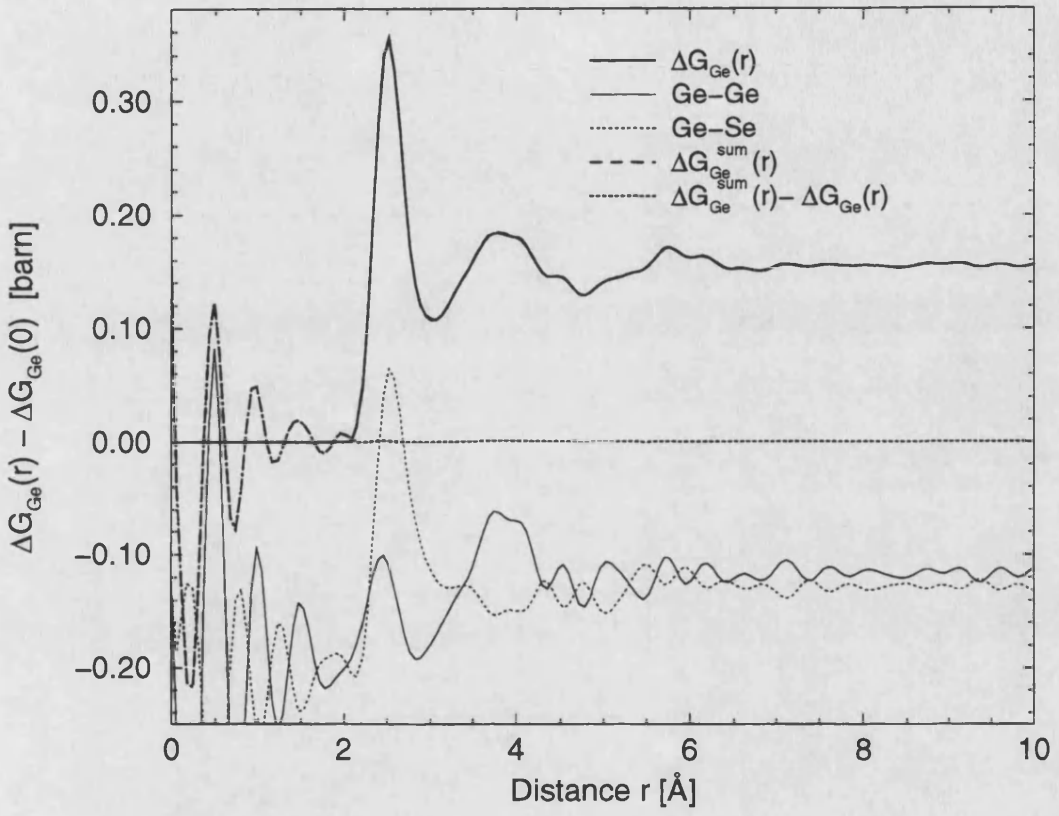

Figure 4.10: $\Delta G_{Ge}(r)$ obtained from the Fourier transform of $\Delta_{Ge}(Q)$ shown by the error bars in figure 4.5 shifted up by $-\Delta G_{Ge}(0)$ (thick solid curve) compared with the function built up from the neutron weighted Ge-Ge and Ge-Se contributions, called $\Delta G_{Ge}^{sum}(r)$ (thick dashed curve). The difference, $\Delta G_{Ge}^{sum}(r) - \Delta G_{Ge}(r)$, shows that above functions are indistinguishable on the scale of the plot. (The individual Ge-Ge and Ge-Se contributions are shifted down by 0.2 barn.)

The first order difference function serves as a critical test for the self-consistency of the obtained partial structure factors, since several systematic errors are strongly reduced on its formation, see section 3.4. A comparison of $\Delta G_{Ge}(r)$, obtained from the total structure factors, with its reconstruction using the partial pair distribution functions $g_{GeGe}(r)$ and $g_{GeSe}(r)$ weighted according to equation 4.4, is shown

in figure 4.10. It can be seen from the difference between these two functions that they agree very well. The first peak in $\Delta G_{Ge}(r)$ is dominated by the Ge-Se correlations, but the Ge-Ge homopolar bond contribution cannot be ignored. The high-r shoulder on $g_{GeSe}(r)$ contributes to the second peak in $\Delta G_{Ge}(r)$, which arises predominantly from the Ge-Ge correlations.

4.5 Comparison with the high and low temperature structures of GeSe

The low temperature (LT) crystal structure of GeSe is orthorhombic with unit cell dimensions of $a_0 = 4.387\,\text{Å}$, $b_0 = 3.837\,\text{Å}$ and $c_0 = 10.83\,\text{Å}$, the space group is $D_{2h}^{16} - Pcmn$ (e.g. Wiedemeier & Siemers[9]). The lattice sites are occupied alternatively by Ge and Se atoms and each atom has three near and in the opposite direction three further-removed unlike neighbours, leading to a distorted NaCl structure with a sequence of double-layers perpendicular to the c-axis, see figure 4.11 below.

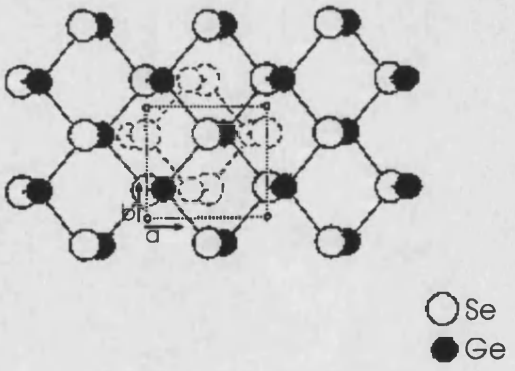

Figure 4.11: LT-crystal structure of GeSe, viewed down the [c] axis, showing two layers in the unit cell. The broken lines correspond to the lower layer, the dotted line marks the unit cell. (Reproduced from Dutta & Jeffrey[10].)

X-ray diffraction studies by Wiedemeier & Siemers[9] suggested that the unit cell of GeSe approaches cubic symmetry with increasing temperature, and at 651(5) °C it undergoes a first-order phase transformation to a normal NaCl-type structure, the high temperature (HT) crystalline structure of GeSe.

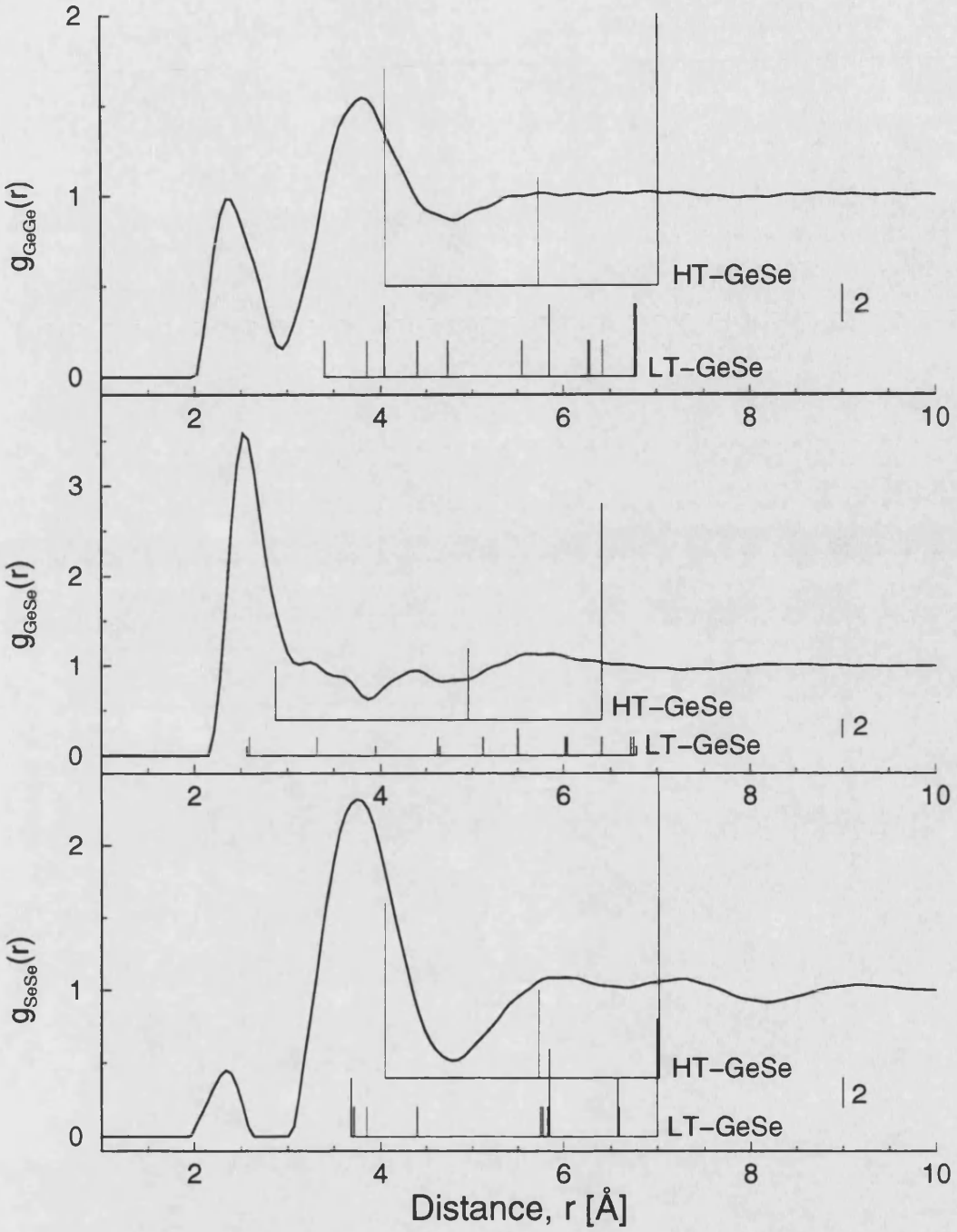

Figure 4.12: Partial pair distribution functions obtained from the spline fitted data sets compared with the corresponding correlations in the HT and LT crystalline phases of GeSe. The height of the vertical bars represents the number of the nearest neighbours in the crystal. In each of the three graphs a vertical bar is given, which corresponds to two neighbours for scaling purposes.

Figure 4.12 compares the measured partial structure factors with the corresponding environments in the HT and LT crystalline phases. In the liquid $g_{GeSe}(r)$ has a first peak at 2.45(2) Å and a shoulder at $\approx$ 3.5 Å (see table 4.6). The first peak gives a Ge-Se coordination number of 3.2(2) which increases to 5.3(3) if the shoulder extending from 3.10 Å to 3.93 Å is included in the integration range. HT-GeSe comprises Ge-centred octahedra with six Ge-Se bonds at 2.87 Å (Wiedemeier & Siemers[9]) while in LT-GeSe each Ge has 1 Se at 2.56 Å and 2 Se at 2.59 Å followed by 2 Se at 3.32 Å and 1 Se at 3.37 Å (Dutta & Jeffrey[10]). On melting, the octahedra of HT-GeSe are therefore disrupted and the first nearest-neighbour Ge-Se correlations in the melt resemble those in LT-GeSe (Petri et al.[39]).

The homopolar bonds found in liquid GeSe, which have already been discussed in section 4.4.3, occur in neither of the crystalline phases.

In HT-GeSe, Ge has 12 nearest-neighbour Ge at 4.05 Å (Wiedemeier & Siemers[9]) while in LT-GeSe these 12 nearest-neighbour Ge are distributed between 3.40 Å and 4.73 Å (Dutta & Jeffrey[10]). On melting, the Ge-Ge coordination environment in HT-GeSe is therefore disrupted to give an average of 0.8(1) Ge-Ge homopolar contacts together with 7.4(3) Ge-Ge next nearest-neighbours distributed between 2.91 Å and 4.85 Å (table 4.6). Furthermore, in HT-GeSe, Se has 12 nearest-neighbour Se at 4.05 Å (Wiedemeier & Siemers[9]) while in LT-GeSe there are 10 nearest-neighbour Se located between 3.68 Å and 4.40 Å and two further Se at 5.74 Å (Dutta & Jeffrey[10]). Again the Se-Se coordination environment in HT-GeSe is disrupted on melting to give an average of 0.22(3) Se-Se homopolar contacts together with 8.6(3) next nearest-neighbours distributed between 3.01 Å and 4.85 Å (table 4.6).

Overall, the liquid retains little memory of the HT-GeSe solid phase. Furthermore, although both the first nearest-neighbour Ge-Se distance and coordination number in the melt are comparable to those in LT-GeSe, Ge is not 3+3 coordinated to Se, which was suggested by Salmon & Liu[13] from measurements of the total structure factor, but it is fourfold coordinated to 3.2(2) Se and 0.8(1) Ge. The 9 % volume change on melting is accompanied by a collapse of the cubic close packing associated with HT-GeSe (Petri et al.[39]).

4.6 Comparison with the structure of molten CuSe and CuBr

It is interesting to compare the structure of liquid GeSe with that of the liquids CuSe (Barnes & Enderby[17]) and CuBr (Allen & Howe[18], Saito et al.[19], Pusztai & McGreevy[20]) for which partial structure factors are also available. All three systems contain the same or similar sized electropositive (A = Cu or Ge) and electronegative species (X = Se or Br) but have somewhat different physical characteristics.

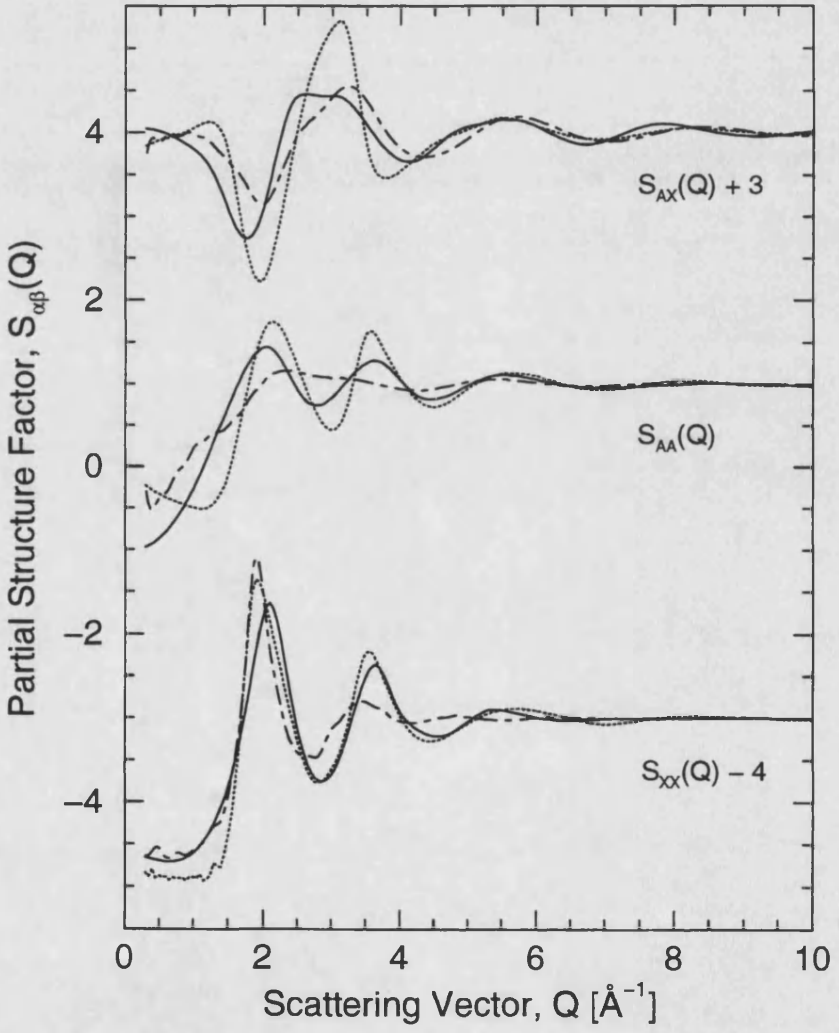

Figure 4.13: The $S_{\alpha\beta}(Q)$ for liquid GeSe at 727 °C (solid curves), CuSe at 700 °C (dotted curves) and CuBr at 515 °C (dot-dashed curves). The partial structure factors for CuSe are taken from Barnes & Enderby[17] and those for CuBr are taken from Pusztai & McGreevy[20].

CuSe melts at $\approx 525\,^{\circ}C$ from a structure wherein two thirds of the Se form pairs, with a characteristic bond length of 2.28 Å (Berry[40]), to give a molten semiconductor with a high electrical conductivity of 1240(20) $\Omega^{-1}\,cm^{-1}$ at 540 °C (Barnes & Enderby[17]). By comparison, CuBr melts at 488 °C from a high-temperature superionic phase, comprising mobile Cu^{2+} ions in a bcc-lattice of Br^{-} ions (Boyce & Huberman[41]), to give a liquid with an electrical conductivity of 2.6 $\Omega^{-1}\,cm^{-1}$ at 527 °C (Janz et al.[42]).

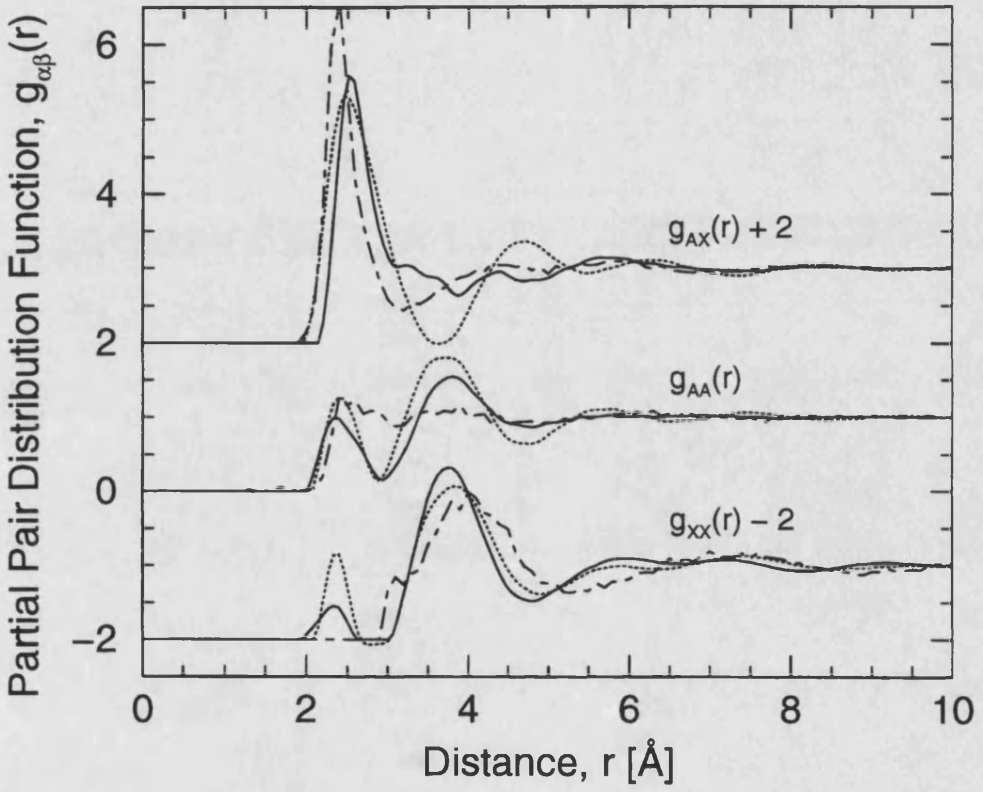

Figure 4.14: The $g_{\alpha\beta}(r)$ for liquid GeSe at 727 °C (solid curves), CuSe at 700 °C (dotted curves) and CuBr at 515 °C (dot-dashed curves). The partial structure factors for CuSe are taken from Barnes & Enderby[17] and those for CuBr are taken from Pusztai & McGreevy[20]. The absence of homopolar bonds in $g_{XX}(r)$ for CuBr should be noted.

The partial structure factors for the AX melts measured by neutron diffraction are compared in figure 4.13. All of these liquids were studied using the instrument D4B, set-up in the same configuration, and the $S_{\alpha\beta}(Q)$ therefore have the same Q-space range and resolution function. It is found that $S_{AA}(Q)$ and $S_{AX}(Q)$ become increasingly structured in the order from CuBr to CuSe via GeSe. For example,

whereas the A-A partial structure factor for CuBr is broad and featureless, that for CuSe comprises well-defined oscillations. Also the 'Coulomb dip' at $\approx 1.5 - 2\,\text{Å}^{-1}$, an indication of charge ordering in $S_{AX}(Q)$, is strongly marked in CuSe. The high-Q oscillations in $S_{XX}(Q)$ for CuBr are more damped than those for GeSe and CuSe.

In liquid GeSe and CuSe there is clear evidence for both A-A and Se-Se homopolar contacts, whereas in the solid state the only homopolar bonds are the Se-Se pairs in CuSe. By contrast, there is no evidence for Br-Br contacts in molten CuBr although short Cu-Cu distances are observed in both the liquid and high-temperature solid phases, in keeping with the relatively high mobility of the Cu^+ ions (Pusztai & McGreevy[20]).

The corresponding partial pair distribution functions are compared in figure 4.14 and the interatomic separations and coordination numbers are summarised in table 4.7.

Liquid	r_{AA} [Å]	$\overline{n}_A^A$	r_{AX} [Å]	$\overline{n}_A^X$	r_{XX} [Å]	$\overline{n}_X^X$
GeSe	2.36(2)	0.8(1)	2.54(2)	3.2(2)	2.34(2)	0.22(3)
	3.81(2)	7.4(3)			3.76(2)	8.6(3)
CuSe	2.43(2)	0.6(3)	2.52(3)	5.6(3)	2.40(2)	0.6(3)
	3.62(2)	10(2)			3.35(2)	10(2)
CuBr[a]	-	-	2.43(2)	3.6(5)	3.89(1)	11.1(1)
CuBr[b]	2.56(2)	1.3(2)	2.39(2)	2.9(2)	4.01(2)	10.2(4)
CuBr[c]	3.0(1)	-	2.37(2)	3.1	3.88(3)	11.4

From the work of [a] Allen & Howe[18], [b] Pusztai & McGreevy[20] or [c] Saito et al.[19] (from anomalous X-ray scattering measurements)

Table 4.7 : Interatomic separations and coordination numbers in the molten AX systems. The $r_{\alpha\beta}(r)$ denote the peak maximum positions in the $g_{\alpha\beta}(r)$.

In summary, while short A-A distances occur in all three systems, these nearest-neighbour correlations are better resolved for liquid GeSe and CuSe where clearly defined short ranged Se-Se correlations also occur (Petri et al.[39]).

4.7 Comparison with the structure of molten $GeSe_2$

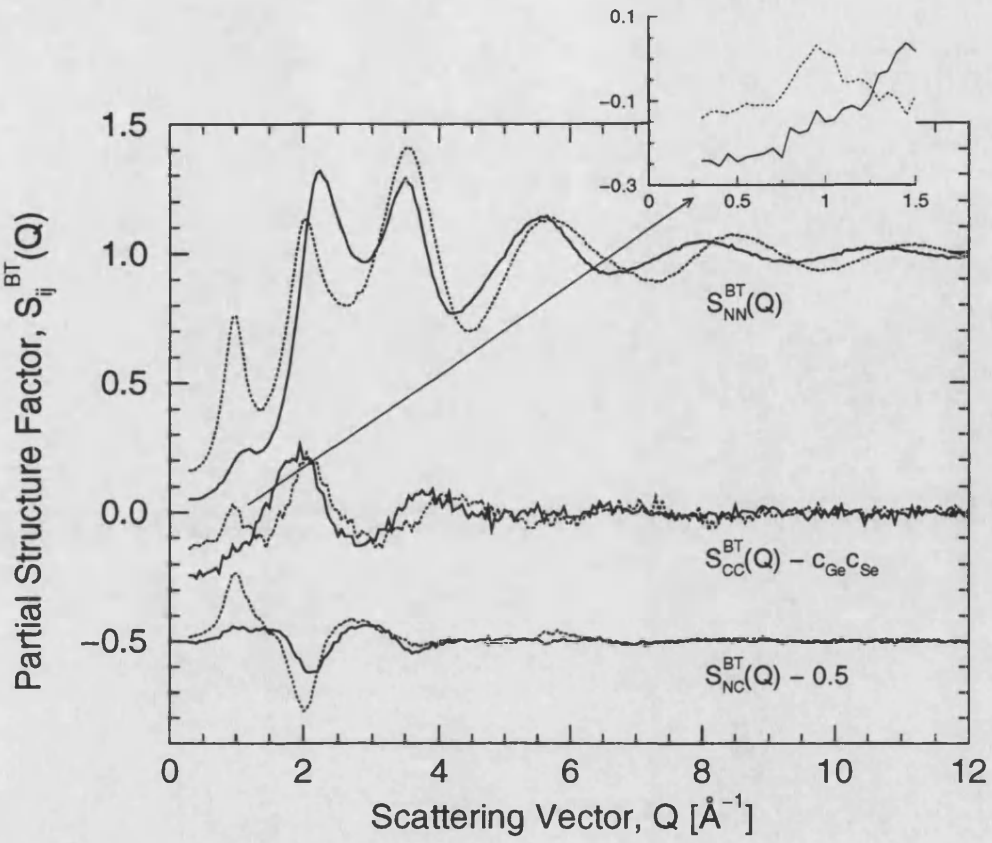

Figure 4.15: Comparison of the Bhatia Thornton partial structure factors for molten GeSe at 727(2) °C (solid curves) and molten $GeSe_2$ at 784(3) °C (dotted curves). The inset shows the area around the FSDP in $S_{CC}^{BT}(Q)$ for $GeSe_2$ on an enlarged scale.

The comparison between the structures of liquid GeSe and $GeSe_2$ is carried out using the formalism of Bhatia & Thornton (see section 2.10), where the correlations giving rise to the global structure of the system are separated from those describing the chemical ordering (Salmon[43]). The Bhatia Thornton partial structure factors are given in figure 4.15 and the corresponding partial pair distribution functions are shown in figure 4.16.

In a previous paper by Salmon & Liu[13] the evolution with x of the topology of the structure in molten Ge_xSe_{1-x} was investigated by using neutron diffraction. Since the coherent scattering lengths of ^{N}Ge and ^{N}Se are very similar the measured total structure factors gave $S_{NN}^{BT}(Q)$ to a good approximation. It was pointed out

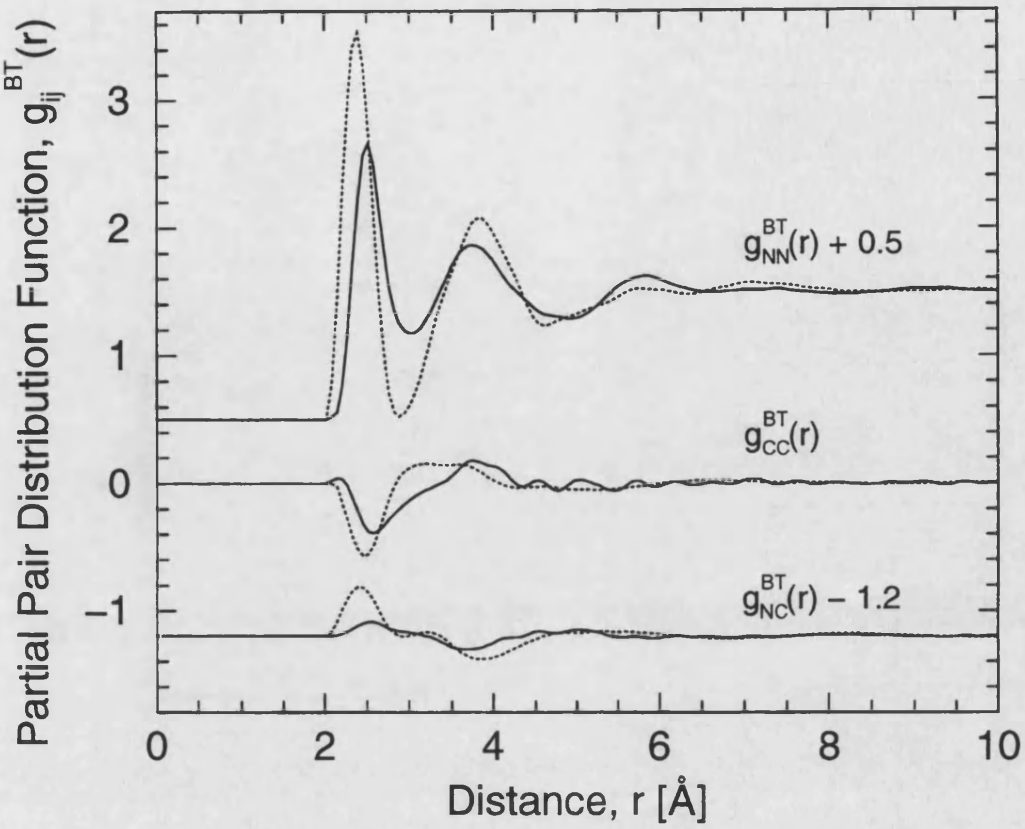

Figure 4.16: The Bhatia Thornton partial pair distribution functions for molten GeSe (solid curves) compared with those for molten $GeSe_2$ (dotted curves).

that the occurrence of a glass forming region with decreasing x is accompanied by the appearance of a FSDP in $S_{NN}^{BT}(Q)$, i.e. with the development of a second length scale associated with intermediate range atomic correlations (see e.g. Salmon[44]). The comparison in figure 4.15 confirms this observation. At $x = 0.5$, i.e. for the GeSe composition, there is a small FSDP at 1.19(2) $Å^{-1}$ in $S_{NN}^{BT}(Q)$. As shown in section 4.4.3 it arises, however, from a cancellation of the partial structure factors in this Q-space. There is no FSDP present at $x = 0$ (Salmon & Liu[13]), but at $x = 1/3$ the FSDP develops to be a significant feature.

Furthermore, although there is a clearly defined FSDP at 0.95(2) $Å^{-1}$ in the measured $S_{CC}^{BT}(Q)$ for molten $GeSe_2$ (Penfold & Salmon[11], Salmon[43]), a feature which has so far been proven not to be reproducible by *ab initio* molecular dynamics methods (see e.g. Massobrio et al.[45] and section 6.7.2), no such feature exists for molten GeSe.

Overall, there is an absence of any strong fluctuations on the scale of the intermediate range atomic ordering in molten GeSe.

4.8 Conclusions

- All three Faber-Ziman partial structure factors were successfully separated from the measured total structure factors.
- The nature of the previously reported solid state phase transition from a distorted to a normal NaCl-type structure was confirmed.
- The local ordering in liquid GeSe is significantly different to that of either its high or low temperature crystalline forms, with homopolar bonds occurring as prominent features in the molten state.
- There are qualitative similarities with the structure of the molten semiconductor CuSe. By comparison, in molten CuBr only short A-A distances with a broader distribution occur, but homopolar X-X homopolar bonds are not present.
- The FSDP in $S_{NN}^{BT}(Q)$ for liquid GeSe is small compared to that for the network melt $GeSe_2$. There is no FSDP in the other Bhatia-Thornton partial structure factors.

Bibliography

[1] Azoulay R, Thibierge H and Brenac A, *J. Non-Cryst. Sol.* **18** (1975) 33.

[2] Tronc P, Bensoussan M, Brenac A and Sebenne C, *Phys. Rev. B* **8** (1973) 5947.

[3] Haisty R W and Krebs H, *J. Non-Cryst. Sol.* **1** (1969) 399.

[4] Ruska J and Thurn H, *J. Non-Cryst. Sol.* **22** (1976) 277.

[5] Tsuchiya Y, *J. Non-Cryst. Sol.* **122** (1990) 205.

[6] Glazov V M and Situlina O V, *J. Dok. Chem.* **187** (1969) 587.

[7] Ipser H, Gambino M and Schuster W, *Monatshefte f. Chem.* **113** (1982) 389.

[8] Uemura O, Sagara Y and Satow T, *Trans. Japan Inst. Met. Qouy* **17** (1976) 457.

[9] Wiedemeier H and Siemers P A, *Z. Anorg. (Allg.) Chem.* **411** (1975) 90.

[10] Dutta S N and Jeffrey G A, *Inorg. Chem.* **4** (1965) 1363.

[11] Penfold I T and Salmon P S, *Phys. Rev. Lett.* **67** (1991) 97.

[12] Penfold I T and Salmon P S, *Phys. Rev. Lett.* **68** (1992) 253.

[13] Salmon P S and Liu J, *J. Phys.: Cond. Mat.* **6** (1994) 1449.

[14] Rovere M and Tosi M P, *Rep. Prog. Phys.* **49** (1986) 1001.

[15] Eisenberg S, Jal J-F, Chieux P and Knoll W, *Z. Phil. Mag. A* **46** (1982) 195.

[16] Bellisent R, Bergman C, Ceolin R and Gaspard J P, *Phys. Rev. Lett.* **59** (1987) 661.

[17] Barnes A C and Enderby J E, *Phil. Mag. B* **58** (1988) 497.

[18] Allen D A and Howe R A, *J. Phys.: Cond. Mat.* **4** (1992) 6029.

[19] Saito M, Park C, Omote K, Sugiyama K and Waseda Y *J. Phys. Soc. Jap.* **66** (1997) 633.

[20] Pusztai L and McGreevy R L, *J. Phys.: Cond. Mat.* **10** (1998) 525.

[21] Uemura A, Sagara Y and Satow T, *Phys. Stat. Sol. (a)* **26** (1974) 99.

[22] Hosokawa S, Hari Y, Kouchi T, Ono I. Sato H, Taniguchi M, Hiraya A, Takata Y, Kosugi N and Watanabe M *J. Phys.: Cond. Mat.* **10** (1998) 1931.

[23] Okada T, Satoh T, Matsumura M and Ohno S, *J. Phys. Soc. Jap.* **65** (1996) 230.

[24] Glazov V M, Kurbatov V A and Faradzhov A I, *Sov. Phys. Semicond.* **21** (1987) 295.

[25] Cusack N E, *The Physics of Structurally Disordered Matter*, Hilger: Bristol (1987).

[26] Sears V F, *Neutron News* **3** (1992) 26.

[27] Salmon P S, Xin S and Fischer H E, *Phys. Rev. B* **58** (1998) 6115.

[28] Petri I, Salmon P S and Fischer H E, *J. Non-Cryst. Sol.* **250-252** (1999) 405.

[29] Okazaki A, *J. Phys. Soc. Jap.* **13** (1958) 1151.

[30] Kannewurf C R, Kelly A and Cashman R J, *Acta Cryst.* **13** (1960) 449.

[31] Hulliger F, *Physics and Chemistry of Materials with Layered Structures*, vol 5, ed. Levy F, D. Reidel Publishing Company: Dordrecht, Holland (1976).

[32] Salmon P S and Benmore C J, *Recent Developments in the Physics of Fluids*, ed. Howells W S and Soper A K, Hilger: Bristol (1992) F225.

[33] Edwards F G, Enderby J E, Howe R A, Page D I, *J. Phys. C: Sol. State Phys.* **8** (1975) 3483.

[34] Enderby J E and Barnes A C, *Rep. Prog. Phys.* **53** (1990) 85.

[35] Barnes A C, Lague S B, Salmon P S and Fischer H E, *J. Phys.: Cond. Mat.* **9** (1997) 6159.

[36] Etherington G, Wright A C, Wenzel J T, Dore J C, Clarke J H and Sinclair R N, *J. Non-Cryst. Sol.* **48** (1982) 265.

[37] Dalba G, Fornasini P, Grazioli M and Rocca F, *Phys. Rev. B* **52** (1995) 11034.

[38] Hohl D and Jones R O, *Phys. Rev. B* **43** (1991) 3856.

[39] Petri I, Salmon P S and Fischer H E, *J. Phys.: Cond. Mat.* **11** (1999) 7051.

[40] Berry L G, *Am. Mineralogist* **39** (1954) 504.

[41] Boyce J B and Huberman B A, *Phys. Rep.* **51** (1979) 189.

[42] Janz G J, Dampier F W, Lakshminarayanan P K, Lorenz P K and Tomkins R P T, *Natl. Bur. Stand. Ref. Data Ser.* **15** (1968) 1.

[43] Salmon P S, *Proc. R. Soc.* **A 437** (1992) 591.

[44] Salmon P S, *Proc. R. Soc.* **A 445** (1994) 351.

[45] Massobrio C, Pasquarello A and Car R, *Phys. Rev. Lett.* **80** (1998) 2342.

Chapter 5

The structure of liquid $GeSe_2$ at high temperatures : A semiconductor to metal transition?

5.1 Introduction and previous work

In this chapter the results of a neutron diffraction study on the structure of the proto-typical glass forming liquid $GeSe_2$ as a function of increasing temperature are presented.

A variety of measurements on liquid $GeSe_2$ give evidence for a breakdown of the network structure and an eventual semiconductor-metal transition with increasing temperature (Andreev et al.[1]). Haisty & Krebs[2] found that the electrical resistivity decreases strongly with raising temperature. At high temperatures of $\approx$ 1000 °C the measured specific resistivities indicate a metallic-like electrical conductivity of the melt. The measurements of Okada et al.[3] show that the conductivity gap in the liquid decreases from 1.4 eV at 750 °C to about zero at 1073 °C while the electrical conductivity σ rises from 0.04 $\Omega^{-1}\,cm^{-1}$ to 90 $\Omega^{-1}\,cm^{-1}$, but $d\sigma/dT$ remains positive. However Ohno et al.[4] found evidence from their electrical conductivity measurements that the density of states at the Fermi-level, $N(E_F)$, for liquid $GeSe_2$ increases rapidly with increasing the temperature, which corresponds

to a semiconductor-metal transition. Accompanying these changes in molten $GeSe_2$ is an anomalous density behaviour, namely an increase in the mass density with temperature (Ruska & Thurn[5]), and a reduction in viscosity that is much more rapid than for other Ge-Se liquids (Glazov & Situlina[6], Laugier et al.[7]).

Another glass forming binary network melt that exhibits a semiconductor-metal transition with increasing temperature is As_2Se_3 (Hosokawa et al.[8],[9], Tamura et al.[10]). X-ray diffraction studies on the structure of liquid As_2Se_3 as a function of temperature and pressure show a marked change in the measured Bhatia-Thornton (BT) number-number structure factors, $S_{NN}(Q)$, that are directly measured in the x-ray diffraction experiment since $Z(As) = 33 \approx Z(Se) = 34$, when the semiconductor to metal transition occurs. For example, the first sharp diffraction peak in $S_{NN}(Q)$ at $\approx 1.2\,\text{Å}^{-1}$ disappears and the second and third peaks merge (Hosokawa et al.[9]). These changes in the topology of the melt are very similar to the changes observed in $S_{NN}(Q)$ for the liquid Ge_xSe_{1-x} system as x is increased from zero to unity and the nature of the electrical conductivity changes from semiconducting to metallic, see Salmon & Liu[11].

Neutron diffraction experiments by Maruyama et al.[12] on molten $GeSe_2$ at 800 °C and 900 °C demonstrate that the first sharp diffraction peak decreases strongly between these two temperatures, indicating that the intermediate range order breaks down with increasing temperature. In our experiments we measure the structure of liquid $GeSe_2$ at 800 °C, 1000 °C and 1100 °C. Since the coherent scattering length of germanium b_{Ge}(8.185 fm) is comparable in magnitude to selenium, b_{Se}(7.970 fm), the measured total structure factors will yield a direct measurement of the BT partial structure factor, $S_{NN}(Q)$. Information on the topology of molten $GeSe_2$ can therefore be obtained at both short and intermediate length scales.

5.2 Sample preparation and neutron diffraction experiments

Glassy $GeSe_2$ samples were prepared using high purity elemental Ge lumps (99.9999 %, Aldrich) and Se pellets (99.999 %, Johnson Matthey) following the procedure outlined in section 4.2, except that the elements were not sealed in dou-

ble walled silica tubes, as this would have reduced the quench-rate of the samples.

The heating in the rocking furnace followed the same procedure as for the GeSe samples. However after keeping them at 1000 °C for 48 hours they were cooled down slowly (1 °C/min) to 850 °C, where they were left to equilibrate, before being quenched in an ice/salt-water mixture at -5 °C.

The resultant $GeSe_2$ glass was then separated from the silica tube in a high purity argon filled glove box and transferred to a cylindrical silica tube of 7 mm inner diameter and 1 mm wall-thickness designed for the experiment on LAD. To reduce the Se vapour pressure and thereby keep the sample composition close to the stoichiometric composition, the ampoule was sealed under argon gas (99.998 %) at a pressure of 0.41 atm after it had been evacuated as usual to approximately 10^{-5} torr on the vacuum line. The procedure which was used for sealing the ampoule under an argon atmosphere followed that used by Wasse[13] to seal $KCl - BiCl_3$ glasses under chlorine gas, and is described below. The experimental set-up is shown in figure 5.1.

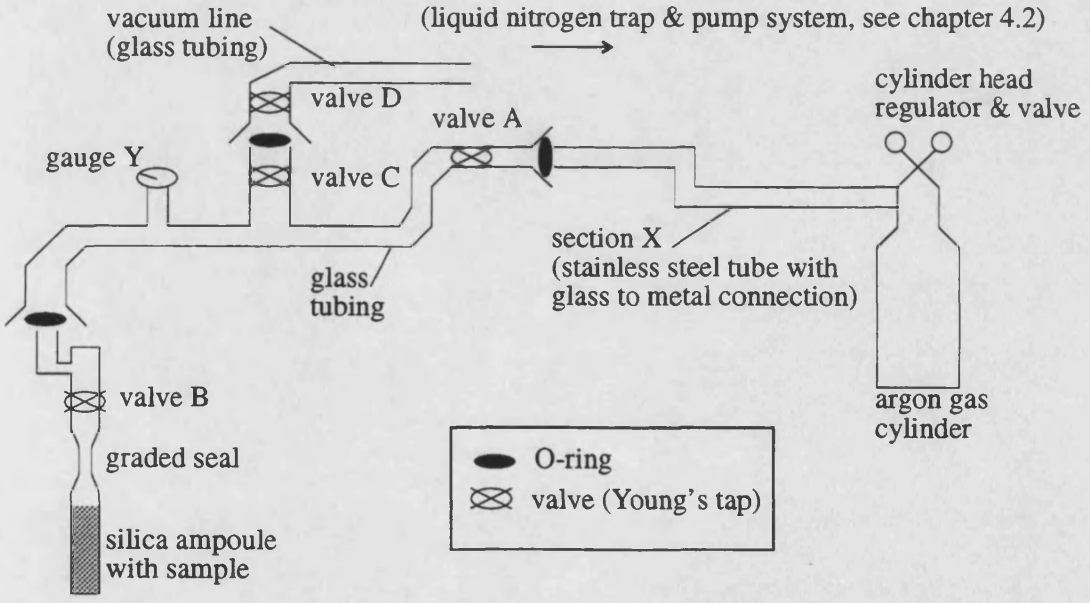

Figure 5.1: Sketch of the set-up used to seal the $GeSe_2$ sample under an argon atmosphere.

When the silica ampoule with the sample is connected all valves are closed. The glass tubing is then evacuated using the rotary and diffusion pump system of the vacuum line by opening valves C and D. When the vacuum is better than 10^{-5} torr, valve B is opened and the sample is evacuated to approximately the

same pressure. Then the sample is isolated by closing valve B, and the vacuum line by closing valves C and D.

Argon gas is conducted from the cylinder into section X and valve A is opened. The pressure of the argon is measured with the analogue gauge Y. When an argon atmosphere of approximately 1 atm is measured, the valve on the cylinder head and valve A are closed. In the glass tubing remains a mixture of argon and the air that could not be evacuated from section X before.

The argon/air gaseous mixture is evacuated with the rotary and diffusion pump system to 10^{-5} torr by opening valves C and D.

The above two steps are repeated three times to purge the remaining air out of the system.

Argon is finally administered into the system as described above to a pressure of 0.5 atm, and valve B is opened, conducting argon into the silica ampoule containing the sample. The argon pressure decreases to 0.41 atm, and the sample is sealed off under this argon atmosphere.

The argon pressure was such that at the high temperatures of the neutron diffraction experiment, 800 °C, 1000 °C and 1100 °C, the pressure of the argon above the sample was estimated to be 1.56 atm, 1.82 atm and 1.94 atm respectively, assuming a negligible solubility of argon in the liquid. By considering the $GeSe_2$ sample at 1100 °C to be a system of two non-interacting liquids in equilibrium with Se_2 dimers in the gas phase, a ratio of 1 Ge: 1.95 Se is estimated for the melt by using the vapour pressures for pure Ge and Se (Weast[14]). The actual stoichiometry is anticipated to be much closer to 1 Ge: 2 Se owing to the Ge-Se bonding and the presence of the argon gas overpressure.

The neutron diffraction experiments were carried out at the Rutherford Appleton Laboratory on the LAD diffractometer. The complete experiment comprised the measurement of the diffraction patterns for the molten $GeSe_2$ sample ($\approx$ 6.4 g) in the silica ampoule in the heater at three temperatures (800(3) °C, 1000(3) °C and 1100(3) °C), an empty silica ampoule of the same dimensions as the one containing the sample in the heater at 778(3) °C and 1000(3) °C, a 8.37 mm diameter vanadium rod in the heater at room temperature for the data normalisation, and the empty heater with nothing placed at the sample position to perform the back-

ground corrections. The 'Leicester' furnace served as the heater and it is shown schematically in figure 5.2.

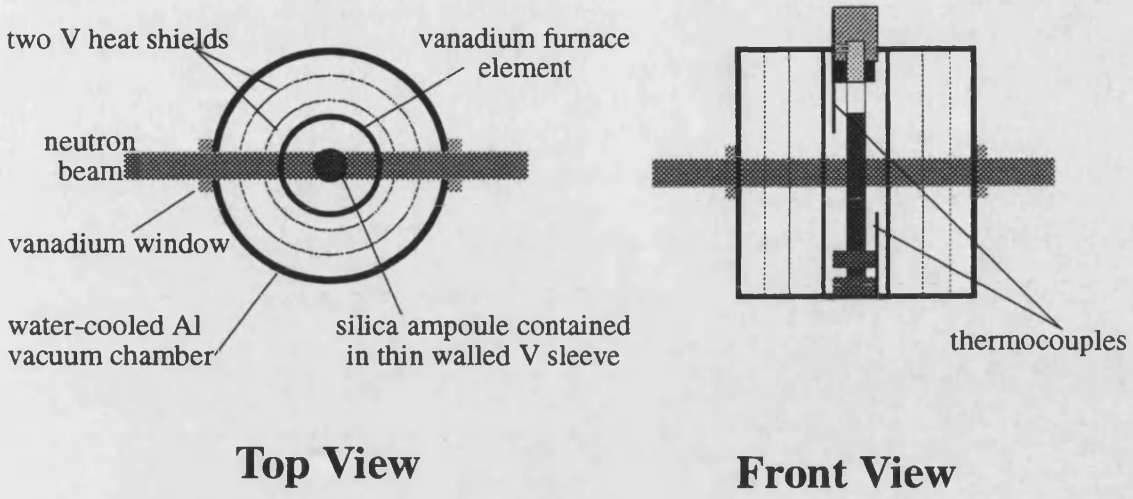

Figure 5.2: Schematic diagram of the 'Leicester' furnace used in the LAD experiment.

The silica cells were supported by a thin vanadium sheath, which conserved their shape at the relatively high temperatures that were used. The sample was fully illuminated at all temperatures by a rectangular beam, 35 mm high and 40 mm wide.

The scattering lengths and cross-sections for Ge and Se are summarised in table 5.1.

Element	$\overline{b}$ [fm]	$\sigma_{free,coh}$ [barn]	$\sigma_{free,inc}$ [barn]	σ_{abs} (@ 1.798 Å) [barn]
Ge	8.185(20)	8.19(4)	0.18(7)	2.20(4)
Se	7.970(9)	7.78(2)	0.31(6)	11.7(2)

Table 5.1 : Scattering lengths and cross-sections of Ge and Se taken from Sears[15]. Their statistical errors are given in brackets.

The wavelength dependence of the total cross-sections $\sigma^{total}(\lambda) = \sigma_{free,sc} + \sigma_{abs}(\lambda)$ for the $GeSe_2$ sample is shown in fig. 5.3 and was calculated assuming $\sigma_{abs} \propto \lambda$.

The measured total structure factors, F(Q), can be written either as a linear

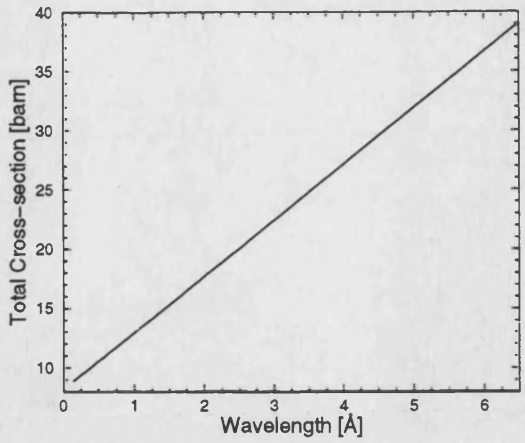

Figure 5.3: Calculated $\sigma^{\text{total}}(\lambda) = \sigma_{\text{free,sc}} + \sigma_{\text{abs}}(\lambda)$ for glassy $GeSe_2$.

combination of the Faber-Ziman partial structure factors,

$$F(Q)/barn = 0.0744(4)[S_{GeGe}(Q)-1]+0.2899(8)[S_{GeSe}(Q)-1]+0.2823(6)[S_{SeSe}(Q)-1] \tag{5.1}$$

or as a linear combination of the Bhatia-Thornton (BT) partial structure factors (section 2.10),

$$\begin{aligned} \frac{F(Q)}{<b>^2} &= [S_{NN}(Q)-1] + c_{Ge}c_{Se}(\Delta b)^2/<b>^2 \left[\frac{S_{CC}(Q)}{c_{Ge}c_{Se}} - 1\right] \\ &\quad +2\Delta b/<b> S_{NC}(Q) \\ &= [S_{NN}(Q)-1] + 1.6(3)*10^{-4}\left[\frac{S_{CC}(Q)}{0.2222} - 1\right] + 0.054(5)S_{NC}(Q)\,, \end{aligned} \tag{5.2}$$

and the total pair distribution function follows from the Fourier transform relation,

$$\begin{aligned} \frac{G(r)}{<b>^2} &= \frac{1}{2\pi^2 n_0 r}\int_0^\infty \frac{F(Q)}{<b>^2} Q\, sin(Qr)dQ \\ &= [g_{NN}(r)-1] + 1.6(3)*10^{-4} g_{CC}(r) + c_{Ge}c_{Se}\cdot 0.054(5) g_{NC}(r) \end{aligned} \tag{5.3}$$

where c_α and b_α denote the atomic fraction and coherent scattering length of chemical species α, $\Delta b = b_{Ge} - b_{Se}$, $<b> = c_{Ge}b_{Ge} + c_{Se}b_{Se}$ and the BT pair distribution functions, $g_{NN}(r)$, $g_{NC}(r)$ and $g_{CC}(r)$, are defined by equation 2.71. From the above equation it can be seen that the Bhatia-Thornton number-number partial structure factor, $S_{NN}(Q)$, accounts for 95 % of the total structure factor, i.e. the contributions from the other partial structure factors can, to first order, be neglected.

The melting point of $GeSe_2$ is at 742(2) °C (Ipser et al.[16]). The mass densities for molten $GeSe_2$ at 800 °C and 1000 °C were taken from Ruska & Thurn[5]. The

mass density at 1100 °C was obtained by an extrapolation of the density values given by Ruska & Thurn. These densities, the number densities, and the low-r limits, $G(0) =< b >^2$ and sum-rule parameters ($2\pi^2 n_0 G(0)$) at the three temperatures are summarised in table 5.2.

Temperature	ρ [g/cm^3]	n_0 [Å^{-3}]	G(0) [barn]	sum-rule [barn/Å^3]
800 °C	3.974(5)	0.0312(2)	-0.6467(11)	-0.3976(7)
1000 °C	4.050(5)	0.0317(2)	-0.6467(11)	-0.4052(7)
1100 °C	4.102(5)	0.0322(2)	-0.6467(11)	-0.4104(7)

Table 5.2 : Sample parameters at the different temperatures.

LAD comprises 14 groups of detectors with differing instrumental resolution functions (see section 3.2.3). The final total structure factors, F(Q), were constructed by merging all those diffraction patterns from the different groups that showed good agreement, see table 5.3.

2θ[°]	±5	±10	±20	±35	±60	±90	±150
Resolution $\Delta Q/Q$ [%]	11	6	2.8	1.7	1.2	0.8	0.5
Q-range for	0.5-3	0.5-6.5	1.6-8	2-13	2.3-25	4-30	10-30
800 °C [Å^{-1}]	0.5-1.1	1.9-3.9	1.5-10	2-8.7	2.3-13.6	3.9-9	10.1-30
Q-range for	0.5-3	0.5-6.5	1.6-5.9	2-13	2.3-25	4-30	10-30
1000 °C [Å^{-1}]	0.5-1.1	-	1.5-10	2.1-8.7	2.4-13.6	3.9-9	20-30
Q-range for	0.5-3	0.5-6.5	1.6-10.5	2-13	2.3-26	4-18.5	13-19
1100 °C [Å^{-1}]	0.5-0.75	-	1.5-10	2.1-8.7	2.4-26	3.9-26	12.5-30

Table 5.3 : Contributions of the different detector banks to the total structure factor at the three temperatures. The top and bottom lines for each temperature correspond to the left-hand-side and right-hand-side detector banks of the instrument respectively, see figure 3.2.

The data analysis followed the procedure described in section 3.3.2 and was performed using the ATLAS suite of programs (Soper et al.[17]). It was checked that the resultant F(Q)'s tend to the correct high-Q limit and obey the sum-rule relations (Salmon & Benmore[18]). In order to obtain good overall agreement between the measured data and the back Fourier transform of the corresponding real-space functions after the unphysical low-r oscillations have been set to their

calculated limits, effective number densities of $0.92 * n_0$ and $0.85 * n_0$ had to be used in the data analysis procedure for the 1000 °C and 1100 °C data respectively. This is a typical problem associated with high-temperature experiments (see e.g. Salmon[19]).

5.3 Total structure factors

The measured total structure factors for the three temperatures are shown in figure 5.4. The bars represent the statistical errors on each data point of F(Q) and the smooth solid curves correspond to a cubic spline fit to $Q * F(Q)$.

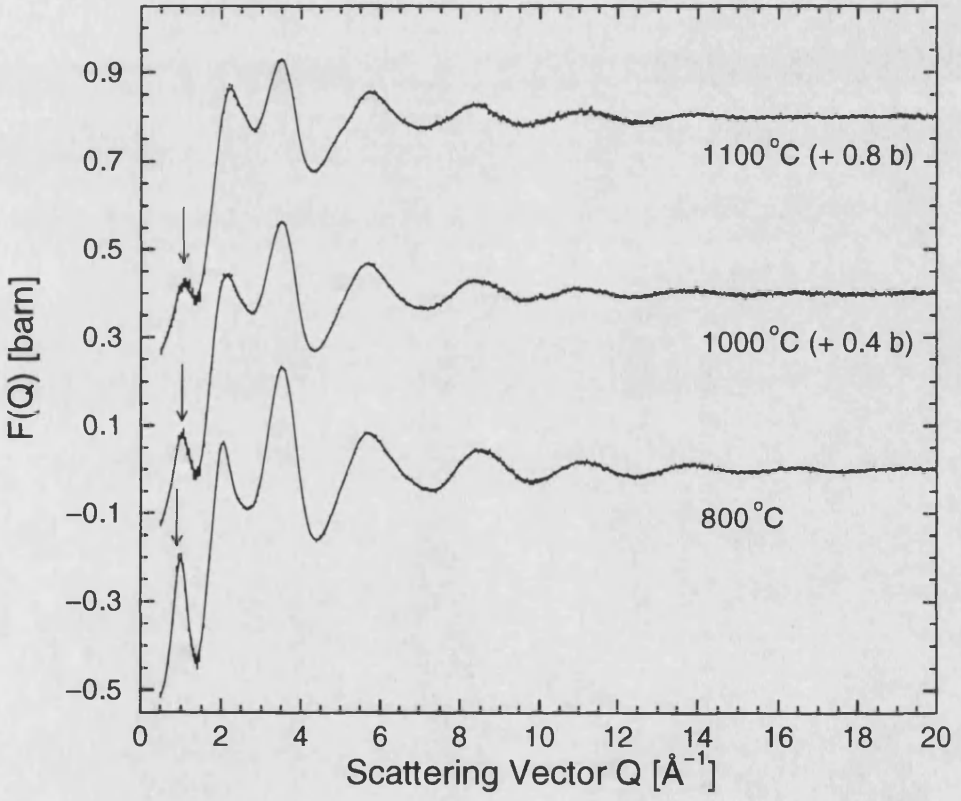

Figure 5.4: Total structure factors for molten $GeSe_2$ at 800 °C, 1000 °C and 1100 °C. The bars represent the statistical errors on the data points and the solid curves are the smoothed F(Q)'s obtained by using a cubic spline fit to the data points weighted by Q.

With increasing temperature marked changes occur to the FSDP (indicated by arrows in figure 5.4): it decreases in height and shifts to higher-Q values. Also the

ratio of the third to the second peak intensity decreases. All these changes will be discussed in detail in the next chapter.

The data sets are truncated at a maximum Q-value of $Q_{max} = 20\,\text{Å}^{-1}$, where for the 1000 °C and 1100 °C data sets the high-Q oscillations are fully damped.

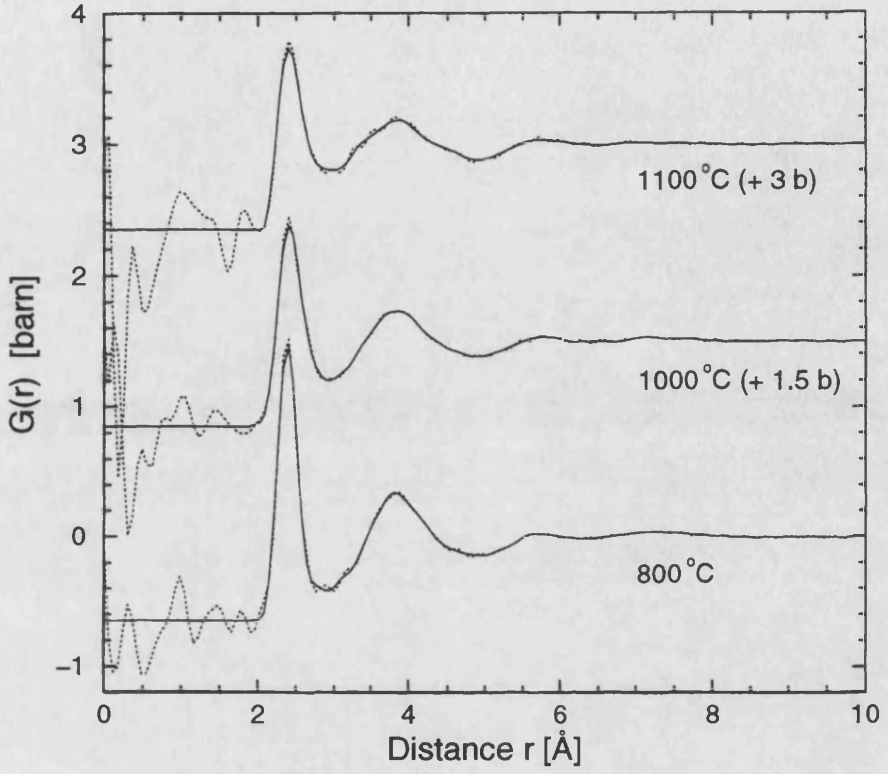

Figure 5.5: Total pair distribution functions for molten $GeSe_2$. The dotted curves correspond to the Fourier transforms of the error bars in figure 5.4, and the solid curves to the Fourier transforms of the smoothed data sets. Additionally the unphysical low-r oscillations have been set to their theoretical G(0) limits.

The G(r)'s for all three temperatures have the same overall profiles, a sharp first peak followed by a broad second peak. With increasing temperature the first peak decreases in height and broadens, but there is little change in its position.

It is seen from figure 5.5 that the silica container correction has been performed properly since for the 800 °C and 1000 °C data sets (dotted curves) no peak is observed at the Si-O bond distance of 1.6 Å (see e.g. Barnes et al.[20]). Additionally it was checked that the small negative going peak at $\approx$ 1.6 Å in the 1100 °C data set is not due to the subtraction of too much silica. Reducing the container correction by 10 % did not influence this peak.

5.4 Bhatia-Thornton number-number partial structure factors

The measured Bhatia-Thornton number-number partial structure factors, $S_{NN}(Q)$, as obtained from equation 5.2 by assuming $A = B = 0$, are shown in figure 5.6. The data, illustrated by the error bars, are obtained by using the smoothed data sets shown in figure 5.4. The data agrees very well with its Fourier back transform over the whole Q-range for the 800 °C measurement. The agreement is slightly poorer for the 1000 °C and 1100 °C data, mainly in the region between $2 \leq Q[\text{Å}^{-1}] \leq 8$.

It is seen that when the temperature is increased the height of the FSDP decreases markedly. Its position Q_1 moves from $0.99(1)\,\text{Å}^{-1}$ to $1.05(1)\,\text{Å}^{-1}$ via $1.02(1)\,\text{Å}^{-1}$ and its full width at half-maximum ΔQ_1, as measured on making the peak symmetrical by reflecting its low-Q part about Q_1 (see dotted curves in figure 5.6), increases from $0.43(1)\,\text{Å}^{-1}$ to $0.51(1)\,\text{Å}^{-1}$ via $0.50(1)\,\text{Å}^{-1}$. At the same time the third peak becomes smaller relative to the second and the high-Q oscillations become increasingly damped, consistent with a broadening of the distribution of nearest-neighbours in real-space. Similar trends with increasing temperature have also been observed for liquid As_2Se_3 from x-ray diffraction experiments (Hosokawa et al.[9]). The parameters describing the estimated number-number partial structure factors, including the measured $S_{NN}(Q)$ for molten $GeSe_2$ at 784(3) °C (Penfold & Salmon[21]) and molten GeSe at 727(2) °C (section 4.7 and Petri et al.[22]), are summarised in table 5.4.

Liquid	T [°C]	Q_2 [Å^{-1}]	$\frac{Q_1}{Q_2}$	$\frac{Q_3}{Q_2}$	$\frac{Q_4}{Q_2}$	$S_{NN}(Q_2)$	$\frac{S_{NN}(Q_1)}{S_{NN}(Q_2)}$	$\frac{S_{NN}(Q_3)}{S_{NN}(Q_2)}$	$\frac{S_{NN}(Q_4)}{S_{NN}(Q_2)}$
$GeSe_2$	784	2.02(2)	0.49	1.75	2.80	1.14(1)	0.67	1.24	1.00
	800	2.03(1)	0.49	1.73	2.81	1.10(1)	0.63	1.24	1.03
	1000	2.13(1)	0.48	1.64	2.66	1.07(1)	0.47	1.18	1.04
	1100	2.22(1)	0.47	1.57	2.58	1.10(1)	0.38	1.09	0.99
GeSe	727	2.23(1)	0.53	1.57	2.51	1.32(1)	0.19	098	0.86

Table 5.4 : Parameters describing $S_{NN}(Q_\epsilon)$ for molten $GeSe_2$ and GeSe, where Q_ϵ ($\epsilon = 1, 2, 3, 4$) gives the maximum for peak ϵ.

The corresponding BT number-number partial pair distribution functions are shown in figure 5.7. The parameters describing the first and second nearest-

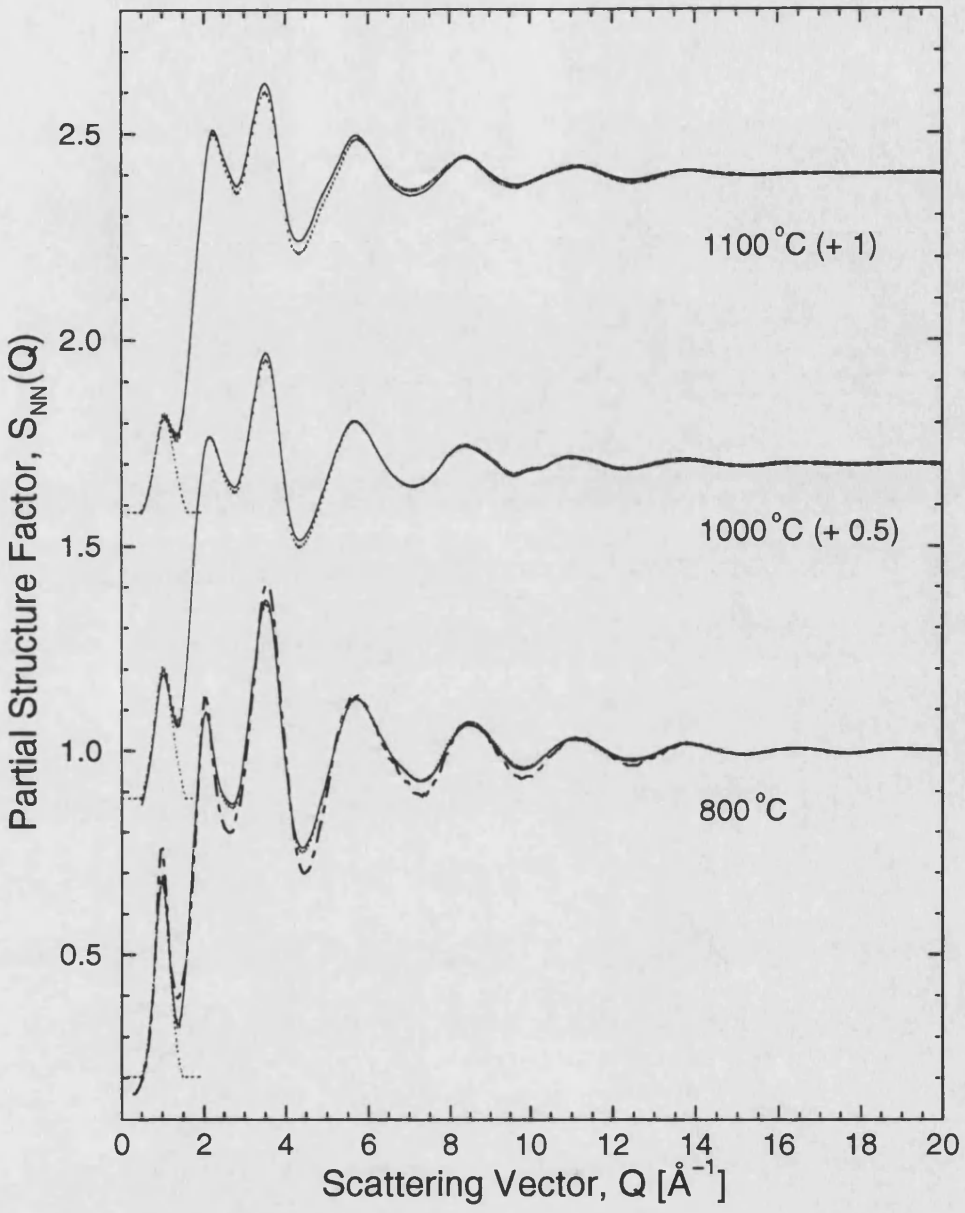

Figure 5.6: The measured $S_{NN}(Q) = F(Q)/ < b >^2 +1$ for liquid $GeSe_2$ at 800 °C, 1000 °C and 1100 °C. The bars represent the statistical errors on the data points and the thin solid curve shows the corresponding Fourier back transforms after the unphysical low-r oscillations in $g_{NN}(r)$ (figure 5.7) have been set to their theoretical limit. The chained curve superimposed on the lower data set gives $S_{NN}(Q)$ for molten $GeSe_2$ at 784 °C (Penfold & Salmon[21]). The FSDPs, defined by the symmetrisation of the peaks about their maximum are indicated by the dotted curves.

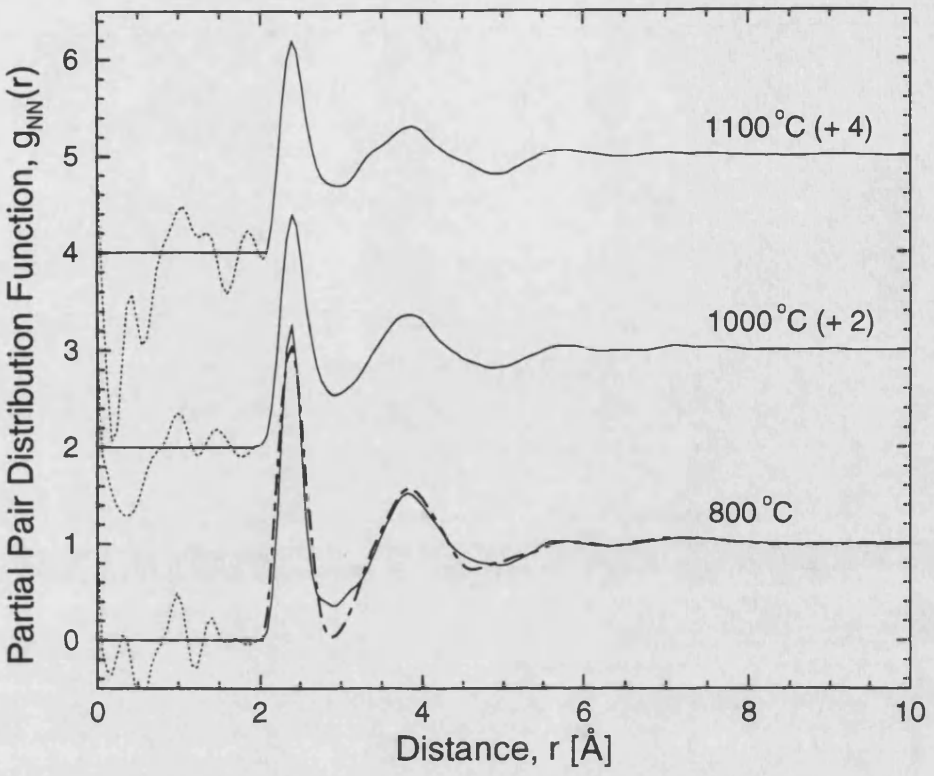

Figure 5.7: The measured $g_{NN}(r)$ for molten $GeSe_2$ at 800 °C, 1000 °C and 1100 °C as obtained by Fourier transforming the $S_{NN}(Q)$ shown in figure 5.6. The unphysical low-r oscillations about the $g_{NN}(0)$ limits are shown by the broken curves. The chained curve superimposed on the lower data set gives $g_{NN}(r)$ for liquid $GeSe_2$ at 784(3) °C (Penfold & Salmon[21]).

neighbours are summarised in table 5.5 together with the corresponding quantities for the measured $g_{NN}(r)$ for molten $GeSe_2$ at 784(3) °C (Penfold & Salmon[21]) and molten GeSe at 727(2) °C (section 4.7 and Petri et al.[22]).

The r_1 and $\overline{n}$ (see equation 3.27) values are in accordance with those measured for $GeSe_2$ in the temperature range from 800 to 900 °C by Maruyama et al.[12]. It is found that although there is a notable broadening of the first two peaks (see figure 5.8) with increasing temperature, neither their position nor the average coordination number $\overline{n}$ change within the experimental error.

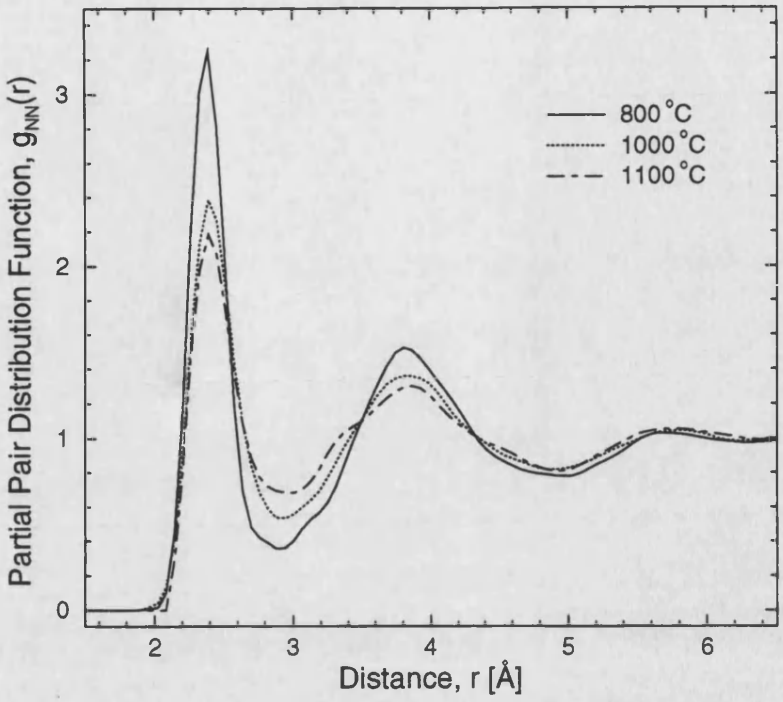

Figure 5.8: Comparison of the measured $g_{NN}(r)$ for molten $GeSe_2$ at 800 °C, 1000 °C and 1100 °C to illustrate the broadening of the first two peaks.

Liquid	T [°C]	r_1 [Å]	r_2/r_1	$\overline{n}$	Integration range [Å]
$GeSe_2$	784	2.38(2)	1.609	2.8(1)	2.02(1)-2.95(1)
	800	2.38(2)	1.605	2.7(1)	1.90(1)-2.95(2)
	1000	2.40(2)	1.596	2.7(1)	1.90(1)-3.01(2)
	1100	2.40(2)	1.608	2.6(1)	2.09(1)-3.01(2)
GeSe	727	2.52(2)	1.452	3.5(3)	2.09(2)-3.04(2)

Table 5.5 : Interatomic distances and coordination numbers for molten $GeSe_2$ and GeSe, where r_1 and r_2 give the positions of the first and second nearest-neighbours in $g_{NN}(r)$. The coordination numbers $\overline{n}$ were obtained by integrating over the first peak in $g_{NN}(r)$ to the first minimum.

5.4.1 Discussion and comparison with isotopic substitution results for molten $GeSe_2$ at 784 °C

The number-number partial structure factor $S_{NN}(Q)$ measured by a full partial structure factor analysis of molten $GeSe_2$ at 784(3) °C (Penfold & Salmon[21]) is compared in figure 5.6 with that at 800(3) °C derived from the present work. The overall profiles of the functions are comparable, the sharper peaks in the 784 °C measurement corresponding to a lower liquid temperature.

The limitations of the approximation $A = B = 0$ in equation 5.2 is most readily noticed in real-space as shown in figure 5.7 where $g_{NN}(r)$ at 784 °C is compared with the approximate $g_{NN}(r)$ at 800 °C. The latter is found to be higher in the regions around the first peak at 2.38(2) Å and the first minimum at 2.94(3) Å and lower in the region around the second peak at 3.82(2) Å. These discrepancies can be ascribed to the finite value of B in equation 5.2 which gives an additional contribution to G(r) from the number-concentration partial pair distribution function $g_{NC}(r)$, the Fourier transform of $S_{NC}(Q)$. From equation 2.71 it can be seen that $g_{NC}(r)$ has additional positive contributions from $g_{GeSe}(r)$ and $g_{GeGe}(r)$ and a negative contribution from $g_{SeSe}(r)$. The discrepancies in figure 5.7 can thereby be rationalised since the strongest real-space features are the first main peaks in $g_{GeSe}(r)$, $g_{GeGe}(r)$ and $g_{SeSe}(r)$ at 2.42(2) Å, $\approx$ 3.3 Å and 3.80(2) Å respectively (Penfold & Salmon[21]). However, the overall level of agreement between the measured and estimated $g_{NN}(r)$ functions shows that the approximation made in the present work is good to a first order and reveals where the second order effects appear (Petri et al.[23]).

If it assumed that the first peak in each of the G(r) functions comprises Ge-Se correlations alone, then mean coordination numbers $\overline{n}_{Ge}^{Se}$ of 3.9(1), 4.0(2) and 3.9(2) are obtained for 800 °C, 1000 °C and 1100 °C respectively. These results suggest that $GeSe_{4/2}$ tetrahedra remain the dominant structural motifs at all three temperatures. They are, however, larger than the value $\overline{n}_{Ge}^{Se} = 3.6(3)$ obtained from the measured $g_{GeSe}(r)$ for liquid $GeSe_2$ at 784(3) °C, which is consistent with the presence of homopolar bonds (Penfold & Salmon[21]). Unfortunately no information about the development of the homopolar bonds with temperature can be obtained from our measurements since the Faber-Ziman partial structure factors are not

available.

There is no evidence for an increase in the coordination number from four to six with increasing temperature and density in contrast with an earlier deduction based on several of the physico-chemical properties of $GeSe_2$ (Ruska & Thurn[5]). Rather, the density increase results from a breakdown of the intermediate range atomic ordering of the network melt with increasing temperature as evidenced by the changes in the FSDP. This feature has a dominant contribution from the Ge-Ge correlations (Penfold & Salmon[21]) and the shift in its position to higher-Q values implies a reduction in the periodicity $2\pi/Q_1$ of the corresponding density fluctuations. The decrease in its height implies a reduction in the magnitude of these fluctuations and the increase in its width implies a reduction in the coherence length from $2\pi/Q_1 = 14.6(3)$ Å at 800 °C to 12.4(3) Å at 1100 °C (Salmon[24]). Thus, although the changes in height and position of the FSDP are comparatively small between the glass at low temperature and the liquid above its melting point (Susman et al.[25]), substantial changes are clearly apparent as the liquid temperature is raised.

5.4.2 Comparison with the neutron diffraction results for GeSe

The observed trend in the profiles of $S_{NN}(Q)$ and $g_{NN}(r)$ for liquid $GeSe_2$ with increasing temperature strongly resembles that observed in the liquid phase as germanium is added to $GeSe_2$ to form GeSe (Salmon & Liu[11]). For example, the FSDP disappears with increasing germanium content, the second peak in $S_{NN}(Q)$ becomes comparable in height to the third peak and the first peak in $g_{NN}(r)$ undergo a strong reduction in height. The measured $S_{NN}(Q)$ and $g_{NN}(r)$ functions for liquid GeSe at 727(2) °C (section 4.7 and Petri et al.[22]) are compared with those for $GeSe_2$ at 1100 °C in figure 5.9. The similarity is not anticipated to result from a significant loss of selenium from the melt in the present work, see section 5.2.

Several of the physico-chemical properties of liquid $GeSe_2$ at high temperatures are similar to those for liquid GeSe at a somewhat lower temperature. For example, the electrical conductivity is $\approx 60\,\Omega^{-1}\,cm^{-1}$ for $GeSe_2$ at 1050 °C and GeSe at 700 °C, the thermopower is $100\,\mu V\,K^{-1}$ for $GeSe_2$ at ≈ 1020 °C and GeSe at

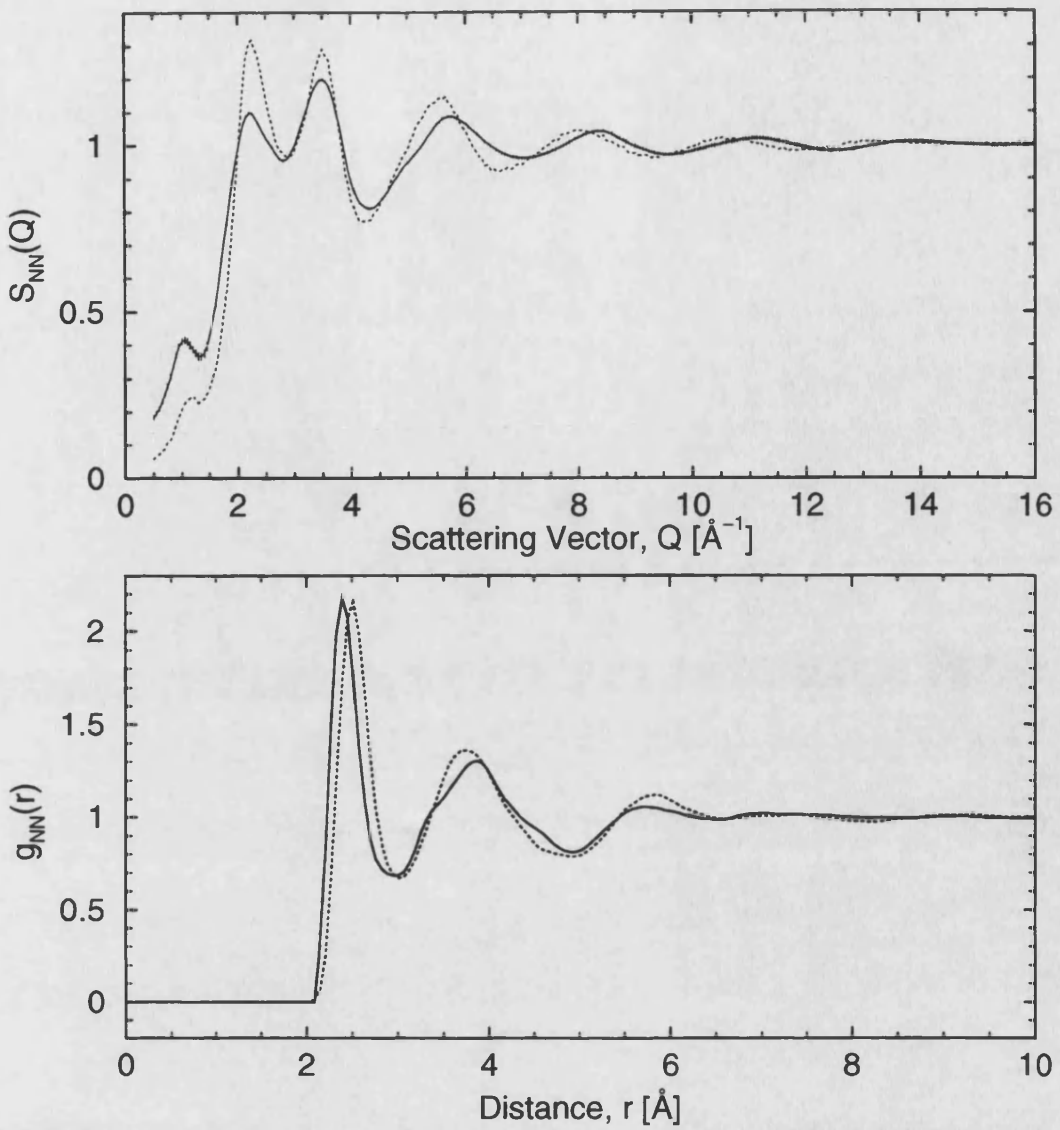

Figure 5.9: Comparison of the measured $S_{NN}(Q)$ and $g_{NN}(r)$ functions for liquid GeSe at 727(2) °C (dotted curves) with those for $GeSe_2$ at 1100(3) °C (solid curves).

$\approx$ 700 °C, and the conductivity gap is zero for $GeSe_2$ at 1073 °C and GeSe at 750 °C (Okada et al.[3]). Also the viscosity of $GeSe_2$ rapidly becomes comparable to that for GeSe with increasing temperature (Glazov & Situlina[6]). Therefore similarities in the corresponding structures might be anticipated.

Both $S_{NN}(Q)$ functions show a small pre-peak at a comparable position, although this peak is still larger for $GeSe_2$ at 1100 °C than for GeSe, where it was shown to originate from a cancellation of the partial structure factors (section 4.4.3) rather than from a peak in any one of the Faber-Ziman partial structure factors. Also the second and the third peaks in $S_{NN}(Q)$ occur at similar positions, but for

$GeSe_2$ the second peak is still smaller than the third one. These results indicate that diffraction experiments on $GeSe_2$ at even higher temperatures would enhance the agreement between the $S_{NN}(Q)$ functions. However, although the profiles of $g_{NN}(r)$ for liquid GeSe at 727(2) °C and liquid $GeSe_2$ at 1100 °C are comparable (figure 5.9), the structures are not identical as shown, for example, by the nearest-neighbour distance which is 5 % larger at 2.52(2) Å in liquid GeSe and by the higher average coordination number $\overline{n}$ in GeSe, see table 5.5 (Petri et al.[23]).

5.4.3 Significance of the results for molecular dynamics simulations

In a recent Car-Parinello type *ab initio* molecular dynamics study of liquid $GeSe_2$ at ca. 747 °C the results obtained by treating the electronic structure using two different approximations within density functional theory, which differ by the way in which the exchange and correlation energy is accounted for, were considered. The first is a generalised gradient approximation (GGA) and the second is the local density approximation (LDA) (Massobrio et al.[26]). It was found that when compared with the LDA scheme, the GGA scheme gives rise to a stronger charge transfer between germanium and selenium and therefore to an increase in the ionic character of the bonding. This results in a reduction of the number of homopolar bonds, and the accompanying enhancement in the chemical ordering results in the formation of more $GeSe_{4/2}$ tetrahedral units, which in turn leads to the establishment of intermediate range atomic ordering as manifest by the appearance of a FSDP. Use of the GGA functional was required to obtain best agreement with the partial structure factors measured for liquid $GeSe_2$ at 748 °C (Massobrio et al.[27]) and it was concluded that this scheme is crucial for describing the structural ordering in disordered covalent systems (Massobrio et al.[26]). In figure 5.10 a comparison is made between the total structure factor obtained within the GGA and our measured structure factor at 800 °C, and also between the structure factor obtained within the LDA and our measured one at 1100 °C.

Notably, the structure calculated for $GeSe_2$ at ca. 747 °C using the LDA scheme bears a strong resemblance to that measured for liquid $GeSe_2$ at the higher temperature of 1100 °C (figure 5.10) in addition to that measured for liquid GeSe

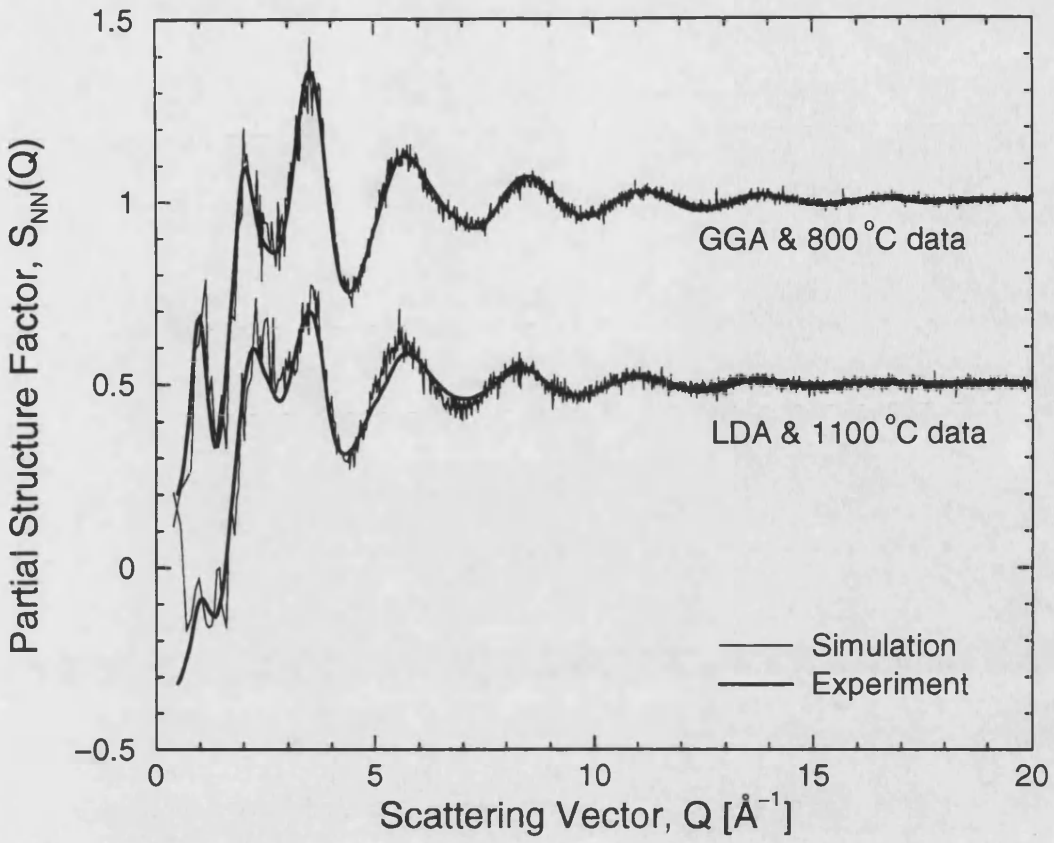

Figure 5.10: Total structure factors for molten $GeSe_2$ obtained within the GGA and LDA (shifted down by -0.5) approximation compared with our experimental results for molten $GeSe_2$ at 800 °C and 1100 °C.

at 727 °C. It would therefore be interesting to investigate the sensitivity to both temperature and concentration of the structures simulated by using both the LDA and GGA schemes as it appears that the Ge-Se binary system will serve as a sensitive test-system for the methods used in current *ab initio* molecular dynamics simulations.

Finally, liquid GeSe at 727 °C has a substantial number of homopolar bonds, each Ge being surrounded by an average of 3.2(2) Se at 2.54(2) Å and 0.8(2) Ge at 2.36(2) Å while each Se has 0.22(3) nearest-neighbouring Se at 2.34(2) Å (table 4.6 and Petri et al.[22]). Further, the structure of $GeSe_2$ simulated using the LDA scheme has more homopolar bonds than that calculated using the GGA scheme. The overall similarity of the Bhatia-Thornton number-number partial structure factor measured for $GeSe_2$ at 1100 °C with that for GeSe measured at 727 °C, and also the agreement between the total structure factor for $GeSe_2$ at 1100 °C and that

calculated for $GeSe_2$ using the LDA, might therefore be taken as a signature for the number of homopolar bonds in liquid $GeSe_2$ increasing with temperature. For comparison, in liquid As_2Se_3 an increase in the number of As-As bonds with increasing temperature has been observed from extended x-ray absorption fine structure experiments (Tamura et al.[10]). The detailed structure of bulk quenched $GeSe_2$ and As_2Se_3 glasses should therefore depend on the temperature from which the melt is quenched in addition to the quench rate (Petri et al.[23]).

5.5 Conclusions

- The total structure factors for liquid $GeSe_2$ have been measured successfully at the temperatures of 800 °C, 1000 °C and 1100 °C.
- With increasing temperature there is a broadening in the distribution of nearest-neighbours but their mean position and coordination number $\overline{n}$ do not change at the level of $g_{NN}(r)$.
- The increase in density and decrease in viscosity are found to result from a destruction of the intermediate range ordering associated with the Ge-Ge correlations.
- The changes in the profiles of $S_{NN}(Q)$ and $g_{NN}(r)$ with increasing temperature resemble those observed as the composition of molten $GeSe_2$ is altered to the GeSe stoichiometry by the addition of germanium. Therefore further diffraction experiments on $GeSe_2$ at higher temperatures would be interesting to observe the structure through the semiconductor to metal transition and to see if $S_{NN}(Q)$ begins to resemble the structure factor for metallic liquid germanium.

Bibliography

[1] Andreev A A, Melekh B T and Turgunov T, *Sov. Phys. Solid State* **18** (1976) 141.

[2] Haisty R W and Krebs H, *J. Non-Cryst. Sol.* **1** (1969) 399.

[3] Okada T, Satoh T, Matsumura M and Ohno S, *J. Phys. Soc. Jap.* **65** (1996) 230.

[4] Ohno S, Mizushina Y and Okada T, *J. Phys. Soc. Jap.* **65** (1996) 2917.

[5] Ruska J and Thurn H, *J. Non-Cryst. Sol.* **22** (1976) 277.

[6] Glazov V M and Situlina O V, *J. Dok. Chem.* **187** (1969) 587.

[7] Laugier A, Chaussemy G and Fornazero J, *J. Non-Cryst. Sol.* (1977) 419.

[8] Hosokawa S, Sakaguchi Y, Hiasa H and Tamura K, *J. Phys.: Cond. Mat.* **3** (1991) 6673.

[9] Hosokawa S, Sakaguchi Y and Tamura K, *J. Non-Cryst. Sol.* **150** (1992) 35.

[10] Tamura K, Hosokawa S, Inui M, Yao M, Endo H and Hoshino H, *J. Non-Cryst. Sol.* **150** (1992) 351.

[11] Salmon P S and Liu J, *J. Phys.: Cond. Mat.* **6** (1994) 1449.

[12] Maruyama K, Misawa M, Inui M, Takeda S, Kawakita Y and Tamaki S *J. Non-Cryst. Sol.* **205-207** (1996) 106.

[13] Wasse J C, *Ph.D. Thesis, University of East Anglia* (1998).

[14] Weast R C, ed. *CRC Handbook of Chemistry and Physics* 67$^{\text{th}}$ edition, CRC Press: Boca Raton (1986).

[15] Sears V F, *Neutron News* **3** (1992) 26.

[16] Ipser H, Gambino M and Schuster W, *Monatshefte f. Chem.* **113** (1982) 389.

[17] Soper A K, Howells W S and Hannon A C, *ATLAS - Analysis of Time-of-flight diffraction data from Liquid and Amorphous Samples* Laboratory report RAL-89-046 (1989).

[18] Salmon P S and Benmore C J, *Recent Developments in the Physics of Fluids*, ed. Howells W S and Soper A K, Hilger: Bristol (1992) F225.

[19] Salmon P S, *J. Phys. F* **18** (1988) 2345.

[20] Barnes A C, Lague S B, Salmon P S and Fischer H E, *J. Phys.: Cond. Mat.* **9** (1997) 6159.

[21] Penfold I T and Salmon P S, *Phys. Rev. Lett.* **67** (1991) 97.

[22] Petri I, Salmon P S and Fischer H E, *J. Phys.: Cond. Mat.* **11** (1999) 7051.

[23] Petri I, Salmon P S and Howells W S, *J. Phys.: Cond. Mat.* (1999) (in press).

[24] Salmon P S, *Proc. R. Soc.* **A 445** (1994) 351.

[25] Susman S, Volin K J, Montague D G and Price D L, *J. Non-Cryst. Sol.* **125** (1990) 168.

[26] Massobrio C, Pasquarello A and Car R, *J. Am. Chem. Soc.* **121** (1999) 2943.

[27] Massobrio C, Pasquarello A and Car R, *Phys. Rev. Lett.* **80** (1998) 2342.

Chapter 6

The structure of the proto-typical glass $GeSe_2$

6.1 Introduction

In recent years there has been a strong interest in the study of chalcogenide glasses from both scientific and technological viewpoints. These glasses are used as switching devices, memory elements and optoelectronic device materials (Afify[1]). Ge-Se glasses are also interesting as materials for infrared optics, as they exhibit a large range of transparency from 0.6 to 30 μm and good mechanical properties. They have long been under development for use as passive optical components in the infrared region and as active electronic device components for photocopying, ultra-microlithography and electronic switching (see Susman et al.[2]).

The microscopic structure of the proto-typical network glass $GeSe_2$ has long been a subject of controversy. There are two competing models describing the structure of these material. They both agree in that the fundamental building blocks of $GeSe_2$ are the $GeSe_{4/2}$ tetrahedral units, but they differ in the description of the intermediate-range order as well as in the explanation of the nature of the like-atom (homopolar) bonds. The first model is that originally proposed by Zachariasen[3] in 1932, which describes the structure in terms of a chemically ordered continuous random network (COCRN), where homopolar bonds may occur as defects (see e.g. Tronc et al.[4], Fischer-Colbrie & Fuoss[5] and Sugai[6]). The second model describes the structure as an aggregate of motifs that keep a memory

of the high-temperature crystalline phase of the material and in which homopolar bonds exist as an integral part (e.g. Bridenbaugh et al.[7], Bresser et al.[8] and Boolchand et al.[9]).

There are features in $GeSe_2$ that still remain a subject of controversy despite a large number of investigations. Neutron diffraction studies on $GeSe_2$ show a first sharp diffraction peak (FSDP) at a scattering vector $Q \approx 1\,\text{Å}^{-1}$ in the glass that exhibits an anomalous temperature dependence. The FSPD remains in the liquid state and while the heights of all the other peaks in the structure factor decrease markedly on going from the glass to the liquid, the height of the FSDP does not. Susman et al.[2] found a reduction in the height of the FSDP of $\approx 10\,\%$ when the temperature was raised from $-263\,^{\circ}\text{C}$ to $811\,^{\circ}\text{C}$. Raman spectroscopy experiments show in addition to the A_1 symmetrical breathing mode of corner sharing tetrahedra at 198 - 199 cm^{-1} (Bridenbaugh et al.[7], Inoue et al.[10]) a companion mode A_1^C between 212 - 216 cm^{-1}, which is still a matter of controversy. The intensity of this companion mode varies with composition in the Ge-Se system and is largest for $GeSe_2$. Like the FSDP the A_1^C mode survives the melting transition (Magana & Lannin[11]). The two competing models provide different explanations for the structural origin of this mode.

In the first model, based on the COCRN, the edge sharing tetrahedra are thought of as giving rise to the A_1^C companion mode. The intermediate range order (IRO), which is due to the random packing of the $GeSe_{4/2}$ tetrahedra, is considered to account for the FSDP (Nemanich et al.[12] and Sugai[6]) and also for a three-dimensional structure. The coordination number of each species is given by the '8-n' rule (Mott[13]), where n is the valence of each species, such that every atom has a filled outer shell of electrons.

In the second model, known as 'Outrigger Raft Model' (ORM), the network is also presumed to consist predominantly of corner and edge sharing $GeSe_{4/2}$ tetrahedra, but these units are covalently bonded together in rafts or fragmented layers similar to those found in the crystal. Each layer consists of parallel chains of corner sharing tetrahedra cross linked via pairs of edge sharing tetrahedra and the layers are terminated by Se-Se dimers parallel to the chains, see figure 6.1.

The lateral size of these rafts is thought to be in the range of $10 - 20\,\text{Å}$. Mössbauer data by Bresser et al.[8] have, however, been interpreted in terms of

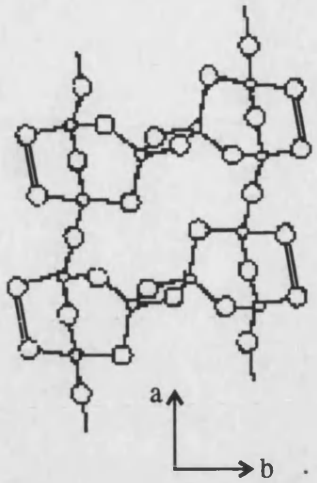

Figure 6.1: The laterally smallest fragmented raft of the ORM. The small circles represent the Ge atoms and the large circles the Se atoms. The Se-Se dimers which terminate the raft are marked with double lines. (Reproduced from Bridenbaugh et al.[7].)

the rafts being 60 Å wide. In this model the A_1^C companion mode has been attributed to the vibrational motion of the Se-Se dimers and the FSDP arises from interlayer correlations which also give rise to a Bragg diffraction peak at ≈ 1.06 Å^{-1} in the high-temperature crystalline phase of $GeSe_2$ (Bridenbaugh et al.[7]).

A first step to solving the outstanding problem of the correct model for $GeSe_2$ requires experimental information on the full set of partial pair correlation functions describing the atomic positions to provide a test for the quantitative predictions of both models, and to give direct evidence for the existence of structural motifs such as homopolar bonds. Here this outstanding challenge is met by applying the method of isotopic substitution in neutron diffraction and results will be presented that allow an extensive comparison of the structure of the glass with the high-temperature crystalline phase of $GeSe_2$. Evidence is found for a substantial number of 'defects', i.e. structural motifs that do not exist in the high-temperature crystalline phase, and the results permit a comparison with the structure of liquid $GeSe_2$ at the level of the partial structure factors.

6.2 Sample preparation

The three samples, $^{N}Ge^{N}Se_2$, $^{70}Ge^{N}Se_2$ and $^{73}Ge^{76}Se_2$ were prepared using the same Ge and Se high purity elements and isotopes as for the isotopic substitution

experiment on GeSe described in chapter 4.

The cleaning and loading of the silica ampoules follows the description in section 4.2, and the three glassy $GeSe_2$ samples were prepared as described in section 5.2.

6.3 Diffraction experiment and neutron parameters

The neutron diffraction experiments were carried out at the ILL using the instrument D4B (see section 3.2.1) at an incident wavelength of 0.7046 Å. The samples (2.5 to 3 g) were in the form of a coarse powder and were loaded under high purity argon gas into a cylindrical vanadium container of 4.8 mm inner diameter and 0.1 mm wall thickness and were sealed with a greased O-ring to prevent air contamination. The container then was placed in an ultrasonic bath to increase the packing fraction of the samples to approximately 55 %. The sample was fully illuminated by a rectangular beam, 40 mm high and 11 mm wide. The effective density of the samples, which is required for the calculation of the attenuation factors and multiple scattering corrections, was determined by weighing the loaded samples and measuring their volumes after the ultrasonic bath treatment.

The experiment comprised the measurement of the diffraction patterns of the three samples in their container, the empty container, a cadmium rod of 5 mm diameter for the background correction at low angles, nothing placed at the sample position, and a vanadium rod of 6.05 mm diameter for normalisation purposes. All of these measurements were performed at 26(1) °C.

The run-times for the individual samples and the empty container were optimised by taking into account the volume illuminated by the neutron beam, the effective number densities, the total scattering cross-sections and attenuation factors, and the factors of the inversion matrix (see section 2.12) used to obtain the partial structure factors. The data analysis followed the procedure outlined in section 3.3.1.

The scattering length and cross-section parameters of the elements and isotopes were calculated in accordance with their isotopic enrichments and are shown in table 4.1. The cross-sections of the $GeSe_2$ samples, calculated using these values, are

given in table 6.1.

Sample	$\sigma_{free,sc}$ [barn]	σ_{abs} (@ 1.798 Å) [barn]	$\sigma^{total} = \sigma_{free,sc} + \sigma_{abs}$ (@ λ) [barn]
$^{N}Ge^{N}Se_2$	8.19(6)	8.53(15)	11.53(8)
$^{70}Ge^{N}Se_2$	9.48(14)	8.80(20)	12.93(16)
$^{73}Ge^{76}Se_2$	13.7(3)	61.6(4.8)	37.8(1.9)

Table 6.1 : Cross-sections of the samples used in the data analysis procedure. Here λ (= 0.7046 Å) denotes the wavelength of the incident neutrons.

The sample mass densities were 4.26 g/cm^3 (given by Azoulay et al.[14]), 4.21 g/cm^3 and 4.15 g/cm^3 for $^{N}Ge^{N}Se_2$, $^{70}Ge^{N}Se_2$ and $^{73}Ge^{76}Se_2$ respectively. They correspond to a number density of 0.0334(1) Å^{-3}, which is used in the Fourier transform procedure and in the calculation of the coordination numbers. The packing fractions used in the calculation of the attenuation factors and multiple scattering corrections were 53.2 % for the $^{N}Ge^{N}Se_2$ sample, 56.8 % for the $^{70}Ge^{N}Se_2$ sample and 48.0 % for the $^{73}Ge^{76}Se$ sample. For the first two samples they agree well (within 5 %) with the measured packing fractions. However for the $^{73}Ge^{76}Se_2$ sample the discrepancy between the measured packing fraction and the one used in the data analysis procedure is about 9 %.

The measured total structure factors F(Q) are given as linear combinations of the three partial structure factors $S_{GeGe}(Q)$, $S_{GeSe}(Q)$ and $S_{SeSe}(Q)$ (see section 2.12),

$$F(Q) = A[S_{GeGe}(Q) - 1] + B[S_{GeSe}(Q) - 1] + C[S_{SeSe}(Q) - 1] \qquad (6.1)$$

where $A = c_{Ge}^2 b_{Ge}^2$, $B = 2c_{Ge}c_{Se}b_{Ge}b_{Se}$ and $C = c_{Se}^2 b_{Se}^2$. These weighting factors are summarised in table 6.2 and the corresponding total pair distribution function is given by,

$$G(r) = A[g_{GeGe}(r) - 1] + B[g_{GeSe}(r) - 1] + C[g_{SeSe}(r) - 1]\,. \qquad (6.2)$$

Sample	A [barn]	B [barn]	C [barn]	G(0) [barn]	sum-rule [barn/Å^3]
$^{N}Ge^{N}Se_2$	0.0744(4)	0.2899(8)	0.2823(6)	-0.6467(11)	-0.4261(7)
$^{70}Ge^{N}Se_2$	0.1111(22)	0.354(4)	0.2823(6)	-0.748(6)	-0.493(4)
$^{73}Ge^{76}Se_2$	0.0288(5)	0.276(3)	0.6615(11)	-0.966(13)	-0.637(9)

Table 6.2: Weighting coefficients, low-r limits G(0) and sum-rule relations. The statistical errors are given in the brackets. G(0) and the sum-rule were calculated using equations 4.2 and 4.3 respectively.

Several of the systematic errors resulting from the correction procedure can be eliminated by forming the first order difference function, $\Delta_{Ge}(Q)$, see section 3.4. Therefore it is advisable to use it as an additional criterion for checking the data self-consistency, even when the full set of partial structure factors can be obtained by solving the matrix equation (see section 2.12). By using the ${}^{N}_{N}F(Q)$ and ${}^{70}_{N}F(Q)$ total structure factors, the Se-Se correlations can be eliminated,

$$\begin{aligned} \Delta_{Ge}(Q)\,/\text{barn} &= {}^{70}_{N}F(Q) - {}^{N}_{N}F(Q) \\ &= 0.0367(22)[S_{GeGe}(Q)-1] + 0.064(4)[S_{GeSe}(Q)-1] \end{aligned} \tag{6.3}$$

The real-space function corresponding to $\Delta_{Ge}(Q)$ is denoted by $\Delta G_{Ge}(r)$ and is obtained by replacing the $S_{\alpha\beta}(Q)$ by the partial pair distribution functions $g_{\alpha\beta}(r)$ in the above equation. The low-r limit, $\Delta G_{Ge}(0)$, is given by

$$\begin{aligned} \Delta G_{Ge}(0) &= -\left[c^2_{Ge}[b^2(^{70}Ge) - b^2(^{N}Ge)] + 2c_{Ge}c_{Se}b_{Se}[b(^{70}Ge) - b(^{N}Ge)]\right] \\ &= -0.101(4)\,\text{barn} \end{aligned} \tag{6.4}$$

and the sum-rule by

$$2\pi^2 n_0 \Delta G_{Ge}(0) = -0.069(3)\,\text{barn/Å}^3\,. \tag{6.5}$$

It is also possible to eliminate the Ge-Ge correlations by subtracting a scaled total structure factor ${}^{N}_{N}F(Q)$ or ${}^{70}_{N}F(Q)$ from ${}^{73}_{76}F(Q)$,

$$\Delta^{(1)}_{Se}(Q)\,/\text{barn} = {}^{73}_{76}F(Q) - \frac{b^2(^{73}Ge)}{b^2(^{N}Ge)}\,{}^{N}_{N}F(Q) = I[S_{GeSe}(Q)-1] + K[S_{SeSe}(Q)-1] \tag{6.6}$$

$$\Delta^{(2)}_{Se}(Q)\,/\text{barn} = {}^{73}_{76}F(Q) - \frac{b^2(^{73}Ge)}{b^2(^{70}Ge)}\,{}^{70}_{N}F(Q) = I[S_{GeSe}(Q)-1] + K[S_{SeSe}(Q)-1]$$

with

$$I = 2c_{Ge}c_{Se}\left[b(^{73}Ge)b(^{76}Se) - \frac{b^2(^{73}Ge)}{b^2('Ge)} \cdot b('Ge)b(^{N}Se)\right] \quad (6.7)$$

$$K = c_{Se}^2\left[b^2(^{76}Se) - \frac{b^2(^{73}Ge)}{b^2('Ge)}b^2(^{N}Se)\right]$$

where $'Ge$ stands for ^{N}Ge and ^{70}Ge in $\Delta_{Se}^{(1)}(Q)$ and $\Delta_{Se}^{(2)}(Q)$ respectively.

Difference Function	I [barn]	K [barn]	$\Delta G_{Se}(0)$ [barn]	sum-rule [barn/Å^3]
$\Delta_{Se}^{(1)}(Q)$	0.164(3)	0.5523(11)	- 0.716(3)	- 0.486(2)
$\Delta_{Se}^{(2)}(Q)$	0.184(3)	0.5884(11)	- 0.773(3)	- 0.525(2)

Table 6.3: Weighting coefficients, low-r limits $\Delta G_{Se}(0) = -(I + K)$ and sum-rule relations.

The partial structure factors are obtained by solving the matrix representation of linear equations, as described in section 2.12, and are given by,

$$\begin{bmatrix} S_{GeGe}(Q) - 1 \\ S_{GeSe}(Q) - 1 \\ S_{SeSe}(Q) - 1 \end{bmatrix} = \begin{bmatrix} -102(38) & 74(28) & 11.9(4.4) \\ 43(16) & -27(10) & -6.8(2.5) \\ -13(5) & 8(3) & 3.8(1.5) \end{bmatrix} \begin{bmatrix} {}_{N}^{N}F(Q) \\ {}_{N}^{70}F(Q) \\ {}_{76}^{73}F(Q) \end{bmatrix} \quad (6.8)$$

The weighting factors in this equation are quoted in units of barn, and a measure of reliability (conditioning) with which the partial structure factors are obtained, given by the normalised determinant of the weighting factors, $|A_n|$, is -0.011.

6.4 Results

6.4.1 DSC measurements

The thermal properties of the three $GeSe_2$ samples were measured in a differential scanning calorimetry (DSC) experiment on a TA Instruments Thermal Analyst 2000 machine. The temperature range covered was 20 - 450 °C, with a heating rate of 10 °C/min. About 20 mg of each sample were placed in a hermetically sealed aluminum pan, and the chamber was kept under a constant stream of dry oxygen free nitrogen purge gas at 40 ml/min.

Since the glass transition temperature does not correspond to a sharp transition (Elliott [16]), it is important to define the way T_g is obtained. In our analysis both the onset and 'midpoint' or inflection point of the transition are given (see figure 6.2). The midpoint values are determined by drawing construction lines parallel to the baselines before and after the transition. A tangent to the DSC signal is then drawn and where it intercepts the two baselines the onset and completion temperature are defined. The value for T_g is taken to be the temperature where the tangent touches the DSC signal. At least two measurements per sample were made to ensure the reproducibility of the measured T_g.

Figure 6.2 shows the DSC traces for the glass transition region of the three samples used in the neutron diffraction experiment. The temperatures for onset and inflection points are summarised in table 6.4.

	$^{N}Ge^{N}Se_2$	$^{70}Ge^{N}Se_2$	$^{73}Ge^{76}Se_2$	$^{N}Ge^{N}Se_2$ Sarrach et al.[17]	$^{N}Ge^{N}Se_2$ Wang et al.[18]
onset [°C]	397(3)	399(3)	387(3)		
midpoint [°C]	414(3)	417(3)	400(3)	422	405(10)*
sample mass [mg]	23.32	18.15	17.29		

Table 6.4 : Measured glass transition temperatures using DSC compared with values in the literature. *)In the paper it is not defined if the given value relates to the onset or midpoint.

The glass transition temperature, T_g, for the $^{N}Ge^{N}Se_2$ and $^{70}Ge^{N}Se_2$ samples agrees within the errors, but for $^{73}Ge^{76}Se_2$ a slightly lower T_g is measured, although the preparation procedure was the same for all three samples. The mass of all

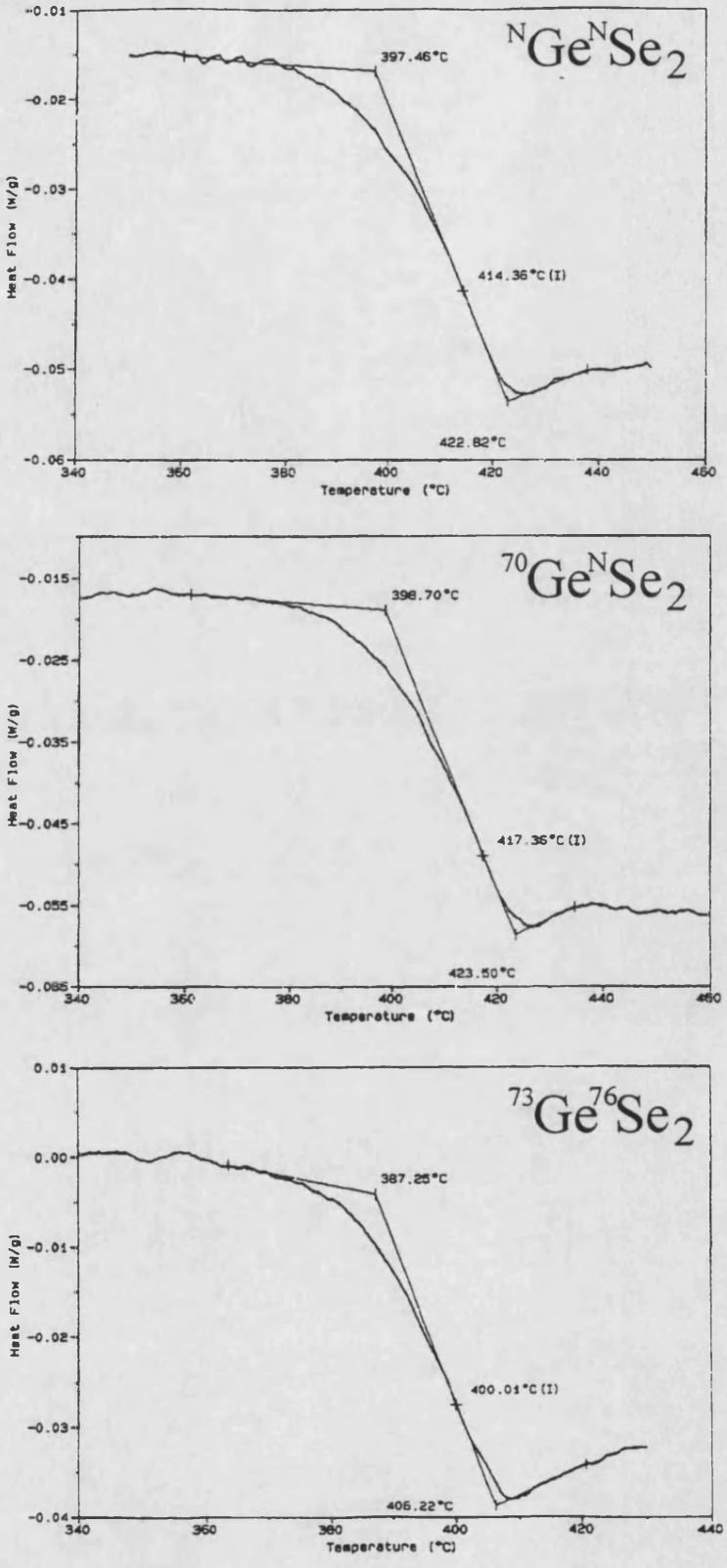

Figure 6.2: DSC traces measured for the $^{N}Ge^{N}Se_2$, $^{70}Ge^{N}Se_2$ and $^{73}Ge^{76}Se_2$ samples

investigated samples is about 20 mg, and for each sample the DSC signal starts descending downwards from the baseline at $\approx 380\,^{\circ}C$. However, T_g is measured to be lower in the $^{73}Ge^{76}Se_2$ glass. The reason for this could not be found. Our values for $^{N}Ge^{N}Se_2$ and $^{70}Ge^{N}Se_2$ are just in between the values given by Sarrach et al.[17], which was measured by DSC with a heating rate of 20 °C/min on a sample that was water quenched from about 990 °C, and the value measured by Wang et al.[18], also obtained by DSC using a heating rate of 10 °C/min for a sample quenched from 900 °C.

6.4.2 Total structure factors

The total structure factors, F(Q), are shown in figure 6.3.

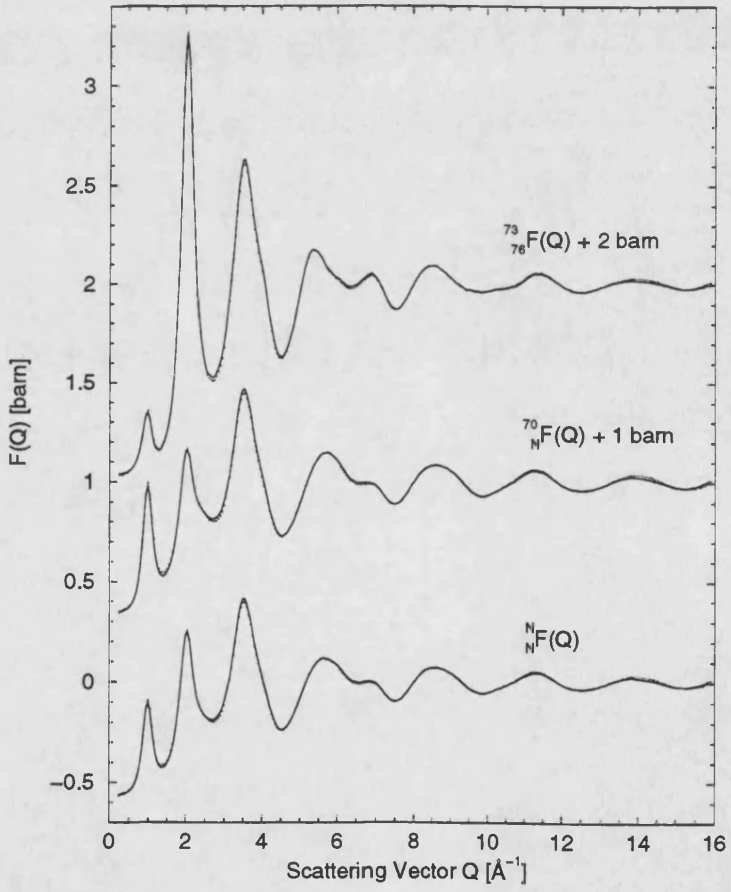

Figure 6.3: The measured total structure factors $^{N}_{N}F(Q)$, $^{70}_{N}F(Q)$ and $^{73}_{76}F(Q)$ for glassy $GeSe_2$. The bars represent the statistical errors on the data points and the solid curves are the Fourier back transforms of the corresponding real-space functions obtained after setting the unphysical low-r oscillations to their calculated limiting value, G(0).

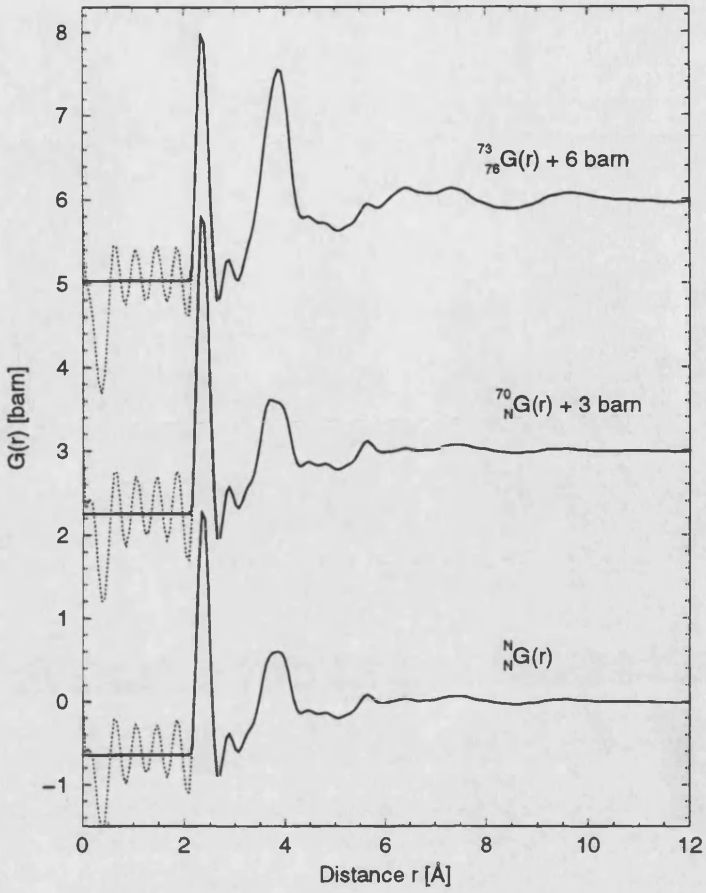

Figure 6.4: Measured G(r)'s. The solid curves give the real-space representation of the total structure factors obtained by Fourier transforming the data points given by the error bars in figure 6.3, the dotted curves for approximately r $\leq$ 2.1 Å show the corresponding unphysical low-r oscillations.

All three total structure factors exhibit a clear first sharp diffraction peak (FSDP) at 1.00(2) $Å^{-1}$ for $^{N}Ge^{N}Se_2$ and $^{70}Ge^{N}Se_2$ and at 0.99(2) $Å^{-1}$ for $^{73}Ge^{76}Se_2$, and its intensity increases with increasing Ge scattering length (see table 4.1). There are marked oscillations in the F(Q)'s up to the maximum measured scattering vector of 15.9 $Å^{-1}$, which indicate the existence of well defined short range order in the glasses.

The corresponding real-space functions are given in figure 6.4. For all three samples the first peak in G(r) is well defined and is a very sharp feature. Truncation effects ('truncation wiggles') are visible on both sides of this peak, impeding the discussion of the data in the region beyond the first peak up to $\approx$ 3 Å. On the basis of a comparison with the crystal structure of the high temperature phase of

$GeSe_2$, this first peak will comprise Ge-Se contributions. However it will be shown in section 6.4.4 that Ge-Ge and Se-Se nearest neighbour correlations (homopolar bonds) also contribute. The broader second physical peak in G(r) contains predominantly Ge-Ge and Se-Se contributions. This can be concluded from comparing the shape and maximum positions of this peak in $^{70}Ge^{N}Se_2$ and $^{73}Ge^{76}Se_2$ and comparing the distances with those found in the HT crystalline phase of $GeSe_2$. The peak shifts from 3.73(2) Å in $^{70}Ge^{N}Se_2$ to 3.89(2) Å in $^{73}Ge^{76}Se_2$ and seems to comprise two contributions, one at a slightly lower value of r than the other. The lower-r contribution is emphasized for $^{70}Ge^{N}Se_2$, indicating that it comprises Ge-Ge correlations. The higher-r contribution is strongly accentuated in $^{73}Ge^{76}Se_2$, where the Se-Se contributions have the largest weighting of the three samples. The oscillations, which are visible in all of the total pair distribution functions out to high values of $r > 10$ Å, indicate the presence of strong intermediate range order in the $GeSe_2$ glasses.

The peak positions and $\overline{n}_{Ge}^{Se}$ coordination numbers for the data sets shown in figure 6.4, assuming no homopolar bonds, are summarised in table 6.5.

sample	1st peak [Å]	$\overline{n}_{Ge}^{Se}$	2nd peak [Å]	3rd peak [Å]
$^{N}Ge^{N}Se_2$	2.36(2)	4.2(2)	3.85(2)	5.65(2)
$^{70}Ge^{N}Se_2$	2.36(2)	4.2(2)	3.73(2)	5.65(2)
$^{73}Ge^{76}Se_2$	2.36(2)	4.4(2)	3.89(2)	5.67(2)

Table 6.5 : Peak positions in the total pair distribution functions. The $\overline{n}_{Ge}^{Se}$ are obtained by integrating over the region $2.09 \leq r\,[Å] \leq 2.61$ and they are given as an illustration, since it will be shown in section 6.4.4 that homopolar bonds contribute to the first peak.

6.4.3 First order difference functions

The first order difference functions, $\Delta_{Ge}(Q)$, $\Delta_{Se}^{(1)}(Q)$ and $\Delta_{Se}^{(2)}(Q)$ obtained by using equations 6.4 and 6.7 respectively, are displayed in figure 6.5 together with the back Fourier transforms of the corresponding real-space functions after the unphysical low-r oscillations have been set to their theoretical limiting values. The agreement between the data and back transforms is very good for all the functions.

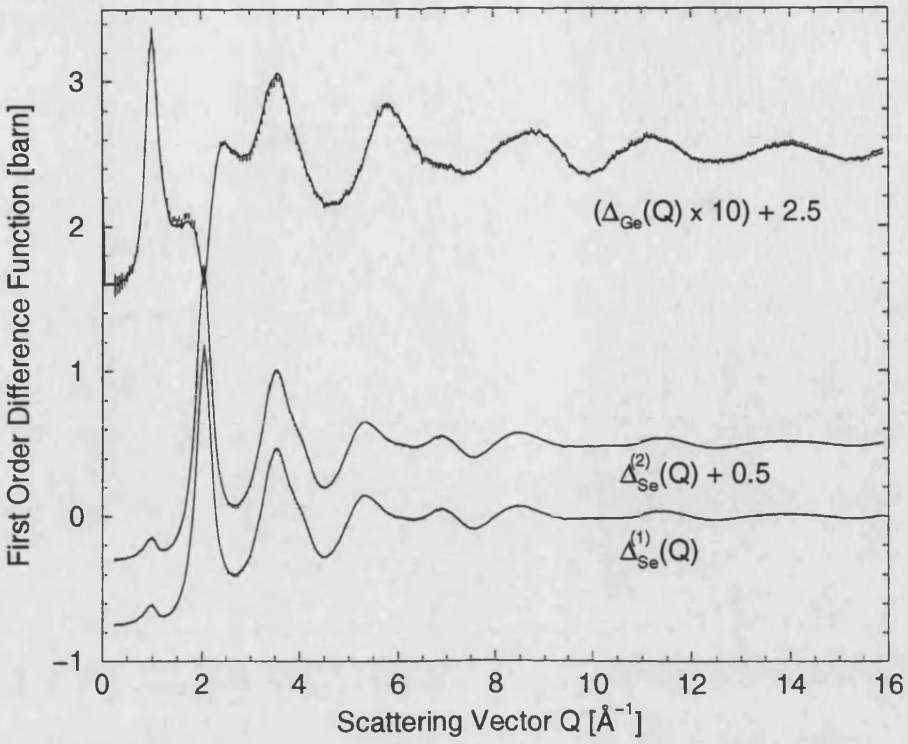

Figure 6.5: First order difference functions $\Delta_{Ge}(Q)$ multiplied by 10 and $\Delta^{(1)}_{Se}(Q)$ and $\Delta^{(2)}_{Se}(Q)$. The bars represent the statistical errors on each data point and the solid curves are the back Fourier transforms of the corresponding real-space functions after the unphysical low-r oscillations have been set to their theoretical limits.

The real-space functions at low-r oscillate around the correct calculated limits, see figure 6.6.

All of the first order difference functions show a FSDP. It is marked in $\Delta_{Ge}(Q)$ at a position of 1.00(2) Å^{-1}. In the $\Delta_{Se}(Q)$ functions, where the Ge-Ge correlations are removed, the FSDP is very small and found at 0.98(2) Å^{-1}. This indicates that in addition to a strong intermediate atomic ordering (IRO) of the Ge-Ge correlations there are also other correlations with some degree of IRO. There are high-Q oscillations extending to $Q \geq Q_{max}$.

In real-space, $\Delta G_{Ge}(r)$ exhibits a first peak at 2.36(2) Å, which is much more intense than the second at 3.62(2) Å. In the $\Delta G_{Se}(r)$ functions the first peak at 2.35(2) Å is much lower relative to the second because of the low weighting of the Ge-Se contributions in comparison to the weighting of the like-atom contributions, see equation 6.7 and table 6.3. The shift of this first peak, although within the errors, can be taken as an indication for the presence of Se-Se homopolar bonds

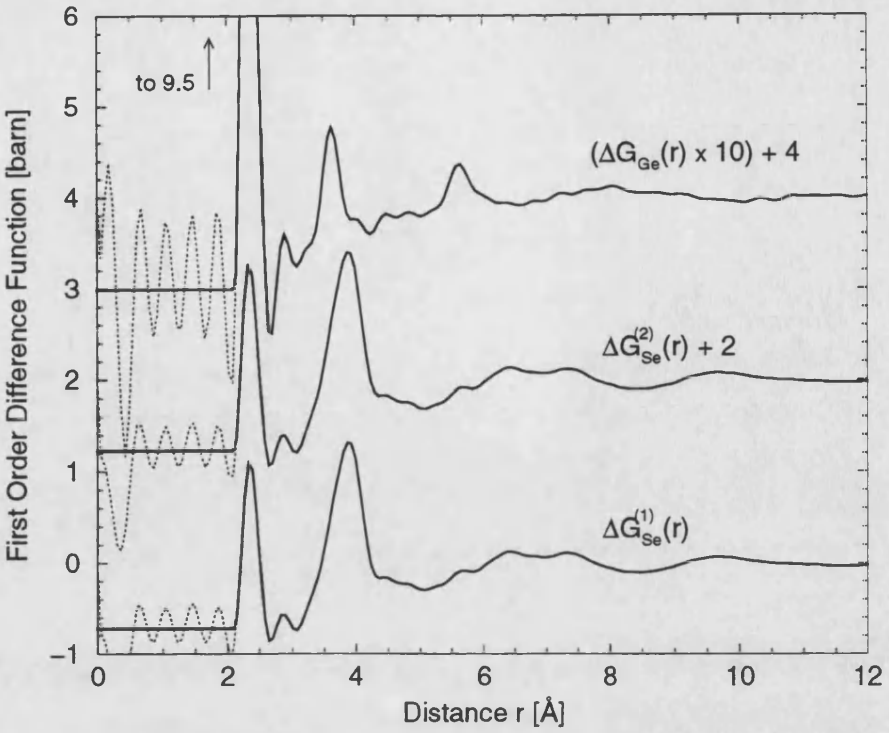

Figure 6.6: First order difference functions for $GeSe_2$ in real-space, $\Delta_{Ge}(Q)$ scaled by a factor of 10, $\Delta^{(1)}_{Se}(Q)$ and $\Delta^{(2)}_{Se}(Q)$. The dotted curves for approximately $r \leq 2.1$ Å show the corresponding unphysical low-r oscillations.

which, as will be shown in the next section, are apparent in the $GeSe_2$ glass and have a nearest neighbour distance of 2.32(2) Å. Due to the high weighting of the Se-Se contributions in $\Delta G_{Se}(r)$ they might contribute sufficient intensity to shift the first peak to a slightly lower-r value. Integrating the first peak over the range $2.09 \leq r[Å] \leq 2.61$ and assuming heteropolar bonds only gives coordination numbers $\overline{n}^{Se}_{Ge}$ of 4.1(1) for $\Delta G_{Ge}(r)$ and 4.7(1) for both $\Delta G_{Se}(r)$ functions, therefore indicating again the presence of homopolar bonds. The second peak occurs at 3.62(2) Å in $\Delta G_{Ge}(r)$ and at 3.89(2) Å in $\Delta G_{Se}(r)$. This again indicates that the Ge-Ge correlations peak at a lower value of r than the Se-Se correlations.

Our measured first order difference functions can be compared with the results obtained from the differential anomalous x-ray scattering (DAS) experiments of Fischer-Colbrie & Fuoss[5]. They make two difference functions using the Ge K-edge and the Se K-edge. The first eliminates the Se-Se correlations and the second the Ge-Ge correlations, therefore these functions are comparable to $\Delta_{Ge}(Q)$ and $\Delta_{Se}(Q)$. In reciprocal-space they also found that the FSDP that is marked in the

Ge K-edge difference function almost vanishes in the Se K-edge function, and that like for our data (figure 6.5) the second peak at 2.05 Å is very strong in the Se K-edge difference function but negative for the Ge K-edge function. In real-space Fischer-Colbrie & Fuoss[5] found in the Ge K-edge difference function the first peak at the same position of 2.36 Å like us and also their coordination number $\overline{n}^{Se}_{Ge}$, assuming no homopolar bonds, of 4.21 is in agreement with our value of 4.1(1). They also measure the peak shift of the second peak to lower-r values. In the Se K-edge difference function they measure the first peak at 2.34 – 2.36 Å and the second peak at 3.86 Å, which again agrees well with our measurements.

6.4.4 Partial structure factors

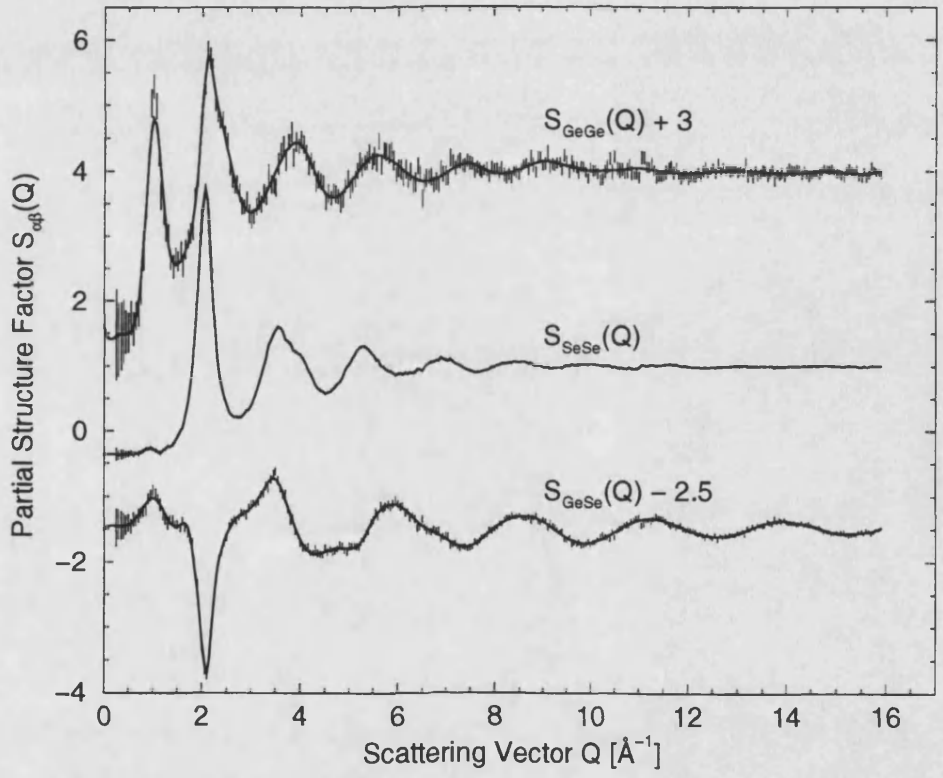

Figure 6.7: Partial structure factors obtained by direct inversion of the matrix equation (error bars) and cubic spline fits (solid curve). For $S_{SeSe}(Q)$ the spline fit and the raw data are identical.

The Faber-Ziman partial structure factors, $S_{\alpha\beta}(Q)$, obtained by direct inversion of the total structure factors using equation 6.8 are shown in figure 6.7 by the error bars. Cubic spline fits to these $S_{\alpha\beta}(Q)$ are shown in this figure by the solid

curves. The corresponding $g_{\alpha\beta}(r)$ are given in figure 6.8 as broken and full curves respectively.

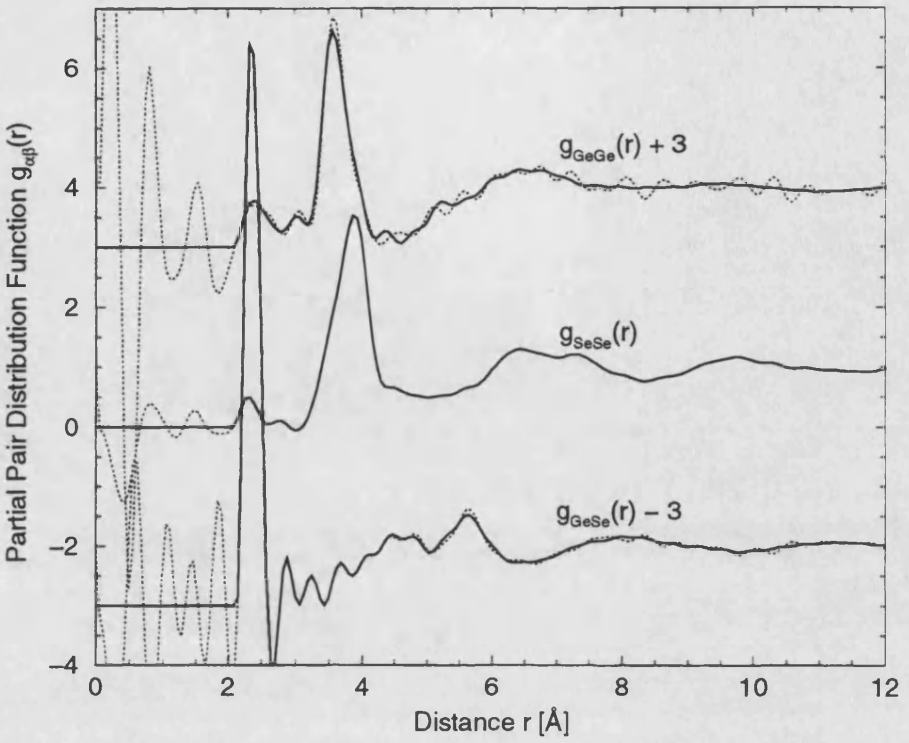

Figure 6.8: Partial pair distribution functions. The dotted curves correspond to the Fourier transform of the error bars given in figure 6.7 and the solid curves show the Fourier transform of the cubic spline fits (in this case the corresponding unphysical low-r oscillations have been set to their theoretical value.)

The measured partial structure factors fully satisfy the sum rules and inequality relations given by Edwards et al.[19]. Also, they are in good agreement with the Fourier back transforms of the corresponding $g_{\alpha\beta}(r)$ after the unphysical low-r oscillations are set to the $g_{\alpha\beta}(0) = 0$ limit and they give $g_{\alpha\beta}(r)$ that oscillate about this correct low-r limit. Also the neutron weighted $S_{\alpha\beta}(r)$ can be added up to reproduce the total structure factor, see figure 6.12 and the sum of the neutron weighted $g_{\alpha\beta}(r)$ perfectly represents both first order difference functions, see figure 6.14.

The partial structure factors are measured using a finite Q-space range with $Q_{max} = 15.9\,\text{Å}^{-1}$ which implies that the corresponding real-space functions are modified by the Fourier transform of the Q-space window function, an effect that is particularly marked for the first peak in $g_{GeSe}(r)$ (see description in section 3.5 and

Petri et al.[20]). To separate those features that are artefacts of the finite Q-range from the remainder, the functions $t_{\alpha\beta}(r) = 4\pi n_0 r[g_{\alpha\beta}(r) - 1]$ were fitted following the procedure described in section 3.5 (for a listing of the fitted Gaussians see appendix A). In the fit the $g_{\alpha\beta}(r)$ obtained from the spline fits to the data sets were used, since the effect of noise is reduced when compared to the Fourier transform of the unsmoothed data points.

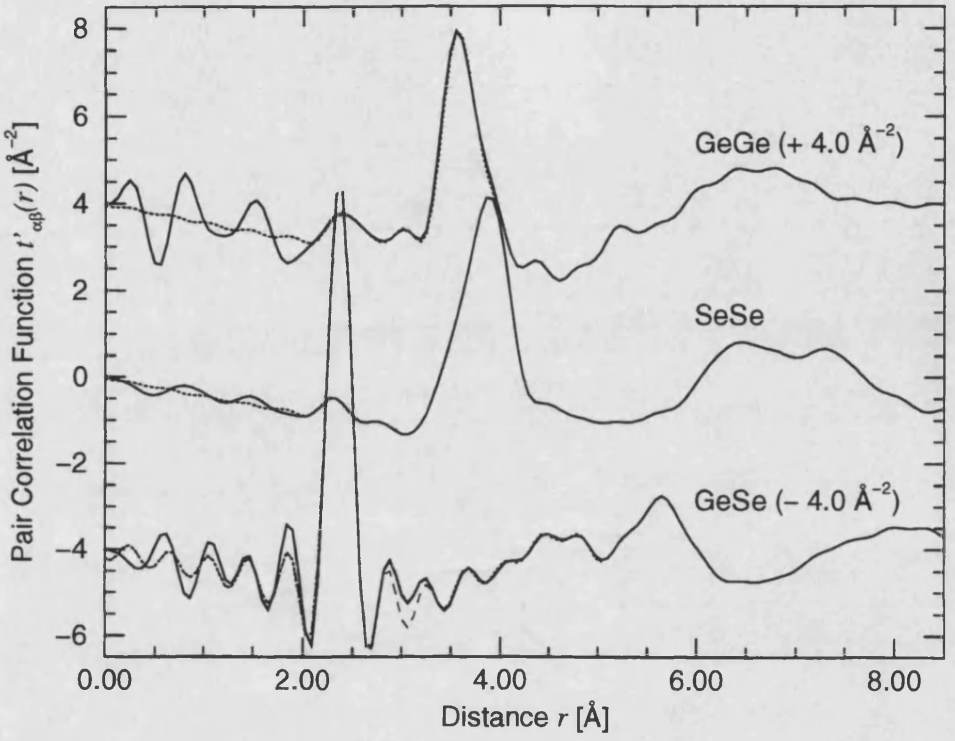

Figure 6.9: Fits to the functions $t'_{\alpha\beta}(r)$. The smoothed data sets are given by the thick solid curves, the fits by the dotted curves. The fitted functions are identical to $t'_{\alpha\beta}(r)$ at large-r values. The thin dashed curve shows the effect of omitting the defect peak at 3.02 Å in the Ge-Se correlations (see text).

As shown in figure 6.9 this approach provides a good representation of the measured data sets and enables those features that are artefacts of the finite Q-space measurement window to be distinguished from the remainder. The R-factors for the fits, which are defined as

$$\sum_{i=1}^{last\ fitted\ i} \left(\frac{data(i) - fit(i)}{data(i)} \right)^2 \tag{6.9}$$

where $data(i)$ is the i^{th} data point in $t_{\alpha\beta}(r)$ and $fit(i)$ the i^{th} point of the fit, are given in table 6.6. The resulting partial pair distribution functions are displayed

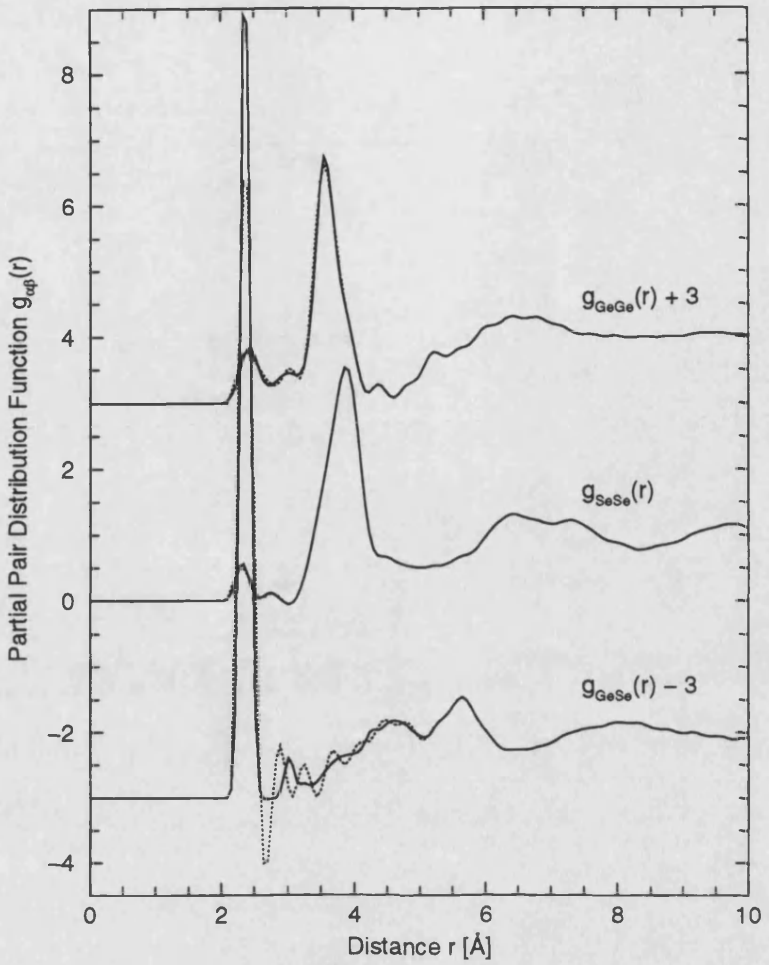

Figure 6.10: Partial pair distribution functions after the effects of the finite Q-space measuring window have been removed (bold curves), compared with the direct Fourier transforms of the cubic spline fits shown in figure 6.7 (dotted curves).

in figure 6.10 together with those obtained by the direct Fourier transformation of the spline fitted data sets. From this figure the strong influence of the finite Q-space window can be seen especially for the $g_{GeSe}(r)$ partial structure factor. To show that these $g_{\alpha\beta}(r)$ give a reasonable account of the measured partial structure factor, the back Fourier transforms of the corresponding $g_{\alpha\beta}(r)$ are compared with the partial structure factors obtained from the measured data sets in figure 6.11. The corresponding χ^2 values are given in table 6.6.

Features occur in the $g_{\alpha\beta}(r)$ that are not expected from the structure of the high-temperature crystalline phase of $GeSe_2$. For example, there are peaks corresponding to homopolar bonds at low-r in $g_{GeGe}(r)$ and $g_{SeSe}(r)$ and there are correlations at 3.02 Å in $g_{GeSe}(r)$. The effect of omitting these 'defect' peaks on

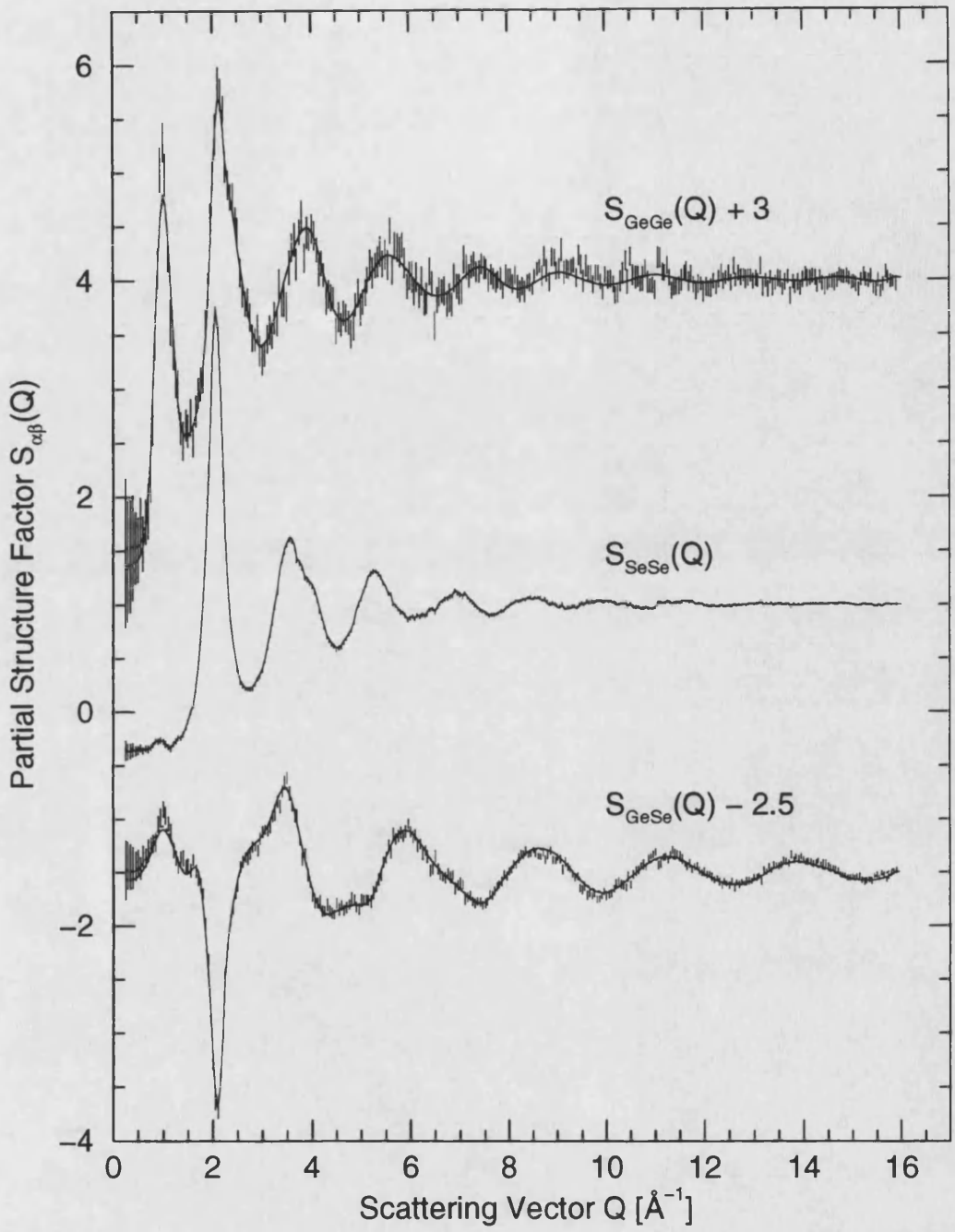

Figure 6.11: The partial structure factors for glassy $GeSe_2$. The bars represent the errors on the data points (neglecting errors on the scattering cross-sections and concentrations), the solid curves are the Fourier transforms of the fitted $g_{\alpha\beta}(r)$ (solid curves in figure 6.10). The solid curves are in good agreement with the Fourier back transforms (dotted curves) of the spline fitted data sets, shown by the dotted curves in 6.10.

the R-factors and χ^2 values is given in table 6.6. Clearly their removal has a detrimental effect on the quality of the fits.

	R-factor	number of points for R-factor	range of fit	χ^2
$g_{GeGe}(r)^{a)}$	0.165	34	2.09 – 4.17 Å	262.2
$g_{GeGe}(r)^{b)}$	37.16	34		327.0
$g_{GeSe}(r)^{a)}$	0.498	49	2.15 – 5.15 Å	357.4
$g_{GeSe}(r)^{b)}$	2.928	49		519.2
$g_{SeSe}(r)^{a)}$	0.002	15	2.02 – 2.95 Å	126.5
$g_{SeSe}(r)^{b)}$	2.784	15		1230.3

[a)] defect peaks (homopolar bonds in $g_{GeGe}(r)$ and $g_{SeSe}(r)$ and peak at 3.02 Å in $g_{GeSe}(r)$) included, [b)] defect peaks neglected

Table 6.6 : R-factors and χ^2 values (for 314 data points) obtained for the fits to the partial structure factors.

It can be seen from figures 6.7 and 6.11 that all three partial structure factors contribute to the FSDP, but that it arises predominantly from the Ge-Ge correlations, i.e. from the real-space intermediate range ordering of Ge-centred structural motifs. This agrees with the results found for liquid $GeSe_2$, see Penfold & Salmon[21]. The positions of the FSDPs are given in table 6.7.

$S_{\alpha\beta}(Q)$	position of FSDP [$Å^{-1}$]	
	raw data	spline fitted data
$S_{GeGe}(Q)$	1.00(1)	1.01(1)
$S_{GeSe}(Q)$	1.00(1)	0.99(1)
$S_{SeSe}(Q)$	0.95(2)	0.95(2)

Table 6.7 : Positions of the FSDPs in the partial structure factors, obtained from the direct inversion of equation 6.8 and from the spline fits to these functions.

The first main peaks in $g_{GeSe}(r)$, $g_{GeGe}(r)$ and $g_{SeSe}(r)$, at 2.36(2) Å, 3.57(2) Å and 3.89(2) Å (figure 6.10), give Ge-Se, Ge-Ge and Se-Se coordination numbers of 3.7(1), 3.2(3) and 9.3(3) respectively. Since the ratio of the Ge-Se:Se-Se distances

is 0.607(6), close to the value of $\sqrt{3/8} = 0.612$ expected for perfect tetrahedral coordination, the results imply that there are a large number of tetrahedral $GeSe_{4/2}$ structural motifs, the basic building blocks of crystalline $GeSe_2$. The main Ge-Ge peak is preceded by a smaller peak at 3.02(2) Å, with a corresponding Ge-Ge coordination number of 0.34(5), see appendix A. The like-atom $g_{\alpha\beta}(r)$ show Ge-Ge and Se-Se correlations at 2.42(2) Å and 2.32(2) Å, with homopolar coordination numbers of 0.25(5) and 0.20(5) respectively. This means that within the experimental error Ge and Se are, on average, four-fold and two-fold coordinated, i.e. they have a full outer shell of eight electrons. Figure 6.10 also gives evidence of further Se-Se correlations at 2.74(2) Å, and there are Ge-Se correlations also at 3.02(2) Å.

The maxima and coordination numbers of the first few features for all the $g_{\alpha\beta}(r)$ shown in figures 6.8 and 6.10 are summarised in the table 6.8.

	1st peak position [Å]	$\bar{n}^{\beta}_{\alpha}$	integration range [Å]	2nd peak position [Å]	$\bar{n}^{\beta}_{\alpha}$	integration range [Å]	3rd peak position [Å]	$\bar{n}^{\beta}_{\alpha}$	integration range [Å]
$g_{GeGe}(r)$									
a)	2.42(2)	0.25(5)	2.02 - 2.73	3.02(2)	0.34(5)	2.73-3.19	3.57(2)	3.2(3)	3.19 - 4.23
b)	2.39(2)	0.29(5)	2.09 - 2.79	3.03(2)	0.2(1)	2.79-3.13	3.57(2)	3.3(3)	3.13 - 4.26
c)	2.38(2)	0.30(5)	2.09 - 2.85	3.06(2)	0.2(1)	2.85-3.19	3.58(2)	3.3(3)	3.19 - 4.26
$g_{GeSe}(r)$									
a)	2.36(2)	3.7(1)	2.09 - 2.61	3.02(2)	0.29(5)	2.61 - 3.16			
b)	2.36(2)	3.8(1)	2.09 - 2.61	-	-	-			
c)	2.36(2)	3.8(1)	2.09 - 2.61	-	-	-			
$g_{SeSe}(r)$									
a)	2.32(2)	0.20(5)	2.02 - 2.55	2.74(2)	0.06(3)	2.55-3.09	3.89(2)	9.3(3)	3.09 - 4.39
b)	2.31(2)	0.22(5)	2.09 - 2.61	2.78(2)	0.05(3)	2.61-3.09	3.89(2)	9.3(3)	3.09 - 4.39
c)	2.31(2)	0.22(5)	2.09 - 2.61	2.78(2)	0.05(3)	2.61-3.09	3.89(2)	9.3(3)	3.09 - 4.39

a) $g_{\alpha\beta}(r)$ obtained from the fit

b) $g_{\alpha\beta}(r)$ obtained from the Fourier transform of the spline fits

c) $g_{\alpha\beta}(r)$ obtained from the Fourier transform of the raw data sets

Table 6.8 : Peak positions in g(r), coordination numbers and integration ranges from the differently obtained $g_{\alpha\beta}(r)$.

The total structure factor for the $^{N}Ge^{N}Se_2$ sample together with each of the partial structure factors $S_{\alpha\beta}(Q)$ weighted according to the factors given in table 6.2 are shown in figure 6.12. It can be seen that the FSDP in the total structure factor is predominantly due to the Ge-Ge correlations. However, the contribution from the Ge-Se correlations is also marked. The second peak mainly arises from the Se-Se

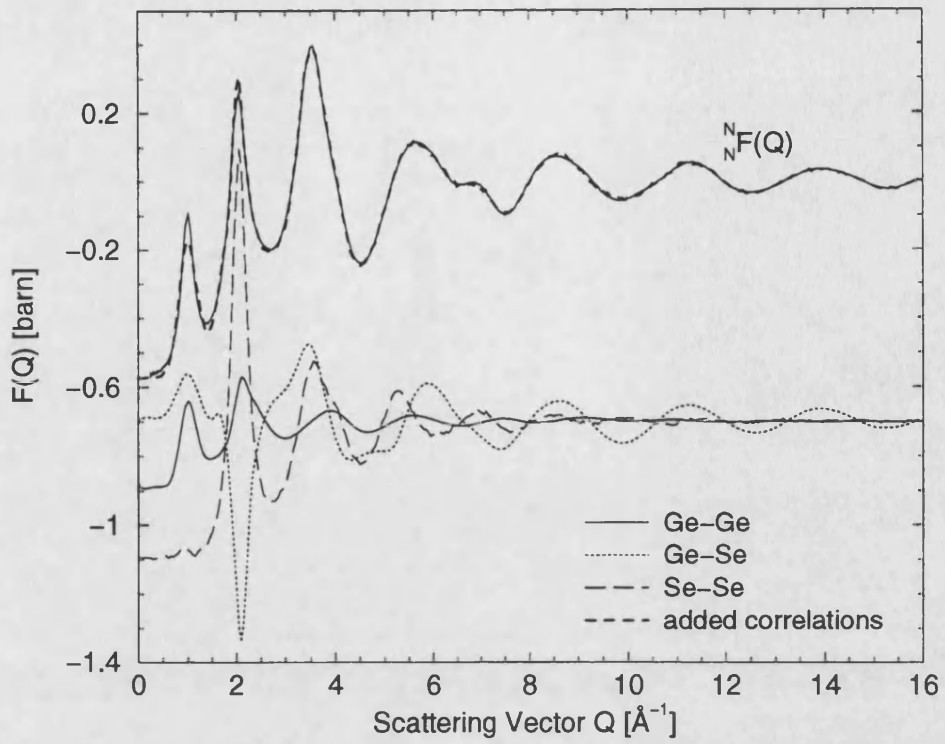

Figure 6.12: F(Q) together with the weighted Ge-Ge, Ge-Se and Se-Se contributions (spline fitted data sets, shifted by -0.7 barn). The contributions of the single $S_{\alpha\beta}(Q)$ to the total structure factor become obvious in this representation.

contributions. This has already been inferred from a comparison of the first order difference functions, $\Delta_{Ge}(Q)$ and $\Delta_{Se}(Q)$, in section 6.4.3. The large negative Ge-Se contribution, coinciding with the positive Ge-Ge and Se-Se contributions, strongly reduces the height of this peak. Finally the high-Q oscillations in $S_{GeSe}(Q)$ give rise to the oscillations observed in F(Q). As an additional self-consistency check the contributions from the partial structure factors are added up and compared with the total structure factor. The agreement is good (see figure 6.12), except for the FSDP region where the spline fit to the measured $S_{GeGe}(Q)$ smoothes the data by too much, see figure 6.7.

The contributions of the partial pair distribution functions $g_{\alpha\beta}(r)$ to G(r) in real-space are shown in figure 6.13. It is clear that the first peak in G(r) is mainly produced by the Ge-Se correlations, but that the homopolar bonds are necessary to reproduce the full height of this first peak. It is interesting to note that the low-r contributions from the Ge-Ge and Se-Se bonds are partly concealed by the truncation effects on Ge-Se. The second physical peak in G(r) can be seen to com-

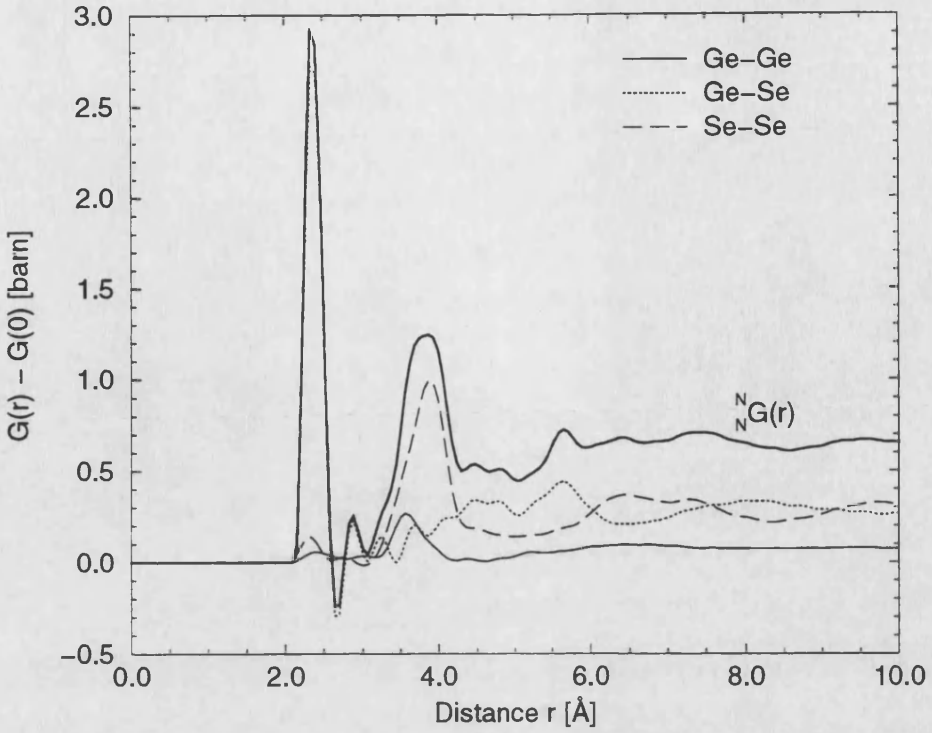

Figure 6.13: G(r) - G(0) for the $^{N}Ge^{N}Se_2$ sample (thick solid curve) with the contributions from the neutron weighted Ge-Ge, Ge-Se and Se-Se partial pair distribution functions (from the spline fits).

prise contributions from all three $g_{\alpha\beta}(r)$, although the Se-Se correlations dominate. The double shoulder on the high-r side of the second peak and the peak at ≈ 5.7 Å are due to Ge-Se contributions. The IRO in G(r) is obscured, because the Ge-Se and Se-Se correlations are in antiphase at distances $r \geq 6$ Å, and the IRO inherent in $g_{GeGe}(r)$ is not apparent in G(r) because of the small weighting of the Ge-Ge contributions.

The self-consistency of the data can be checked by a comparison of the first order difference functions in real-space, $\Delta G_{Ge}(r)$ and $\Delta G_{Se}(r)$, with the reconstructions obtained from the neutron weighted partial pair distribution functions. This serves as a critical test for self-consistency since $S_{GeGe}(Q)$ and $S_{GeSe}(Q)$ are the two least well conditioned partial structure factors and also because several types of systematic errors are reduced or essentially eliminated in $\Delta_{Ge}(Q)$ (see e.g. Salmon et al.[15] and section 3.4).

In figure 6.14 this comparison is shown. The agreement of both over the whole r-space range is striking for $\Delta G_{Ge}(r)$ and $\Delta G_{Se}(r)$. It is also clear that the homopolar

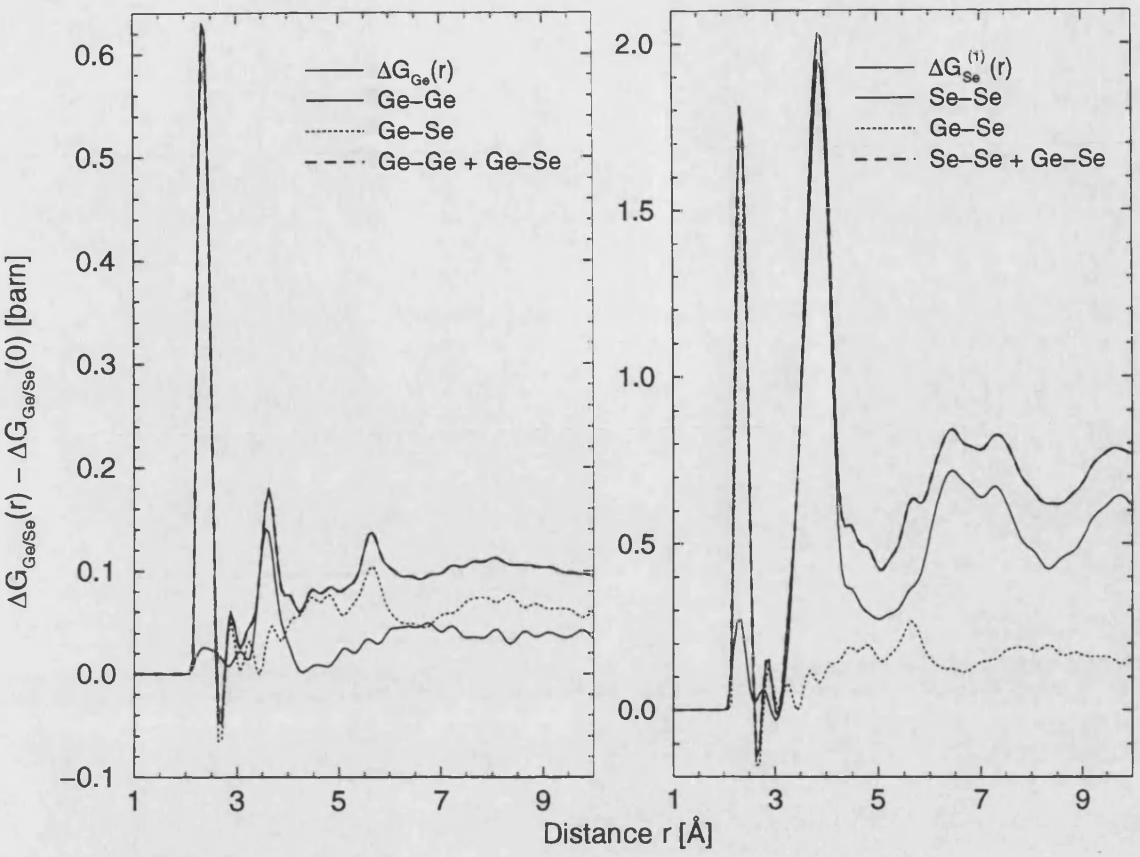

Figure 6.14: $\Delta G_{Ge}(r)$ and $\Delta G_{Se}^{(1)}(r)$ compared with the functions built up by the corresponding neutron weighted Ge-Ge, Ge-Se and Se-Se correlations obtained from the measured data points (thick dashed curves).

bonds for Ge-Ge as well as for Se-Se are necessary to reproduce the first peak of the measured first order difference functions.

6.5 Comparison with crystalline $GeSe_2$

There are two known crystalline phases of $GeSe_2$, the low temperature (LT or $\alpha - GeSe_2$) and high temperature (HT or $\beta - GeSe_2$) phase. Both comprise $GeSe_4$ tetrahedra as their main structural units and only heteropolar bonds between nearest neighbours exist. While in the LT phase solely corner sharing tetrahedra occur (Dittmar & Schäfer[22]), the HT form contains equal amounts of corner and edge sharing $GeSe_{4/2}$ tetrahedra (Dittmar & Schäfer[23]). It was shown before that the structure of glassy $GeSe_2$ (Susman et al.[2], Nemanich et al.[12]) and the structure of molten $GeSe_2$ (e.g. Penfold & Salmon[21]) resemble the HT-crystalline phase.

HT $-$ $GeSe_2$ has a layered, monoclinic structure (C^5_{2h}) and its unit-cell parameters are a = 7.016(3) Å, b = 16.796 Å, c = 11.831(5) Å and β = 90.65(5) °.

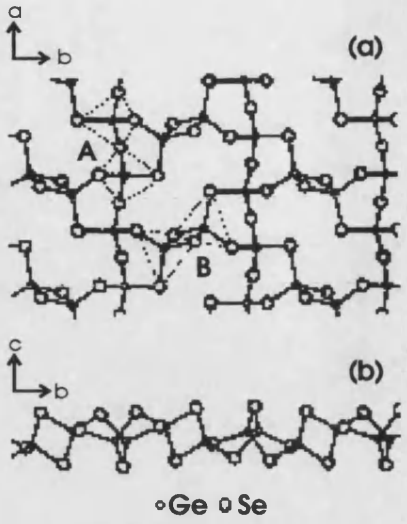

Figure 6.15: Fragment of a mono-layer of HT-$GeSe_2$ in the a-b plane (a) and b-c plane (b). The smaller circles denote Ge atoms, the larger circles denote Se atoms. The broken lines illustrate $GeSe_{4/2}$ tetrahedra, A : corner sharing chain tetrahedra, B : edge sharing bi-tetrahedra. (Reproduced from Matsuda et al.[24].)

Figure 6.15 shows projections of the atomic arrangement for a mono-layer of β $-$ $GeSe_2$ in the a-b and b-c planes respectively. In the structure there are corner sharing tetrahedra (A in the figure) that form chains along the a-axis and edge sharing bi-tetrahedra (B) that connect the chains like bridges. The shortest Ge-Ge and Se-Se correlations are at distances of 3.049 Å and 3.45 Å respectively. In the crystal there are two-, three- and eight-fold rings, creating void space. The rings are defined by starting from one Ge atom, moving to the next neighbouring Se atom, then to the next Ge atom, until returning to the original Ge atom via the shortest direct route. An n-fold ring therefore contains n Ge and n Se atoms.

Figures 6.16- 6.18 show a comparison of the $g_{\alpha\beta}(r)$ we obtained by the least square fitting procedure (see section 6.4.4) with the corresponding coordination environments in the HT-$GeSe_2$ crystalline phase.

From figure 6.16 it can be seen that there are edge sharing tetrahedra present in glassy $GeSe_2$. The small peak at 3.02(2) Å in $g_{GeGe}(r)$ for the glass almost matches the Ge-Ge distance for edge sharing tetrahedral motifs in HT $-$ $GeSe_2$ at 3.049 Å. The corresponding coordination number of 0.34(5) is consistent with 34(5) % of

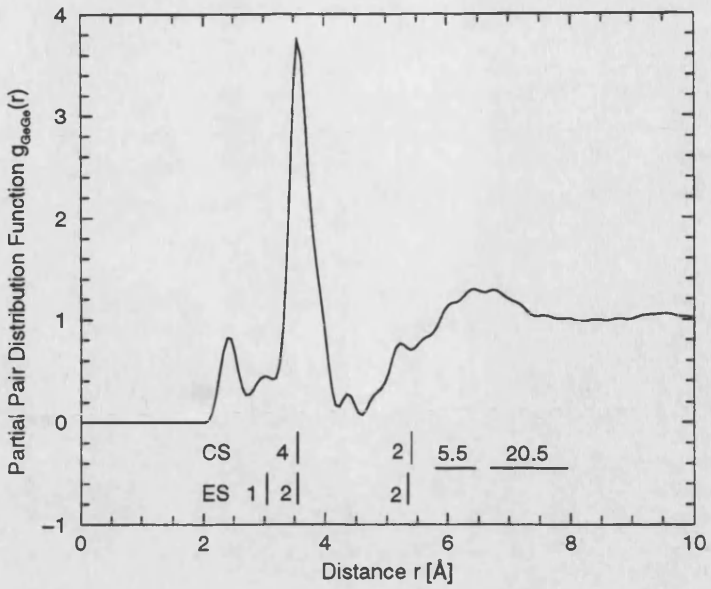

Figure 6.16: $g_{GeGe}(r)$ obtained by the fitting procedure described in section 6.4.4 in comparison with the Ge-Ge coordination environment in HT – $GeSe_2$. At low r ($r \leq 5.4$ Å) the Ge correlations are separated into corner sharing (CS) and edge sharing (ES) correlations. At higher r the average coordination number (using both edge and corner sharing Ge sites) is given. Vertical lines denote the positions of the Ge atoms, while horizontal lines indicate a range of atomic positions. The accompanying numbers give the average coordination numbers in the crystal.

the Ge being in edge sharing tetrahedra in accordance with the previous estimate of ≈ 40 % given by Susman et al.[2]. The coordination number of $\overline{n}^{Ge}_{Ge} = 3.2(3)$ (see table 6.8), obtained by integrating over the range from 3.19 Å to 4.23 Å under the main peak in $g_{GeGe}(r)$, excludes the contribution of the first edge sharing Ge site and therefore has to be compared with an average coordination number of 3.0 in the HT crystal (there are equal numbers of edge and corner sharing sites in HT-$GeSe_2$). The Ge-Ge correlations in the crystal at ≈ 5.4 Å seem to be represented in the structure of the glass by a feature in $g_{GeGe}(r)$ at the same distance. It should be noted that for distances ≥ 5.4 Å average coordination numbers are quoted in figure 6.16, i.e. the correlations are not separated into edge and corner sharing contributions.

Figure 6.17 compares the Ge-Se correlations in the glass and in the crystal. The position of the first peak in $g_{GeSe}(r)$ agrees very well with the Ge-Se distance in the HT crystalline form although the coordination number is less at $\overline{n}^{Se}_{Ge} = 3.7(1)$. The shoulder at $\approx 3.7 - 4.0$ Å found in $g_{GeSe}(r)$ coincides with edge sharing sites in the

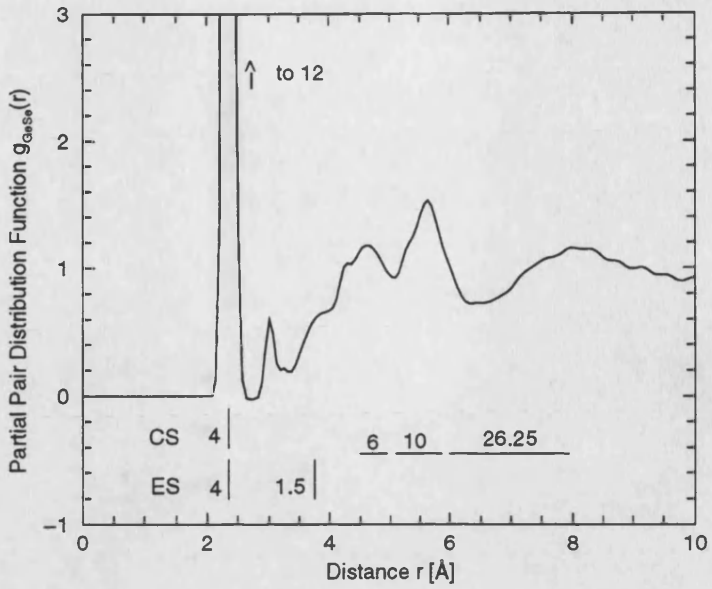

Figure 6.17: $g_{GeSe}(r)$ obtained by the fitting procedure described in section 6.4.4. The correlations in HT c-$GeSe_2$ at low r ($r \leq 4$ Å) are split into corner sharing (CS) and edge sharing (ES) contributions. The vertical lines denote the positions of the Se atoms, the horizontal lines indicate a range of atomic positions and the accompanying numbers give the average coordination numbers in the crystal.

crystal and therefore confirms the existence of edge sharing $GeSe_{4/2}$ tetrahedra in the glass.

In figure 6.18 our measured $g_{SeSe}(Q)$ is compared with the Se-Se correlations in HT – $GeSe_2$. The coordination number of $\overline{n}_{Se}^{Se} = 9.3(3)$ obtained for the glass for the range $3.09 \leq r[Å] \leq 4.39$ agrees well with the coordination number of 9.75 found between 3.454 Å and 4.25 Å in the crystal. The IRO in all three partial pair distribution functions is shown by the structure that extends to high values of r.

In summary, it has been found that the structure of glassy $GeSe_2$ comprises both corner and edge sharing tetrahedra and that the short range order of the glass is similar to that of the HT crystalline phase. However the partial pair distribution functions provide clear evidence for a substantial number of defects which will be discussed in the following section.

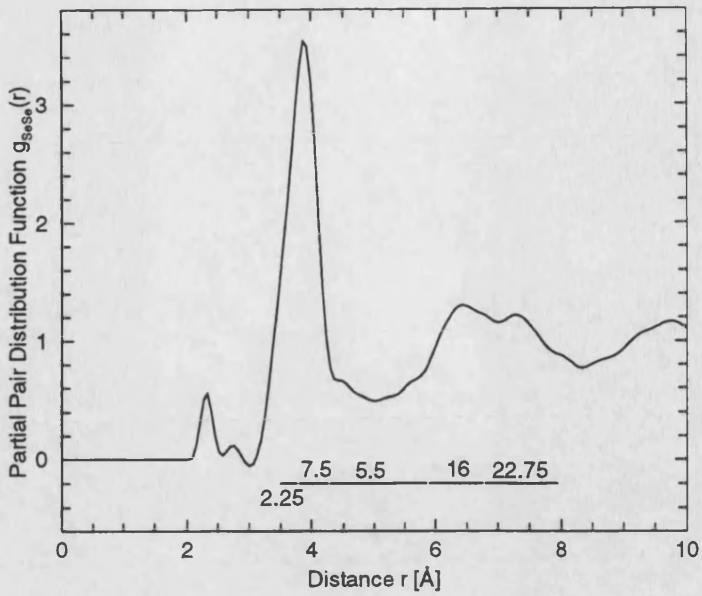

Figure 6.18: $g_{SeSe}(Q)$ obtained by the fitting procedure described in section 6.4.4 compared with the Se-Se coordination environment in HT – $GeSe_2$. As there is little difference between the Se-Se correlation arising from edge and corner sharing sites the average correlations of both are drawn.

6.6 Discussion of the defects in glassy $GeSe_2$

It has been shown that the measured Faber-Ziman partial pair distribution functions $g_{\alpha\beta}(r)$ provide clear evidence for a substantial number of defects, i.e. structural units that are not present in the HT phase of crystalline $GeSe_2$ (Dittmar & Schäfer[23]). For example, the like-atom $g_{\alpha\beta}(r)$ show Ge-Ge and Se-Se correlations at typical homopolar single bond distances of 2.42(2) Å for Ge-Ge, which is close to the distance of 2.45 – 2.47 Å observed in crystalline or amorphous Ge (Etherington et al.[32], Dalba et al.[33]), and at 2.32(2) Å for Se-Se, which agrees within the errors with the distance of 2.34(2) Å measured for amorphous Se (see section 7.5). There is evidence of further Se-Se correlations at 2.74(2) Å and there are also Ge-Se correlations at 3.02(2) Å. The Ge-Ge and Se-Se homopolar bond coordination numbers are 0.25(5) and 0.20(5). They give a maximum number of Ge and Se involved in homopolar bonds of 25(5) % and 20(5) %, respectively, which corresponds to the case of exclusive dimer formation. The number of these bonds is roughly the same, giving a ratio for the number of Ge-Ge (or Se-Se) bonds to the total number of bonds in the glass of $\approx 4\%$, in agreement with an estimate based on the law

of mass action assuming the following bond energies (see Feltz[34]), 225 k J mol^{-1} for Ge – Se bonds, 188 k J mol^{-1} for Ge – Ge bonds, and 227 k J mol^{-1} for Se – Se bonds. Mamedov et al.[35] quote an even higher estimate of $\approx 6\,\%$ for this ratio, obtained by analysing the chemical shifts of the Ge and Se K_{α_1} lines measured in x-ray emission spectroscopy experiments. The difference in the Ge-Ge and Ge-Se bond energies gives preference to the formation of heteropolar bonds. Therefore the large fraction of homopolar bonds has to be explained by them being formed at temperatures above the melting point by, for example, the dissociation of $GeSe_4$ tetrahedra. The quenching procedure then freezes-in $GeSe_2$ the structural fragments produced by this dissociation process (Mamedov et al.[35]). This indicates a strong influence of the sample preparation procedure on the detailed structure of $GeSe_2$ glasses.

Although the presence of homopolar bonds and defects in the stoichiometric glass $GeSe_2$ has been inferred from some spectroscopic experiments, like Raman spectroscopy (Bridenbaugh et al.[7]) and Mössbauer spectroscopy (Bresser et al.[8], Boolchand et al.[9]), their existence has proved controversial (Tronc et al.[4], Sugai[6]), and they have not previously been identified by using diffraction (Fischer-Colbrie & Fuoss[5], Susman et al.[2]) or EXAFS (extended x-ray absorption fine structure) (Zhou et al.[36]) methods. This results, in part, from the similar neutron scattering lengths for Ge and Se of natural isotopic abundance and their close atomic numbers and sizes. Application of the present diffraction method has, however, enabled these important structural features to be resolved and thus allows for a test of the models for the intrinsic broken chemical order.

As an illustration, if the predominant Ge-centred motifs are regular $GeSe_{4/2}$ tetrahedra and $Se_{3/2}Ge - GeSe_{3/2}$ ethane-like dimers, as in the discussed 'Outrigger Raft Model' (ORM) (Bridenbaugh et al.[7], Bresser et al.[8], Boolchand et al.[9]), then the upper limit of 25(5) % on the number of Ge involved in dimers is consistent with an estimate of 16(1) % from Mössbauer experiments by Boolchand et al.[9] where they used Sn as a Ge probe. However a more detailed analysis must include the Ge-Se defect peak at 3.02(2) Å. When tetrahedral coordination with distances found in the experiment is assumed, it is found that this defect peak cannot be due to intramolecular Ge-Se distances in ethane-like units, since this expected Ge-Se distance in ethane-like units is ≈ 3.91 Å. Therefore the defect peak may

be associated with additional Ge-centred motifs comprising three-fold coordinated Ge in defected $GeSe_{4/2}$ tetrahedra and one-fold coordinated Se (see figure 6.19). These motifs were found by Cobb et al.[26] from molecular dynamics calculations at a Ge-Se distance of 3.2 Å in glassy $GeSe_2$.

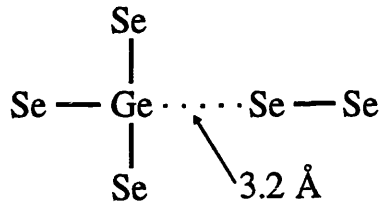

Figure 6.19: Schematic drawing of a defected tetrahedra as described in the text.

The coordination number for this peak of 0.29(5) yields a maximum fraction (if we assume there is only one long bond per tetrahedron) of Ge in the defected tetrahedra of 29(5) % such that the minimum fraction of Ge in regular tetrahedra is 54(6) %. These fractions together with the fraction of 25(5) % of Ge-Ge dimers adds up, within the errors, to unity as required. These fractions are roughly similar to those found in the recent molecular dynamics calculations of Cobb et al.[26]: 61 % of Ge form undistorted $GeSe_{4/2}$ tetrahedra, 25 % of Ge form ethane-like units, and 15 % of Ge take part in defected tetrahedra. Such a large number of intrinsic defects invokes the question as to how they can be reconciled with the appearance of pronounced intermediate range ordering.

Our measured defect concentrations are also in accordance with the Raman results of Nemanich et al.[37] on as-deposited and annealed $GeSe_2$ films. A ratio of Ge dimers to $GeSe_{4/2}$ tetrahedra of 0.16(3) for the as-deposited film and of 0.03(1) for the annealed film was measured. Our results give a ratio of 0.14(4) if we divide the number of Ge dimers by the sum of the defected and regular tetrahedra. The results by Nemanich et al.[37] suggest that the number of homopolar bonds will decrease if amorphous $GeSe_2$ is annealed near the glass transition temperature.

In summary it can be concluded that our results allow for a detailed discussion of the defects. The concentration of homopolar bonds we measure is neither consistent with the random covalent network (RCN) model, which gives a ratio for the number of Ge-Ge (or Se-Se) bonds to the total number of bonds of 25 %, nor with the chemically ordered network (CON) model, which does not give any homopolar

bonds for the stoichiometric $GeSe_2$ composition (for details on both models see e.g. Elliott[16]). Also the obtained coordination numbers for homopolar bonds cannot be used as a basis for distinguishing between the defected COCRN and the ORM models, since both models give equal numbers of Ge and Se atoms involved in homopolar bonds, i.e. in both models $\overline{n}_{Ge}^{Ge} = 2\,\overline{n}_{Se}^{Se}$.

6.7 Comparison of the structure of glassy and liquid $GeSe_2$ with first-principles molecular dynamics studies

In this section a comparison of the structure of glassy $GeSe_2$ and liquid $GeSe_2$, measured on D4B at the ILL at a temperature of 784(3) °C by Penfold & Salmon [21], [25], will be made at the partial structure factor level. Both data sets will also be compared with the recent results obtained from first-principles molecular dynamics studies by Cobb et al.[26], [27] and by Massobrio et al.[28].

6.7.1 Faber-Ziman partial structure factors

In figures 6.20 - 6.22 the partial structure factors, $S_{\alpha\beta}(Q)$, and partial pair distribution functions, $g_{\alpha\beta}(r)$, of the liquid and the glass are shown in comparison with the results obtained from the molecular dynamics studies. The structure factors shown for liquid $GeSe_2$ in reciprocal-space are spline fits to the measured data. In real-space the Fourier transform of these spline fits are shown together with minimum noise solutions (MIN), see section 3.5, which allow for homopolar bonds in the Ge-Ge and Se-Se correlation functions (Penfold & Salmon[21], [25]). Cobb et al.[26] studied glassy $GeSe_2$ at 27 °C and liquid $GeSe_2$ [27] at 727 °C using a 216 atom model. Massobrio et al.[28] also chose a temperature of 727 °C for liquid $GeSe_2$ and a stoichiometric composition of 120 atoms.

A striking feature in the comparison of $S_{GeGe}(Q)$ for the liquid and the glass is the survival FSDP. Its position hardly changes (1.01 $Å^{-1}$ in the glass vs. 0.98 $Å^{-1}$ in the liquid, see Penfold & Salmon[21]) and it is of the same height and width. This observation confirms previous neutron diffraction work at the total structure

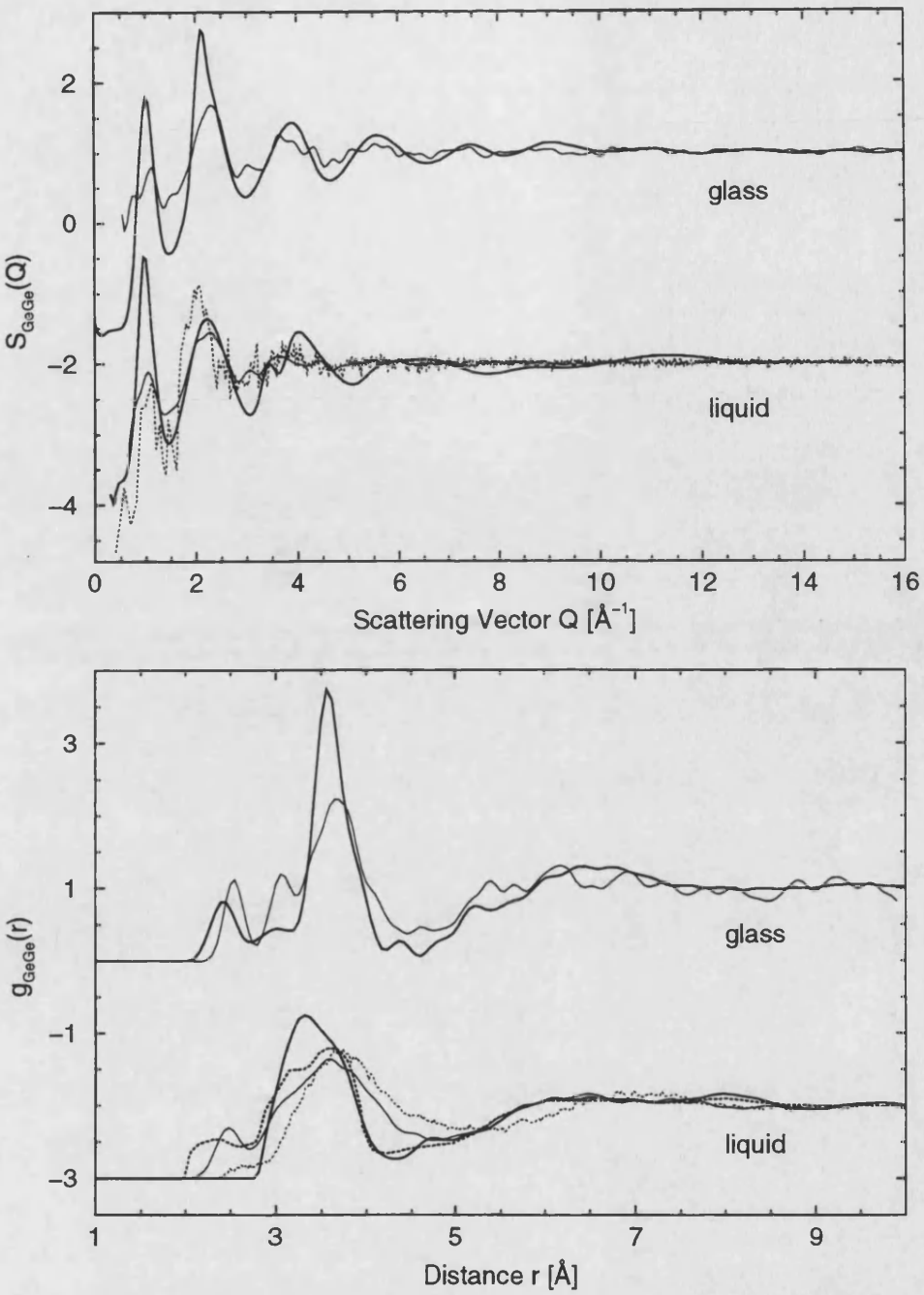

Figure 6.20: Comparison of $S_{GeGe}(Q)$ and $g_{GeGe}(r)$. The thick solid curves represent the experimental data for the glass and for the liquid (shifted by -3). The spline fitted data sets are used for both the glass and the liquid in reciprocal-space, and the partial pair distribution function obtained from the Gaussian fit is used for the glass in real-space (thick solid curve). For the liquid in real-space the direct transform of the spline fit (thick solid curve) and a minimum noise (MIN) solution, allowing for homopolar bonds (thick dotted curve), are given. The thin solid curves for the liquid and glass correspond to the Cobb et al.[26], [27] studies and the fine dotted curves for the liquid show the Massobrio et al.[28] results.

factor level by Susman et al.[2], who found that the height of the FSDP in the liquid is 10 % less than in the glass at 10 K and that the positions and halfwidths are identical. This behaviour has been interpreted in terms of an increase with density of the 'frustration' associated with the packing of Ge centred structural units (Petri et al.[20]). The second peak in $S_{GeGe}(Q)$ is markedly smaller in the liquid and the low-Q shoulder on the third peak in the liquid is not found in the glass. In real-space in the spline fit the main peak in the liquid is shifted to lower-r, but the coordination number associated with this peak agrees with the number we measure for the glass (table 6.9). The coordination number for the homopolar bonds $\overline{n}_{Ge}^{Ge} = 0.2$, found from the MIN solution for the liquid, agrees within the errors with the value found for the glass of 0.25(5). However, the Ge-Ge distance is lower in the liquid at 2.33(3) Å compared with 2.42(2) Å in the glass. In the MIN solution the second peak in $g_{GeGe}(r)$ splits into a small low-r peak and a larger high-r peak (see figure 6.20), which occurs at a position comparable with the second peak in the glass (table 6.9).

In $S_{GeGe}(Q)$ the agreement between the experimental data and the molecular dynamics studies are not very satisfactory. For both the liquid and the glass data the calculated FSDPs are too small and slightly shifted to higher Q. All of the calculations do not produce the correct high-Q oscillations. In real-space the calculations of Cobb et al.[26],[27] yield homopolar bonds with a Ge-Ge contact distance larger than in the experiments (table 6.9). Also the main peaks are shifted to higher-r. Between the homopolar bond and the main peak, i.e. at 3.06 Å for the glass and at 3.08 Å for the liquid Ge-Ge contributions from edge sharing tetrahedra are found in the calculations, giving rise to about 40 % edge sharing tetrahedra in the glass and 50 % in the liquid (Cobb et al.[26],[27]).

	1st peak position [Å]	$\overline{n}_{\alpha}^{\beta}$	2nd peak position [Å]	$\overline{n}_{\alpha}^{\beta}$
$g_{GeGe}(r)$				
glass, this study	2.42(2)	0.25(5)	3.57(2)	3.2(3)
glass, Cobb et al.[26]	2.46		3.5 & 3.8	
liquid, Penfold & Salmon[21]	-	-	3.31(2)	3.3(6)
liquid, Penfold & Salmon[21]*)	2.33(3)	0.2(1)	3.59(2)	
liquid, Cobb et al.[27]	2.48		3.6	3.4
$g_{GeSe}(r)$				
glass, this study	2.36(2)	3.7(1)		
glass, Cobb et al.[26]	2.37			
liquid, Penfold & Salmon[21]	2.42(2)	3.6(3)		
liquid, Cobb et al.[27]	2.37	3.6		
$g_{SeSe}(r)$				
glass, this study	2.32(2)	0.20(5)	3.89(2)	9.3(3)
glass, Cobb et al.[26]	$\approx$ 2.32		3.8	
liquid, Penfold & Salmon[21]	-	-	3.80(2)	10.3(5)
liquid, Penfold & Salmon[21]*)	2.30(2)	0.2(1)	3.75(2)	
liquid, Cobb et al.[27]	2.43		3.8	10.4

Table 6.9 : Peak positions and coordination numbers of the experimental data compared with the results from molecular dynamics studies. *) Values obtained from the MIN solution.

The $S_{GeSe}(Q)$ obtained from the spline fitted data set for the liquid shows no marked FSDP, see figure 6.21 although the position that Penfold & Salmon[21] give for the unspline fitted partial structure factor, 0.95(5) $Å^{-1}$, agrees within the errors with the 0.99(3) $Å^{-1}$ value we obtain for the glass. The glass exhibits a sharper negative second peak around 2.0 $Å^{-1}$ and in the liquid the high-Q oscillations are more rapidly damped. In real-space the first peak in the liquid is shifted to a slightly higher value of r (table 6.9) and is lower and broader, as would be expected due to the higher temperature. Also the peak in the glass at $\approx$ 5.7 Å, which is due to Ge correlations with Se on neighbouring tetrahedra, is not as clearly defined in the liquid.

The agreement between the molecular dynamics results and experiment for the Ge-Se correlations is considerably better than for the Ge-Ge correlations, but there are still problems in, for example, correctly calculating the FSDP. For the glass it occurs at a lower-Q value, and for the liquid its intensity is too high in both calculations. In real-space the first peak for the glass is much lower and broader in

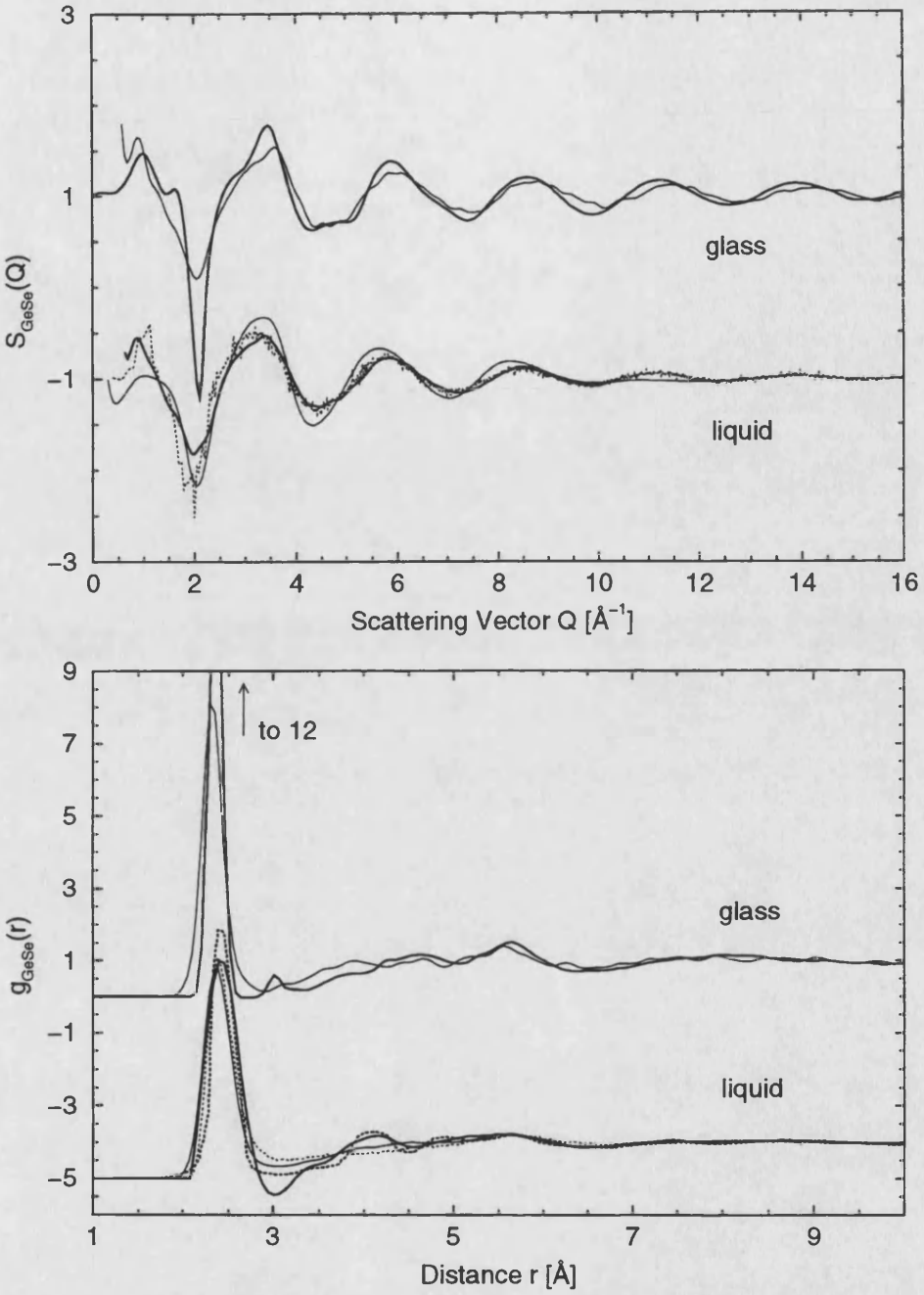

Figure 6.21: Comparison of the Ge-Se correlations in reciprocal and real-space. The thick solid curves represent the experimental data for the glass and for the liquid (shifted by -2 in reciprocal and by -5 in real-space). The spline fitted data sets are used for both in Q-space, and the partial pair distribution function obtained from the Gaussian fit is used for the glass in real-space (thick solid curve). For the liquid the direct transform of the spline fit (thick solid curve) and a minimum noise (MIN) solution, removing the unphysical negative going region behind the first peak (thick dotted curve), are given. The thin solid curves for the liquid and glass correspond to the Cobb et al.[26], [27] studies and the dotted curves for the liquid show the Massobrio et al.[28] results.

the molecular dynamics study, but the peak positions agree within the errors. The calculations do not reproduce the defect peak found at 3.02(2) Å by the experiment, but they do reproduce the peak found at $\approx$ 5.7 Å. For the liquid the first peak in real-space is well represented by both molecular dynamics studies, although again a slight shift in the peak position occurs. For higher-r the calculations show less structure compared with the experimental results.

For the Se-Se correlations (figure 6.22) the liquid and glass structure factors show a small FSDP at 0.93(1) $Å^{-1}$ and 0.95 $Å^{-1}$ respectively and the high-Q oscillations are more strongly damped in the liquid. In real-space the number and position of homopolar bonds found in the liquid and glass agree within the errors. The main peak in the spline fitted data set for the liquid occurs at a slightly lower-r value (table 6.9) and is more smeared out than for the glass. The coordination number associated with the peak is higher for the liquid compared to the glass, but the value of 10.3(5) includes the right hand side shoulder of the peak at approximately 4.75 Å, whereas our quoted value of 9.3(3) (table 6.9) for the glass does not. If we include the broad shoulder and integrate to 5.0 Å for the glass, we obtain $\overline{n}_{Se}^{Se} = 11.5(5)$. The ratio of the Ge-Se:Se-Se distances for the glass is 0.607(6), which is closer to the value of $\sqrt{3/8} = 0.612$ expected for perfect tetrahedral coordination than the value of 0.637(6) obtained for the liquid. This implies that the tetrahedral $GeSe_{4/2}$ structural motifs are more regular in the glass than in the liquid.

In reciprocal-space the molecular dynamics results for the glass do not agree well with the experimental data. The FSDP is overestimated, all of the higher-Q peaks have a considerably too low amplitude and are too broad. For the liquid the agreement is much better, although Cobb et al.[27] obtain a slightly larger FSDP and Massobrio et al.[28] do not seem to obtain a FSDP at all. Their results do however better represent the peak heights of the second and third peaks. In real-space in the glass the homopolar bonds occur at the same distance in the experimental and molecular dynamics results. Although in the calculation no indication of a second peak at 2.74(2) Å is given, a shoulder on the low-r side of the main peak is present and the main peak is to some extent shifted to lower-r (table 6.9) compared to the experiment. Both experiment and simulation show IRO, although there is no quantitative agreement. The agreement is much better for the liquid. Both

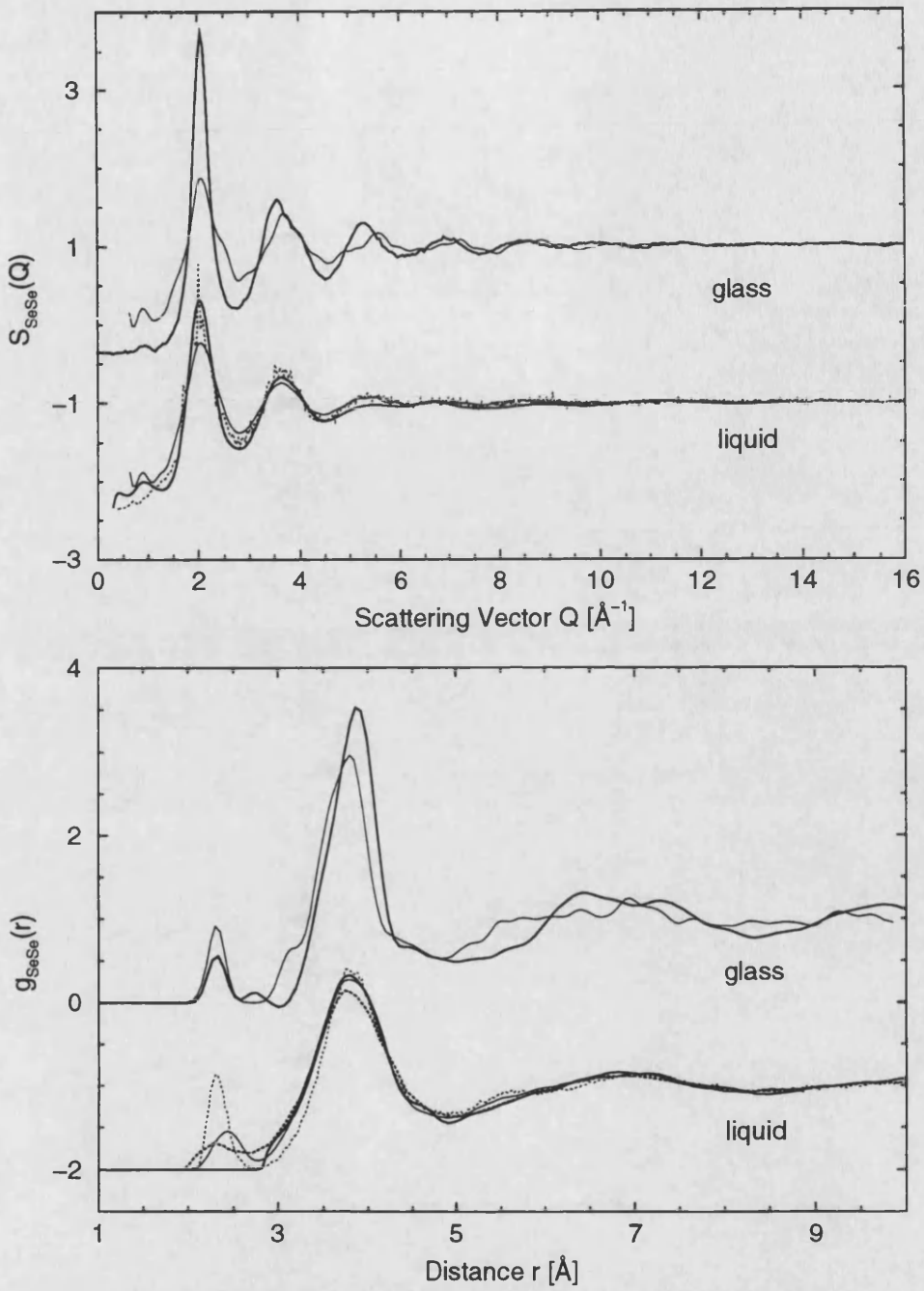

Figure 6.22: Comparison of $S_{SeSe}(Q)$ and $g_{SeSe}(r)$. As in figure 6.20 the thick solid curves represent the experimental data for the glass and for the liquid (shifted by -2). The spline fitted data sets are used for both the glass and the liquid in Q-space, and the partial pair distribution function obtained from the Gaussian fit is used for the glass in real-space (thick solid curve). For the liquid in real-space the direct transform of the spline fit (thick solid curve) and a minimum noise (MIN) solution, allowing for homopolar bonds (thick dotted curve), are given. The thin solid curves for the liquid and glass correspond to the Cobb et al.[26],[27] studies and the dotted curves for the liquid show the Massobrio et al.[28] results.

molecular dynamics studies show rather different peaks for the homopolar bonds, but at $r \geq 3$ Å they represent the experimental data very well.

In general it was found that all the simulated $S_{\alpha\beta}(Q)$ and $g_{\alpha\beta}(r)$ for the glass do not show sharp enough structures, the peaks are predominantly too low and too broad. The agreement with the experimental data is significantly better for the liquid data. Cobb et al.[27] attribute this to the fact that simulating the quenching process with femtosecond time scales makes the system more disordered than the real glass.

6.7.2 Bhatia Thornton partial structure factors

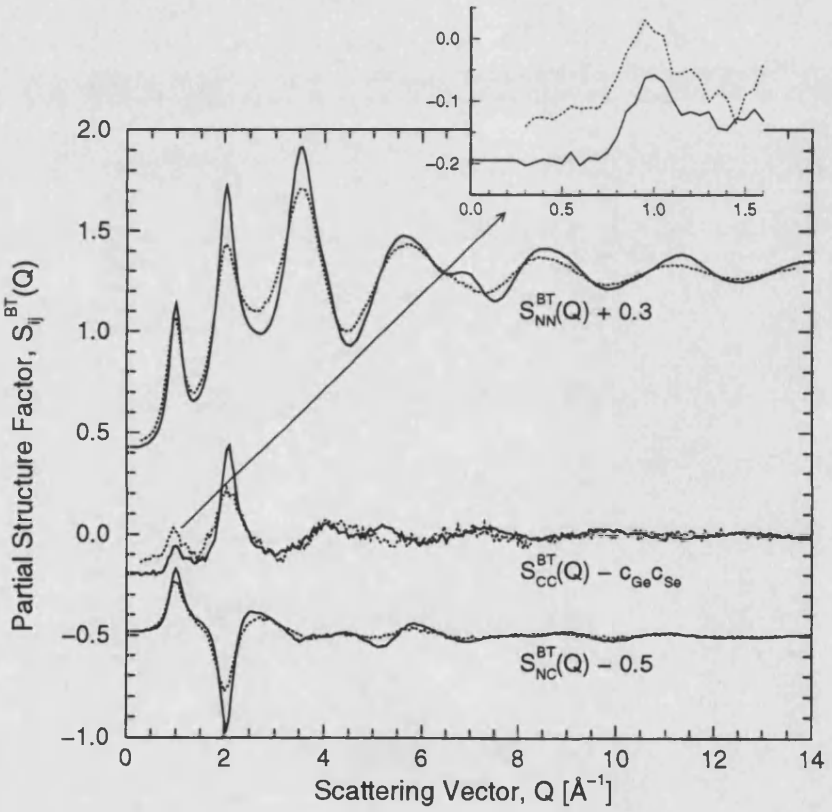

Figure 6.23: Comparison of the Bhatia Thornton partial structure factors, $S_{ij}^{BT}(Q)$, for the liquid (dotted curves) and the glass (solid curves). The small inset shows the area of the FSDP in $S_{CC}(Q)$ on an enlarged scale for better comparison.

The data can also be presented in terms of the Bhatia Thornton partial structure factors (see section 2.10), $S_{NN}^{BT}(Q)$, $S_{NC}^{BT}(Q)$ and $S_{CC}^{BT}(Q)$, which are linear combinations of the Faber-Ziman partial structure factors. This formalism is particularly

useful as it separates those correlations that give rise to the global structure of the system from those which describe the chemical ordering (see e.g. Salmon[30]).

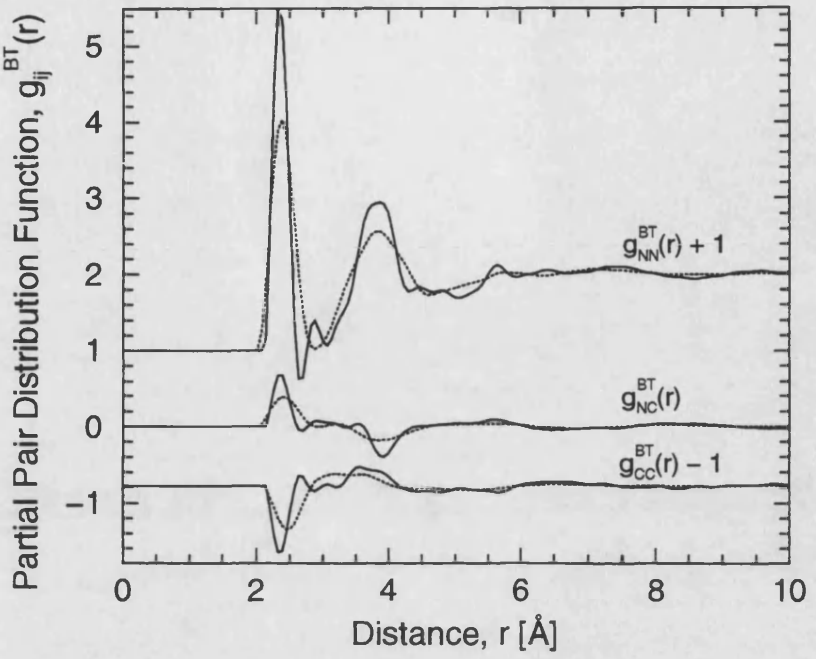

Figure 6.24: Bhatia Thornton partial pair distribution functions, $g_{ij}^{BT}(r)$ for the liquid (dotted curves) and the glass (solid curves).

In figures 6.23 and 6.24 the Bhatia Thornton partial structure factors and their real-space representations are illustrated. Since the scattering lengths of Ge and Se are very similar, $S_{NN}^{BT}(Q)$, which describes the topology of the system, closely resembles the total structure factor, ${}^{N}_{N}F(Q)$. Therefore its real-space representation $g_{NN}^{BT}(r)$ is closely related to ${}^{N}_{N}G(r)$.

In keeping with the reduced temperature, the peaks $S_{NN}^{BT}(Q)$ at $Q > 1.5\,\text{Å}^{-1}$ for glassy $GeSe_2$ are much sharper than for the liquid. However the FSDP, at 0.98 Å^{-1} in the liquid (Penfold & Salmon[21]) and 1.00 Å^{-1} in the glass, is reduced in height by about 13 % in the liquid. This observation confirms previous neutron diffraction experiments by Susman et al.[2] on the total structure factors, who found a reduction of $\approx 10\,\%$. They also reported the disappearance of the high-Q shoulder on the fourth peak upon melting, which we observe.

The large deviation in the number-concentration pair distribution function, $g_{NC}^{BT}(r)$, from zero indicates that $GeSe_2$, neither as a melt nor as a glass, can be

considered as a substitutional alloy, i.e. Ge and Se have different mean coordination environments.

It is of particular interest to compare the concentration-concentration structure factor, $S_{CC}^{BT}(Q)$, of the liquid with the glass, since in the melt a FSDP at $Q \approx 1$ Å^{-1} has been observed (Penfold & Salmon[21]), which implies that there are concentration fluctuations on the scale of the intermediate range order. It has not proved possible to reproduce this peak by using a variety of theoretical methods including conventional molecular dynamics (Vashishta et al.[31]) and *ab initio* molecular dynamics (Cobb et al.[26],[27] and Massobrio et al.[28]) simulations, see figure 6.25.

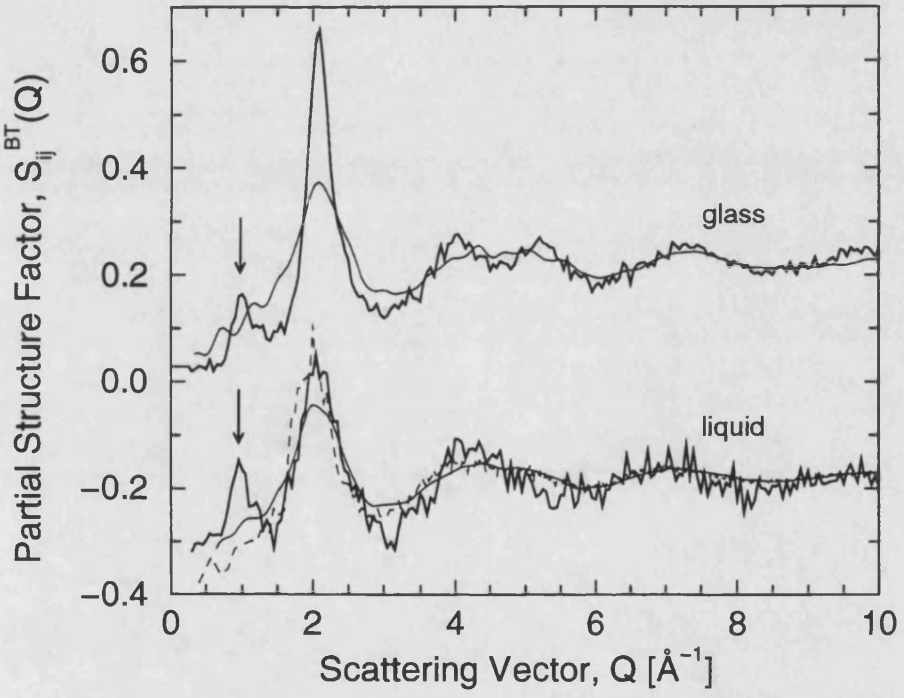

Figure 6.25: Concentration-concentration structure factors from the experiments (thick solid curves) compared with the *ab initio* molecular dynamics results by Cobb et al.[26],[27] for the liquid and glass (thin solid curves) and by Massobrio et al.[28] for the liquid (thin dashed curve). The $S_{CC}^{BT}(Q)$ from the molecular dynamics studies were obtained by a linear combination of the functions given in figures 6.20- 6.22. The vertical arrows point out the FSDPs in the experimental data.

It is seen from figure 6.23 that the new results for the glassy phase of $GeSe_2$ also show a FSDP in the concentration-concentration partial structure factor. The position, full width at half maximum and height of the FSDPs are 1.00(2) Å^{-1}, 0.37(5) Å^{-1} and 0.13(1) for the glass, and 0.95(2) Å^{-1}, 0.36(5) Å^{-1} and 0.15(2)

for the liquid, respectively. This implies that the structural models used in the molecular dynamics studies are still insufficient to explain the physical origin of the FSDP in $S_{CC}(Q)$ (Massobrio et al.[28]). More realistic interaction models for these disordered network materials are therefore needed.

The emergence of this FSDP in $S_{CC}(Q)$ for molten and glassy $GeSe_2$ might be explained by the covalent bonding that yields a relatively open arrangement of the atoms within the system, characterised be large voids, which in turn lead to a non-uniform density distribution on the scale of the IRO.

Additionally the deviation of $S_{CC}(Q)$ from $c_{Ge}c_{Se}$ shows that the distribution of atoms is not random. The negative peak in $g_{CC}(r)$ at $\approx 2.4\,\text{Å}$ for both the liquid and the glass, indicates the preference for heteropolar bonding.

6.8 Conclusions

- All three partial structure factors contribute to the intermediate range ordering in glassy $GeSe_2$, but it is dominated by the Ge-Ge correlations, i.e. by the real-space intermediate range ordering of Ge-centred structural motifs.

- The short range order in glassy $GeSe_2$ is very similar to that in the HT crystalline phase, although a substantial number of defects are present. In the glass 34(5) % of Ge are in edge sharing tetrahedra compared to 50 % in the crystal.

- Defects in glassy $GeSe_2$ have been identified for the first time by diffraction methods. An analysis of the defects yields a maximum fraction of Ge in defected tetrahedra of 29(5) %, a minimum fraction of Ge in regular tetrahedra of 54(6) % and a fraction of Ge in Ge-Ge dimers of 25(5) %.

- In keeping with the reduced temperature, the peaks in the partial structure factors at $Q > 1.5$ Å^{-1} for glassy $GeSe_2$ are sharper than for the corresponding liquid. However, the FSDP in $S_{GeGe}(Q)$ and in $S_{NN}(Q)$ is of comparable height and at a comparable position to the FSDP in these functions measured for the liquid.

- Problems are inherent in the molecular dynamics studies by Cobb et al.[26] to reproduce the structure of the $GeSe_2$ glass. In reciprocal and real-space the simulated peaks are too low and too broad. Real problems are encountered in the simulation in the region of the homopolar bonds for $g_{GeGe}(r)$, which are found at a too large distance. Further, the FSDP in the Bhatia-Thornton concentration-concentration structure factor has not been possible to be reproduced.

Bibliography

[1] Afify N, *Phys. Rev. B* **48** (1993) 16304.

[2] Susman S, Volin K J, Montague D G and Price D L, *J. Non-Cryst. Sol.* **125** (1990) 168.

[3] Zachariasen W H, *J. Am. Chem. Soc.* **54** (1932) 3841.

[4] Tronc P, Bensoussan M, Brenac A and Sebenne C, *Phys. Rev. B* **8** (1973) 5947.

[5] Fischer-Colbrie A and Fuoss P H, *J. Non-Cryst. Sol.* **126** (1990) 1.

[6] Sugai S, *Phys. Rev. B* **35** (1987) 1345.

[7] Bridenbaugh P M, Espinosa G P, Griffiths J E, Phillips J C and Remeika J P, *Phys. Rev. B* **20** (1979) 4144.

[8] Bresser W J, Boolchand P, Suranyi P and de Neufville J P, *Phys. Rev. Lett.* **46** (1981) 1689.

[9] Boolchand P, Grothaus J, Bresser W J and Suranyi P, *Phys. Rev. B* **25** (1982) 2975.

[10] Inoue K, Matsuda O and Murase K, *J. Non-Cryst. Solids* **150** (1992) 197.

[11] Magana J R and Lannin J S, *J. Non-Cryst. Solids* **59 & 60** (1983) 1055.

[12] Nemanich R J, Galeener F L, Mikkelsen J C, Connell G A N, Etherington G, Wright A C and Sinclair R N, *Physica B* **117 & 118** (1983) 959.

[13] Mott N F, *Phil. Mag.* **19** (1969) 835.

[14] Azoulay R, Thibierge H and Brenac A, *J. Non-Cryst. Sol.* **18** (1975) 33.

[15] Salmon P S, Xin S and Fischer H E, *Phys. Rev. B* **58** (1998) 6115.

[16] Elliott S R, *Physics of Amorphous Materials*, 2nd Ed., Longman Group UK Limited: Essex (1990).

[17] Sarrach D J, De Neufville J P and Haworth W L, *J. Non-Cryst. Sol.* **22** (1976) 245.

[18] Wang Y, Matsuda O, Inoue K, Yamamuro O, Matsuo T and Murase K, *J. Non-Cryst. Sol.* **232-234** (1998) 702.

[19] Edwards F G, Enderby J E, Howe R A, Page D I, *J. Phys. C: Sol. State Phys.* **8** (1975) 3483.

[20] Petri I, Salmon P S and Fischer H E, *ILL Annual Report 98* (1999) 52.

[21] Penfold I T and Salmon P S, *Phys. Rev. Lett.* **67** (1991) 97.

[22] Dittmar G and Schäfer H, *Acta Cryst. B* **32** (1976) 1188.

[23] Dittmar G and Schäfer H, *Acta Cryst. B* **32** (1976) 2726.

[24] Matsuda O, Inoue K and Murase K, *Sol. State Com.* **75** (1990) 303.

[25] Penfold I T and Salmon P S, *Phys. Rev. Lett.* **68** (1992) 253.

[26] Cobb M, Drabold D A and Cappelletti R L, *Phys. Rev. B* **54** (1996) 12162.

[27] Cobb M and Drabold D A, *Phys. Rev. B* **56** (1997) 3054.

[28] Massobrio C, Pasquarello A and Car R, *Phys. Rev. Lett.* **80** (1998) 2342.

[29] Penfold I T, *Ph.D. Thesis, University of East Anglia* (1990).

[30] Salmon P S, *Proc. R. Soc.* **A 437** (1992) 591.

[31] Vashishta P, Kalia R K, Rino J P, Ebbsjö I, *Phys. Rev. B* **41** (1990) 12197.

[32] Etherington G, Wright A C, Wenzel J T, Dore J C, Clarke J H and Sinclair R N, *J. Non-Cryst. Sol.* **48** (1982) 265.

[33] Dalba G, Fornasini P, Grazioli M and Rocca F, *Phys. Rev. B* **52** (1995) 11034.

[34] Feltz A, in *Physics of disordered materials*, eds. Adler D, Fritzsche H and Ovshinsky S R, Plenum : New York (1985) 203.

[35] Mamedov S B, Aksenov N D, Makarov L L and Batrakov Y F, *J. Non-Cryst. Sol.* **195** (1996) 272.

[36] Zhou W, Paesler M and Sayers D E, *Phys. Rev. B* **43** (1991) 2315.

[37] Nemanich R J, Connel G A N, Hayes T M and Street R A, *Phys. Rev. B* **18** (1978) 6900.

Chapter 7

The topology of Ge_xSe_{1-x} $(0 \leq x \leq 0.4)$ glasses

7.1 Introduction

In the preceding chapters the structures of disordered Ge_xSe_{1-x} materials at two compositions, GeSe and $GeSe_2$, were discussed in detail. It is also interesting to study the structure of glasses in the Ge_xSe_{1-x} system as a function of the Ge content x, since the structure of the corresponding melts has been shown to undergo marked changes on both the short and intermediate length scales (Salmon & Liu[1]). Glasses can be formed by bulk quenching methods over a wide composition range, covering $0 \leq x \leq 0.42$ (Azoulay et al.[2]), but the glass-forming ability varies notably with x, see figure 7.1.

It was shown by Tronc et al.[3] that glassy Ge_xSe_{1-x} compounds show significant changes in their optical properties, e.g. in their optical absorption coefficient and in their Raman spectra, with variation in the Ge content x. Particularly, compositions around $GeSe_4$ are of interest since on the basis of mean-field constraint theory there is a rigidity percolation threshold in a covalent network glass which occurs at an average coordination number of 2.4, corresponding to $x = 0.2$, in Ge_xSe_{1-x} (Wang et al.[4]). Direct evidence for this threshold has been found by experiments, see for example Wang et al.[4] and Feng et al.[5]. Additionally, glasses in the Ge-Se system have several commercial applications. For instance, Ge-Se glasses doped with As or Sb are available to be used as lenses for infrared sensors, and Smektala et

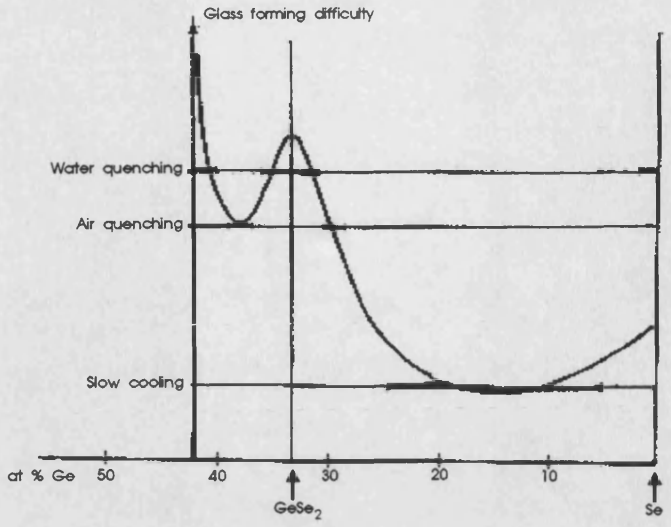

Figure 7.1: Glass forming difficulty as a function of the Ge content. (Reproduced from Azoulay et al.[2]).

al.[6] recently discovered that $GeSe_4$ is a favourable material for ultrafast nonlinear optical applications, for example in all-optical switching telecommunication uses.

Since the coherent neutron scattering lengths for naturally occurring Ge and Se are very similar, the measured total structure factor F(Q) reduces to the single Bhatia-Thornton partial structure factor $S_{NN}(Q)$ in a first order approximation (see section 5.2). The Fourier transform of this function, $g_{NN}(r)$, describes the average sites of the scattering particles, but is not concerned with their chemical identity. Therefore it contains information on the topology of the system. The F(Q) for many binary glasses exhibit a characteristic three-peak structure (Wright et al.[7]) for $0 \leq Qr_1 \leq 10$, where r_1 is the nearest neighbour distance, whose origin can be traced to $S_{NN}(Q)$ (Salmon[8]). The first of these three peaks is the so called 'First Sharp Diffraction Peak' (FSDP), that has already been discussed in detail in the preceding chapters. It is found in a wide variety of oxide, halide and chalcogenide disordered systems at low values of Qr_1 between ≈ 2.1 and ≈ 3.1 (Price et al.[9]). Since the FSDP refers to the intermediate range order (IRO) in the system, the presented experiments on the Ge_xSe_{1-x} system will provide information on the topology at both short and intermediate length scales.

Due to its importance as a proto-typical glass forming system, Ge_xSe_{1-x} glasses have been subjected to numerous studies. A summary of their mechanical, electronic, magnetic and optical properties can be found in Borisova[10]. Their thermal

properties, mainly the glass transition temperatures, have been measured by DTA (differential thermal analysis), see e.g. Azoulay et al.[2], DSC (differential scanning calorimetry), e.g. Sarrach et al.[11], and Modulated DSC, see Wagner et al.[12] and Feng et al.[5]. The results of these measurements will be compared with our results in section 7.3. A plethora of Raman scattering experiments have been carried out on the Ge_xSe_{1-x} system (e.g. Tronc et al.[3], Boucenter & Duval[13], Wang et al.[4] and Feng et al.[5]), leading to models to describe the glasses. There are reports using electron diffraction (Fawcett et al.[14], Uemura et al.[15]), x-ray diffraction (Hafiz et al.[16]), and EXAFS (Zhou et al.[17]) on the structure of Ge-Se amorphous alloys.

Very recently Rao et al.[18] published results of a neutron diffraction study on the structure of Ge_xSe_{1-x} glasses for different Ge contents. Our results will mainly be compared with these findings, although in our experiments the data was measured up to higher values of the scattering vector Q, and therefore truncation effects are reduced when the data is Fourier transformed into real-space (see section 3.5). Additionally our measurements are carried out with a better instrumental resolution $\Delta Q/Q$, and we also studied a wider range of compositions in addition to GeS_2. Importantly, we performed a thermal characterisation of our glassy alloys using DSC since their structure, e.g. the number of homopolar bonds (see chapters 5 and 6), is influenced by the method of preparation, e.g. by quench temperatures, the quench rate (Feltz & Lippmann[19]), and the thermal history.

7.2 Sample Preparation

The Se, $GeSe_4$, $GeSe_3$, $GeSe_2$ and $GeSe_{1.5}$ samples were prepared by mixing high purity elemental Ge lumps (99.9999 %, Aldrich) and Se pellets (99.999 %, Johnson Matthey) following the procedure described in section 4.2. All of the sample handling and preparation was carried out in a high purity argon filled glove box to prevent any oxygen or hydrogen contamination of the samples. The samples were contained in silica tubes of 5 mm internal diameter and 0.1 mm wall thickness during the preparation process.

The heating procedure used for $GeSe_4$, $GeSe_3$, $GeSe_2$ and $GeSe_{1.5}$ is the same as for the $GeSe_2$ samples described in sections 4.2 and 5.2, with the exception that

$GeSe_3$ and $GeSe_{1.5}$ were quenched from a temperature of 750 °C and $GeSe_4$ from 650 °C into an ice/salt-water mixture at -5 °C. The glassy Se sample was prepared by heating the silica tube containing the sample by 1 °C/min up to 210 °C, the melting temperature of Se. After equilibrating at this temperature for three hours it was heated up further to 450 °C with the same heating rate, and quenched after maintaining it at 450 °C for approximately 12 hours.

Glassy GeS_2 was prepared using high purity germanium (99.9999 %, Aldrich) and sulfur flakes (99.998 %, Aldrich). Because of the high vapour pressure of sulfur, the heating rate was reduced to 0.9 °C/min. During the heating process the sample was equilibrated for four hours at the melting temperature of S (110 °C) and for another four hours at 500 °C, before heating it up to 950 °C. It remained at this temperature for 19 hours, then the rocking furnace was set vertically, the sample cooled down slowly (1 °C/min) to 900 °C and, after allowing it to equilibrate at this temperature, it was quenched like all the other samples into an ice/salt-water mixture at -5 °C. The glasses containing Se were dark-reddish in their appearance whereas GeS_2 was yellow-brown.

7.3 DSC measurements

The thermal properties of the Ge_xSe_{1-x} and GeS_2 samples were measured in a differential scanning calorimetry (DSC) experiment using a TA Instruments Thermal Analyst 2000 machine. The temperature range covered depended on the particular sample, but was in most cases 20 - 400 °C and the heating rate was 10 °C/min. For Se and $GeSe_{1.5}$ about 10 mg of sample was contained in a small sealed glass ampoule (inner diameter approximately 0.86 mm, 0.32 mm wall thickness). This was held in an aluminium pan which was heated under a constant stream of oxygen free nitrogen purge gas at 40 ml/min. For the $GeSe_4$, $GeSe_3$, $GeSe_2$ and GeS_2 samples the sensitivity of this set-up was too low to observe the glass transition. Therefore these samples were contained in hermetically sealed aluminum pans, which provide a better thermal contact with the temperature sensor. Additionally the pans can contain approximately 5-10 mg more sample and have a lower thermal mass.

In our analysis both the onset and 'midpoint' or inflection point (obtained as described in section 6.4.1) of the transition were determined. Additionally at least

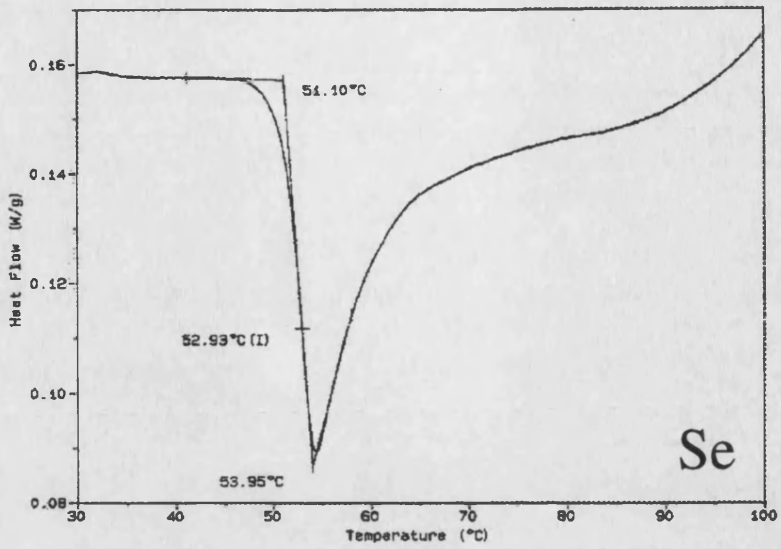

Figure 7.2: DSC trace in the glass transition region measured for Se sealed in a small glass ampoule. The scan rate was 10 °C/min.

two samples were measured to ensure the reproducibility of our measurements. For all the samples, except pure Se, the measurement was limited to the glass transition region, as crystallisation and melting take place at such high temperatures that either the glass ampoules start to soften or the vapour pressure of Se (S) is sufficiently high to promote sample leakage, thus contaminating the DSC cell.

The measured DSC traces in figures 7.2- 7.4 show that, except for pure Se, the glass transition in the investigated samples in the Ge-Se system is a very low enthalpy event. The glass transition temperature increases monotonically with the germanium content x up to the $GeSe_2$ composition then decreases again. A summary of our results for T_g is given in table 7.1.

	Se	$GeSe_4$	$GeSe_3$	$GeSe_2$	$GeSe_{1.5}$	GeS_2
onset [°C]	51(2)	167(4)	231(4)	396(3)	341(3)	487(10)
midpoint [°C]	53(2)	191(3)	253(3)	415(3)	351(3)	491(6)

Table 7.1 : Measured glass transition temperatures using DSC.

Our glass transition temperatures lie well within the values given in the literature. In figure 7.5 our results for the Ge_xSe_{1-x} samples are compared with the DTA measurements of Feltz & Lippmann[19] and Azoulay et al.[2], with the DSC

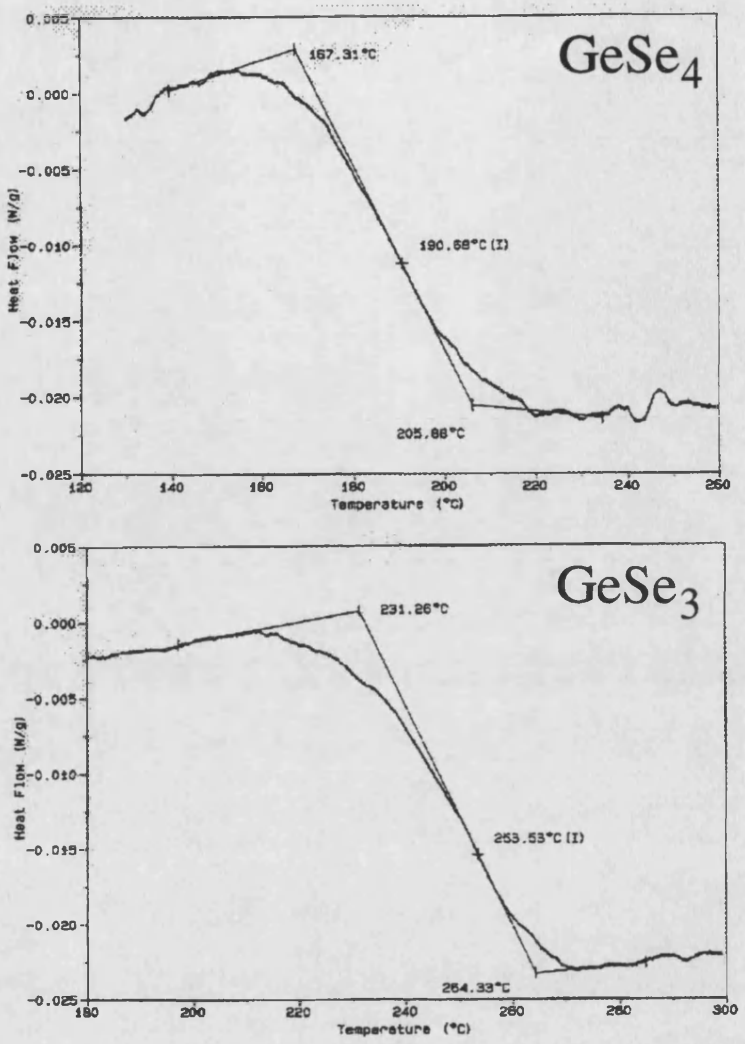

Figure 7.3: DSC traces for $GeSe_4$ and $GeSe_3$, both in hermetically sealed Al pans, measured in the glass transition region. The scan rate was 10 °C/min.

results of Sarrach et al.[11] (heating rate 20 °C/min, given T_g is inflection point) and Wang et al.[4] (heating at 10 °C/min), and with the Modulated DSC (MDSC) measurements of Wagner et al.[12] (heating rate 20 °C/min, onset points for T_g are given) and Feng et al.[5] (heating at 3 °C/min). The differences between the results obtained from the different authors might be due to different preparation methods used for the samples (especially different quench rates and quench temperatures) or due to the different experimental conditions used for the thermal measurements (e.g. heat rate and purge gas). Additionally, only Sarrach et al.[11] and Wang et al.[4] state how their T_g was extracted from the DSC traces, i.e. if the onset or inflection point of the transition is quoted. Details of the glass preparation proce-

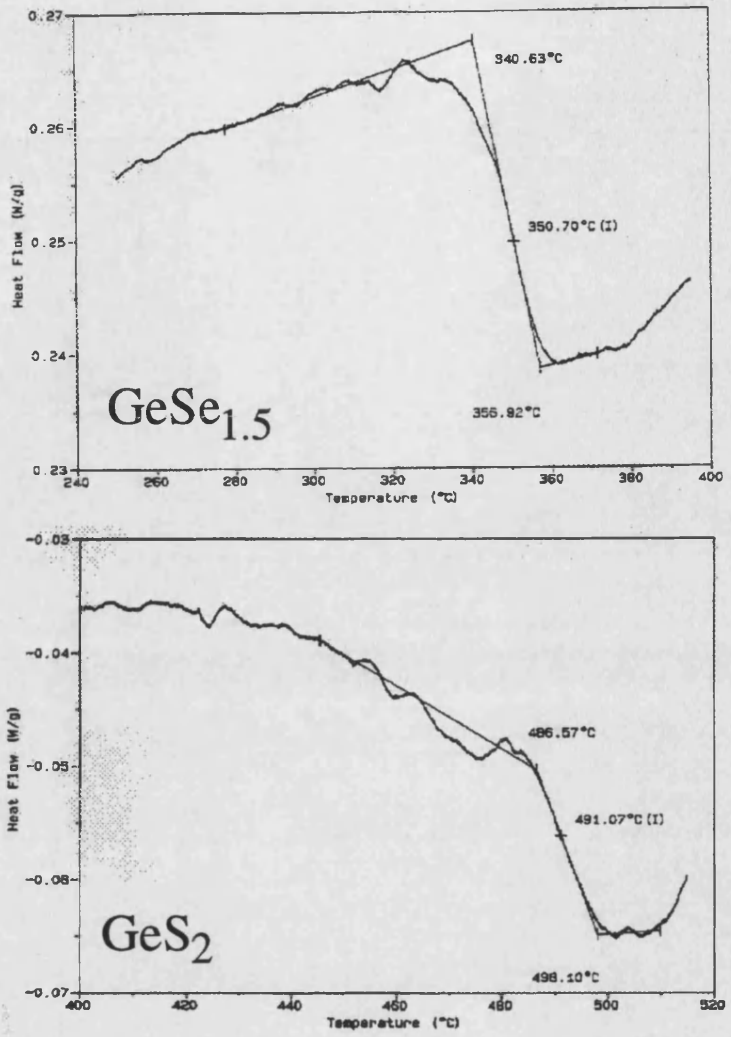

Figure 7.4: DSC traces measured for $GeSe_{1.5}$, in a glass ampoule, and GeS_2, in an Al pan. (The trace for $GeSe_2$ is already shown in figure 6.2.) The scan rate was 10 °C/min.

dures, as far as they are quoted in the literature, are given in table 7.2.

	Feltz & Lippmann[19]	Azoulay et al.[2]	Sarrach et al.[11]	Wang et al.[4]	Wagner et al.[12]	Feng et al.[5]
quench temp.	800-900°C		≈ 990°C	900°C	1000°C	liquidus temp.+50°C
method	H_2O qu.	H_2O qu.	H_2O qu.		H_2O qu.	H_2O qu.

Table 7.2 : Temperatures from which samples were quenched and method of quenching.

Figure 7.4 shows that T_g for the GeS_2 sample is very difficult to determine. Our value of 491(6) °C is lower than the T_g of 520 °C given by Feng et al.[5], who

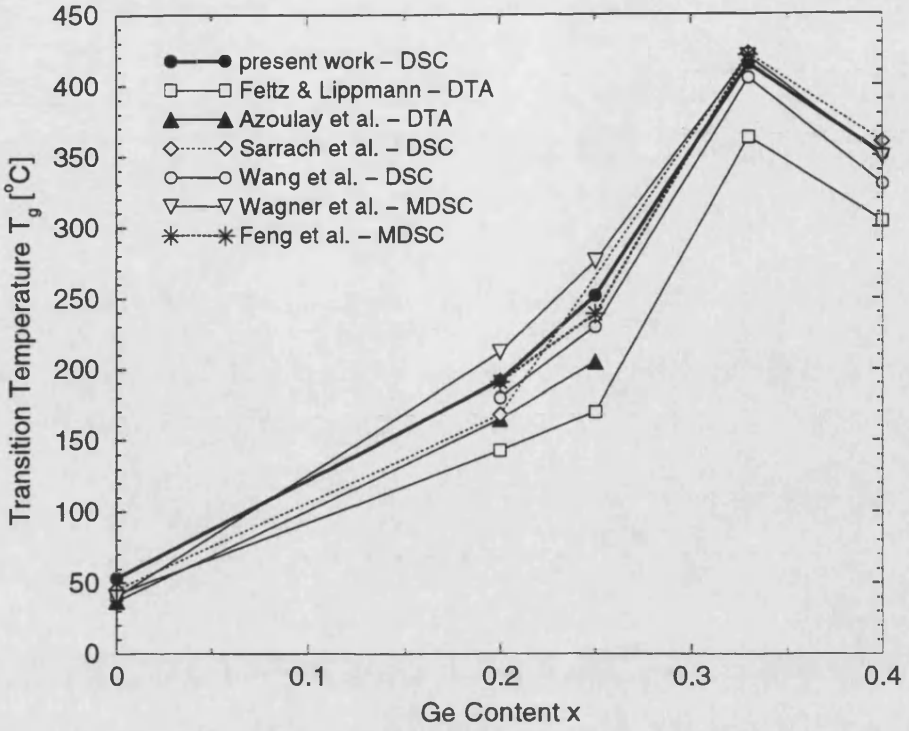

Figure 7.5: Comparison of the glass transition temperatures (inflection points are given for our measurements) with literature values. The lines are drawn as a guide for the eye.

used MDSC with a heating rate of 20 °C/min.

7.4 Neutron parameters and experiments

The diffraction experiments were carried out using two different instruments. Glassy $GeSe_4$ and GeS_2 were investigated using D4B (see section 3.2.1) at an incident wavelength of 0.7047 Å, while all of the other samples were measured at the Rutherford Appleton Laboratory using the SANDALS diffractometer (section 3.2.2).

About 2.8 g of GeS_2 or 4.6 g of $GeSe_4$, in the form of a coarse powder, were contained in a cylindrical vanadium container of 6.8 mm inner diameter and 0.1 mm wall thickness (see section 4.3). The packing fractions were maximised by placing the cans in an ultrasonic bath for 10 minutes and the samples were fully illuminated by a rectangular beam, 35 mm high and 13 mm wide.

For the SANDALS experiment the samples were also in the form of a coarse powder. Glassy Se, $GeSe_3$, $GeSe_{1.5}$ (each $\approx$ 8 g) were loaded into cylindrical vana-

dium containers of 8.8 mm inner diameter and $GeSe_2$ ($\approx$ 4 g) was loaded into a cylindrical vanadium container of 6.8 mm inner diameter. Both containers had a wall thickness of 0.1 mm, and they were sealed with a greased O-ring after the samples were loaded. All of the sample handling was again carried out under a high purity argon gas atmosphere. To increase the packing fraction of the powder the samples were left in an ultrasonic bath for 10 minutes before fully illuminating them by a circular neutron beam of radius 1.6 cm.

Both the D4B and SANDALS diffraction experiments comprised the measurement of the diffraction patterns of the samples in their cans, the empty vanadium cans, nothing placed at the sample position and a vanadium rod of 6.08 mm (D4B) or 6.06 mm (SANDALS) diameter for normalisation purposes. On D4B the intensity for a Cd rod of 7 mm diameter placed at the sample position was also measured to perform the background correction at low angles. All of the diffraction experiments were carried out at room temperature, 26(1) °C.

The scattering lengths, nuclear and absorption cross-sections for Ge, Se and S are given in table 7.3.

Element	$\overline{b}$ [fm]	$\sigma_{free,coh}$ [barn]	$\sigma_{free,inc}$ [barn]	σ_{abs} (@ 1.798 Å) [barn]
Ge	8.185(20)	8.19(4)	0.18(7)	2.20(4)
Se	7.970(9)	7.78(2)	0.31(6)	11.7(2)
S	2.847(1)	0.9579	0.007(5)	0.53(1)

Table 7.3 : Scattering lengths and cross-sections of Ge, Se and S (Sears[20]). Their statistical errors are given in brackets.

The wavelength dependence of the total cross-sections $\sigma^{total}(\lambda) = \sigma_{free,sc} + \sigma_{abs}(\lambda)$ for the samples measured on SANDALS is shown in fig. 7.6. It was calculated by setting the scattering cross-section equal to the free nuclear cross-section for all wavelengths, and assuming that $\sigma_{abs} \propto \lambda$. The total cross-sections $\sigma^{total} = \sigma_{free,sc} + \sigma_{abs}(\lambda = 0.7047\text{Å})$ for $GeSe_4$ and GeS_2 are 11.99(8) barn and 3.86(3) barn respectively, and they are also indicated in fig. 7.6.

The total structure factors F(Q) for the glassy alloys can be written as,

$$F(Q) = A[S_{GeGe}(Q) - 1] + B[S_{GeY}(Q) - 1] + C[S_{YY}(Q) - 1] \qquad (7.1)$$

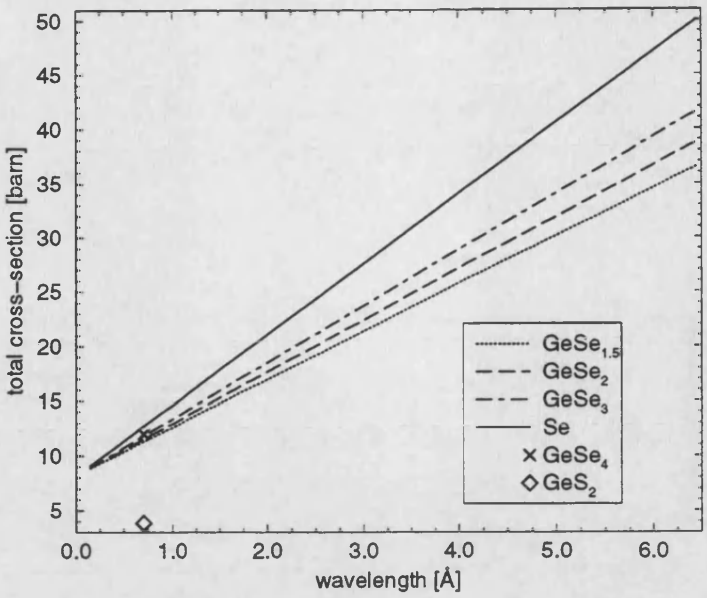

Figure 7.6: Calculated $\sigma^{\text{total}}(\lambda)$ for glassy Ge_xSe_{1-x} and GeS_2 alloys.

where $A = c_{Ge}^2 b_{Ge}^2$, $B = 2c_{Ge}c_Y b_{Ge}b_Y$ and $C = c_Y^2 b_Y^2$, and Y denotes Se or S. The weighting factors, low-r limits and sum-rule relations (see equations 4.2 and 4.3) are summarised in table 7.4.

Glass	A [barn]	B [barn]	C [barn]	G(0) [barn]	sum-rule [barn/Å^3]
Se	-	-	0.6352(14)	-0.6352(14)	-0.4100(9)
$GeSe_4$	0.02680(13)	0.2088(6)	0.4065(9)	-0.6421(11)	-0.4296(7)
$GeSe_3$	0.04187(20)	0.2446(7)	0.3573(8)	-0.6438(11)	-0.4308(7)
$GeSe_2$	0.0744(4)	0.2899(8)	0.2823(6)	-0.6467(11)	-0.4261(7)
$GeSe_{1.5}$	0.1072(5)	0.3131(8)	0.2287(5)	-0.6490(11)	-0.4367(7)
GeS_2	0.0744(4)	0.1036(3)	0.03603(3)	-0.2140(5)	-0.1517(4)

Table 7.4 : Weighting coefficients, low-r limits and sum-rule relations.

The total structure factors can also be expressed as a linear combinations of the Bhatia-Thornton (BT) number-number, $S_{NN}(Q)$, concentration-concentration, $S_{CC}(Q)$, and number-concentration, $S_{NC}(Q)$, partial structure factors (see section 2.10):

$$F(Q) = < b >^2 [S_{NN}(Q) - 1] + x(1-x)(\Delta b)^2 \left[\frac{S_{CC}(Q)}{x(1-x)} - 1\right] + 2 < b > (\Delta b) S_{NC}(Q) \tag{7.2}$$

where $< b >= xb_{Ge} + (1-x)b_Y$ and $\Delta b = (b_{Ge} - b_Y)$. The weighting factors are given in table 7.5, together with the mass densities and number densities of the investigated samples.

Glass	x	$< b >^2$ [barn^2]	x(1-x)$(\Delta b)^2$ [barn^2]	2< b > (Δb) [barn^2]	ρ [g/cm^3]	n_0 [Å^{-3}]
Se	0	0.6352(14)	-	-	4.288*	0.0327
$GeSe_4$	0.2	0.6421(11)	0.00007(2)	0.034(4)	4.372*	0.0339
$GeSe_3$	0.25	0.6438(11)	0.00009(2)	0.035(4)	4.355*	0.0339
$GeSe_2$	0.33	0.6467(11)	0.00010(2)	0.035(5)	4.26(1)$^+$	0.0334(1)
$GeSe_{1.5}$	0.4	0.6490(11)	0.00011(2)	0.035(5)	4.325*	0.0341
GeS_2	0.33	0.2140(5)	0.014(2)	0.494(1)	2.717(6)$^{\&}$	0.0359(8)

Table 7.5 : Weighting factors for the Bhatia-Thornton partial structure factors and further sample parameters. The density values were taken from *Borisova[10], $^+$Azoulay et al.[2] or $^{\&}$Feltz et al.[21].

The data analysis followed the procedure outlined in section 3.3.1 for the D4B data and section 3.3.2 for the SANDALS data. The packing fractions used to calculate the attenuation factors and multiple scattering corrections were 70 % for Se, 63 % for $GeSe_2$ and GeS_2, 65 % for $GeSe_{1.5}$, 54 % for $GeSe_4$ and 53 % for $GeSe_3$. The final F(Q)'s for the SANDALS data were obtained by merging all of the diffraction pattern from the 18 different detector banks. However the patterns from the low-resolution detector banks 8 - 10 were only used in the very low-Q region ($Q \leq Q_{FSDP}$, with Q_{FSDP} being the position of the maximum of the first sharp diffraction peak). Since the element Se has an absorption resonance at an energy of 2.6 eV (Soper et al.[22]), the diffraction patterns from the detector banks were truncated at Q-values well before any influence of this resonance could be observed. For all of the Q-space data sets it was tested that they tend to the correct high-Q limit, fulfil the sum-rule relations, and that they agree well with the back Fourier transforms of the corresponding real-space functions after the unphysical low-r oscillations have been set to their G(0) limiting values, given in table 7.4.

7.5 Results

7.5.1 Total structure factors:

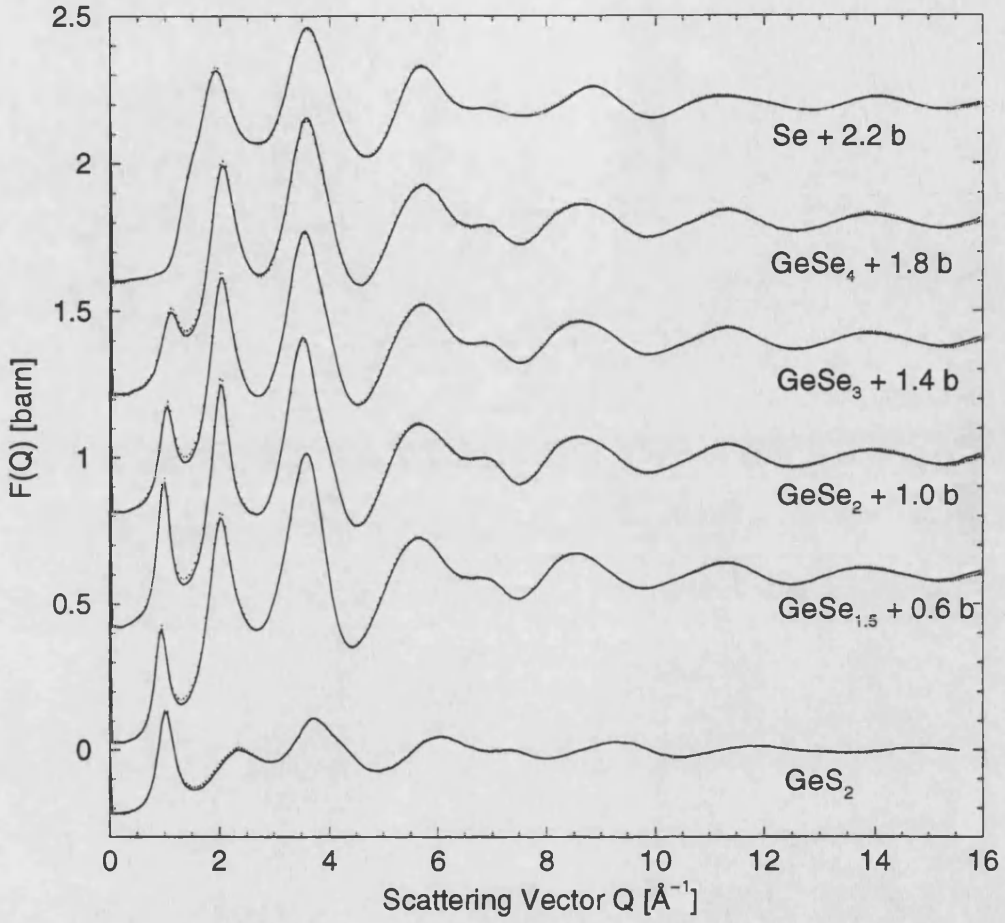

Figure 7.7: The measured total structure factors for several Ge_xSe_{1-x} glasses and glassy GeS_2. The bars give the statistical errors for each data point and the solid curves are the back Fourier transforms of the G(r)'s given by the solid curves in figure 7.8.

The measured total structure factors, F(Q), for all of the investigated samples and their real-space representations, G(r), are shown in figures 7.7 and 7.8 respectively. It is seen from these two figures that with increasing Ge content from $x = 0$ to $x = 0.4$ there are changes in the short range order (G(r)'s) as well as in the intermediate range order (FSDPs in the F(Q)'s). These changes will be discussed in detail in section 7.6.

As the total structure factor of $GeSe_2$ was measured on both the diffractometer

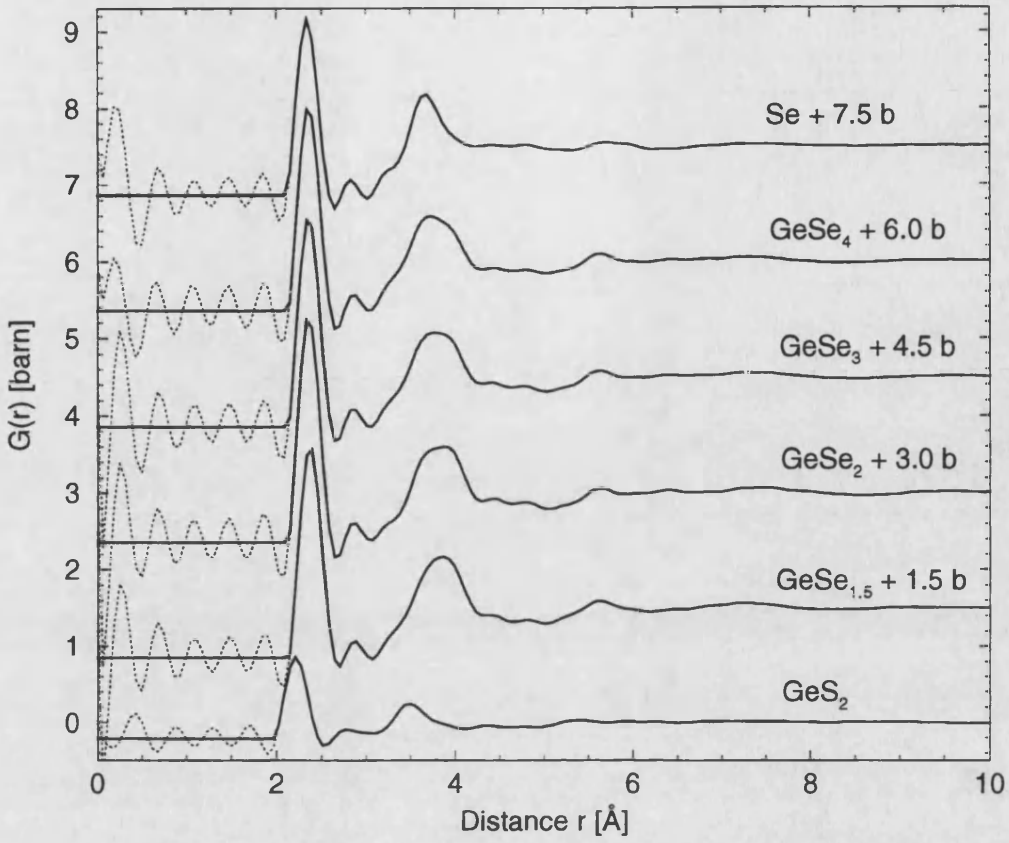

Figure 7.8: Measured G(r)'s for several Ge_xSe_{1-x} glasses and glassy GeS_2. The solid curves give the real-space representation of the total structure factors given by the error bars in figure 7.7 and the dotted curves for approximately $r \leq 2.09$ Å show the corresponding unphysical low-r oscillations.

D4B at the reactor source of the ILL (see chapter 6) and on the pulsed source diffractometer SANDALS, which at the time of the experiment had been newly equipped with four detector banks in the range $29° \leq 2\theta \leq 41°$, a short note on the correspondence of both instruments can be made. The two investigated samples came from different batches, but were prepared using exactly the same procedure. Figure 7.9 compares the measured F(Q) and G(r) functions.

Although the differences are small they exceed the statistical errors on the data points. There is no indication that any of the differences are due to the different resolution functions of the instruments, since e.g. the width of the FSDP measured on both instruments is the same. Nevertheless the measured differences do not have any quantifiable effect on the coordination numbers and peak-positions at the total

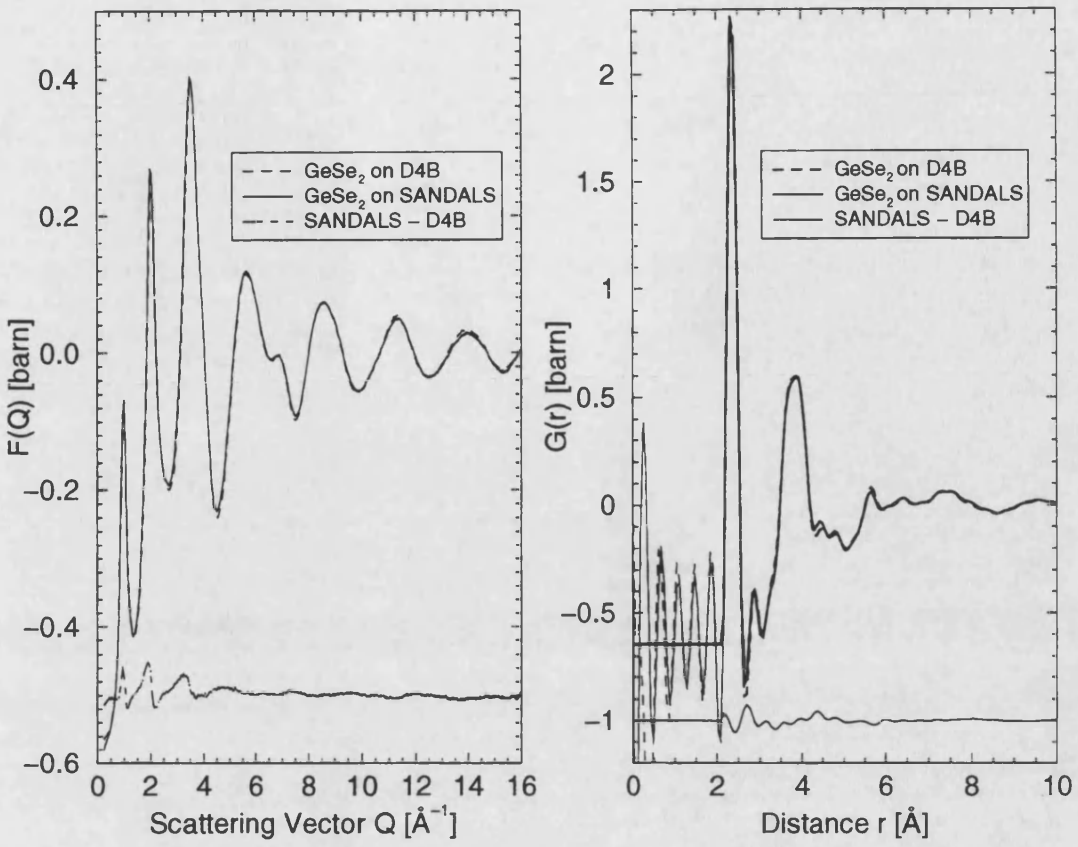

Figure 7.9: Comparison of the measurements for $GeSe_2$ in reciprocal and real-space. The total structure factor for the SANDALS data is drawn as solid curve together with its statistical errors that for the D4B data without its errors and as a dashed curve. Both F(Q)'s were truncated at the same Q-value, $Q_{max} = 16\,Å^{-1}$. G(r) from the D4B data is given by the dashed curve, for the SANDALS data by the solid curve. The differences of the SANDALS data minus the D4B data are also included in the graphs.

structure factor level.

The structure of GeS_2 will now be compared with the structure of $GeSe_2$ at the total structure factor level. Figure 7.10 shows that both total structure factors comprise the similar four peak structure, with a FSDP at 1.02(2) Å^{-1} and 0.99(2) Å^{-1} for GeS_2 and $GeSe_2$ respectively. The FSDP is followed by two peaks of increasing height and a fourth peak, at 6.00(2) Å^{-1} for GeS_2 and 5.95(2) Å^{-1} for $GeSe_2$, which has a shoulder on its high-Q side. The larger relative height of the FSDP for GeS_2 demonstrates that it also arises primarily from intermediate range Ge-Ge correlations. Since the weighting of these correlations in GeS_2 is much

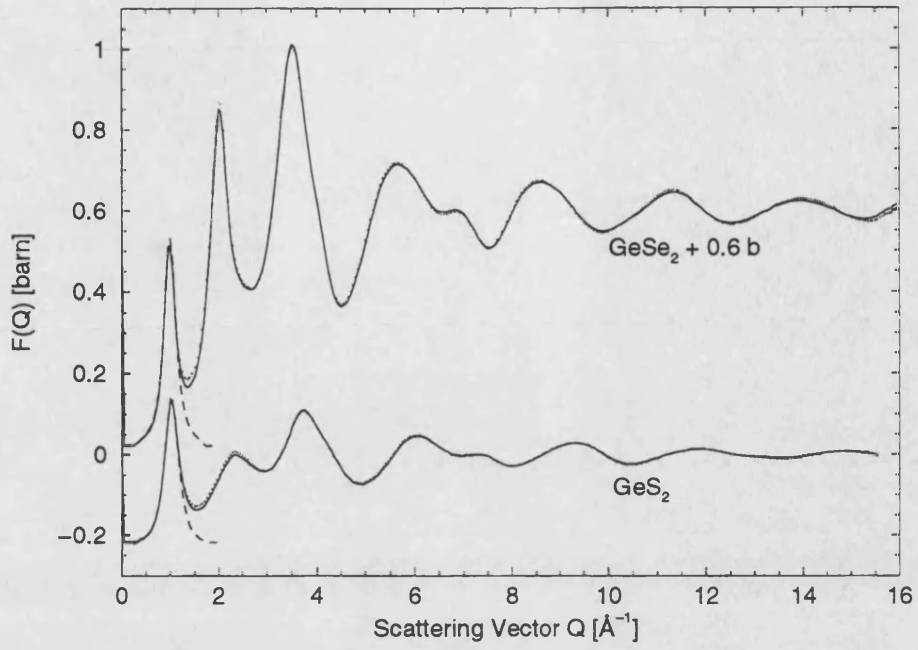

Figure 7.10: Total structure factors of GeS_2 and $GeSe_2$ shown by the error bars, and their Fourier back transforms after the unphysical low-r oscillations have been removed. The dashed curves show the FSDPs obtained by the symmetrisation of the peaks around their maximum.

higher than in $GeSe_2$ ($\frac{A}{A+B+C} = 35\,\%$ for GeS_2 and only $12\,\%$ for $GeSe_2$, see table 7.4) they give rise to a peak in F(Q) with a higher relative intensity.

GeS_2 and $GeSe_2$ both melt from a monoclinic C^5_{2h} high temperature form (Hulliger[23]), which has already been described in chapter 6 for $GeSe_2$. The similarity between GeS_2 and $GeSe_2$ is also reflected in their total pair distribution functions, G(r), shown in fig. 7.11. This close correspondence has also been reported by Feltz et al.[21] on the basis of total x-ray diffraction experiments. The first peak with a maximum at 2.35(2) Å for $GeSe_2$ and at the lower value of 2.21(2) Å for GeS_2, reflecting the smaller covalent radius of S compared to Se, comprises the Ge-Y (Y = Se or S) nearest neighbours. For $GeSe_2$ it is shown in chapter 6 that there are also contributions from homopolar Ge-Ge and Se-Se bonds to this first peak. The area under the first peak for GeS_2 accounts very well for the same number of nearest neighbours as found for glassy $GeSe_2$ in the isotopic substitution experiment. If $\overline{n}^{S}_{Ge} = 3.7$ and $\overline{n}^{Ge}_{Ge} = 0.25$ are assumed as measured for $GeSe_2$, a $\overline{n}^{S}_{S} = 0.18$ is obtained that agrees with the measured $\overline{n}^{Se}_{Se} = 0.20(5)$ (table 6.8)

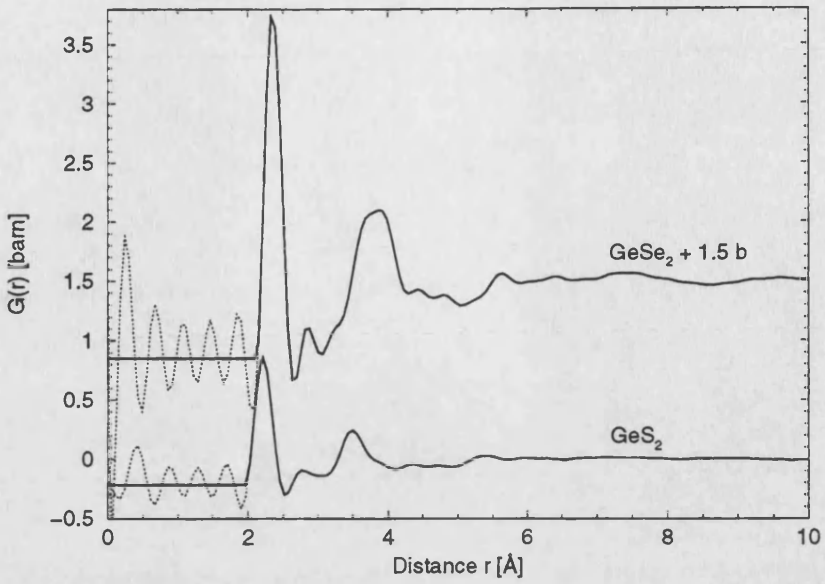

Figure 7.11: Total pair distribution functions, G(r), measured for GeS_2 and $GeSe_2$. The dotted curves show the unphysical low-r oscillations.

and see figure 7.12. Also it can be seen in this figure that the neutron weighted Ge-Se contributions alone are insufficient to account for all of the intensity under the first peak in GeS_2. However, if the homopolar bonds are included a good account is given of the first measured peak in G(r) for GeS_2. Using the second peaks at 3.49(2) Å (GeS_2) and 3.88(2) Å ($GeSe_2$), the ratio r_2/r_1, where r_i is the position of the maximum of the i^{th} peak in G(r), can be calculated. It is 1.579 and 1.651 for GeS_2 and $GeSe_2$ respectively, i.e. it is just below and above the value of $\sqrt{8/3} = 1.633$ expected for a perfect tetrahedron. The parameters describing the total structure factors and total pair distribution functions of GeS_2 and $GeSe_2$ are summarised in table 7.6.

To summarise, it has been found that the structures of glassy GeS_2 and $GeSe_2$ are very much alike, comprising $GeS_{4/2}$ and $GeSe_{4/2}$ tetrahedral units as their basic building blocks like in the crystalline structures from which they melt. By comparison with the results obtained from the isotopic substitution measurements on $GeSe_2$, the existence of homopolar bonds in GeS_2 can be inferred.

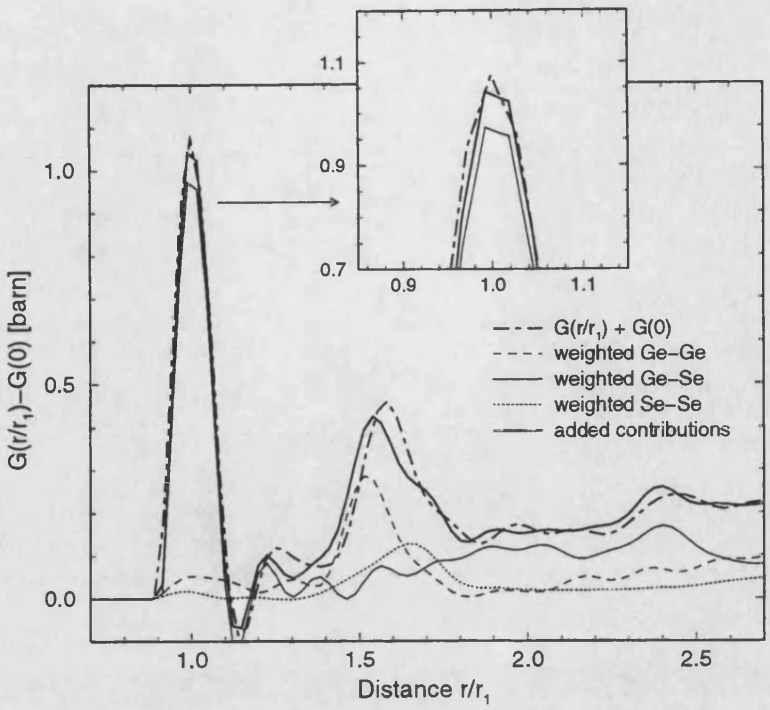

Figure 7.12: $G(r/r_1)$ for glassy GeS_2 shifted up by -G(0) (thick solid curves) compared with the representation obtained using the measured partial pair distribution functions for $GeSe_2$, see chapter 6, after scaling them accordingly to the weighting factors appropriate for GeS_2, see table 7.4. It is seen that the Ge-Ge homopolar bonds are necessary if a good account is to be given of the first peak (see small inset).

Glass	Position of FSDP [$Å^{-1}$]	Height of FSDP	FWHM of FSDP [$Å^{-1}$]	r_1 [Å]	r_2/r_1	$\overline{n}^{Y}_{Ge}$
$GeSe_2$	0.99(2)	0.509(5)	0.30(1)	2.35(2)	1.651	4.1(1)
GeS_2	1.02(2)	0.355(5)	0.35(1)	2.21(2)	1.579	4.1(1)

Glass	Q_2 [$Å^{-1}$]	$\frac{Q_1}{Q_2}$	$\frac{Q_3}{Q_2}$	$\frac{Q_4}{Q_2}$	$F(Q_2)$ [barn]	$\frac{F(Q_1)}{F(Q_2)}$	$\frac{F(Q_3)}{F(Q_2)}$	$\frac{F(Q_4)}{F(Q_2)}$
$GeSe_2$	2.02(2)	0.49	1.74	2.80	0.269(1)	-0.258	1.497	0.441
GeS_2	2.35(2)	0.43	1.58	2.55	0.009(1)	15.3	12.1	5.4

Table 7.6 : Parameters describing the F(Q) and G(r) functions for glassy $GeSe_2$ and GeS_2. The FSDP was defined by reflecting its low-Q part about Q_1. r_i (i = 1, 2, 3 or 4) denotes the position of the maximum of the i^{th} peak in G(r), Q_i the i^{th} maximum in F(Q) and $F(Q_i)$ its value. $\overline{n}^{Y}_{Ge}$ calculated under the assumption that only Ge-Y correlations contribute to the first peak in G(r) and by integrating over 2.09 Å $\leq r \leq$ 2.61 Å for $GeSe_2$ and 1.96 Å $\leq r \leq$ 2.52 Å for GeS_2.

7.5.2 Bhatia-Thornton number-number partial structure factors

The weighting factors for the $S_{NN}(Q)$ in table 7.5 show that the measured total structure factors for the Ge_xSe_{1-x} alloys are dominated by the number-number partial structure factor $S_{NN}(Q)$. Therefore $S_{NN}(Q)$ is set equal to $F(Q) < b >^{-2} +1$ and plotted in figure 7.13 as a function of Qr_1, where r_1 is the position of the maximum of the first peak in $g_{NN}(r)$. Many binary glasses exhibit a characteristic three-peak structure (Wright et al.[7]) for $0 \leq Qr_1 \leq 10$, where the first one is the FSDP, see section 7.1.

Table 7.7 summarises the parameters defining the $S_{NN}(Q)$ and $g_{NN}(r)$ functions for the glassy Ge-Se system and GeS_2.

Glass	Position of FSDP [Å^{-1}]	Height of FSDP	FWHM of FSDP [Å^{-1}]	r_1 [Å]	r_2/r_1	$\overline{n}$	$\overline{n}^{Se}_{Ge}$
Se	-	-	-	2.34(2)	1.573	2.10(10)	-
$GeSe_4$	1.12(2)	0.455(5)	0.44(1)	2.35(2)	1.583	2.55(10)	6.3(1)
$GeSe_3$	1.04(2)	0.586(5)	0.34(1)	2.35(2)	1.609	2.62(10)	5.2(1)
$GeSe_2$	0.99(2)	0.787(5)	0.30(1)	2.35(2)	1.651	2.78(10)	4.1(1)
$GeSe_{1.5}$	0.94(2)	0.618(5)	0.29(1)	2.37(2)	1.629	2.79(10)	3.5(1)

Glass	Q_2 [Å^{-1}]	$\frac{Q_1}{Q_2}$	$\frac{Q_3}{Q_2}$	$\frac{Q_4}{Q_2}$	$S_{NN}(Q_2)$	$\frac{S_{NN}(Q_1)}{S_{NN}(Q_2)}$	$\frac{S_{NN}(Q_3)}{S_{NN}(Q_2)}$	$\frac{S_{NN}(Q_4)}{S_{NN}(Q_2)}$
Se	1.92(2)	-	1.88	2.96	1.196(1)	-	1.171	1.012
$GeSe_4$	2.04(2)	0.55	1.75	2.81	1.325(2)	0.414	1.161	0.909
$GeSe_3$	2.03(2)	0.51	1.75	2.81	1.355(1)	0.501	1.155	0.882
$GeSe_2$	2.02(2)	0.49	1.74	2.80	1.416(1)	0.631	1.146	0.836
$GeSe_{1.5}$	2.02(2)	0.47	1.78	2.80	1.325(1)	0.554	1.234	0.904

Table 7.7 : Parameters describing the $S_{NN}(Q)$ and $g_{NN}(r)$ functions for the glassy Ge-Se system. The FSDP was defined by reflecting its low-Q part about Q_1. r_i (i = 1, 2, 3 or 4) denotes the position of the maximum of the i^{th} peak in $g_{NN}(r)$, Q_i the i^{th} maximum in the reciprocal-space function and $S_{NN}(Q_i)$ its value. $\overline{n} = 4\pi n_0 \int_{r_1}^{r_2} r^2 g_{NN}(r)dr = c_{Ge}(\overline{n}^{Ge}_{Ge} + \overline{n}^{Se}_{Ge}) + c_{Se}(\overline{n}^{Se}_{Se} + \overline{n}^{Ge}_{Se})$ is the average coordination number. It was calculated by integrating over the area defined by the two minima on either side of $g_{NN}(r)$, i.e. 2.09 Å $\leq r \leq$ 2.61 Å. $\overline{n}^{Se}_{Ge}$ was calculated under the assumption that only Ge-Se correlations contribute to this first peak.

The data fulfil the obligational inequality relation, $S_{NN}(Q) \geq 0$ (see e.g. Bhatia

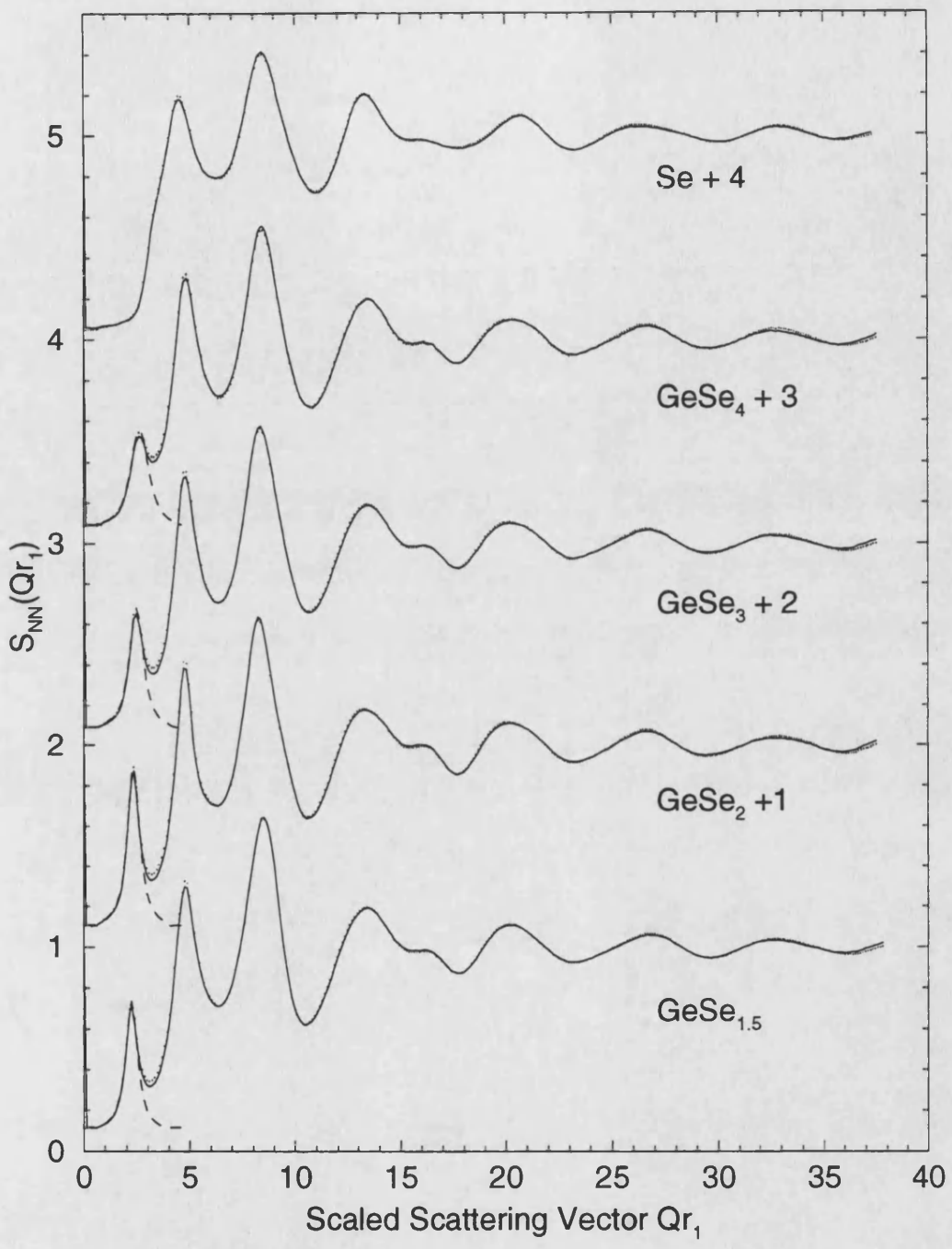

Figure 7.13: Measured $S_{NN}(Q)$'s for glassy Ge_xSe_{1-x} alloys plotted as a function of Qr_1, where r_1 is the position of the maximum of the first peak in $g_{NN}(r)$. The vertical lines give the statistical errors on each data point and the solid curves are the back Fourier transforms of the corresponding $g_{NN}(r)$ functions shown in fig. 7.14, after the unphysical low-r oscillations are set to their calculated limiting value. The dashed curves represent the FSDPs.

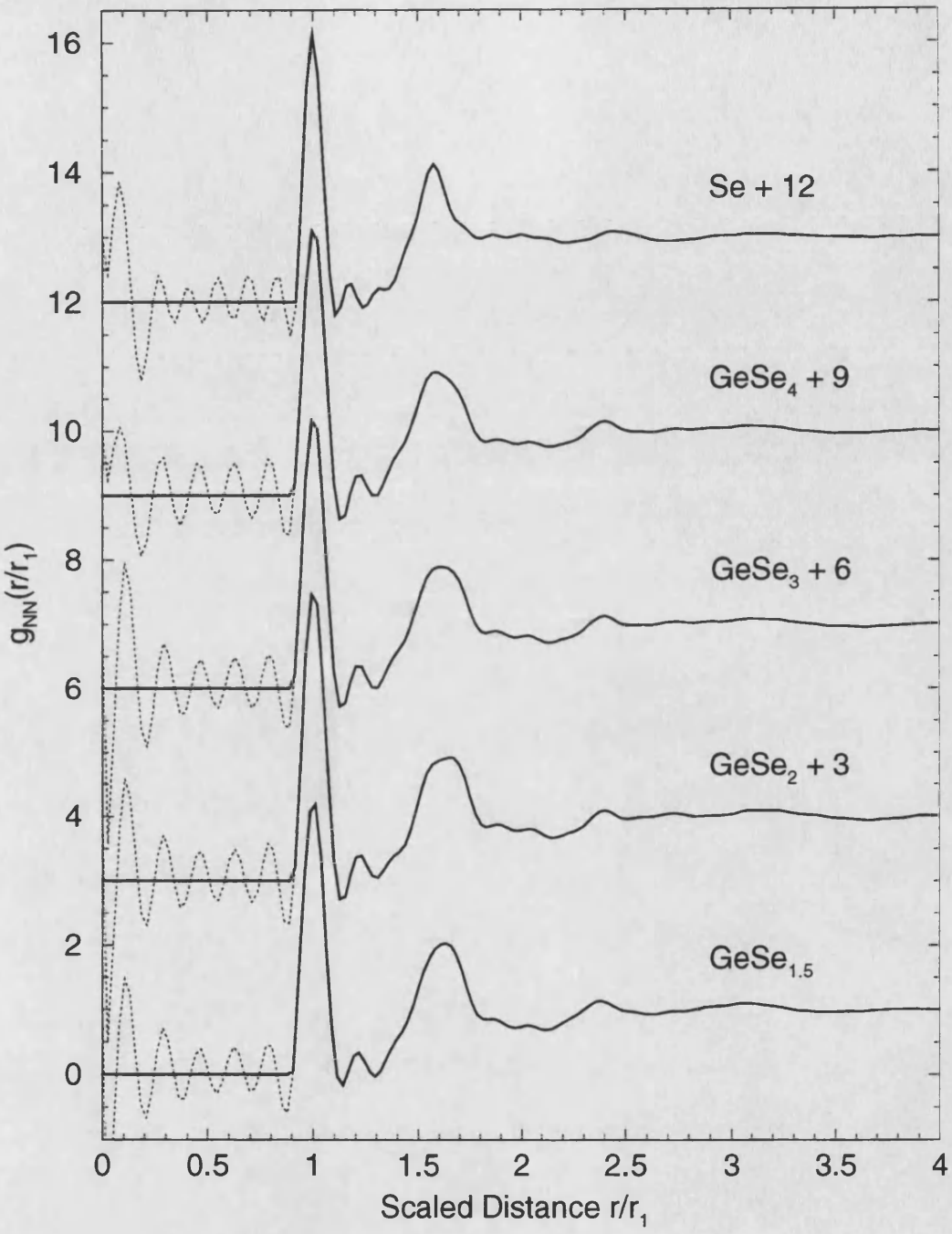

Figure 7.14: The $g_{NN}(r)$ plotted as a function of r/r_1, where r_1 is the position of the maximum of the first peak. The dotted curves show the unphysical low-r oscillations obtained by Fourier transforming the $S_{NN}(Q)$'s given in fig. 7.13.

& Thornton[24]), and agree well with the back Fourier transforms of the corresponding $g_{NN}(r)$'s, shown in figure 7.14, after the unphysical low-r oscillations are set to their calculated limiting value $g_{NN}(0) = 0$.

7.6 Discussion

7.6.1 Number-number partial structure factor, $S_{NN}(Q)$

The most apparent change with increasing Ge content happens in the FSDP at about 1 $Å^{-1}$. With the addition of 20 % Ge to pure Se a new intermediate range ordering (IRO) develops, as evidenced by the appearance of the FSDP. The intensity of the FSDP increases with increasing Ge content and reaches its maximum for $x = 0.33$, then it decreases again. All of the $S_{NN}(Q)$ for glasses containing Ge show the characteristic three-peak structure for $0 \leq Qr_1 \leq 10$ discussed in the introduction. The second and third peaks show a slight tendency to increase in height as x is increased to 0.33, and they tend to shift closer together. The second peak for $GeSe_{1.5}$ does not shift relative to $GeSe_2$ and has a lower intensity (see table 7.7).

7.6.2 Short range order (SRO)

The first peak in $g_{NN}(r)$ shifts marginally to larger values of r with increasing Ge content, from 2.34(2) Å for pure Se to 2.37(2) Å for $GeSe_{1.5}$. The second peak, defined by a maximum at 3.68(2) Å, i.e. at $r_2/r_1 = 1.57$ for Se, becomes notably broader with the addition of Ge and its maximum shifts to higher r-values. The peak at 5.64(2) Å, i.e. at $r_3/r_1 = 2.4$, does not exhibit any shifts with increasing x and has the highest intensity for the $GeSe_4$ composition. These observed trends are in agreement with the recent neutron results by Rao et al.[18].

Table 7.8 summarises the parameters defining the SRO for the investigated samples and gives a comparison with literature values.

Sample	r_1 Å	r_2/r_1	$\overline{n}$	Probe, Method	Preparation	Reference
Se	2.34(2)	1.573	2.10(10)	neutrons	melt qu.	present work*
Se	2.36	-	2.0	neutrons	l. 250 °C	Maruyama et al.[26]*
Se	2.350(5)	-	1.8(2)	EXAFS	melt qu.	Zhou et al.[17]
Se	2.34(1)	1.603	2.2(1)	electrons	evaporation	Uemura et al.[15]**
$GeSe_4$	2.35(2)	1.583	2.55(10)	neutrons	melt qu.	present work*
$GeSe_4$	2.39(3)	1.611	2.78	x-rays	melt qu.	Hafiz et al.[16]**
$GeSe_4$	2.38(1)	1.609	2.38(20)	x-rays	melt qu.	Malaurent et al.[27]***
$GeSe_4$	2.368(5)[a]	-	2.4(2)	EXAFS	melt qu.	Zhou et al.[17]
	2.35(2)[b]					
$GeSe_4$	2.34(1)	1.608	2.4(1)	electrons	evaporation	Uemura et al.[15]**
$GeSe_3$	2.35(2)	1.609	2.62(10)	neutrons	melt qu.	present work*
$GeSe_3$	2.378(5)	1.623	2.68	neutrons	melt qu.	Rao et al.[18]**
$GeSe_3$	2.37(3)	1.624	2.76	x-rays	melt qu.	Hafiz et al.[16]**
$GeSe_3$	2.38(1)	1.618	2.43(20)	x-rays	melt qu.	Malaurent et al.[27]***
$GeSe_3$	2.35[a]	1.638	2.5	AWAXS	melt qu.	Armand
	2.38[b]					et al.[28]***
$GeSe_3$	2.366(5)[a]	-	2.5(2)	EXAFS	melt qu.	Zhou et al.
	2.35(2)[b]					[17]
$GeSe_2$	2.35(2)	1.651	2.78(10)	neutrons	melt qu.	present work*
$GeSe_2$	2.386(5)	1.630	2.77	neutrons	melt qu.	Rao et al.[18]**
$GeSe_2$	2.385	1.648	2.74	neutrons	melt qu.	Susman et al.[25]**
$GeSe_2$	2.36	-	2.5	neutrons	l. 800 °C	Maruyama et al.[26]*
$GeSe_2$	2.39(2)	1.607	2.6(1)	neutrons	l. 784 °C	Salmon & Liu[1]**
$GeSe_2$	2.364(5)[a]	-	2.5(2)	EXAFS	melt qu.	Zhou et al.[17]
$GeSe_2$	2.37(3)	1.646	2.8(4)	DAS	melt qu.	Fuoss et al.[29]***
$GeSe_2$	2.34(1)	1.613	2.63	electrons	evaporation	Uemura et al.[15]**
$GeSe_{1.5}$	2.37(2)	1.629	2.79(10)	neutrons	melt qu.	present work*
$GeSe_{1.5}$	2.392(5)	1.651	2.92	neutrons	melt qu.	Rao et al.[18]**
$GeSe_{1.5}$	2.41(2)	1.618	2.8(2)	neutrons	l. 784 °C	Salmon & Liu[1]**
$GeSe_{1.5}$	2.39(1)	1.619	2.7(2)	x-rays	melt qu.	Malaurent et al.[27]***
$GeSe_{1.5}$	2.365(5)[a]	-	2.7(2)	EXAFS	melt qu.	Zhou et al.[17]
	2.41(2)[c]					
$GeSe_{1.5}$	2.38(2)	1.616	2.65(10)	electrons	evaporation	Uemura et al.[15]**
GeSe	2.52(2)	1.452	3.5(3)	neutrons	l. 727 °C	present work*
GeSe	2.52(2)	1.520	3.6(3)	neutrons	l. 728 °C	Salmon & Liu[1]**

Table 7.8 : Parameters obtained for samples in the Ge-Se system (only the investigated com-

positions are included). r_1 and r_2 are the maximum positions of the first and second peak in $g_{NN}(r)^*$, $r\,g_{NN}(r)^{**}$ or $r^2\,g_{NN}(r)^{***}$ and 'l.' stands for 'liquid at'.

[a] : r_{GeSe}, [b] : r_{SeSe} and [c] : r_{GeGe}

AWAXS : anomalous wide angle x-ray scattering,

EXAFS : extended x-ray absorption fine structure

DAS : differential anomalous scattering.

Se :

Our structure factor for pure amorphous Se exhibits the typical features measured previously (Johnson et al.[30]). In real-space it shows a nearest-neighbour distance of 2.34(2) Å that agrees, within the error, with the values of 2.359(5) Å and 2.346 Å measured by Johnson et al.[30] using neutron diffraction and EXAFS respectively. The nearest-neighbour coordination number of 2.1(1) obtained from the integration range of $2.09 \leq r[Å] \leq 2.61$ is consistent with the value of 2.03 given by Johnson et al.[30], and with a $(Se)_n$ chain structure, as found in the trigonal crystalline form of Se.

$GeSe_4$:

With the addition of 20 % Ge to pure Se to give $GeSe_4$, the first peak in $g_{NN}(r)$ moves to 2.35(2) Å. This can be explained by the appearance of the tetrahedral $GeSe_{4/2}$ units, having a Ge-Se bonding distance of 2.36(2) Å as measured for glassy $GeSe_2$ (see section 6.4.4). The first peak therefore comprises both Ge-Se and Se-Se correlations on the basis of the '8-N' rule. It is not possible to unambiguously identify the relative contributions from these correlation functions. However Zhou et al.[17] found in their EXAFS measurements on bulk-quenched $GeSe_4$ coordination numbers $\overline{n}_{Ge}^{Se} = 4.1(2)$ and $\overline{n}_{Se}^{Se} = 0.7(2)$. Our data gives similar results, i.e. by fixing $\overline{n}_{Ge}^{Se}$ at 4.1 a slightly higher Se-Se coordination number of $\overline{n}_{Se}^{Se} = 1.1(1)$ is obtained by integrating over the first peak. Very recent first-principles molecular dynamics simulations of liquid $GeSe_4$ by Haye et al.[31] gave coordination numbers of $\overline{n}_{Se}^{Ge} = 3.87$, $\overline{n}_{Se}^{Se} = 1.04$ and $\overline{n}_{Ge}^{Ge} = 0.06$, which yields an average coordination number of $\overline{n} = 2.40$, which is outside the errors of our measured value of $\overline{n} = 2.55(10)$. If we fix $\overline{n}_{Ge}^{Se}$ at 4.0 we obtain $\overline{n}_{Se}^{Se} = 1.16(10)$ which agrees within the errors with

the value of 1.3(2) found by Rao et al.[18] and also with the values expected using the chemically ordered continuous random network (COCRN).

To explain the shift in the second peak in $g_{NN}(r)$ towards higher-r values with the addition of germanium, the second nearest neighbour Se-Se distance in our measured distribution function for Se at r = 3.68(2)Å is compared with the Se-Se distance within the $GeSe_{4/2}$ tetrahedron of 3.89(2)Å (chapter 6). Therefore the observed shift can be understood in terms of the appearance and increase in the number of $GeSe_{4/2}$ units.

As the partial structure factors for glassy $GeSe_2$ were measured (chapter 6) and the fundamental building blocks of $GeSe_2$, the $GeSe_{4/2}$ units, are also apparent in $GeSe_4$, the Faber-Ziman partial pair distribution functions are used to construct the total pair distribution function for $GeSe_4$, see figure 7.15, by applying suitable weighting factors (table 7.4). From the regions where the measured and created G(r)'s disagree it becomes obvious that the Se-Se distribution function describing $GeSe_2$ cannot be used to express the Se-Se correlations in $GeSe_4$. Additionally, using the measured distribution function for pure Se to describe the Se-Se correlations does not represent the measured G(r) for $GeSe_4$. However it can be seen from figure 7.15 that by using a combination of the two it should be possible to reproduce the short range structure of $GeSe_4$. This is consistent with the Raman results of Wang et al.[4] which indicate that for a Ge content of $0.18 \leq x \leq 0.25$ glassy Ge_xSe_{1-x} comprises both $(Se)_n$ chains and $GeSe_{4/2}$ tetrahedra.

$GeSe_3$:

For $GeSe_3$ the average nearest-neighbour coordination number increases to 2.62(10) and the maximum of the second peak in $g_{NN}(r)$ shifts to slightly higher values of r. Figure 7.15 shows that by using the weighted partial pair distribution functions measured for $GeSe_2$, a better agreement with the total pair distribution function is obtained than for $GeSe_4$. This indicates that the number of $GeSe_{4/2}$ tetrahedra increases with increasing Ge content (up to x = 0.33) and a higher percentage of the Se atoms are arranged in these units. This has also been confirmed by Raman measurements (e.g. Wang et al.[4]). The first peak in $g_{NN}(r)$ is again assumed to comprise Ge-Se and Se-Se correlations. Zhou et al.[17] obtained from their EXAFS measurements coordination numbers of $\overline{n}_{Ge}^{Se} = 4.1(2)$ and $\overline{n}_{Se}^{Se} = 0.4(2)$ whereas our

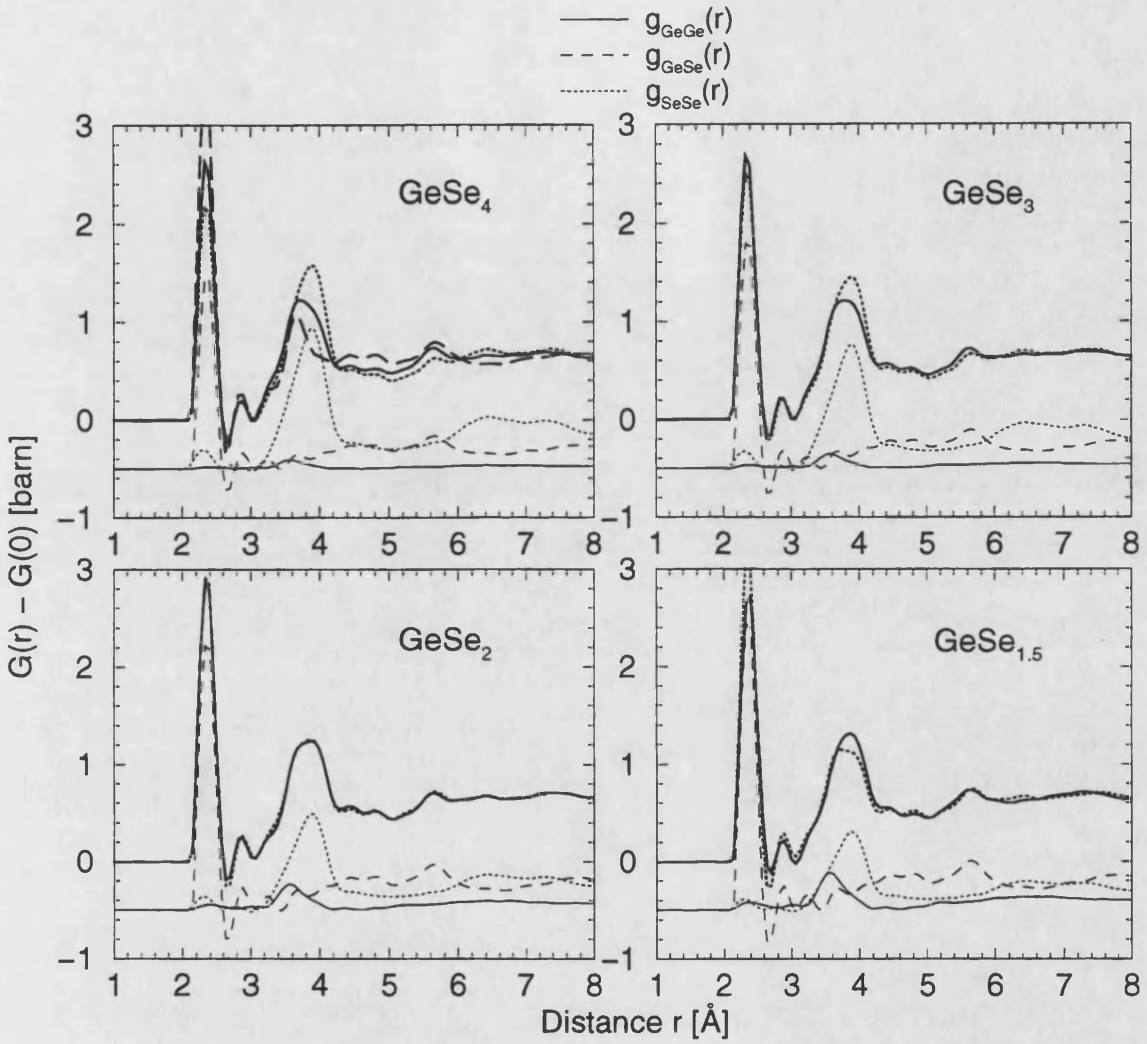

Figure 7.15: Measured pair distribution functions for Ge_xSe_{1-x} (thick solid curves) compared with the functions obtained by a linear combination of the spline fitted pair distribution functions measured for glassy $GeSe_2$ which have been weighted according to the composition (thick dotted curves). For $GeSe_4$ the reconstruction is also shown when the Se-Se correlations are described by the measured distribution function for pure Se (thick long dashes). The neutron weighted contributions are shifted down by 0.5 barn for clarity.

data by fixing $\overline{n}_{Ge}^{Se}$ at a value of 4.1 and integrating over the first peak in $g_{NN}(r)$ yields a higher $\overline{n}_{Se}^{Se}$ of 0.7(1). If we compare with the COCRN and fix $\overline{n}_{Ge}^{Se}$ at 4.0, we obtain $\overline{n}_{Se}^{Se} = 0.8(1)$, which is close to the expected value of $0.\overline{6}$ (see Elliott[32]).

$GeSe_2$:

The structure of $GeSe_2$ was discussed in detail in chapter 6. Glassy $GeSe_2$ comprises approximately 34 % of edge sharing $GeSe_{4/2}$ tetrahedral units with a Ge-Se coordination number of 3.8(1) and a ratio r_{GeSe}/r_{SeSe} of the bond distances of 0.608 which is close to the ratio $\sqrt{3/8} = 0.612$ expected for perfect tetrahedral coordination. The substantial number of Ge-Ge and Se-Se homopolar bonds in which about 24 % of the Ge and 20 % of the Se are involved show that $GeSe_2$ cannot be treated as a chemically ordered network (cf. Elliott[32]).

$GeSe_{1.5}$:

A further increase of the Ge content to x = 0.4 to give $GeSe_{1.5}$ causes the first peak in $g_{NN}(r)$ to shift to the higher value of r = 2.37(2)Å which can be understood by the disappearance of Se-Se homopolar bonds and an increase in Ge-Ge homopolar bonds which have a longer bond distance $r_{GeGe} = 2.42$Å (see table 6.8). Additionally the average coordination number for the first peak increases to 2.79(10). If we assume $\overline{n}_{Ge}^{Ge} = 1$ and $\overline{n}_{Se}^{Se} = 0$ our data yield a $\overline{n}_{Ge}^{Se} = 3.1(1)$ which agrees within the errors with the value expected from the COCRN model and exactly with the value found by Rao et al.[18] and also with the $\overline{n}_{Ge}^{Ge} = 1.0(2)$ and $\overline{n}_{Ge}^{Se}$ of about 3 found by Zhou et al.[17]. Therefore we agree with them in suggesting that each Ge atom has on average three Se atoms and one Ge atom as its nearest neighbours. This gives support to the presence of $Ge_2Se_{6/2}$ ethane-like units, the occurrence of which was also supported by the x-ray emission spectroscopy investigations by Mamedov et al.[33].

7.6.3 Intermediate range order

The FSDP can be viewed as a signature of the atomic intermediate range order (IRO) present in the system. Using the properties of Fourier transforms, its position Q_1 is related to intermediate ranged oscillations in real-space of a periodicity given

by $2\pi/Q_1$. Its full width at half maximum (FWHM) and intensity define the modulation of those oscillations (Salmon[34]). For example a high FSDP indicates that the oscillations in real-space have a large amplitude, and a narrow peak is the manifestation of a slow decay of these oscillations. A quantity often called the 'coherence length L' (e.g. Rao et al.[18]) can be defined by $L = 2\pi/FWHM$.

The FSDPs in our measured data were obtained by symmetrising the first peaks around their maxima. They are shown in figure 7.13 and their positions, intensities and FWHMs are summarised in table 7.7. With increasing Ge content the position of the FSDPs shift to lower values of Q, from 1.12Å^{-1} for $GeSe_4$ to 0.94Å^{-1} for $GeSe_{1.5}$. This indicates that the characteristic periodicity of the intermediate range oscillations increases with increasing Ge content. This trend was also found by Rao et al.[18]. A comparison of our data with these results can be found in table 7.9.

	$GeSe_4$	$GeSe_3$	$GeSe_2$	$GeSe_{1.5}$	
$2\pi/Q_1$	5.61(10)	6.04(11)	6.35(13)	6.68(14)	present data
[Å]	5.74	-	6.36	6.51	Rao et al.[18]
$L = 2\pi/FWHM$	14.2(3)	18.4(5)	21.2(7)	21.7(7)	present data
[Å]	(20.9)	-	(28.6)	(28.6)	Rao et al.[18] *)

Table 7.9 : Parameter defining the FSDPs for the Ge-Se system. Our results are compared with the recent measurements of Rao et al.[18]. *) Rao et al.[18] extrapolated the low-Q part of the second peak into the FSDP region. The FSDP was then obtained by subtracting this background. Hence the method used is different to ours.

The coherence length L increases for our samples up to $x = 0.4$, which indicates that the IRO is stronger in glasses with $x = 0.33$ and $x = 0.4$ than in glasses with a lower Ge content. By contrast, in liquid $GeSe_2$ and $GeSe_{1.5}$, there is no significant change in the position and width of the FSDP between these two compositions (Salmon & Liu[1]). However a decrease in intensity of the FSDP when x is increased from 0.33 to 0.4 was found in both the liquid and glassy states. In our investigation the intensity of the FSDP increases up to the $GeSe_2$ composition ($x \leq 0.33$) with increasing Ge content. A further increase in x leads to a reduction of the height of the FSDP. Thus it is concluded that the underlying features of the IRO have the

highest amplitude for the $GeSe_2$ composition.

The measured Faber-Ziman partial structure factors for $GeSe_2$, shown in chapter 6, prove that the FSDP primarily arises from the Ge-Ge correlations, i.e. from the relative positions of the $GeSe_{4/2}$ tetrahedron centers. Thus it is understandable that the intensity of the FSDP reaches its maximum for $GeSe_2$, where the maximum number of these tetrahedra is found, and with a further increase in the Ge content the FSDP and the associated intermediate range order becomes weaker, until at GeSe it is lost (chapter 4).

7.7 Conclusions

- Our DSC measurements show that the glass transition temperature, T_g, increases with the germanium content for $x \leq 0.33$ and decreases with higher germanium content.

- Changes in the topology of Ge_xSe_{1-x} glasses in the range $0 \leq x \leq 0.4$ are clearly evident, both in reciprocal and in real-space, although the nearest neighbour bonding remains characterised by coordination numbers for Ge and Se of 4 and 2 respectively, which is independent of the concentration.

- Compositions with $0.2 \leq x \leq 0.4$ are characterised by a number-number partial structure factor $S_{NN}(Qr_1)$ that shows the typical three-peak structure for $0 \leq Qr_1 \leq 10$.

- The intermediate range order changes in the investigated compositions. The amplitude increases with increasing Ge content up to $x = 0.33$ and decreases again with a further increase of the Ge content up to $x = 0.4$, however the periodicity and coherence length increase up to $x = 0.4$.

- The average coordination number $\overline{n}$ and the nearest neighbour distance r_1 increase with increasing x, giving rise to a slightly closer-packed structure.

- In $GeSe_4$, $GeSe_3$ $GeSe_{1.5}$ heteropolar bonding is favoured and their structures measured on the total structure factor level are in agreement with the chemically ordered continuous random network (COCRN) (Elliott[32]). However since deviations from this model are found from the full partial structure factor analysis for $GeSe_2$, deviations for the other compositions might be expected.

Bibliography

[1] Salmon P S and Liu J, *J. Phys.: Cond. Mat.* **6** (1994) 1449.

[2] Azoulay R, Thibierge H and Brenac A, *J. Non-Cryst. Sol.* **18** (1975) 33.

[3] Tronc P, Bensoussan M, Brenac A and Sebenne C, *Phys. Rev. B* **8** (1973) 5947.

[4] Wang Y, Matsuda O, Inoue K, Yamamuro O, Matsuo T and Murase K, *J. Non-Cryst. Sol.* **232-234** (1998) 702.

[5] Feng X, Bresser W J and Boolchand P, *Phys. Rev. Lett.* **78** (1997) 4422.

[6] Smektala F, Quemard C, Leneindre L, Lucas J, Barthelemy A and De Angelis C, *J. Non-Cryst. Sol.* **239** (1998) 139.

[7] Wright A C, Sinclair R N and Leadbetter A J, *J. Non-Cryst. Sol.* **71** (1985) 295.

[8] Salmon P S, *Proc. R. Soc.* **A 437** (1992) 591.

[9] Price D L, Reijers R, Saboungi M-L and Susman S, *J. Phys. C: Sol. State Phys.* **21** (1988) L1069.

[10] Borisova Z U, *Glassy Semiconductors*, Plenum Press: New York (1981).

[11] Sarrach D J, De Neufville J P and Haworth W L, *J. Non-Cryst. Sol.* **22** (1976) 245.

[12] Wagner T, Kasap S O and Maeda K, *J. Mater. Res.* **12** (1997) 1892.

[13] Boucenter A and Duval E, *Phil. Mag. B* **77** (1998) 557.

[14] Fawcett R W, Wagner C N J and Cargill III G S, *J. Non-Cryst. Sol.* **8-10** (1972) 369.

[15] Uemura A, Sagara Y and Satow T, *Phys. Stat. Sol. (a)* **26** (1974) 99.

[16] Hafiz M M, Hammad F H and El-Kabany N A, *Physica B* **183** (1993) 392.

[17] Zhou W, Paesler M and Sayers D E, *Phys. Rev. B* **43** (1991) 2315.

[18] Rao R N, Krishna P S R, Basu S, Dasannacharya B A, Sangunni K S and Gopal E S R, *J. Non-Cryst. Sol.* **240** (1998) 221.

[19] Feltz A and Lippmann F-J, *Z. Anorg. (Allg.) Chem.* **398** (1973) 157.

[20] Sears V F, *Neutron News* **3** (1992) 26.

[21] Feltz A, Pohle M, Steil H and Herms G, *J. Non-Cryst. Sol.* **69** (1985) 271.

[22] Soper A K, Howells W S and Hannon A C, *ATLAS - Analysis of Time-of-flight diffraction data from Liquid and Amorphous Samples* Laboratory report RAL-89-046 (1989).

[23] Hulliger F, *Physics and Chemistry of Materials with Layered Structures*, vol 5, ed. Levy F, D. Reidel Publishing Company: Dordrecht, Holland (1976).

[24] Bhatia A B and Thornton D E, *Phys. Rev. B* **2** (1970) 3004.

[25] Susman S, Volin K J, Montague D G and Price D L, *J. Non-Cryst. Sol.* **125** (1990) 168.

[26] Maruyama K, Misawa M, Inui M, Takeda S, Kawakita Y and Tamaki S *J. Non-Cryst. Sol.* **205-207** (1996) 106.

[27] Malaurent J C and Diximier J, *J. Non-Cryst. Sol.* **35 & 36** (1980) 1227.

[28] Armand P, Ibanez A, Philippot E, Ma Q and Raoux D, *J. Non-Cryst. Sol.* **150** (1992) 371.

[29] Fuoss P H, Eisenberger P, Warburton W K and Bienenstock A, *Phys. Rev. Lett.* **46** (1981) 1537.

[30] Johnson R W, Price D L, Susman S, Arai M, Morrison T I and Shenoy G K, *J. Non-Cryst. Sol.* **83** (1986) 251.

[31] Haye M J, Massobrio C, Pasquarello A, De Vita A, De Leeuw S W and Car R, *Phys. Rev. B* **58** (1998) R14661.

[32] Elliott S R, *Physics of Amorphous Materials*, 2nd Ed., Longman Group UK Limited: Essex (1990).

[33] Mamedov S B, Aksenov N D, Makarov L L and Batrakov Y F, *J. Non-Cryst. Sol.* **195** (1996) 272.

[34] Salmon P S, *Proc. R. Soc.* **A 445** (1994) 351.

Chapter 8

Ion-Ion and Ion-Valence Electron Structure Factors in Liquid Lithium

In this chapter the results of the analysis of neutron diffraction data for liquid lithium will be presented. The actual experiments were carried out in August 1995 by Dr Paul de Jong and Dr Peter Verkerk from the Interfaculty Reactor Institute of the Delft University of Technology.

8.1 Introduction

Liquid lithium is a very interesting liquid metal to study. It has an electronic configuration, $1s^2 2s$, i.e. the ratio of valence to core electrons is larger than in all other metals, except for beryllium which is, however, an extremely difficult material to handle as a liquid. It is possible to treat liquid lithium as a binary mixture of electrons and ions, and therefore to describe it in terms of the ion-ion $S_{II}(Q)$, ion-valence electron $S_{IE}(Q)$, and valence electron-valence electron $S_{EE}(Q)$ partial structure factors (see e.g. Silbert[1]). In a diffraction experiment, neutrons are scattered by the nuclei[1] and directly determine the ion-ion structure factor.

[1] Li has an unpaired electron, therefore magnetic scattering might be expected to be important. However, the unpaired electron is a conduction electron and the Pauli paramagnetic susceptibility has a minute size characteristic of diamagnetic susceptibilities (Ashcroft & Mermin[2]).

X-rays are, however, scattered by the electrons and yield a combination of all three structure factors. Following Chihara's approach (Chihara[3]), it is possible to extract $S_{IE}(Q)$ for a liquid metal from the ratio of the x-ray and neutron diffraction structure factors. Due to the electronic configuration of lithium, it is hoped that $S_{IE}(Q)$ will be large enough for it to be measured with current instrumentation.

In recent years the ionic structure and dynamics of liquid lithium have been studied thoroughly using various simulations and calculations. For example, González et al.[4],[5] carried out VMHNC (Variational Modified Hypernetted Chain) integral equation calculations to calculate the structure and Canales et al.[6] used classical molecular dynamics simulations to predict the static and dynamic structure factors at different temperatures. Recently Anta & Madden[7] used the so-called Orbital-Free *ab initio* molecular dynamics method to obtain the ion-ion and ion-electron static structure factors for liquid lithium. Therefore reliable experimental results are needed to check the accuracy of the different theoretical approaches.

Previous diffraction experiments on liquid lithium have shown that its investigation at a microscopic level involves significant problems. X-ray diffraction is not straight forward because the proportion of valence (delocalised) electrons is very high in lithium compared to other alkali metals, and therefore the corrections arising from the inelastic Compton scattering are large (see e.g. Olbrich et al.[8]). Also the determination of the ionic structure factor from neutron diffraction experiments is not undemanding due to the small mass of the lithium nucleus, which complicates the correction of the data for inelasticity effects (see section 2.9), and there are problems following from the high velocity of sound (see Ohse[9]). In every neutron diffraction experiment there exists an accessible kinematic $Q-\omega$ range, which is determined, in part, by the velocity of the incident neutrons. The integration path of the detector has to cover the main features of the dynamical structure factor, $S(Q,\omega)$ if the static structure factor is to be reliably obtained, especially the Brillouin excitations at low-Q, whose position in energy is determined by the speed of sound.

Former experiments on liquid lithium using neutrons were carried out by Ruppersberg & Egger[10] and Olbrich et al.[8] using neutrons of wavelength $\lambda = 0.7\,\text{Å}$. In their data analysis procedures they were not aware that $S(Q,\omega)$ did not fall

completely within the kinematically allowed $Q-\omega$ range of the experiment. De Jong[11] showed that considerable parts of the dynamic structure factor at low-Q values lie outside the integration path of the detector in the case of incident neutrons with a wavelength of 0.7 Å. Further, the structure factor in the Ruppersberg & Egger[10] and Olbrich et al.[8] experiments was normalised by using the incoherent cross-section σ_i as an adjustable parameter to ensure that the long and small Q-limits were correct (e.g. Olbrich et al.[8]). This lead to a wrong scaling of the data sets and therefore to erroneous peak heights (see de Jong[11]).

All of the above provided motivation for a new experiment to study the structure of liquid lithium. The D4B diffractometer at the ILL (see section 3.2.1) was chosen because at the time of the experiment its set-up was optimised for furnace experiments on liquids. A ^{7}Li sample was selected for the investigation since ^{7}Li is a much weaker absorber of thermal neutrons than ^{6}Li. This hinders the use of natural lithium which comprises 7.5 % ^{6}Li (Sears[12]). The experiments were carried out at two different wavelengths i.e. at 0.7011 Å because at this wavelength the highest neutron flux is attained, and at 0.4962 Å to reduce the inelasticity corrections and to obtain a larger maximum accessible energy transfer $\hbar\omega_{max}$, see section 8.2.1. The experiments were performed at three temperatures above the melting point, $T_M = 180.54\,°C$ (Weast[13]), namely at 197 °C, 452 °C (only for $\lambda = 0.7011$ Å) and 595 °C. The aim was to follow the temperature development of the structure factor S(Q) and the corresponding pair distribution function g(r), and to check that the low-Q limits, S(0), are in agreement with those from isothermal compressibility measurements (see e.g. Squires[14]).

8.2 Additional contributions to the theory important for the liquid lithium experiments

8.2.1 Kinematically allowed $Q-\omega$ range

The effective coherent differential cross-section in a neutron diffraction experiment is given by (see section 2.9)

$$\left(\frac{d\sigma}{d\Omega}\right)^{eff}_{coh} = N\,\frac{\sigma_{coh}}{4\pi}\int_{-\infty}^{\omega_{max}} \frac{k'}{k}\,\eta(k')\,S(Q,\omega)\,d\omega\,, \tag{8.1}$$

where $\hbar\omega_{max} = E_0$, the energy of the incident neutrons, $\eta(k')$ is the detector efficiency, k and k' are the incident and scattered wavevectors respectively, and $S(Q,\omega)$ is the dynamic structure factor. For a reactor experiment the measured differential cross-section is, however, determined experimentally by evaluating the integral over ω at constant angle θ instead of at constant values of the scattering vector Q.

The dynamic structure factor $S(Q,\omega)$ of liquids at low-Q generally comprises three peaks, the Rayleigh peak at $\omega = 0$ accompanied by a Brillouin peak or sound peak on each side at $\omega = \pm c_s Q$, where c_s is the speed of sound in the liquid. Liquid lithium has a large sound velocity, $c_s = 4554\,\mathrm{ms}^{-1}$ at the melting point (Ohse[9]), and therefore the Brillouin modes are anticipated to lie outside the accessible $Q - \omega$ range of the detector for longer wavelength neutrons. In figure 8.1 the expected positions of the sound mode are compared with the detector paths used in our experiment. The normalised variables $\omega^* = \frac{\omega}{\omega_0} = \frac{E}{E_0}$ and $k^* = \frac{Q}{k_0}$ are used in order to obtain the same detector path for the neutrons incident at different wavelengths. In these variables the function describing the position of the sound mode becomes,

$$k^* = \frac{v}{2c_s}\omega^* \tag{8.2}$$

and using the definition of the scattering vector (see figure 2.2) the detector path is given by,

$$k^* = \sqrt{2 - \omega^* - 2\sqrt{1-\omega^*}\cos(2\theta)} \tag{8.3}$$

where v is the velocity of the incident neutrons, 2θ the scattering angle and c_s the sound velocity in lithium, which has a value of $4544\,\mathrm{ms}^{-1}$ at 197 °C, $4389\,\mathrm{ms}^{-1}$ at 452 °C and $4302\,\mathrm{ms}^{-1}$ at 595 °C.

Because of the broad sound mode its width has to be taken into consideration (De Jong[11]) in the comparison with the integration path of the detector. It is seen in figure 8.1 that for the $\lambda = 0.4962$ Å neutrons the integration path of the detector intersects the curve giving the position of the sound mode even when its half width at half maximum (HWHM), given by De Jong[11], is included. Therefore no problems with the accessible $Q - \omega$ range are expected when the detector performs the experimental integration over the dynamical structure factor. For the neutrons with the higher incident wavelength of $\lambda = 0.7011$ Å, however, a problem with the kinematically allowed $Q - \omega$ range occurs when the HWHM of the sound mode is taken into account. The detector path does intersect the curves giving the position

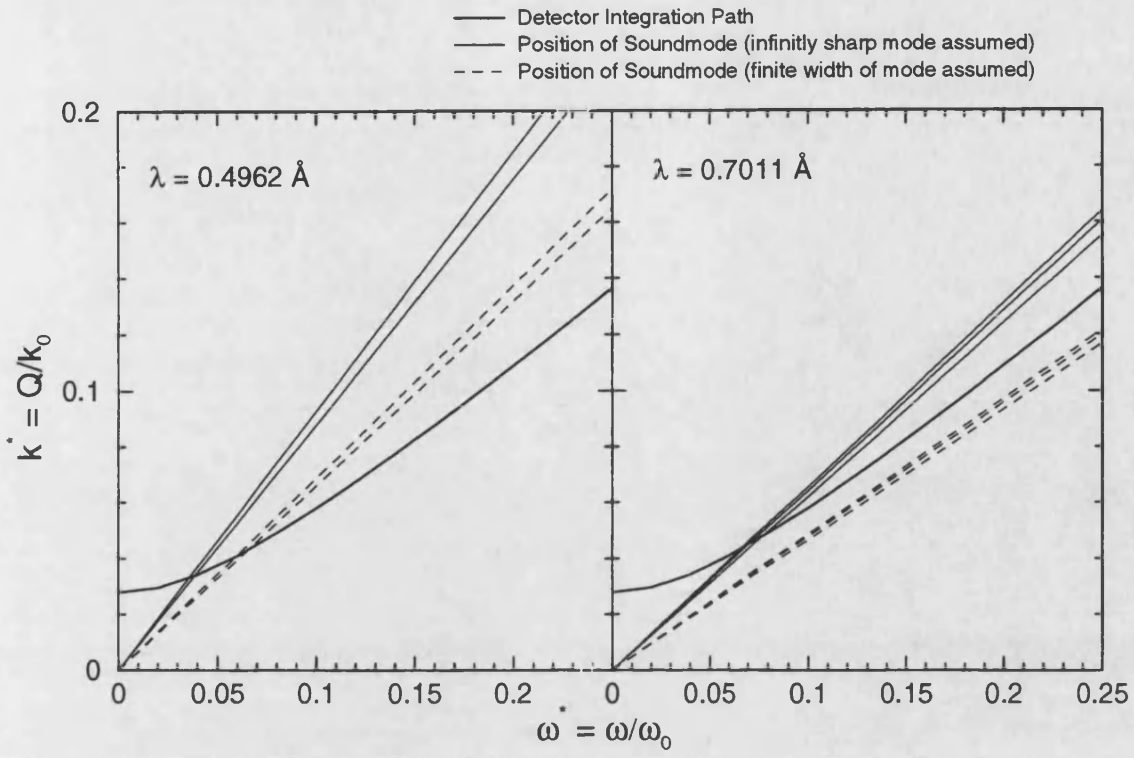

Figure 8.1: Kinematically accessible $Q-\omega$ range for incident neutrons with a wavelength of $\lambda = 0.4962$ Å and $\lambda = 0.7011$ Å respectively. The thick solid curve shows the integration path of the detector used in the experiment and the thin solid curves display the expected position of the sound mode, if the finite width of the mode is neglected. The upper and lower curves for $\lambda = 0.4962$ Å correspond to temperatures of 595 °C and 197 °C respectively and the three curves for $\lambda = 0.7011$ Å correspond to temperatures of 595 °C, 452 °C and 197 °C in descending order. The thin dashed curves give the HWHM of the modes and are only shown on one side of the maxima.

of the sound mode but then at low-Q runs approximately parallel to them and does not intersect the curves giving the HWHM of the sound mode. Therefore the integration of $S(Q,\omega)$ is anticipated to produce a static structure factor S(Q) which has too high an intensity at low-Q. Measured data points at low-Q that are affected by this artefact have therefore to be omitted from the S(Q) for the $\lambda = 0.7011$ Å results.

8.2.2 Inelasticity corrections

It is shown in section 2.9 that the static approximation is problematical for nuclei of low mass, as in this experiment, and incoming neutrons with low energies. Different approaches to correct the resulting data for deviations from the static approximation are therefore considered and compared for our experimental conditions.

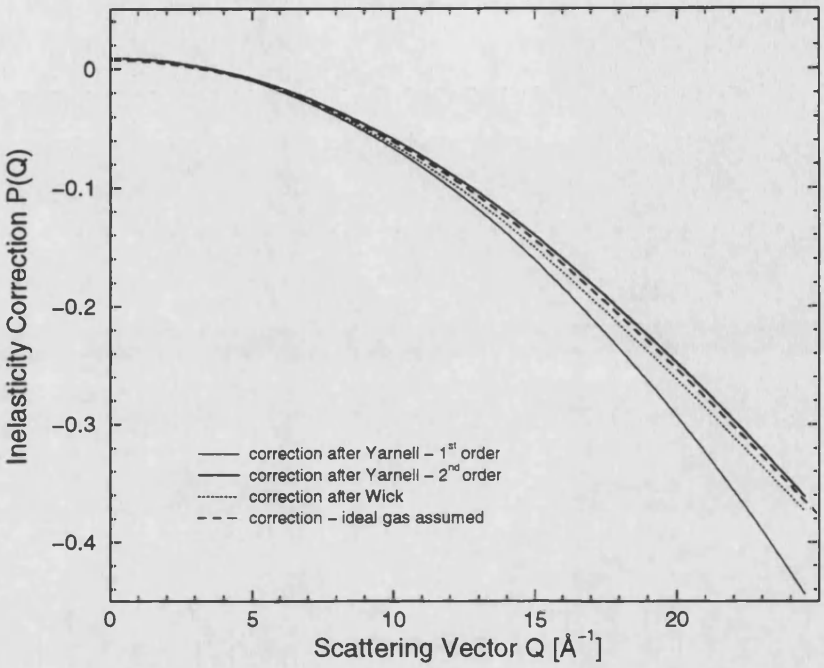

Figure 8.2: Different possibilities to perform the inelasticity corrections on the $\lambda = 0.4962$ Å data sets at a temperature T = 197°C for liquid lithium with the atomic mass of Li= 7.016.

The effective coherent cross-section $\left(\frac{d\sigma}{d\Omega}\right)^{\text{eff}}_{\text{coh}}$, see equation 2.56, can be written as

$$\left(\frac{d\sigma}{d\Omega}\right)^{eff}_{coh} = \eta_0 \frac{\sigma_{coh}}{4\pi}[S(Q) - P(Q)] \tag{8.4}$$

where $\eta_0 = 1 - e^{-\gamma/k_0}$ is the detector efficiency for neutrons having the incident energy E_0 and $P(Q)$ is the inelasticity correction.

In Yarnell et al.'s[15] approach, described in section 2.9, $S(Q,\omega)\,d\omega$ is expanded about $\hbar\omega = 0$ and $P(Q)$ is given by

$$P(Q) = c_1\frac{E_{rec}}{E_0} - O_2(Q) + c_3\frac{E_{rec}}{E_0}\frac{k_BT}{E_0} - \frac{m}{2M}\left(O_2'(Q) + \frac{k_BT}{E_0}\right) \tag{8.5}$$

where m is the mass of the neutron, M the mass of an atom in the scattering system, c_1, c_2 and c_3 are detector constants, E_0 the incident neutron energy and

$E_{rec} = \frac{\hbar^2 Q^2}{2M}$ the recoil energy of the scattering nucleus. The functions $O_2(Q)$ and $O_2'(Q)$ are higher order correction terms that are zero if the correction is carried out to 1st order and for the case of a correction to 2nd order,

$$O_2(Q) = c_2 \left(\frac{E_{rec}}{E_0}\right)^2 , \tag{8.6}$$

$$O_2'(Q) = \frac{E_{rec}}{E_0} . \tag{8.7}$$

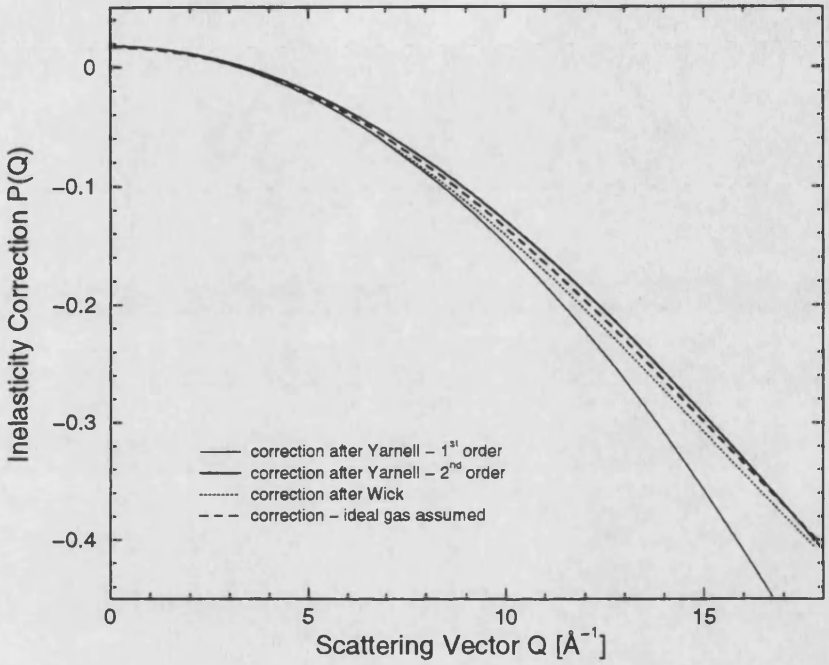

Figure 8.3: Different possibilities to perform the inelasticity corrections on the $\lambda = 0.7011$ Å data sets at a temperature T = 197°C for liquid lithium with the atomic mass of Li= 7.016.

Wick's[16] approach, see section 2.9, is based on an expansion of $S(Q,\omega)$ about the recoil energy E_{rec}, and gives an inelasticity correction $P(Q)$ to first order (Egelstaff & Soper[17]),

$$\begin{aligned} P(Q) \;=\; & \frac{\eta_{k'}}{\eta_0}\left[\frac{M'}{S(\theta)}\left(\frac{S(\theta)+\cos(\theta)}{M'+1}\right)^2 + \frac{k_B T}{M' E_0}\left(\frac{M'}{S(\theta)}\right)^3 \left\{\frac{1}{2} - \frac{3(M'-1)\sin^2(\theta)}{2S(\theta)^2}\right.\right. \qquad (8.8) \\ & -\frac{1-A_r}{(M'+1)^3}\left[S(\theta)(M'-1)(\sin^2(\theta) - 2\cos(\theta)S(\theta)) + 2S(\theta)M'(M'-\cos^2(\theta))\right. \\ & \left.+\frac{1}{2S(\theta)}\left(M'(S(\theta)+\cos(\theta))^2(M'-\cos(\theta)S(\theta)+\sin^2(\theta)) - \cos^2(\theta)\sin^2(\theta)(1+2M')\right)\right] \\ & \left.\left.-\frac{B_r - A_r}{2(M'+1)^4} M'(S(\theta)+\cos(\theta))^2(M'-\cos(\theta)S(\theta)+\sin^2(\theta))\right\}\right] \qquad (8.9) \end{aligned}$$

where $Q = \frac{4\pi}{\lambda}\sin(\theta)$, $S(\theta) = \sqrt{M'^2 - \sin^2(\theta)}$, $M' = M/m$ with M the mass of the scattering nucleus and m the mass of the neutron, and A_r and B_r are the detector

constants, defined by,

$$A_r = 1 - \left(\frac{1}{\eta_{k'}} - 1\right) \ln\left(\frac{1}{1-\eta_{k'}}\right) \tag{8.10}$$

$$B_r = A_r + \left(\frac{1}{\eta_{k'}} - 1\right) \ln^2\left(\frac{1}{\eta_{k'}}\right) \tag{8.11}$$

where $\eta_{k'} = 1 - e^{-\gamma/k'}$ is the counting efficiency of the detector at E_{rec}.

In the third approach (Soper[18]) an integration is made over a model scattering law assuming a perfect gas, $S^{ig}(Q,\omega)$, following the detector integration path (see program 'integideal' at the ISIS facility program suite). $S^{ig}(Q,\omega)$ is given by (e.g. Sears[12]),

$$S^{ig}(Q,\omega) = \frac{1}{\sqrt{4\pi \frac{k_B T}{E_0} \frac{Q^2}{k_0^2} \frac{m}{M}}} \exp\left[- \frac{\left(\frac{E}{E_0} - \frac{Q^2}{k_0^2}\frac{m}{M}\right)^2}{4\frac{k_B T}{E_0}\frac{Q^2}{k_0^2}\frac{m}{M}} \right] . \tag{8.12}$$

The resultant correction functions for liquid lithium (atomic mass = 7.016) at T = 197°C at the incident neutron wavelengths of $\lambda = 0.4962$ Å and $\lambda = 0.7011$ Å are compared in figures 8.2 and 8.3.

8.3 Neutron diffraction experiments

The diffraction experiments were carried out on the D4B diffractometer at the ILL on a sample consisting of enriched ^{7}Li (99.99 at%). For the experiment the sample was contained in a vanadium can of 1.31 cm diameter and 0.2 cm wall thickness that was evacuated and sealed by electron beam welding at the Institut für Kerntechnik und Energiewandlung E.V. (IKE), Stuttgart (Verkerk [19]). The sample was fully illuminated by a 5 cm high and 1.4 cm wide beam.

The experiment included the measurement of the diffraction patterns for the sample at the different temperatures (197 °C, 452 °C and 595 °C) in its container in a cylindrical vanadium furnace, an empty vanadium can of the same dimensions as the one containing the sample at the three temperatures, the empty vanadium heater at the three temperatures, a cadmium rod in the can and the heater at room temperature for the background correction at low angles, and the empty bell jar. Also the diffraction pattern for a vanadium rod of 1.0018 cm diameter without the heater at room temperature was measured for the data normalisation. First the empty can was measured at 197 °C and 595 °C at the lower wavelength, then the

sample at the two temperatures at this wavelength. After this the sample was kept at the higher temperature and the wavelength of the incident neutrons changed to $\lambda = 0.7011$ Å, where measurements were made at 595 °C, 452 °C and 197 °C. Finally all the additional measurements were performed at the two wavelengths.

The following table shows the coherent scattering lengths and cross-sections for the lithium isotopes and the sample. All of the values were taken from Sears[12].

	$\overline{b}$ [fm]	$\sigma_{free,coh}$ [barn]	$\sigma_{free,inc}$ [barn]	σ_{abs} (@ 1.798 Å) [barn]	atomic mass
^{6}Li	2.00(11) - 0.261(1)*i	0.37(4)	0.34(4)	940(4)	6.015
^{7}Li	-2.22(2)	0.474(8)	0.60(2)	0.0454(3)	7.016
sample	-2.22(2)	0.474(8)	0.60(2)	0.1394(5)	7.016

Table 8.1 : Neutron parameters and atomic mass for ^{6}Li, ^{7}Li and the isotopically enriched 99.99 at% ^{7}Li sample used in the diffraction experiments.

The absorption cross-sections of the sample at both wavelengths were calculated from the σ_{abs} (@ 1.798 Å) values assuming $\sigma_{abs} \propto \lambda$. They are 0.0385(1) barn and 0.0544(2) barn for the 0.4962 Å and 0.7011 Å incident neutrons respectively. The mass densities for liquid lithium at the three different temperatures were taken from Ohse[9], and are given in table 8.2 together with the corresponding number densities.

Temperature	ρ [g/cm^3]	n_0 [Å^{-3}]	sum-rule [Å^{-3}]
197(3) °C	0.5134(1)	0.044066(9)	-0.870(2)
452(3) °C	0.4909(1)	0.042135(9)	-0.832(2)
595(3) °C	0.4771(1)	0.040951(9)	-0.808(2)

Table 8.2 : Mass density and number density values for the different temperatures, taken from Ohse[9], and sum-rule relations that have to be fulfilled for F(Q), calculated from $\int_0^\infty [S(Q) - 1]Q^2\,dQ = -2\pi^2 n_0$.

The low-r limit of the total pair distribution function, G(0), is given by

$$G(0) = -\overline{b}^2 = -0.0493(9)\,barn\,, \tag{8.13}$$

8.2 when the atomic mass of Li= 7.016 is used. However, as seen is figure 8.4, it does not give a satisfactory result. (Even using an effective mass of 8 instead of 7.016 in the correction procedure following Yarnell et al.[15] still 'over-corrected' the data set shown in figure 8.4. Changing the mass in the perfect gas approach, see section 8.2, showed that the best result with this approach could be obtained by using an effective mass of ≈ 8, however the curvature of the correction was not entirely correct, therefore an empirical correction was favoured.) It is anticipated that problems for inelasticity effects are arising for the $\lambda = 0.7011$ Å data since the energy of the incident neutrons scales with $\frac{1}{\lambda^2}$ and therefore stronger effects are encountered for longer wavelength neutrons. The $\lambda = 0.7011$ Å data sets could only be corrected satisfactory for inelasticity effects by an empirical method using a polynomial expansion of the form, $P(Q) = a_0 + a_2Q^2 + a_4Q^4$, to fit the difference between the data and the Fourier back transform of the corresponding real-space function after the unphysical low-r oscillations have been set to their theoretical value. This approach followed the inelasticity correction used e.g. for liquid water by Bellissent-Funel et al.[20]. Despite this empirical correction, S(Q) started sloping upwards slightly at values $Q \geq 14\,\text{Å}^{-1}$, therefore a truncation of the data sets at $14\,\text{Å}^{-1}$ was necessary.

The effect of the integration path of the detector on the $\lambda = 0.7011$ Å data sets at low-Q values can best be seen in figure 8.7, where a shifted S(Q)/Q is displayed for all the data sets. The intensity for $Q \rightarrow 0$ increases strongly and to remove this artefact the data sets had to be cut-off at $0.75\,\text{Å}^{-1}$.

For all of the data sets the static structure factors were found to sit on too low a level. To obey the correct high-Q limit, $S(Q \rightarrow \infty) = 1$, an upwards shift of ≈ 0.11 barn to all of the data sets at both wavelengths was necessary. The source of this problem was investigated by testing the effect on the data analysis procedure of changing, for example, the cross-sections within their errors, using the bound scattering cross-section instead of the free scattering cross-section and changing the sample enrichment. Finally, it was concluded that the shift arises from an uncertainty in using the empty heater as background in the data correction procedure. After the shifts had been applied, the structure factors fulfil the correct high-Q limit, the sum-rule relations are obeyed, and the expected $S(Q \rightarrow 0)$ limits were consistent with the data. Consequently, there was no need to impose any

additional scaling of the data, i.e. the normalisation procedure using vanadium was found to be appropriate.

8.4 Results - Static structure factors

In figure 8.5 all of the measured static structure factors, S(Q), are shown together with the Fourier back transforms of the corresponding g(r) after the unphysical low-r oscillations are set to their theoretical limit. For the lower wavelength, the agreement between the data sets and their Fourier back transforms is satisfactory, but not as good as for the 0.7011 Å data sets, see χ^2 values summarised in table 8.3. This may be anticipated since for this higher wavelength an empirical inelasticity correction was used (see section 8.3).

wavelength	197 °C	452 °C	595 °C
0.4692 Å	242.6 for 318 pts.	-	149.4 for 313 pts.
0.7011 Å	120.2 for 275 pts.	26.2 for 278 pts.	134.8 for 275 pts.

Table 8.3 : χ^2 values for the data sets shown in figure 8.5.

With increasing temperature, the first peak in S(Q) moves to lower-Q values, see table 8.4, the peak heights decrease and the higher-Q oscillations are more strongly damped.

wavelength	197 °C	452 °C	595 °C
0.4692 Å	2.48(2) $Å^{-1}$	-	2.43(2) $Å^{-1}$
0.7011 Å	2.49(2) $Å^{-1}$	2.46(2) $Å^{-1}$	2.43(2) $Å^{-1}$

Table 8.4 : Positions of the first peak in the static structure factors, S(Q).

In our work special attention has been drawn to the behaviour of the structure factor, S(Q), at low-Q values. This low-Q region is of strong interest in simple liquid metals since it contains information about the long-ranged part of the interionic forces. In the literature an acute demand for accurate neutron scattering data at small values of Q is found as it is the most important region for the comparison with simulations and calculations (e.g. Canales et al.[6], Silbert[1], March & Silbert[21]). The structure factor in this low-Q region also offers a good guide to the reliability of the applied correction procedures, since the measured data should extrapolate

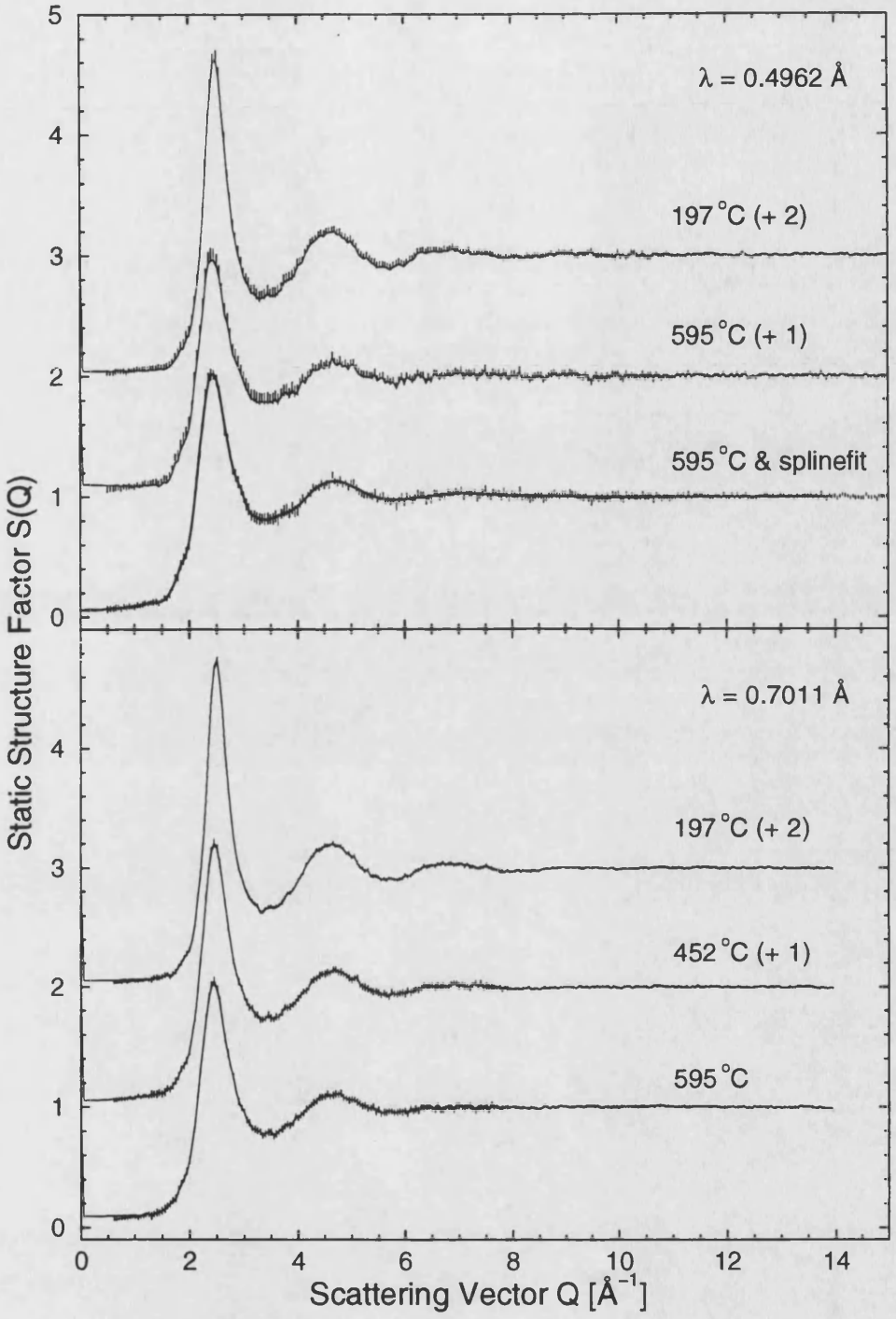

Figure 8.5: Measured static structure factors at both wavelengths (error bars) shown together with the Fourier back transforms of the corresponding g(r) after the unphysical low-r oscillations have been set to their theoretical limit (thin solid curves). Additionally a spline fit to the 595 °C data for the 0.4962 Å wavelength is shown as a thick solid curve and is representative of all the other cubic spline fits that have been used to smooth the measured data sets.

to the S(Q = 0) limit calculated from thermodynamics (e.g. Squires[14])

$$S(0) = \kappa_T n_0 k_B T \,. \tag{8.15}$$

κ_T is the isothermal compressibility, n_0 the number density, k_B Boltzmann's constant, and T the absolute temperature.

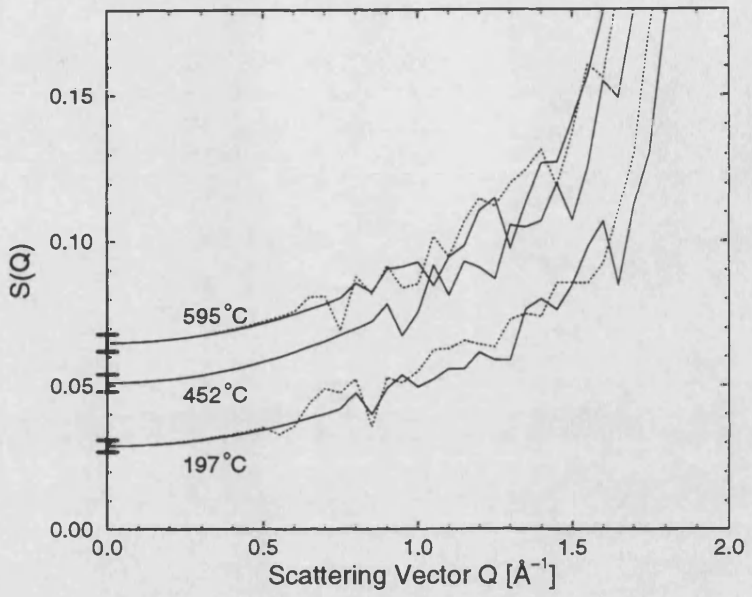

Figure 8.6: Measured structure factors in the low-Q region compared with the S(Q = 0) values calculated from the isothermal compressibility values given in Ohse[9], marked by the error bars. The solid curves correspond to $\lambda = 0.7011$ Å and the dotted curves to $\lambda = 0.4962$ Å.

In figure 8.6 the measured structure factors in the low-Q region are compared with the S(Q = 0) values calculated from the isothermal compressibility values given in Ohse[9]. The limiting values are 0.029(2), 0.051(3) and 0.065(3) for 197 °C, 452 °C and 595 °C respectively. To extrapolate the measured structure factors at low-Q, $\frac{S(Q)-S(0)}{Q}$ was plotted as a function of Q and the data were fitted by a straight line which was constructed to pass through the origin using a least squares algorithm (see figure 8.7). The fitted lines show that the measured neutron structure factors for $Q \leq 1.8\,\text{Å}^{-1}$ has a quadratic profile as expected by the theoretical considerations of, for example, Silbert[1].

In figure 8.8 the structure factors at 197 °C and 595 °C, measured using the two different wavelengths, and their differences are shown. For the two temperatures, both structure factors are in good agreement over the whole measured Q-range except around the first peak position, where serious discrepancies are observed. These

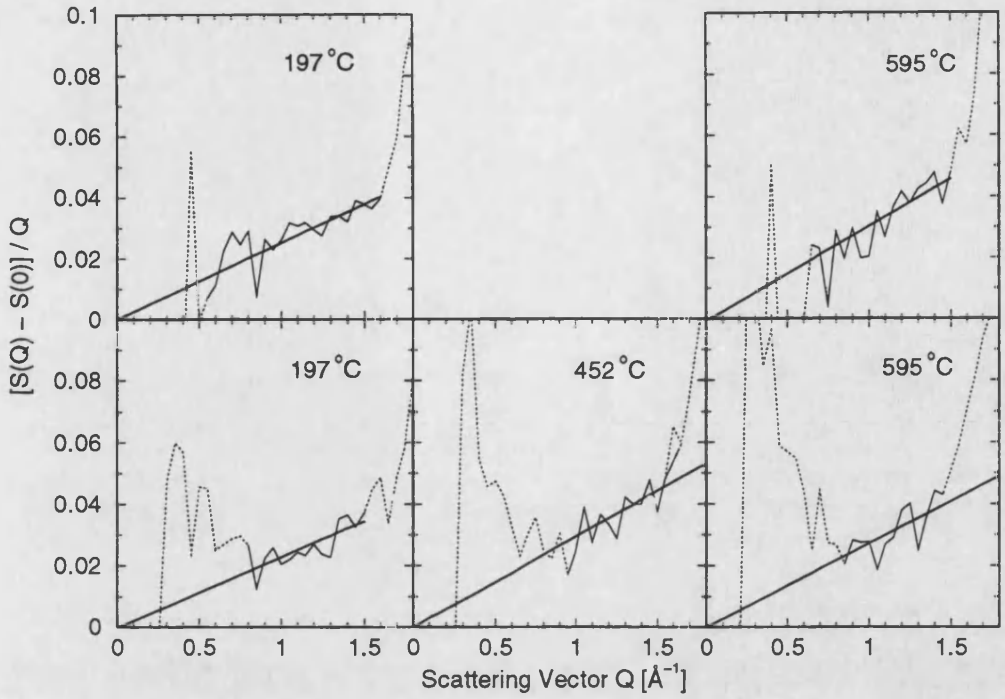

Figure 8.7: Data sets in the low-Q region, plotted as $\frac{S(Q)-S(0)}{Q}$ vs. Q. The two graphs in the first row correspond to $\lambda = 0.4962$ Å, the three graphs in the second row to $\lambda = 0.7011$ Å. The dotted curves correspond to the whole of the measured static structure factor, whereas the solid curves represent that part of S(Q) used for the fit, which is itself displayed by the thick solid curves. The rise in intensity at small-Q values of the $\lambda = 0.7011$ Å data is explained in section 8.3.

result from a small shift to a lower-Q value of the first peak in the $\lambda = 0.4962$ Å data set with regards to the $\lambda = 0.7011$ Å data set and from a lower first peak height for the $\lambda = 0.4962$ Å data set. These differences are found for both temperatures, although they are reduced for the 595 °C data. They are due to the different instrumental resolution functions of the D4B diffractometer at $\lambda = 0.4962$ Å and $\lambda = 0.7011$ Å, which will be discussed in section 8.5.1. The additional small differences between the data sets occurring after the first peak are due to the different approaches to carry out the inelasticity corrections.

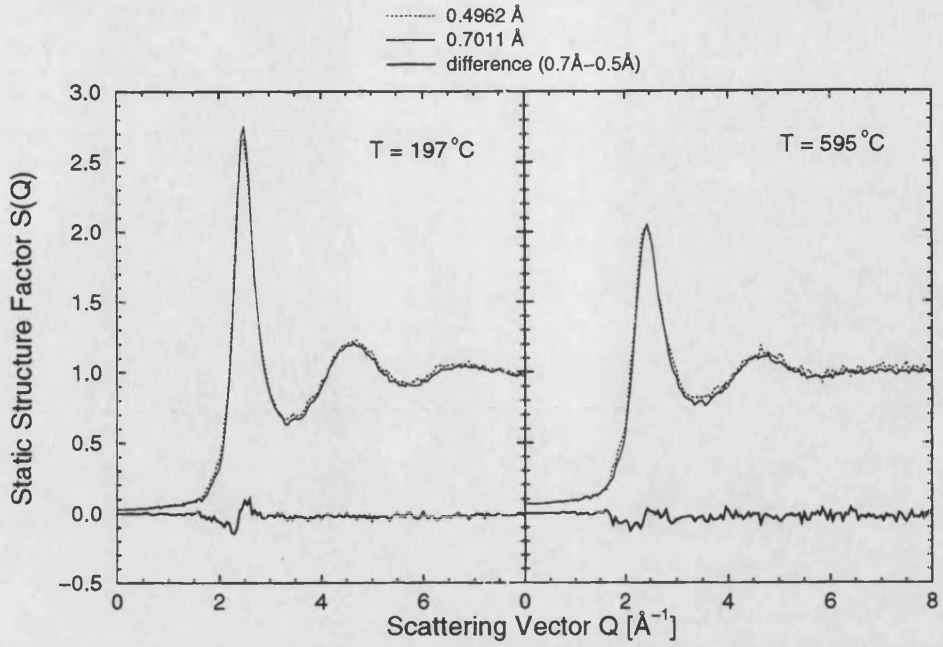

Figure 8.8: Static structure factors at 0.4692 Å and 0.7011 Å at the temperatures of 197 °C and 595 °C and their difference (thick solid curves). The main contrast occurs in the region of the first peak.

8.5 Discussion

The discussion is divided into four parts. In the first part the static structure factors will be corrected for the instrumental resolution function. In the second part the pair distribution functions for the different temperatures will be presented and commented upon. In the third part our results will be compared with the results obtained from simulations and calculations, and in the fourth part the ion-valence electron structure factor obtained from our data in combination with x-ray diffraction data will be presented and compared with simulation results.

8.5.1 Resolution function of the D4B diffractometer

The resolution function of a two-axis diffractometer like D4B is determined by several parameters, e.g. the sample dimensions, the detector height and distance from the sample, and the instrumental set-up. Additionally the so called 'umbrella effect' (see e.g. van Laar & Yelon[22]) causes small peak asymmetries and peak shifts towards lower angles. The umbrella effect arises at low-Q angles from the

intersection of the diffraction rings of the Debye-Scherrer cone with the finite detector. When the radius of a ring is small and the detector elements are large, each element can observe intensity from a diffraction ring at $\theta-$values higher than the scattering angle at which the element is nominally located (see figure 8.9). Hence if the diffraction pattern is increasing in intensity with scattering angle, the measured intensity at the nominal angle will be increased, i.e. peaks will be shifted to lower angles. The correction for this effect only affects the peaks at low-Q values in a measurable way, particularly when large samples are used, like in our experiment (van Laar & Yelon[22]). The effect also increases with decreasing wavelength since the rings of the Debye-Scherrer cone move closer together.

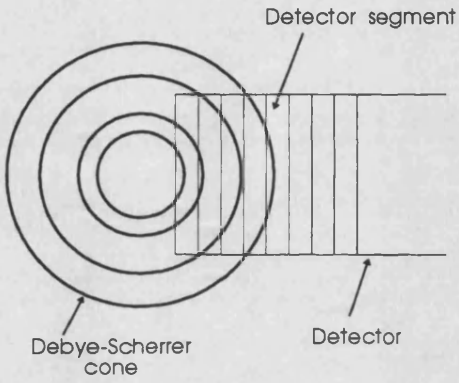

Figure 8.9: Schematic drawing of the umbrella effect. The intersection of the Debye-Scherrer cone with the detector is shown.

Howells[23] showed that the 'moments method' can be used for deconvoluting the structure factor of a liquid from the resolution function of the diffractometer. The measured intensity $I(2\theta_s)$ is expressed by

$$I(2\theta_s) = \int R(2\theta_s, \rho)\, S(2\theta_s + \rho)\, d\rho \tag{8.16}$$

where $2\theta_s$ is the scattering angle, ρ the angular displacement of the detector from $2\theta_s$, and $R(2\theta_s, \rho)$ the resolution function of the instrument. The aim is to use the moments procedure to calculate $S(2\theta_s)$ from the measured $I(2\theta_s)$ when the form of $R(2\theta_s, \rho)$ is known. The moments method, as applied to our experiment, is outlined in appendix B.

The resolution function for the D4B diffractometer in a set-up corresponding to our experimental conditions has been obtained by using the program **d4pro**, now

installed at the D4 programs suite at the ILL (Fischer[24]). The program follows a code originally written by Finger, see e.g. Finger et al.[26], and calculates the resolution function profile for a Bragg peak taking into account the sample width, the sample height, the vertical focussing, the horizontal angular beam dispersion, the detector height, the detector distance, and the umbrella effect (Fischer[24]). Then the moments of the resolution profile can be calculated using the program **mome.exe**, written by Howells[25] and now also installed as part of the D4 programs suite. Using these moments the deconvolution of the measured intensity from the resolution function can be carried out using the program **dec2ta** at the ISIS program suite, Howells[25]. For the liquid lithium data only the first and second derivatives of the measured intensity were included in the correction procedure since the use of more derivatives introduced too much noise in the resultant corrected function.

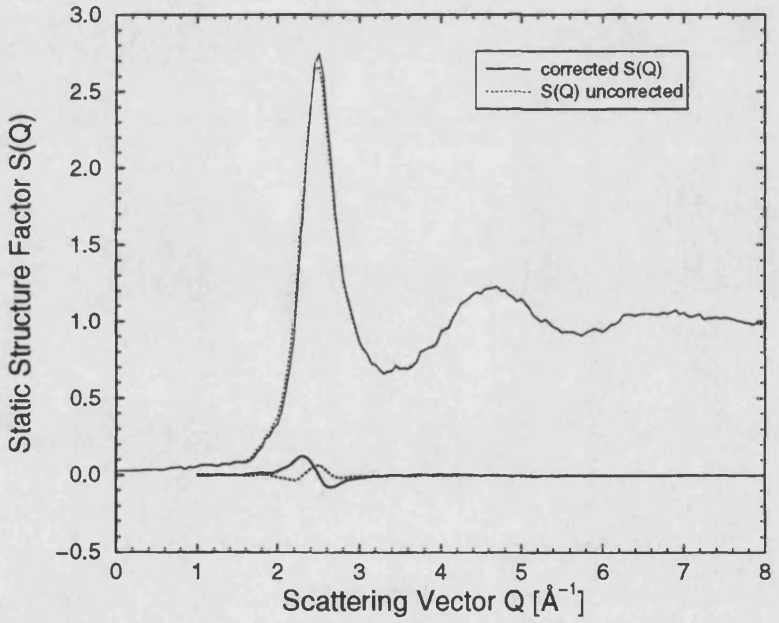

Figure 8.10: Structure factor for the $\lambda = 0.4962$ Å data set at T = 197 °C before and after the resolution function correction together with first and second correction, see appendix B (shown by the thick solid and dotted curves).

In figure 8.10 the structure factor for the $\lambda = 0.4962$ Å data set at T = 197 °C, in which the corrections are largest, is shown before and after the resolution function correction together with the corrections.

A comparison of the structure factors for liquid lithium at the two different

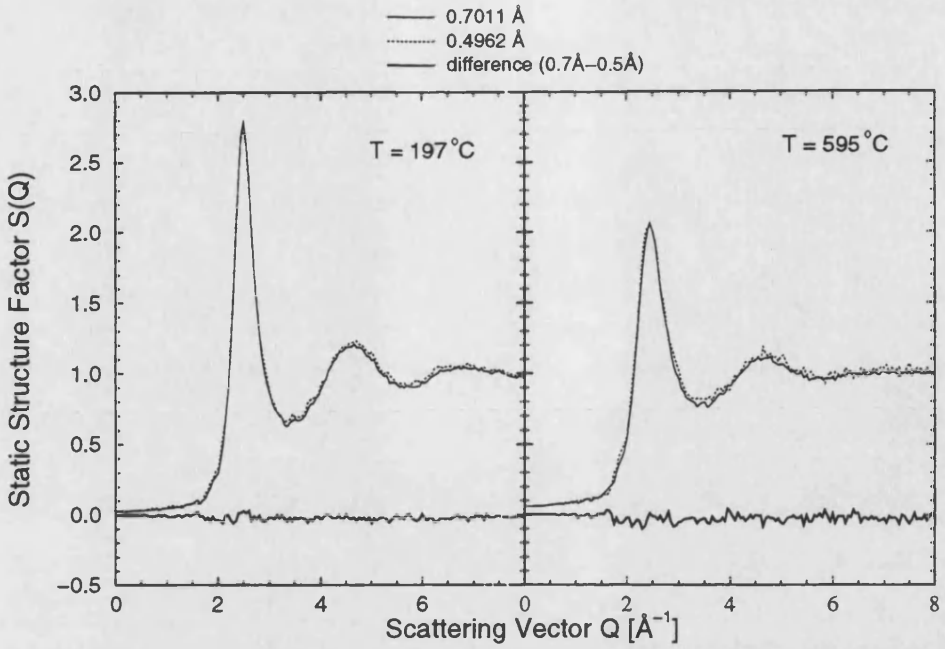

Figure 8.11: Comparison of the structure factors for liquid lithium at the two different wavelengths for T = 197 °C and T = 595 °C. The solid curves give the $\lambda = 0.7011$ Å data sets and the dotted curves the $\lambda = 0.4962$ Å data sets. The difference between them is given by the thick solid curves.

wavelengths is shown in figure 8.11 for the data sets at 197 °C and 595 °C. A comparison of this figure with figure 8.8 shows the impressive effect of the resolution correction. The correction was also applied to the 452 °C data set.

The corrected static structure factors are shown in figure 8.12 together with the Fourier back transforms of the corresponding real-space functions. The agreement is similar to the uncorrected functions shown in figure 8.5 and the data still fulfil the sum-rule relations. The resolution function corrections do not affect the low-Q regions of the data sets used to extrapolate the data to the S(Q = 0) limit in a measurable way.

8.5.2 Pair distribution functions at different temperatures

The pair distribution functions, g(r), obtained at the different wavelengths and temperatures are shown in figure 8.13. All of these pair distribution functions were obtained by a Fourier transform of Q-space functions, corrected for the resolution function and truncated at a $Q_{max} = 14$ Å^{-1}, such that the g(r)'s from the two differ-

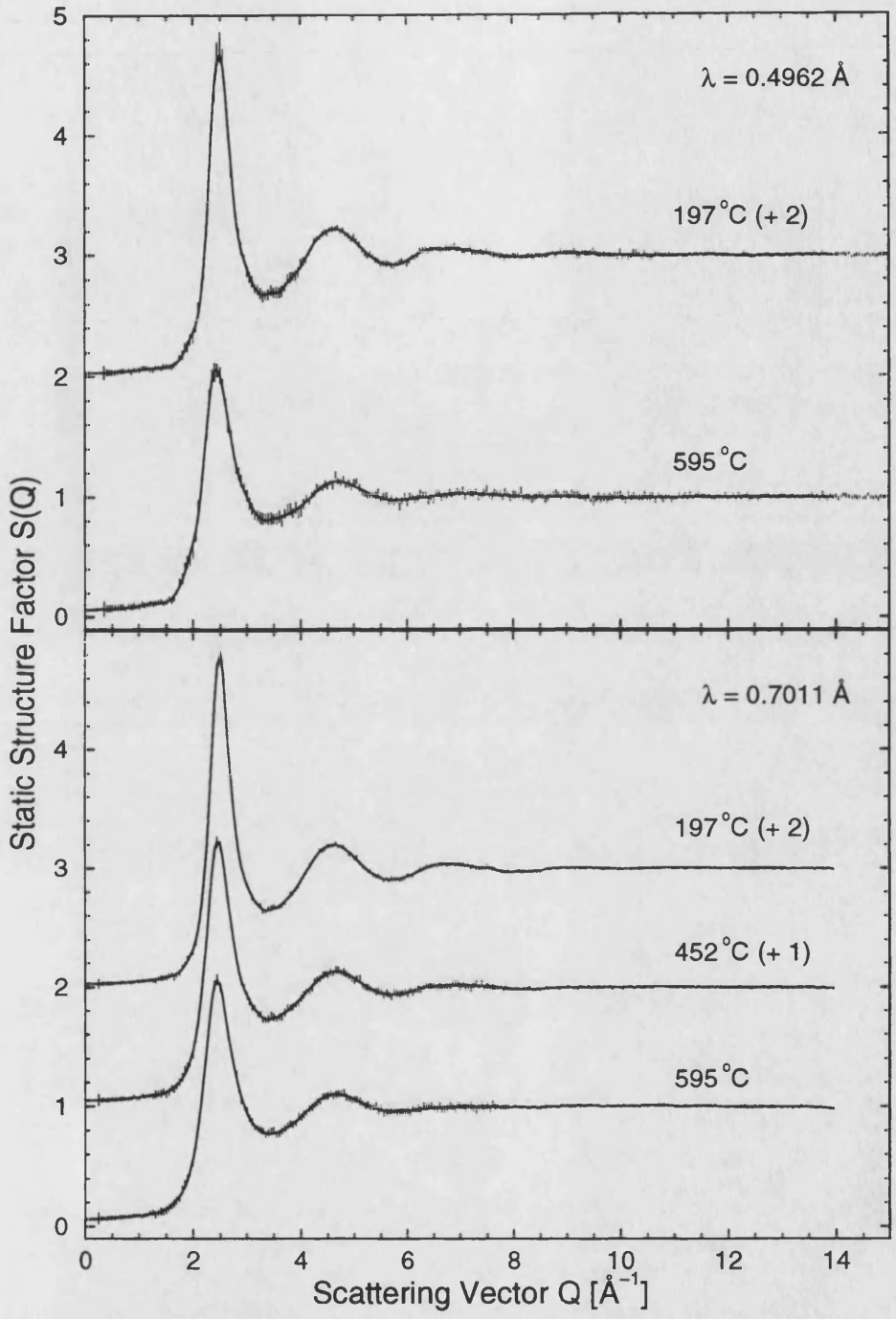

Figure 8.12: Static structure factors obtained after the resolution function correction. The data sets are given by the error bars and the cubic spline fits used to smooth the measured data sets are shown as a thick solid curves.

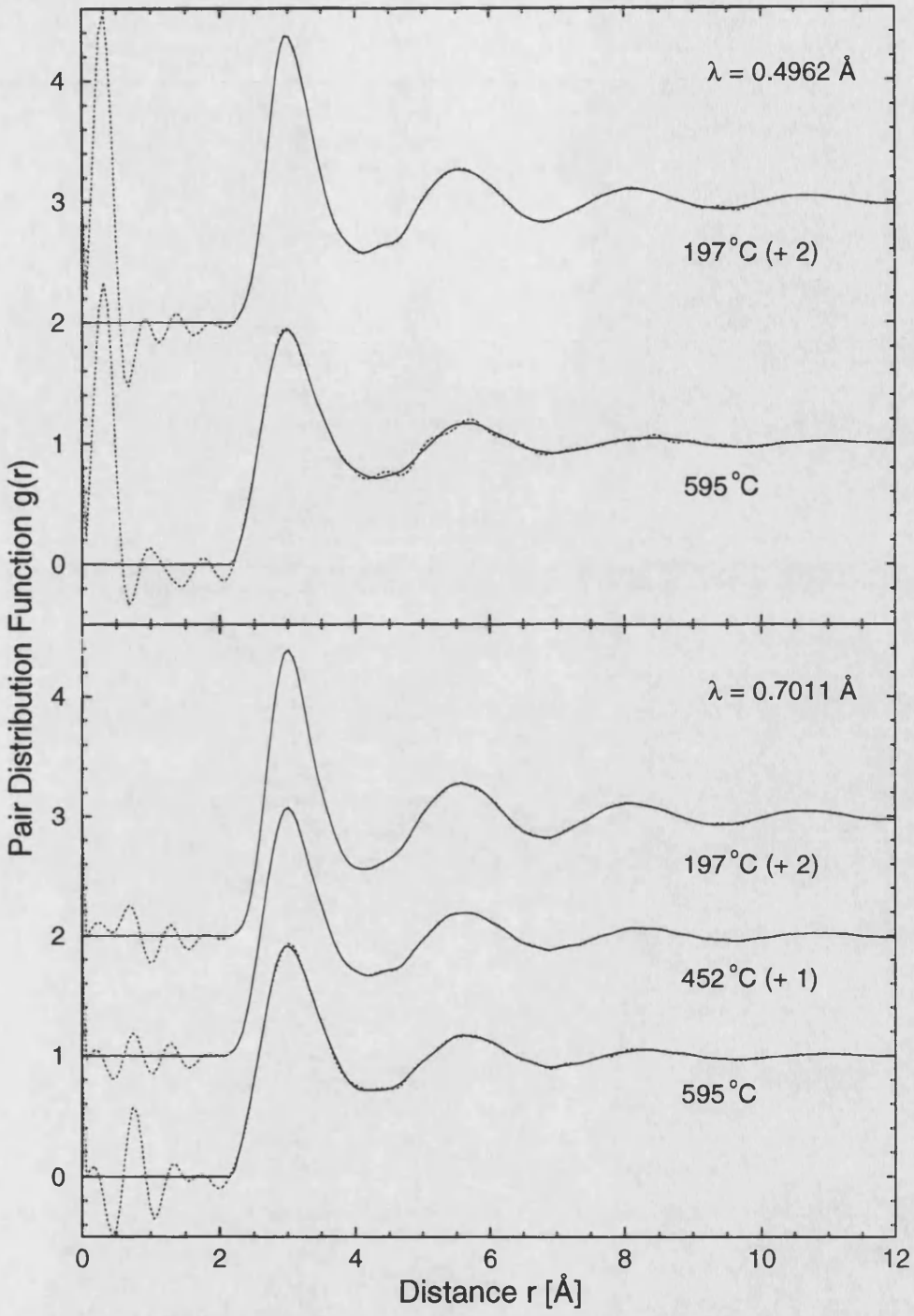

Figure 8.13: Measured pair distribution functions for liquid lithium. The dotted curves represent the Fourier transforms of the measured data points, shown by the error bars in figure 8.12. The solid curves correspond to the real-space functions of the spline fits to the data points, where the unphysical oscillations have been set to their theoretical limit.

ent wavelengths can be directly compared with each other. (Fourier transforming the Q-space functions up to a $Q_{max} = 16\,\text{Å}^{-1}$ for the $\lambda = 0.4962\,\text{Å}$ data did not make any measurable difference to the real-space functions outside the range of the unphysical oscillations.) There is an indication of a slight slope on the $\lambda = 0.4962\,\text{Å}$ data sets, illustrated by the first high positive peak at low-r in the unphysical region of g(r) (see e.g. Xin[27]).

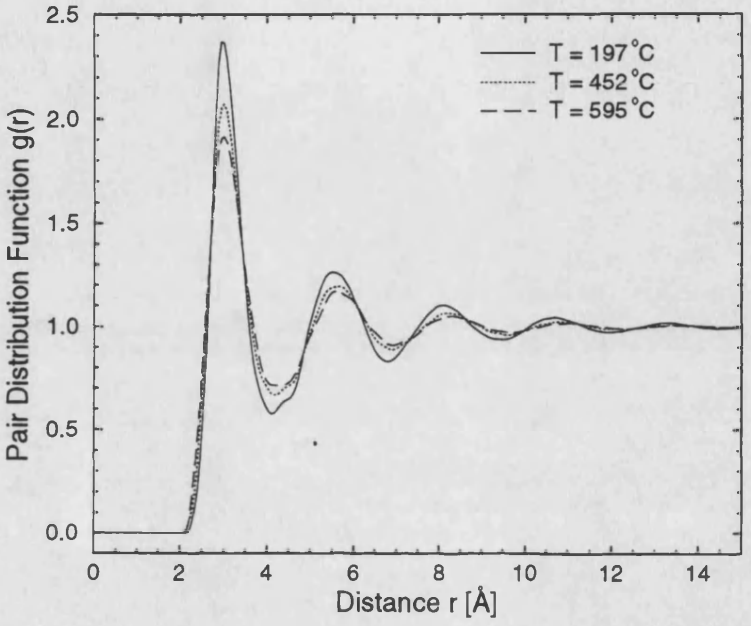

Figure 8.14: Pair distribution functions for the $\lambda = 0.7011\,\text{Å}$ data sets at 197 °C, 452 °C and 595 °C.

he real-space temperature development of the structure of liquid lithium is illustrated in figure 8.14. With increasing temperature the peaks in the pair distribution functions become broader and decrease in height. Also the position of the peaks shifts to higher-r values. These shifts are minor and within the errors for the first peak, but they become larger for successive peaks. The maximum peak positions in g(r) and nearest neighbour coordination numbers are summarised in table 8.5. The coordination numbers obtained by integrating over the first peak to the first minimum in g(r) are rather high. They have a relatively large error of ± 0.5 since the minimum after the first peak is broad and g(r) does not return to its g(0) value.

	r_1 [Å]	shoulder[a] [Å]	$\bar{n}$	integration range [Å]	r_2 [Å]
197 °C					
0.4962 Å*)	2.97(2)	3.52(3)	12.9(5)	2.15-4.17	5.53(3)
0.4962 Å**)	2.98(2)	3.52(3)	12.9(5)	2.15-4.17	5.57(3)
0.7011 Å*)	3.00(2)	3.61(3)	12.9(5)	2.15-4.17	5.55(3)
0.7011 Å**)	3.00(2)	3.61(3)	12.9(5)	2.15-4.17	5.54(3)
452 °C					
0.7011 Å*)	3.00(2)	3.72(3)	12.7(5)	2.09-4.23	5.64(3)
0.7011 Å**)	3.00(2)	3.72(3)	12.7(5)	2.09-4.23	5.57(3)
595 °C					
0.4962 Å*)	2.99(2)	3.78(3)	12.9(5)	2.15-4.30	5.68(3)
0.4962 Å**)	2.99(2)	3.74(3)	12.5(5)	2.15-4.23	5.71(3)
0.7011 Å*)	3.01(2)	3.80(3)	12.5(5)	2.15-4.23	5.59(3)
0.7011 Å**)	3.02(2)	3.89(3)	12.5(5)	2.09-4.23	5.72(3)

[a]The appearance of a shoulder on the high-r side of the first peak is shown and discussed below.

Table 8.5 : Interatomic distances and coordination numbers obtained from the spline fitted data sets (*)) and from the unsmoothed data sets (**)) for liquid lithium. r_1 and r_2 give the positions of the first and second peaks in g(r). The coordination numbers $\bar{n}$ are obtained by integrating over the first peak in g(r) to the first minimum.

By fitting the first peak in the pair distribution function with a fully symmetrised peak in g(r), a shoulder on its high-r side becomes apparent. This is the case for each of the data sets and is shown for the example of the 197 °C spline fitted data set at 0.7011 Å in figure 8.15. It is interesting to carry out a comparison of these results with the local bcc-lattice structure of crystalline lithium (see e.g. Wells[28]). Assuming a local bcc-structure, a 'pseudo'-lattice parameter a_{liquid} can be calculated, using the number density of liquid lithium,

$$a_{liquid} = \sqrt[3]{\frac{atoms\ in\ unit\ cell}{number\ density}} = \sqrt[3]{\frac{2}{n_0}} \quad . \tag{8.17}$$

Hence a comparison of the obtained coordination numbers and the positions of the first peak and its shoulder with the corresponding values expected for a bcc-structure is possible. Equation 8.17 gives an a_{liquid} of 3.57 Å, 3.62 Å and 3.66 Å for the temperatures of 197 °C, 452 °C and 595 °C respectively.

A bcc-lattice is characterised by

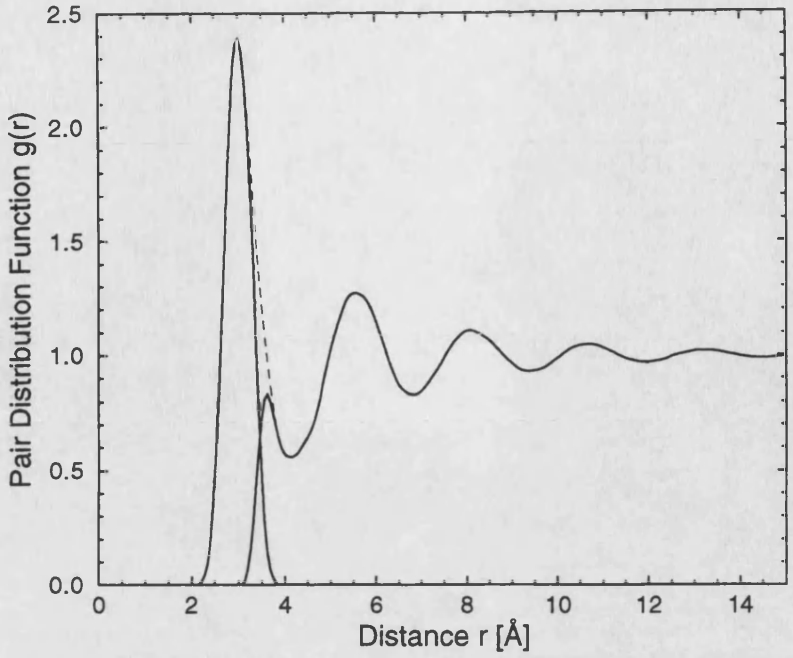

Figure 8.15: Pair distribution function for the 197 °C data set at 0.7011 Å. Fitting the first peak with a fully symmetrised peak emphasizes the high-r shoulder.

8 atoms at $\frac{\sqrt{3}}{2}a$

6 atoms at a

12 atoms at $\sqrt{2}a$, where a is the lattice parameter.

The coordination numbers and distances therefore expected for the data sets are summarised and compared with the measured values in table 8.6.

The coordination numbers corresponding to the first symmetrised peak are found to be between 7.7 and 8.5 for all of the data sets, and the nearest neighbour distances given in table 8.6 show that the first peaks and their shoulders occur close to the expected distances. This indicates that the liquid, at a short range scale, still shows the characteristics of the crystalline structure it melts from.

	distance 1 [Å]	$\overline{n}_1$	distance 2 [Å]	$\overline{n}_2$	distance 3 [Å]
197 °C					
expected	3.09	8	3.57	6	5.05
0.4962 Å	2.97(2)	8.5	3.52(3)	3.2	(5.53)
0.7011 Å	3.00(2)	7.8	3.61(3)	3.2	(5.55)
452 °C					
expected	3.14	8	3.62	6	5.12
0.7011 Å	3.00(2)	8.5	3.72(3)	3.4	(5.64)
595 °C					
expected	3.17	8	3.66	6	5.18
0.4962 Å	2.99(2)	8.4	3.78(3)	4.6	(5.68)
0.7011 Å	3.01(2)	7.7	3.80(3)	4.5	(5.59)

Table 8.6 : Parameters expected for a local bcc-lattice structure in liquid lithium compared with the measured values. $\overline{n}_1$ was obtained by fitting the first peak in the pair distribution function with a fully symmetrised peak in g(r) and $\overline{n}_2$ by fitting the shoulder with a fully symmetrised peak.

8.5.3 Comparison with Molecular Dynamics simulations and theoretical calculations - the ion-ion structure factor

Our neutron diffraction data at $\lambda = 0.7011$ Å and T = 197 °C are first compared in figure 8.16 with the experimental structure factors obtained at comparable temperatures that are available in the literature. Our structure factor differs markedly from the former neutron diffraction data of Olbrich et al.[8], obtained using the D4 diffractometer at the ILL at a temperature of 197 °C with incident neutrons of $\lambda = 0.695$ Å. Olbrich et al.'s[8] structure factor is lower than our data in the region between $1 - 2\,\text{Å}^{-1}$, and the first peak is too high, which can be understood as a consequence of the erroneous scaling (see section 8.1). Waseda's [29] x-ray data taken at 190 °C exhibits a systematic shift of the oscillations for values of $Q \geq 3\,\text{Å}^{-1}$. Olbrich et al.[8]'s x-ray structure factor differs from all the other data sets in the range of $1.0\,\text{Å}^{-1} \leq Q \leq 1.65\,\text{Å}^{-1}$, although differences in the low-Q region are expected between the structure factors obtained from neutron and x-ray

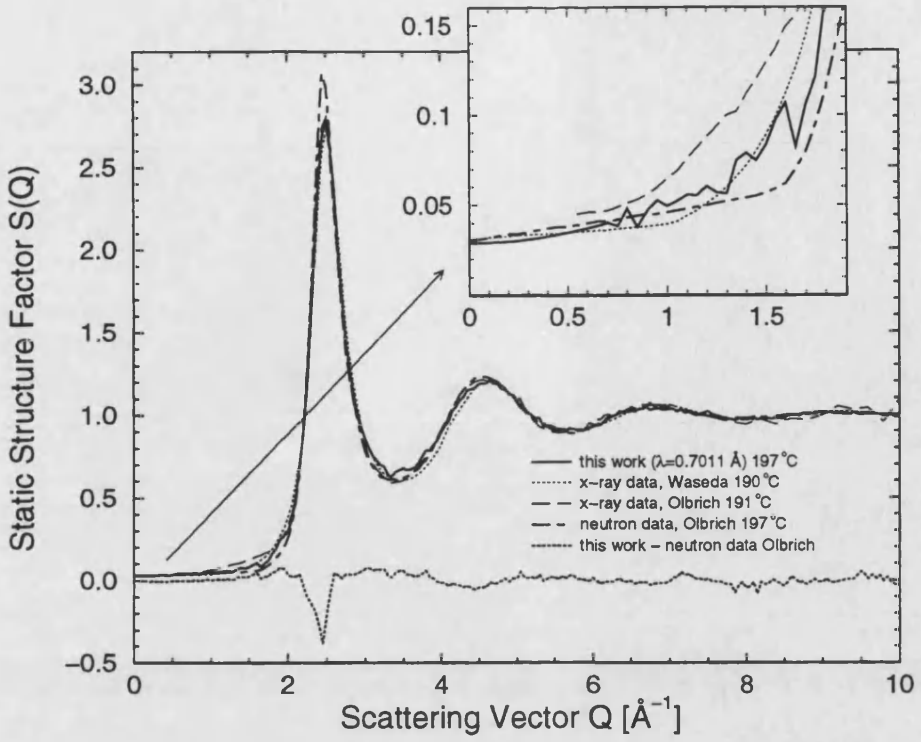

Figure 8.16: Comparison of the experimentally obtained structure factors. Our $\lambda = 0.7011$ Å data at 197 °C is compared with the neutron diffraction data set measured by Olbrich et al.[8] and with the x-ray diffraction data sets measured by Waseda[29] and by Olbrich et al.[8]. The marked difference between the two neutron diffraction data sets is displayed by the thick dotted curve. The inset shows the low-Q region of the structure factor.

diffraction, see section 8.5.4. Olbrich et al.[8] used an experimentally determined correction to try to overcome the problems associated with the correction of x-ray data for inelastic (Compton) scattering, which is rather substantial for Lithium. Therefore the profile of this x-ray structure factor is anticipated to be closer to the real one at low-Q than the profile of Waseda's[29].

González et al.[4], [5] have carried out theoretical integral equation calculations, using the Variational Modified Hypernetted Chain (VMHNC) approximation. They have shown that two different local pseudopotentials yield good results for the static and dynamic structure and for the thermodynamic properties of liquid lithium, although the shape of the pseudopotentials is rather different. One is the Ashcroft empty core potential (Ashcroft[30]), that contains the core radius as a fit parameter, and the other is the NPA (neutral pseudoatom) potential, that leads to an effective interatomic potential without any fitting parameter.

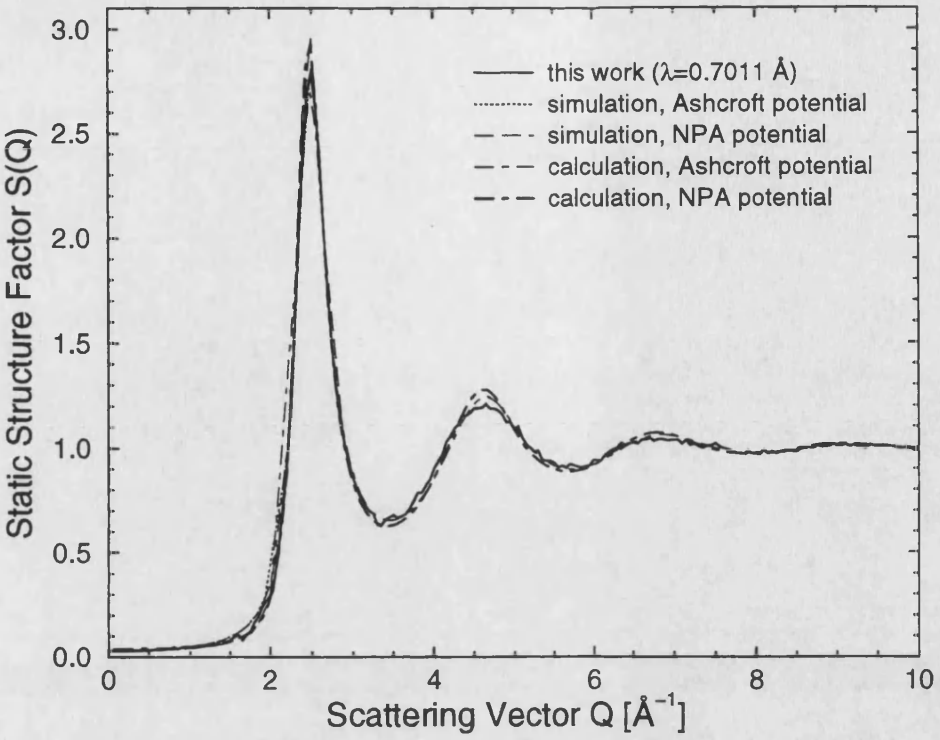

Figure 8.17: Comparison of the measured static structure factor ($\lambda = 0.7011$ Å and T = 197 °C) with the results from classical molecular dynamics simulations (Canales et al.[6] for the NPA, Canales[32] for the Ashcroft empty core potential, data is only given in the range up to ≈ 1.8 Å) and integral equation calculations (González et al.[4], [5] for the NPA and González[32] for the Ashcroft empty core potential), both at a temperature of 197 °C, using two different effective interatomic potentials.

The Ashcroft empty core radius used in the simulations and calculations is determined by the height of the first peak in the structure factor. Our $\lambda = 0.7011$ Å, T = 197 °C neutron diffraction data yielded a correction for this fit parameter, from 1.44 a.u., obtained from Olbrich et al.'s[8] neutron data, to 1.35 a.u. (González et al.[31]). The structure factors were therefore recalculated using the adjusted Ashcroft empty core potential by González & Canales[32]. The results, obtained from the original NPA potential and the adjusted Ashcroft empty core potential, are shown for reciprocal space in figure 8.17 and for real-space in figure 8.18. The effect of the improved fit parameter can be seen in figure 8.19 for the structure factor at low-Q values.

It is seen from figures 8.17 and 8.18 that both pseudopotentials describe the structure of liquid lithium very well in the respect that all of the oscillations in the

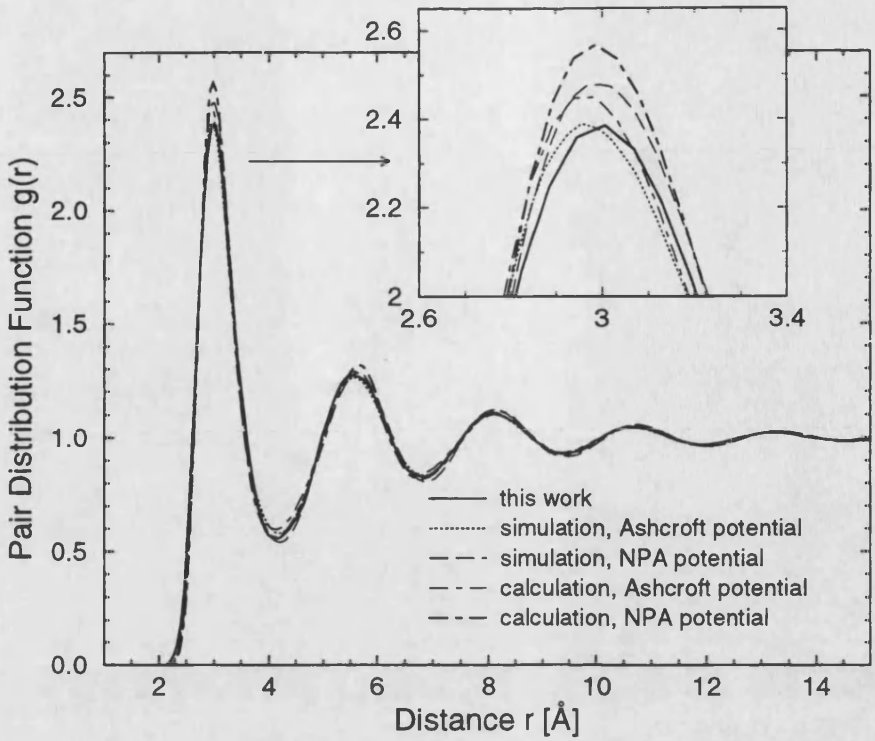

Figure 8.18: Comparison of the pair distribution functions for liquid lithium at 197 °C obtained in our neutron diffraction experiment ($\lambda = 0.7011$ Å) with the results from molecular dynamics simulations by Canales et al.[6] for the NPA, Canales[32] for the Ashcroft empty core potential, and calculations by González et al.[4], [5] for the NPA and González[32] for the Ashcroft empty core potential.

simulated and calculated data sets in reciprocal and real-space are in phase with our experimental data. However the peak heights in S(Q) and g(r) are slightly overestimated in the simulated and calculated results obtained by using the NPA potential and for the calculated results obtained by using the Ashcroft potential. The agreement is better for the simulated data set where the Ashcroft empty core potential is used. This result is not surprising since, as stated above, the height of the first peak in S(Q) was used as a fit parameter for this potential. The inset in figure 8.18 shows that the position of the first peak in real-space for the data sets obtained from the NPA potential at 2.99(1) Å is in accordance with the experimental result of 2.00(2) Å (table 8.5), whereas in the data sets obtained from the Ashcroft potential the first peak appears at the slightly lower value of r = 2.96(1) Å.

Since the crucial range for the comparison of experimental data with the sim-

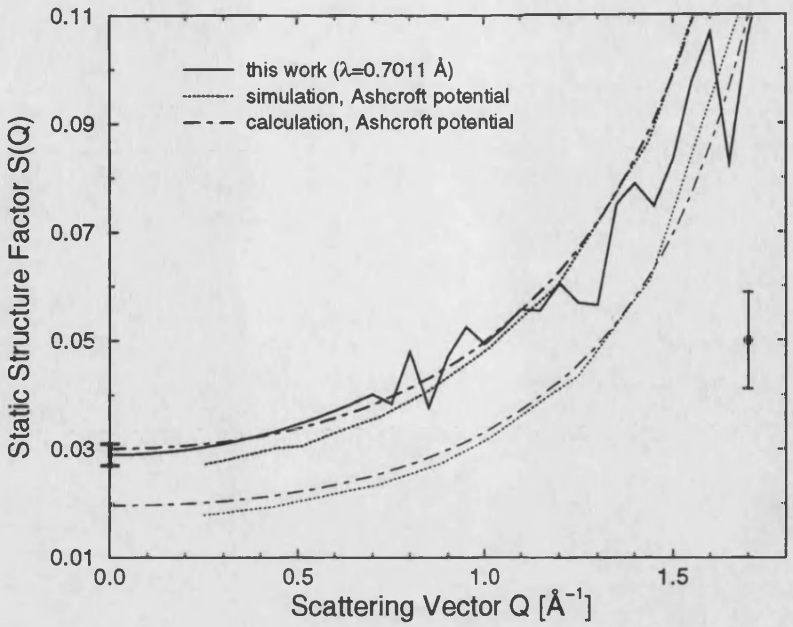

Figure 8.19: Comparison of the static structure factors in the low-Q region for liquid lithium at 197 °C obtained from molecular dynamics simulations by Canales et al.[6],[32] and calculations by González et al.[4],[5],[32] for the Ashcroft empty core potential using the core radius given by the Olbrich et al.[8] neutron data (lower curves) and the new data (upper curves). The agreement with the experimental results is strongly improved by using the new fit parameter. The vertical bar gives a representative error bar on the experimental data.

ulated and calculated results is at low-Q values (Canales et al.[6]), the structure factors are shown on an enlarged scale in this region in figure 8.20. Both Canales et al.[6] in their simulations and González et al.[5] in their calculations found a quadratic behaviour of the static structure factor at $Q \rightarrow 0$, in agreement with our results. The comparison shows that in general the agreement is very good, the data sets agree with the measured structure factor well within its statistical uncertainties, except that the S(Q) obtained from the calculation using the NPA potential tends to a slightly too high $S(Q = 0)$ value. However, this disagreement should not be overstated since it depends on the approximation used in the integral equation calculations. The molecular dynamics results are anticipated to be more reliable, except that the quality of the results at low-Q will be limited by the size of the simulation box.

In summary, the comparison with our experimental results does not, therefore, enable us to make a definite decision about which of the two different pseudopoten-

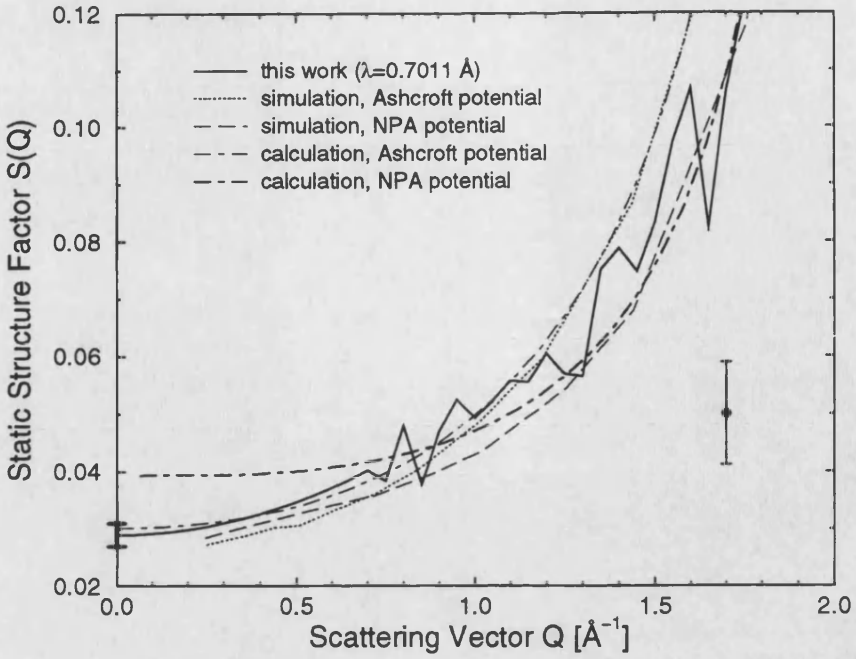

Figure 8.20: Comparison of the static structure factors, given in figure 8.17, in the small-Q region. The error bar gives a representation of the uncertainty on the measured data points.

tials yields a better description of the static structure of liquid lithium. However, Canales et al.[6] found that the sound velocity calculated from the simulated NPA data sets agrees better with the measured values. Also, Sinn et al.[33] obtained in their high resolution inelastic x-ray scattering measurements of the coherent dynamic structure factor in the low-Q region a much better agreement with the molecular dynamics simulations using the NPA potential than with those using the Ashcroft empty core potential. However, at the time of this comparison the empty core radius obtained from the Olbrich et al.[8] neutron data was used. It would be interesting to use the re-parameterised Ashcroft empty core potential and to see how sensitive $S(Q,\omega)$ is to the empty core radius.

Very recently Anta et al.[34],[7] have performed intensive *ab initio* molecular dynamics simulations on the liquid metals Li, Na, Mg, and Al using the Orbital-Free version of the Car-Parrinello technique to obtain the ion-ion and ion-electron structure factors. In figure 8.21 a comparison of the ion-ion structure factors from the simulations (Anta & Madden[7]) with our neutron diffraction results is given. The good agreement proves the validity of the simulation results and of the pseudopotentials used therein. At low-Q, the simulation using pseudopotential 'B' agrees

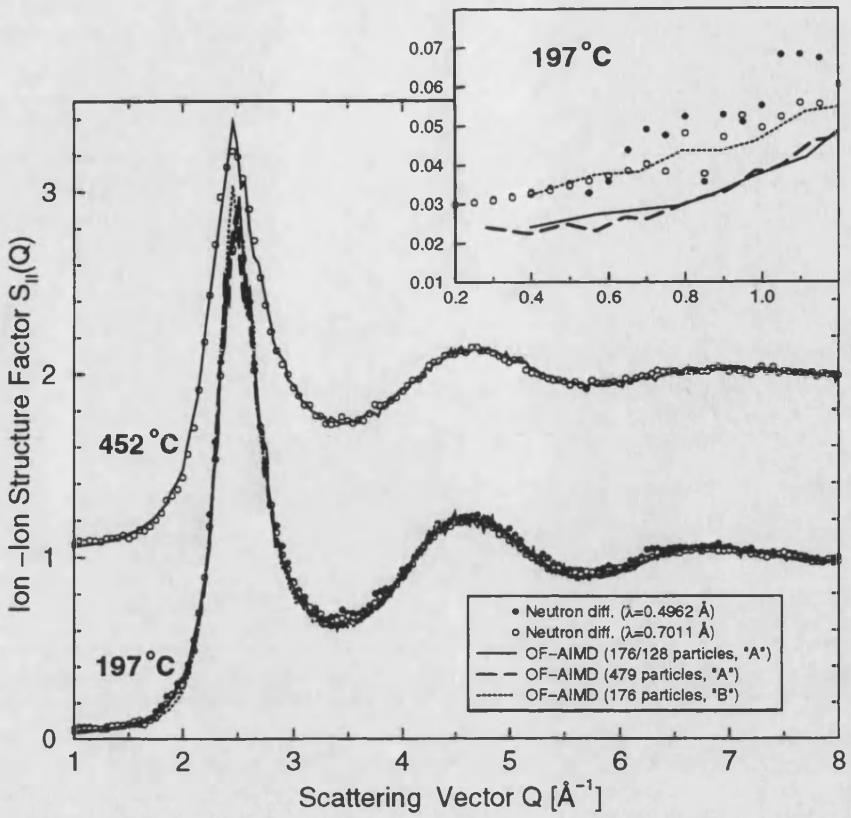

Figure 8.21: Ion-ion static structure factors for liquid lithium at 197 °C and 452 °C. The results for the higher temperature are shifted upwards by unity, and the inset displays the low-Q region of the structure factors.

almost perfectly with the experimental data sets, indicating the high quality of the simulation study. 'A' and 'B' in the simulation denote the two pseudopotentials used by Anta & Madden[7]. Detailed information about the derivation of these pseudopotentials, and the reasons for favouring pseudopotential 'B', can be found in Anta & Madden[7].

8.5.4 The ion-valence electron structure factor

Since Egelstaff et al.[35] pointed out the possibility of separating the *ion-electron*, *electron-electron*, and *ion-ion* correlations in liquid metals by combining the results from three different methods, such as electron, x-ray, and neutron diffraction, several efforts have been made to separate these partial correlations (e.g. Tamaki[36] and Takeda et al.[37],[38]). Following a suggestion by Dobson[39], Chihara[3] has shown that a separation of the ion-electron correlations should be possible from the

difference between only two structure factors, namely $S_N(Q)$ and $S_X(Q)$. $S_N(Q)$ is the structure factor obtained from neutron diffraction experiments and therefore yields the pair correlations between the ions. $S_X(Q)$ is the structure factor obtained from x-rays and therefore comprises the ion-electron, electron-electron and ion-ion type correlations.

Following Chihara[3], and using the Ashcroft-Langreth partial structure factors (see section 2.10, equation 2.60), we obtain for the ion-valence electron structure factor,

$$S_{IE}(Q) = \frac{1}{\sqrt{Z}}\rho(Q)S_{II}(Q) \tag{8.18}$$

and for the electron-electron structure factor

$$S_{EE}(Q) = \frac{|\rho(Q)|^2}{Z}S_{II}(Q) + S^0_{EE}(Q) \ , \tag{8.19}$$

where Z is the number of valence electrons, $\rho(Q)$ the form factor of the valence electrons, $S_{II}(Q)$ is the ion-ion structure factor, and $S^0_{EE}(Q)$ is the incoherent part of the electron-electron structure factor that is measured in an inelastic Compton scattering experiment (Chihara[3]).

$S_{II}(Q) \equiv S_N(Q)$ is related to the coherent scattered intensity of neutrons, $I^N_{coh}(Q)$, via

$$\frac{I^N_{coh}(Q)}{N} = \bar{b}^2 S_{II}(Q) \tag{8.20}$$

where N is the number of ions, and $\bar{b}$ the coherent scattering length (see e.g. section 2.7).

The scattered intensity, $I^X(Q)$ for a liquid metal in an x-ray diffraction experiment, neglecting the forward scattering, is given by (see e.g. Chihara[3]),

$$\begin{aligned} \frac{I^X(Q)}{N} &= |f_I(Q)|^2 S_{II}(Q) + 2f_I(Q)\sqrt{Z}S_{IE}(Q) + ZS_{EE}(Q) + Z_B S^I_{inc}(Q) \\ &= |f_I(Q) + \rho(Q)|^2 S_{II}(Q) + ZS^0_{EE}(Q) + Z_B S^I_{inc}(Q) \end{aligned} \tag{8.21}$$

where

$$ZS^0_{EE}(Q) + Z_B S^I_{inc}(Q) \approx Z_A S^A_{inc}(Q) \tag{8.22}$$

and

$$f_M(Q) = f_I(Q) + \rho(Q) \, . \tag{8.23}$$

In the above equations Z_B and Z_A are the number of bound electrons and the total number of electrons respectively, $f_I(Q)$ represents the ionic x-ray form factor,

$f_M(Q)$ the form factor of the liquid metal, and $f_A(Q)$ the form factor of the free atom. $Z_B S^I_{inc}(Q)$ is the incoherent (Compton) scattering factor of the ion, and $Z_A S^A_{inc}(Q)$ the incoherent (Compton) scattering factor of an atom with atomic number Z_A. Usually, the x-ray structure factor $S_X(Q)$ of a liquid metal is given by (Chihara[3]),

$$\begin{aligned} S_X(Q) &= \frac{I^X(Q)/N - Z_A S^A_{inc}(Q)}{|f_A(Q)|^2} \\ &\approx \left|\frac{f_M(Q)}{f_A(Q)}\right|^2 S_{II}(Q)\,. \end{aligned} \tag{8.24}$$

Therefore it follows for the difference of the x-ray and neutron diffraction structure factors,

$$S_X(Q) - S_N(Q) \approx \left[\left|\frac{f_I(Q)}{f_A(Q)}\right|^2 - 1\right] S_{II}(Q) + \frac{2 f_I(Q)\rho(Q) S_{II}(Q)}{f_A(Q)^2} + \frac{|\rho(Q)|^2 S_{II}(Q)}{f_A(Q)^2} \tag{8.25}$$

and for the form factor of the valence electrons, $\rho(Q)$,

$$\rho(Q) = \sqrt{\frac{|f_A(Q)|^2\, S_X(Q)}{S_N(Q)}} - f_I(Q) \tag{8.26}$$

The valence electron form factor obtained from equation 8.26 using the neutron diffraction structure factor resulting from the average of the measured neutron diffraction structure factors at 197 °C and the x-ray diffraction structure factor at 191 °C given by Olbrich et al.[8] (see figure 8.16) is shown in figure 8.22. For the neutron data, the average of the measured $\lambda = 0.4962$ Å and $\lambda = 0.7011$ Å structure factors was used because of their good agreement (see figure 8.11) to improve the statistics on the data. The equations to calculate the form factors, $f_I(Q)$ and $f_A(Q)$, were taken from the international tables for crystallography[40]. It is seen in figure 8.22 that for low-Q, $\rho(Q)$ tends to the correct limit for lithium of unity within the uncertainties on the data. These uncertainties are an estimate only, since they were calculated using solely the averaged statistical uncertainties on our measured data sets because the errors on the x-ray data were not available. The shape of the derived valence electron form factor also agrees qualitatively with those given by Olbrich et al.[8], which were calculated for the valence electrons of crystalline lithium.

In figure 8.23 the valence electron form factor obtained from the experimental data sets is compared with the differences $[f_A(Q) - f_I(Q)]$ and $[f_M(Q) - f'_I(Q)]$

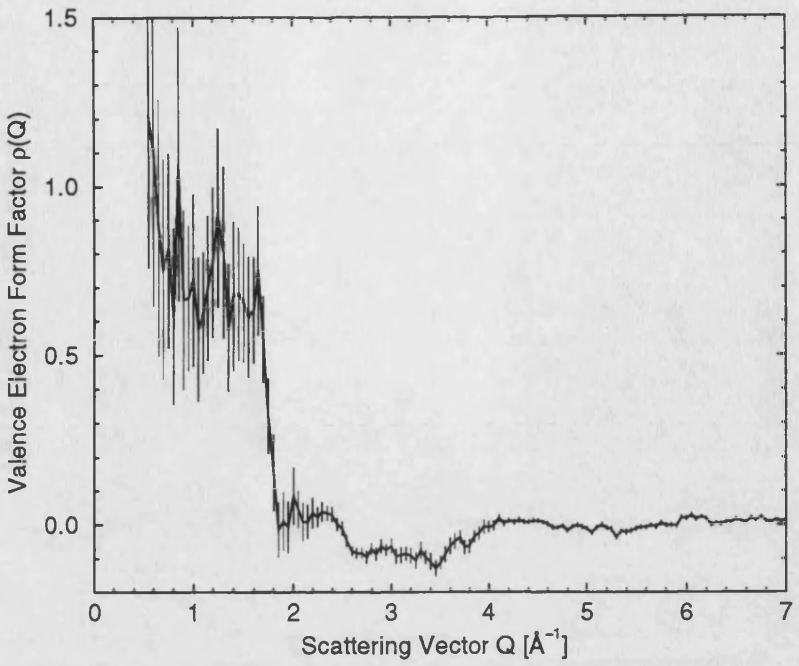

Figure 8.22: Form factor of the valence electrons, $\rho(Q)$, obtained from the combination of our neutron diffraction experiments with the x-ray diffraction measurements of Olbrich et al.[8]. The error bars on the data points are an estimate of the statistical uncertainties (see text).

where $f_M(Q)$ and $f'_I(Q)$ are calculated using the Quantum Hypernetted Chain Approximation by Anta & Louis[41]. It is seen that, especially at low-Q, there are differences between $[f_A(Q) - f_I(Q)]$ and $[f_M(Q) - f'_I(Q)]$, and therefore between the free atom and the metal atom form factors. These differences show the influence of bonding. At $\approx 1 - 1.8\,\text{Å}^{-1}$, the experimental $\rho(Q)$ is higher than both of the other functions. This can be traced to the x-ray data having a high intensity relative to the neutron data in this region, which may be associated with an incoherent background problem which was highlighted by Sinn & Burkel[42] in their x-ray small-angle scattering experiment on lithium. The comparison calls for a new x-ray diffraction experiment to measure the structure factor of liquid lithium using up-to-date methods, e.g. the use of synchrotron radiation.

In their *ab initio* molecular dynamics simulations on the liquid metals Na, Mg, and Al, using the Orbital-Free version of the Car-Parrinello technique, Anta et al.[34] found that their ion-valence electron structure factors differ substantially from the experimental data obtained by Takeda et al.[37],[38], and that the difference between the x-ray and neutron diffraction structure factors should be much

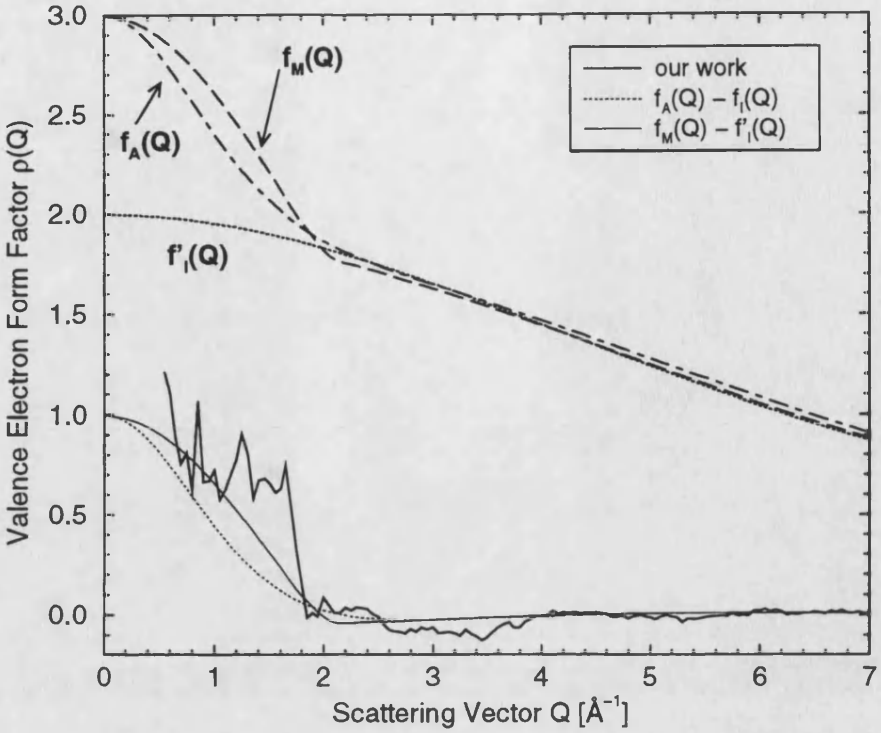

Figure 8.23: Experimental valence electron form factor at T = 197 °C compared with $[f_A(Q) - f_I(Q)]$ and $[f_M(Q) - f'_I(Q)]$. $f_A(Q)$ and $f_I(Q)$ were taken from the international tables for crystallography[40], $f'_I(Q)$ and $f_M(Q)$ from Anta & Louis[41]. These form factors are also included in the figure.

smaller than that encountered in the experiments. Anta et al.[34] point out that for Na, Mg and Al the difference might be even smaller than the intrinsic errors in the experiments. For liquid lithium the difference is expected to be larger due to the high ratio of valence to core electrons (see section 8.1), and Anta et al.[7] used the neutron and x-ray data of Olbrich et al.[8] to obtain the ion-valence electron structure factor, $S_{IE}(Q)$, for a comparison with their results.

Since it was shown in sections 8.1 and 8.5.3 that the structure factor for liquid lithium obtained by Olbrich et al.[8] from their neutron diffraction experiments is superseded, our static structure factor was combined with the Olbrich et al.[8] x-ray data to give $S_{IE}(Q)$. The result is shown in figure 8.24 together with the molecular dynamics simulations by Anta & Madden[7]. In contrast to the situation seen in the earlier experimentally derived $S_{IE}(Q)$'s for the liquid metals Na, Mg, and Al by Takeda et al.[37], our $S_{IE}(Q)$ is of the correct scale compared to that of the theoretical structure factor (Anta & Madden[7]) and has a roughly similar

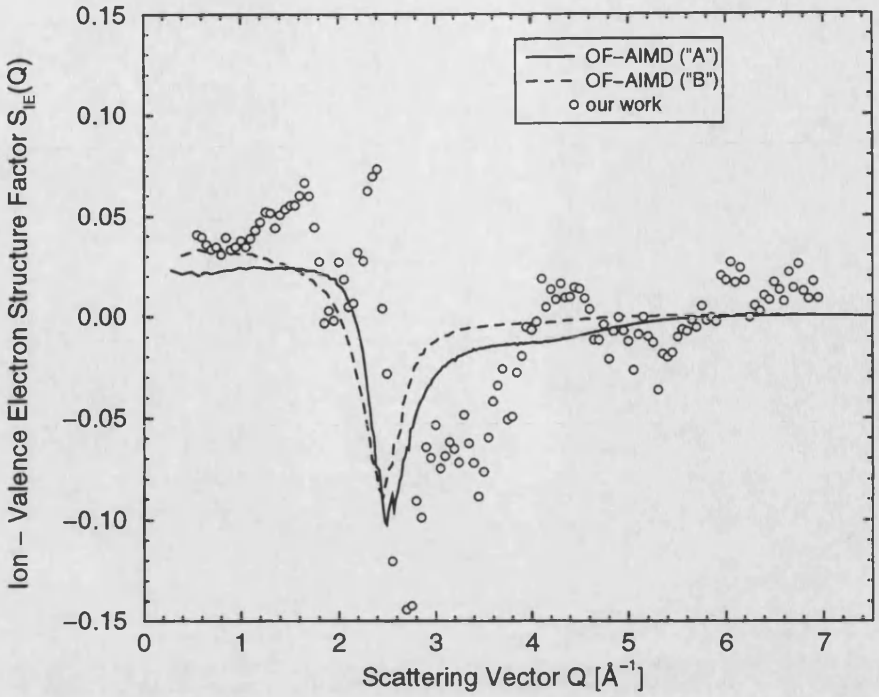

Figure 8.24: Comparison of the ion-valence electron partial structure factor at 197 °C obtained from the Orbital Free *ab initio* molecular dynamics simulations (Anta & Madden[7]) with that obtained from the combination of our neutron diffraction data sets and the Olbrich et al.[8] x-ray data.

profile. However, deviations still can be observed. Our ion-valence electron partial structure factor is too high around 2.4 Å^{-1} and too negative at its minimum around 2.60(2) Å^{-1}. This is in the region of the maximum of the first peak in the static structure factor (see table 8.4), and it can be seen from equation 8.18 that a small uncertainty in $\rho(Q)$ will have a large effect on $S_{IE}(Q)$. Our $S_{IE}(Q)$ is, though, an improvement on the one shown by Anta & Madden[7], which uses the Olbrich et al.[8] neutron data. It is less negative in its first minimum and shows less oscillations around zero at higher-Q values.

In figure 8.25 the experimental $S_{IE}(Q)$ is shown together with the functions for $S_{IE}(Q)$ that are obtained if the valence electron form factors $[f_A(Q) - f_I(Q)]$ and $[f_M(Q) - f'_I(Q)]$ in figure 8.23 are used instead of the experimental $\rho(Q)$. In the case where the free atom form factor was used, the negative peak in $S_{IE}(Q)$ has a smaller intensity compared to the function where the metal atom form factor was used.

The good agreement between the data obtained using $\rho(Q) = [f_M(Q) - f'_I(Q)]$

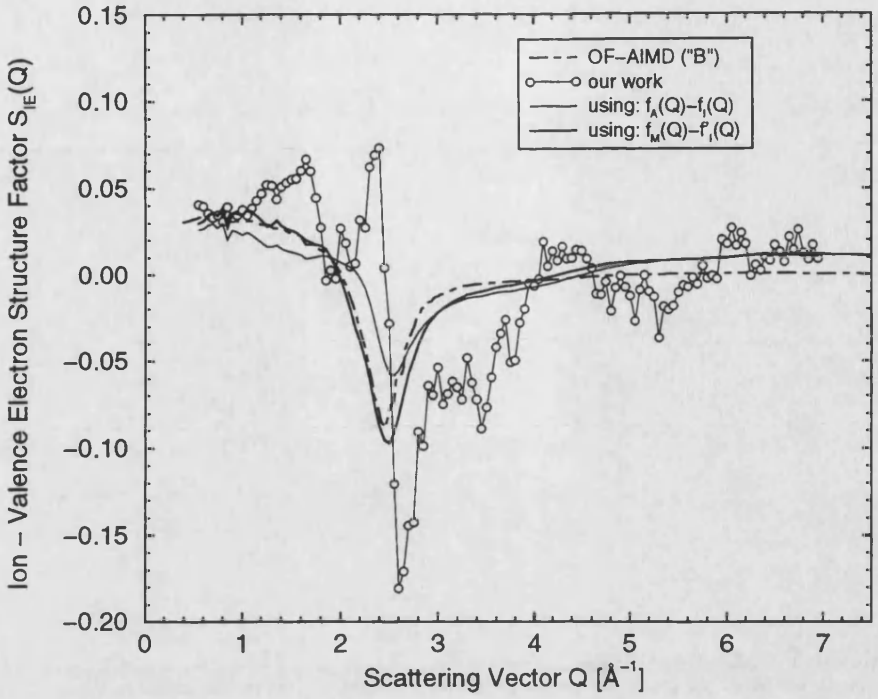

Figure 8.25: Comparison of the ion-valence electron structure factors obtained by combining our neutron data with the experimental $\rho(Q)$ and with the valence electron form factors $[f_A(Q) - f_I(Q)]$ and $[f_M(Q) - f'_I(Q)]$ shown in figure 8.23.

and our neutron data with theory (see figure 8.25) emphasizes the need for new x-ray diffraction data for liquid lithium.

8.6 Conclusions

- The analysis of the neutron diffraction data for liquid lithium was carried out very thoroughly, emphasizing the detector path integration problem and the inelasticity corrections. The data sets were then corrected for the instrumental resolution function to give reliable structure factors. The resolution function correction will now be implemented as part of the general data analysis procedure for D4B neutron diffraction experiments.

- At a short range scale, liquid lithium maintains a memory of the crystalline structure from which it melts.

- The static structure factor yields an improvement to the Ashcroft empty core radius, and the NPA pseudopotential no longer gives clearly better results for the static structure of lithium.

- The valence electron form factor and ion-valence electron partial structure factor were obtained using $S_N(Q)$ from our neutron data and $S_X(Q)$ from Olbrich et al.[8]. The results agree better in intensity and shape with those obtained from Orbital free *ab initio* molecular dynamics simulations than any other experimentally derived $S_{IE}(Q)$. The new neutron diffraction data emphasize the need for new x-ray diffraction experiments on liquid lithium.

Bibliography

[1] Silbert M, *Phys. Chem. Liq.* **13** (1983) 75.

[2] Ashcroft N W and Mermin N D, *Solid State Physics* Holt, Rinehart and Winston: New York; London (1976).

[3] Chihara J, *J. Phys.: Met. Phys.* **17** (1987) 295.

[4] González L E, González D J, Silbert M and Alonso J A, *J. Phys.: Cond. Mat.* **5** (1993) 4283.

[5] González D J, González L E and Hoshino K, *J. Phys.: Cond. Mat.* **6** (1994) 3849.

[6] Canales M, González L E and Padró J A, *Phys. Rev. E* **50** (1994) 3656.

[7] Anta J A and Madden P A, *J. Phys.: Cond. Mat.* **11** (1999) 6099.

[8] Olbrich H, Ruppersberg H and Steeb S, *Z. Naturforsch.* **38a** (1983) 1328.

[9] Ohse R W, Ed. *Handbook of Thermodynamic and Transport Properties of Alkali Metals* Blackwell Scientific Publications: Oxford. 1985

[10] Ruppersberg H and Egger H, *J. Chem. Phys.* **63a** (1975) 4095.

[11] de Jong P H K, *Microscopic dynamics and structure of liquid lithium and liquid lithium-based alloys* PhD thesis, Delft University of Technology 1993.

[12] Sears V F, *Neutron News* **3** (1992) 26.

[13] Weast R C, ed. *CRC Handbook of Chemistry and Physics* 67^{th} edition, CRC Press: Boca Raton (1986).

[14] Squires G L, *Introduction to the theory of thermal neutron scattering*, University Press: Cambridge (1978).

[15] Yarnell J L, Katz M J, Wentzel R G and Koenig S H, *Phys. Rev. A* **7(6)** (1973) 2130.

[16] Wick G C, *Phys. Rev.* **94** (1954) 1228.

[17] Egelstaff P A and Soper A K, *Molec. Phys.* **40 (3)** (1980) 553.

[18] Soper A K, *Private Communication* (1998) .

[19] Verkerk P, *Private Communication* (1996) .

[20] Bellissent-Funel M-C, Bosio L and Teixeira J, *J. Phys.: Cond. Mat.* **3** (1991) 4065.

[21] March N H and Silbert M, *Phys. Chem. Liq.* **13** (1983) 155.

[22] van Laar B and Yelon W B, *J. Appl. Cryst.* **3** (1984) 47.

[23] Howells W S, *Nucl. Inst. Meth. in Phys. Res.* **219** (1984) 543.

[24] Fischer H E, *Private Communication* (1999) .

[25] Howells W S, *Private Communication* (1999) .

[26] Finger L W, Cox D E and Jephcoat A P, *J. Appl. Cryst.* **27** (1994) 892.

[27] Xin S, *Ph.D. Thesis, University of East Anglia* (1996).

[28] Wells A F, *Structural Inorganic Chemistry* (1984) Oxford: Claredon Press.

[29] Waseda Y, *The structure of non-crystalline materials: liquids and amorphous solids*, Mc Graw Hill: New York (1980).

[30] Ashcroft N W, *Phys. Lett.* **23** (1966) 48.

[31] González L E, *Private Communication* (1997).

[32] González L E and Canales M *Private Communication* (1997).

[33] Sinn H, Sette F, Bergmann U, Halcoussos C, Krisch N, Verbeni R and Burkel E, *Phys. Rev. Lett.* **78** (1997) 1715.

[34] Anta J A, Jesson B J and Madden P A, *Phys. Rev. B* **58/10** (1998) 6124.

[35] Egelstaff P A, March N H and McGill N C, *Can. J. Phys.* **52** (1974) 1651.

[36] Tamaki S, *Can. J. Phys.* **65** (1987) 286.

[37] Takeda S, Inui M, Tamaki S, Maruyama K and Waseda Y, *J. Phys. Soc. Jap.* **63** (1994) 1794.

[38] Takeda S, Kawakita Y, Inui M, Maruyama K, Tamaki S, and Waseda Y, *J. Non-Cryst. Sol.* **205-207** (1996) 365.

[39] Dobson P J, *J. Phys. C: Sol. Stat. Phys.* **11** (1978) L295.

[40] Ed. Wilson A J C, *International Tables for Crystallography* Vol. C *Mathematical, Physical and Chemical Tables*, Kluwer Academic Publishers: Dordrecht/Boston/London (1995).

[41] Anta J A and Louis A A, *Phys. Rev. B* (submitted) .

[42] Sinn H and Burkel E, *J. Phys.: Cond. Mat.* **8** (1996) 9369.

Chapter 9

An investigation of the Jahn-Teller effect in Cu^{2+}-Perchlorate solutions

9.1 Introduction and previous studies

In aqueous solutions the rate of water exchange for water bound to Cu^{2+} with the bulk, k_{ex}, is much faster than for most other ions of comparable size and charge. For example, although, Cu^{2+} and Ni^{2+} have very similar crystallographic radii (0.72 Å for Cu^{2+} and 0.69 Å for Ni^{2+}) the ratio of their water exchange rates is $k_{ex}^{Cu}/k_{ex}^{Ni} \approx 1.3 \times 10^5$ at 25 °C with $k_{ex}^{Cu} = 4.4(1) \times 10^9\,s^{-1}$ (Powell et al.[1]). This very fast solvent exchange for Cu^{2+} solutions has also been found by incoherent quasi-elastic neutron scattering (IQENS), indicating an ion to solvent proton binding time $\tau_b \leq 10^{-10}$ s. The fast exchange rate is attributed to the Jahn-Teller effect, which distorts the structure around the $[Cu(H_2O)_6]^{2+}$ complex from an octahedral to a tetragonal symmetry, giving four nearest-neighbour equatorial oxygen sites and two axial oxygen sites at a somewhat larger Cu-O distance (see e.g. Magini[2], Salmon et al.[3], Salmon & Neilson[4] and Nomura & Yamaguchi[5]). The distortion is anticipated to be dynamic, the axis of distortion changing on a characteristic timescale of $\tau_i = 5.1(6) \times 10^{-12}$ s (Powell et al.[1]). The water exchange is likely to occur at the more distant axial positions than at the closer equatorial sites, and the axis of inversion changes rapidly so that after many inversions all of the bound

water molecules will have exchanged with the bulk. Therefore the dynamic Jahn-Teller effect is regarded as having a strong influence on the fast water exchange rate with the bulk and a knowledge of the degree of distortion of the hydration complex is desired.

Several structural studies using EXAFS (extended x-ray absorption fine structure) and x-ray diffraction have been performed on Cu^{2+} solutions, and they will be compared in detail with our results in section 9.5.3. Generally, four equatorial oxygen atoms are observed at a distance $r_{CuO} = 1.95 - 2.00$ Å, but for the positions of the axial atoms the agreement between different authors is poor, probably due to the difficulty of resolving this contribution in the radial distribution function and in some cases due to the penetration of the counter ion into the hydration shell (Powell et al.[1]). The neutron diffraction first-order difference method (with Cu isotopes) has also been applied to several Cu^{2+} solutions, e.g. to $CuCl_2$ and $Cu(ClO_4)_2$ (Salmon et al.[3]), and $Cu(NO_3)_2$ (Salmon & Neilson[4]). For solutions with non-liganding counter ions, four equatorial oxygen atoms are found at a distance $r_{CuO} = 1.96$ Å. However, no definite information has been obtained on the deuterium atom or the axial oxygen atom correlations, as these contributions to the first-order difference pair-distribution function, $\Delta G_{Cu}(r)$, overlap at $r \geq 2.21$ Å. Moreover, the information on the axial oxygen positions that is available from the neutron diffraction work contradicts the x-ray and EXAFS results since the latter place the axial oxygen atoms at the minimum in intensity of the $\Delta G_{Cu}(r)$ function.

Crystal structure:

For the Cu^{2+} ion in the crystalline state a (4+1) or (4+2) structural configuration is most commonly observed (e.g. Wells[6]). In crystalline copper perchlorate hexahydrate, $Cu(ClO_4)_2 \cdot 6H_2O$, however, Gallucci & Gerkin[7] found a rhombic distortion of the $[Cu(H_2O)_6]^{2+}$ complex that gives three characteristic bond lengths. Two oxygen atoms are located at 1.953(1) Å, 2 oxygen atoms at 1.970(4) Å, and a further 2 oxygen atoms at 2.388(2) Å. These water oxygens are linked via hydrogen bonds with the perchlorate oxygens. $Cu(ClO_4)_2 \cdot 6H_2O$ has a monoclinic crystal structure of space group $P2_1/c$ with cell dimensions of a = 5.137(1) Å, b = 22.991(3) Å, c = 13.849(2) Å and $\beta = 90(1)°$. The structure of copper perchlorate hexahydrate

around the Cu^{2+} ion is shown in figure 9.1.

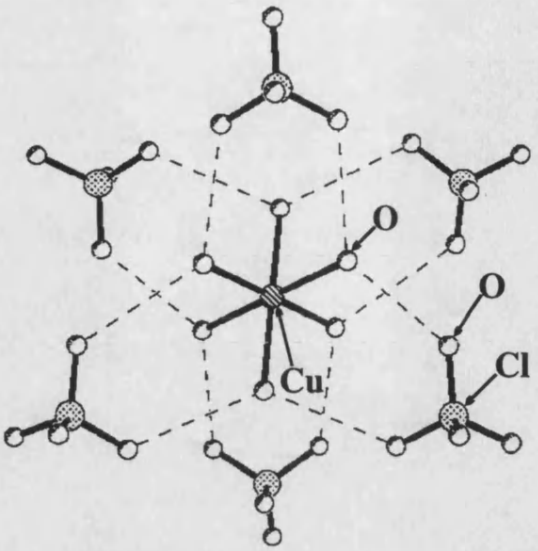

Figure 9.1: Schematic drawing of the copper perchlorate hexahydrate crystal structure around one Cu^{2+} ion (Gallucci & Gerkin[7]). The dashed lines indicate the hydrogen bonds between the oxygen atoms belonging to the water molecules and the oxygen atoms of the perchlorate molecules. The hydrogen atoms are not included in the drawing for clarity.

Gallucci & Gerkin[7] measured a Cu-Cu distance of 5.137 Å and the distances between the Cu^{2+} ion and the chloride and oxygen atoms in the perchlorate ions are all larger than 4.50 Å and 3.85 Å respectively.

Also in an aqueous solution the perchlorate ions are not prone to inner-sphere complexing. This is shown by UV-visible spectroscopy studies and by Raman and NMR spectroscopic measurements (Nomura & Yamaguchi[5]).

In our presented work, the method of neutron first-order difference functions has been used in combination with H/D substitution for $Cu(ClO_4)_2$ aqueous solutions. This challenging technique offers the possibility of directly measuring the Cu-H and Cu-O coordination environments via the measurement of partial pair distribution functions $g_{CuH}(r)$ and $g_{CuO}(r)$, and thus the ability to study the Jahn-Teller distortion of the Cu^{2+} hydration complex in detail.

9.2 Sample preparation

Four copper perchlorate solutions, with different isotopic enrichments, were prepared at the Institut de Chimie Minerale et Analytique, Lausanne, Switzerland.
2.22 molal $^{65}Cu(ClO_4)_2$, 0.11 molal $HClO_4$ in H_2O,
2.22 molal $^{63}Cu(ClO_4)_2$, 0.11 molal $HClO_4$ in H_2O,
2.0 molal $^{65}Cu(ClO_4)_2$, 0.1 molal $DClO_4$ in D_2O and
2.0 molal $^{63}Cu(ClO_4)_2$, 0.1 molal $DClO_4$ in D_2O.
An outline of the preparation procedure, given by Toth[8], can be found in appendix C. The isotopes used were ^{65}Cu (98.6(5) % ^{65}Cu and 1.4(5) % ^{63}Cu) and ^{63}Cu (99.2(5) % ^{63}Cu and 0.8(5) % ^{65}Cu), D (99.95 % D and 0.05 % H), and D_2O (99.96 % deuterated).

The different molal concentrations were chosen to ensure that the atomic fractions of particles are the same for all the solutions. For definiteness each solution will be referred to as a '2 molal solution of $Cu(ClO_4)_2$ in perchloric acid'.

9.3 Neutron diffraction parameters and experiment

The neutron diffraction experiments were performed on the D4B diffractometer at the Institut Laue-Langevin, Grenoble. The wavelength of the incident neutrons was 0.6991 Å. The samples were contained in cylindrical 'zero-alloy' Ti/Zr cans (i.e. the used alloys have a nominal coherent scattering length of zero) with inner diameters of 5 mm and 8 mm for the H_2O and D_2O solutions respectively. Both Ti/Zr cans had a wall thickness of 0.3 mm. The samples were fully illuminated with a rectangular beam of 50 mm height and 14 mm width. Diffraction patterns were measured for the four samples in their Ti/Zr containers, the empty containers, and the instrumental background with nothing placed at the sample position. Measurements of the diffraction patterns for 8.02 mm and 6.07 mm diameter vanadium rods and for 8 mm and 5 mm cadmium bars were used for the data normalisation and for the background correction at low angles (see section 3.3.1) for the deuterated and hydrogenated samples respectively. All of the measurements were carried out at ambient temperature (26 °C).

The run-times for the different solutions were optimised using the procedure outlined in appendix D. Each diffraction pattern was built up by making repeated scans of the detectors over the available range of scattering angles. The single scans agreed well within the expected statistical variations, until one particular scan when the efficiencies of both detectors changed. Thereafter the scans were again in agreement within the experimental statistical variations. The reason for this change could never be tracked down although it is anticipated to be electronic in origin. It was extensively checked that by applying a scaling factor of 1.0041 to detector 1 (i.e. the detector efficiency had decreased by 0.14 %) and of 0.9978 to detector 2 (i.e. the efficiency had increased by 0.22 %) to the scans taken after the change in the detector efficiencies, all of the scans agreed within the statistical variations and could be grouped together. Then the data analysis followed the procedure outlined in section 3.3.1.

The neutron scattering lengths and cross-sections for the elements and isotopes used, calculated for the correct isotopic enrichments, are summarised in table 9.1 which also contains the atomic fractions, c_α, of the species present in the solutions. The solution concentrations correspond to a ratio of $1\,Cu : 2\,ClO_4 : 25\,(H/D)_2O : 0.1\,(H/D)ClO_4$.

Element	$\overline{b}$ [fm]	$\sigma_{free,coh}$ [barn]	$\sigma_{free,inc}$ [barn]	σ_{abs} (@ 1.798 Å) [barn]	c_α
^{65}Cu	10.55(19)	13.6(5)	0.38(1)	2.21(3)	0.0116
^{63}Cu	6.46(15)	5.1(2)	0.009(1)	4.48(2)	0.0116
Cl	9.5770(8)	10.902(2)	5.0(5)	33.5(3)	0.0238
O	5.803(4)	3.749(5)	0.000(8)	0.00019(2)	0.3847
H	-3.7406(11)	*)	*)	0.3326(7)	0.5800
D	6.666(4)	*)	*)	0.000676(7)	0.5799

Table 9.1 : Neutron scattering lengths and cross-sections for the elements and isotopes, calculated for the correct isotopic enrichments (Sears[9]). The statistical errors are given in brackets. *) The cross-sections for hydrogen and deuterium are functions of the energy of the incoming neutrons. Measured values for H_2O and D_2O at the energy 0.167 eV corresponding to $\lambda = 0.6991$ Å, taken from Hughs & Harvey[10], Garber & Kinsey[11] and Stehn et al.[12], were used to calculate $\sigma_{free,sc} = 3.9(.7)$ barn for deuterium (average of the values given in Hughs & Harvey[10] and Garber & Kinsey[11]) and $\sigma_{free,sc} = 28.8(.9)$ barn for hydrogen (average of the values from all three).

The cross-sections of the four solutions were calculated from values given in table 9.1 and are displayed in table 9.2.

Sample	$\sigma_{\text{free,sc}}$ [barn]	σ_{abs} (@ 1.798 Å) [barn]	$\sigma^{\text{total}} = \sigma_{\text{free,sc}} + \sigma_{\text{abs}}$ (@ λ) [barn]
$^{65}Cu(ClO_4)_2$ in D_2O	4.25(41)	0.823(7)	4.56(41)
$^{63}Cu(ClO_4)_2$ in D_2O	4.15(41)	0.849(7)	4.47(41)
$^{65}Cu(ClO_4)_2$ in H_2O	18.7(5)	1.014(7)	19.1(5)
$^{63}Cu(ClO_4)_2$ in H_2O	18.58(54)	1.040(7)	18.98(54)

Table 9.2: Cross-sections of the samples. Here $\lambda = 0.6991$ Å is the wavelength of the incident neutrons.

The mass densities of the solutions at 25 °C have been measured by Toth[8] to be 1.40709 g/cm^3 for $^{65}Cu(ClO_4)_2$ in D_2O, 1.40460 g/cm^3 for $^{63}Cu(ClO_4)_2$ in D_2O, 1.37353 g/cm^3 for $^{65}Cu(ClO_4)_2$ in H_2O, and 1.37220 g/cm^3 for $^{63}Cu(ClO_4)_2$ in H_2O. These mass densities correspond to number densities of $n_0 = 0.0950(1)$ Å^{-3} for the solutions in D_2O and $n_0 = 0.0988(1)$ Å^{-3} for the solutions in H_2O.

Total structure factors :

Each total structure factor $F(Q)$ comprises ten independent partial structure factors, $S_{\alpha\beta}(Q)$,

$$\begin{aligned} F(Q) \;=\; & A[S_{CuCu}(Q)-1] + B[S_{CuO}(Q)-1] + C[S_{CuCl}(Q)-1] + \\ & D[S_{CuH}(Q)-1] + E[S_{OO}(Q)-1] + F[S_{OCl}(Q)-1] + \\ & G[S_{OH}(Q)-1] + H[S_{ClCl}(Q)-1] + I[S_{ClH}(Q)-1] + J[S_{HH}(Q)-1] \end{aligned} \tag{9.1}$$

where A, B,...J are the neutron weighting factors. They are summarised in table 9.3.

Since the four aqueous solutions comprise a large fraction of light elements (table 9.1), the departure from the static approximation is severe, and the Placzek correction (see section 2.9) is not applied. The quantity thus derived from the data

analysis for each solution is the function,

$$F^0(Q) = F(Q) + \delta(Q) \tag{9.2}$$

where δ(Q) is a correction term that predominantly comprises the inelasticity corrections.

	Definition	$^{65}Cu(ClO_4)_2$ in D_2O	$^{63}Cu(ClO_4)_2$ in D_2O	$^{65}Cu(ClO_4)_2$ in H_2O	$^{63}Cu(ClO_4)_2$ in H_2O
A	$c_{Cu}^2 b_{Cu}^2$	0.056(3)	0.150(5)	0.056(3)	0.150(5)
B	$2c_{Cu}c_O b_{Cu}b_O$	3.35(8)	5.46(10)	3.35(8)	5.46(10)
C	$2c_{Cu}c_{Cl}b_{Cu}b_{Cl}$	0.342(8)	0.558(10)	0.342(8)	0.558(10)
D	$2c_{Cu}c_H b_{Cu}b_H$	5.79(13)	9.46(17)	-3.25(8)	-5.30(10)
E	$c_O^2 b_O^2$	49.84(7)	49.84(7)	49.84(7)	49.84(7)
F	$2c_O c_{Cl} b_O b_{Cl}$	10.177(7)	10.177(7)	10.177(7)	10.177(7)
G	$2c_O c_H b_O b_H$	172.59(16)	172.59(16)	-96.87(7)	-96.87(7)
H	$c_{Cl}^2 b_{Cl}^2$	0.51953(9)	0.51953(9)	0.51953(9)	0.51953(9)
I	$2c_{Cl}c_H b_{Cl}b_H$	17.622(11)	17.622(11)	-9.890(3)	-9.890(3)
J	$c_H^2 b_H^2$	149.43(18)	149.43(18)	47.07(3)	47.07(3)

Table 9.3: Weighting factors for the four total structure factors. They are given in units of mbarn, and their statistical uncertainties are quoted in the brackets.

First order difference functions :

The subtraction of the $F^0(Q)$ functions for the two solutions in H_2O gives the first order difference function,

$$^{(H)}\Delta^0{}_{Cu}(Q) = {}^{65}_{H}F^0(Q) - {}^{63}_{H}F^0(Q) = \Delta^{(H)}_{Cu}(Q) + \delta'(Q) \tag{9.3}$$

where

$$\Delta^{(H)}_{Cu}(Q) = A'[S_{CuCu}(Q)-1] + B'[S_{CuO}(Q)-1] + C'[S_{CuCl}(Q)-1] + D'[S_{CuH}(Q)-1] \tag{9.4}$$

while subtraction of the two solutions in D_2O gives,

$$^{(D)}\Delta^0{}_{Cu}(Q) = {}^{65}_{D}F^0(Q) - {}^{63}_{D}F^0(Q) = \Delta^{(D)}_{Cu}(Q) + \delta''(Q) \tag{9.5}$$

where

$$\Delta^{(D)}_{Cu}(Q) = A'[S_{CuCu}(Q)-1]+B'[S_{CuO}(Q)-1]+C'[S_{CuCl}(Q)-1]+D'[S_{CuD}(Q)-1] \tag{9.6}$$

with $A' = c^2_{Cu}[b^2(^{65}Cu) - b^2(^{63}Cu)]$, $B' = 2c_{Cu}c_O b_O[b(^{65}Cu) - b(^{63}Cu)]$,
$C' = 2c_{Cu}c_{Cl}b_{Cl}[b(^{65}Cu) - b(^{63}Cu)]$, $D' = 2c_{Cu}c_H b_{H/D}[b(^{65}Cu) - b(^{63}Cu)]$.

The Placzek correction terms in $F^0(Q)$ are, to a good approximation, eliminated in the difference functions $\Delta^0_{Cu}(Q)$, and the residual correction terms $\delta'(Q)$ and $\delta''(Q)$ are then sufficiently small to allow $\Delta^{(H)}_{Cu}(Q)$ or $\Delta^{(D)}_{Cu}(Q)$ to be derived from ${}^{(H)}\Delta^0_{Cu}(Q)$ or ${}^{(D)}\Delta^0_{Cu}(Q)$ (Soper et al.[13] and section 3.4).

The first order difference functions in real-space, $\Delta G^{(H/D)}_{Cu}(r)$ are obtained from,

$$\begin{aligned} \Delta G^{(H/D)}_{Cu}(r) &= \frac{1}{2\pi^2 n_0 r}\int_0^\infty dQ\Delta^{(H/D)}_{Cu}(Q)Q\sin(Qr) \\ &= A'[g_{CuCu}(r)-1] + B'[g_{CuO}(r)-1] + C'[g_{CuCl}(r)-1] + \\ &\quad D'[g_{CuH/D}(r)-1]\ . \end{aligned} \tag{9.7}$$

The weighting coefficients, the low-r limits $\Delta G^{(H/D)}_{Cu}(0) = -(A' + B' + C' + D')$, and the sum-rule relations, $\int_0^\infty \Delta^{(H/D)}_{Cu}(Q)Q^2\,dQ = 2\pi^2 n_0 \Delta G^{(H/D)}_{Cu}(0)$, are summarised in table 9.4.

Solution	A' [mbarn]	B' [mbarn]	C' [mbarn]	D' [mbarn]	$\Delta G^{(H/D)}_{Cu}(0)$ [mbarn]	sum-rule [mbarn/Å^3]
$Cu(ClO_4)_2$ in D_2O	0.094(6)	2.12(13)	0.216(13)	3.67(22)	-6.10(26)	-11.4(5)
$Cu(ClO_4)_2$ in H_2O	0.094(6)	2.12(13)	0.216(13)	-2.06(12)	-0.37(18)	-0.72(35)

Table 9.4: Weighting coefficients A', B', C' and D', low-r limits $\Delta G^{(H/D)}_{Cu}(0)$, and sum-rule relations. The statistical errors are given in brackets.

Second order difference function :

It is possible to proceed to a second order difference function assuming, at the level of accuracy relevant to this work, that H and D are isomorphic i.e. that $S_{CuD}(Q)$ = $S_{CuH}(Q)$. $S_{CuH}(Q)$ can be constructed by subtracting the first order difference

function in H_2O, $\Delta_{Cu}^{(H)}(Q)$, from the one measured in D_2O, $\Delta_{Cu}^{(D)}(Q)$,

$$S_{CuH}(Q) - 1 = \frac{\Delta_{Cu}^{(D)}(Q) - \Delta_{Cu}^{(H)}(Q)}{[D'(D) - D'(H)]} \tag{9.8}$$

where

$$D'(D) - D'(H) = 2c_{Cu}c_H[b(^{65}Cu) - b(^{63}Cu)][b_D - b_H] = 0.00573(25)\,barn\,. \tag{9.9}$$

The Fourier transform of $S_{CuH}(Q)$ gives the copper-hydrogen partial pair distribution function, $g_{CuH}(r)$.

First order difference function minus weighted second order difference function :

Once $S_{CuH}(Q)$ has been measured it is possible to directly extract the copper-oxygen correlations, $S_{CuO}(Q)$, at least to a first order approximation, by subtracting a suitably weighted copper-hydrogen partial structure factor from the first order difference function :

$$\begin{aligned}
\Delta_{Cu}^{\Delta}(Q) &\equiv \left\{\Delta_{Cu}^{(D)}(Q) - D'(D)[S_{CuH}(Q) - 1]\right\}/B' \\
&= [S_{CuO}(Q) - 1] + \frac{A'}{B'}[S_{CuCu}(Q) - 1] + \frac{C'}{B'}[S_{CuCl}(Q) - 1] \qquad (9.10) \\
&= [S_{CuO}(Q) - 1] + 0.044(4)[S_{CuCu}(Q) - 1] + 0.102(9)[S_{CuCl}(Q) - 1]
\end{aligned}$$

Since the Cu-Cu distance is expected to be larger than ≈ 5 Å and the Cu-Cl distance larger than ≈ 4.5 Å, on the basis of the crystal structure for $Cu(ClO_4)_2 \cdot 6H_2O$, and since the perchlorate ion is not prone to inner-sphere complexing (see section 9.1), $\Delta G_{Cu}^{\Delta}(r)$, the Fourier transform of $\Delta_{Cu}^{\Delta}(Q)$, will be dominated by $g_{CuO}(r)$ for approximately $r < 4.5$ Å.

It has been shown before for solutions of $NiCl_2$ in water (Powell et al.[14]) that the first order difference method combined with H/D substitution is a valid technique and allows for the successful separation of the individual pair distribution functions.

9.4 Results

9.4.1 Total structure factors

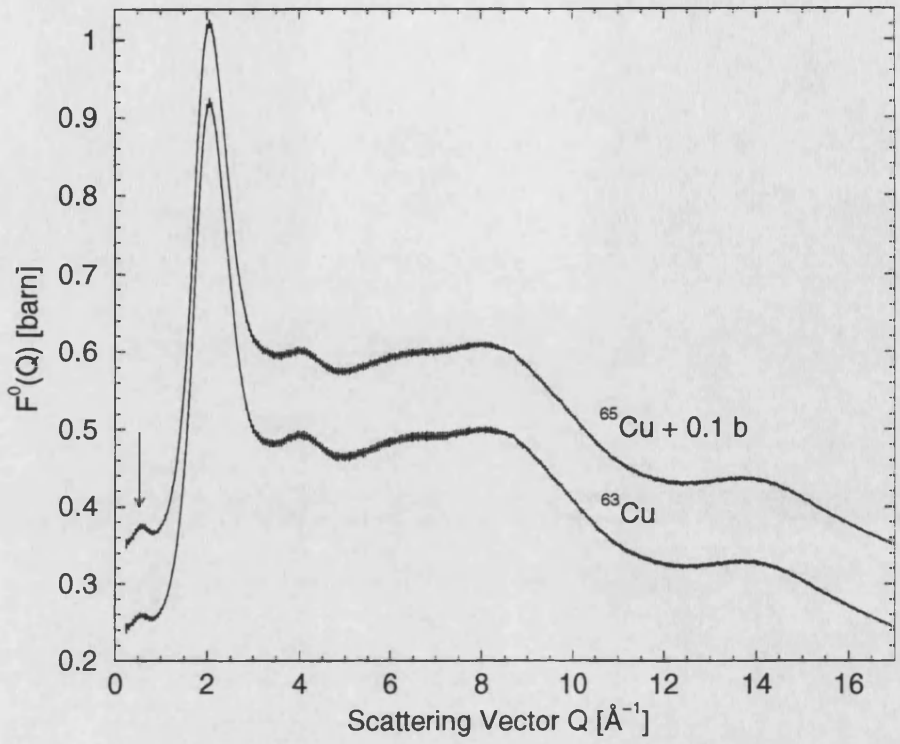

Figure 9.2: Measured total structure factors $^{65}F^0(Q)$ and $^{63}F^0(Q)$ for the solutions of 2.00 molal $Cu(ClO_4)_2$ in deuterated perchloric acid. The bars represent the error on each data point. The arrow indicates the position of the small FSDPs, and the departure from the static approximation (section 2.9) gives the $F^0(Q)$ functions the characteristic droop at high Q.

The $F^0(Q)$ functions for the solutions of 2.00 molal $Cu(ClO_4)_2$ in deuterated perchloric acid are shown in figure 9.2. They both exhibit a small FSDP (first sharp diffraction peak) at $0.58(2)\,\text{Å}^{-1}$, which is most pronounced in the $^{65}Cu^{2+}$ solution. This cation dependence of the FSDP indicates that the Cu-correlations contribute towards it. This is consistent with the measurements of Salmon et al.[3], who found a FSDP at $\approx 0.63\,\text{Å}^{-1}$ in their 2 molal solutions of $Cu(ClO_4)_2$ in D_2O. A similar feature is also observed at $0.60\,\text{Å}^{-1}$ for a 2.180 molal solution of $Cu(CF_3SO_3)_2$ in fully deuterated ethylene glycol (EG), and at $\approx 1\,\text{Å}^{-1}$ in aqueous $NiCl_2$ solutions where it can be identified with the first peak in $S_{NiNi}(Q)$ (Neilson et al.[15], Neilson & Enderby[16]). The FSDP is a feature of intermediate range ordering (Salmon[17]) and it will be discussed in more detail in section 9.5.1.

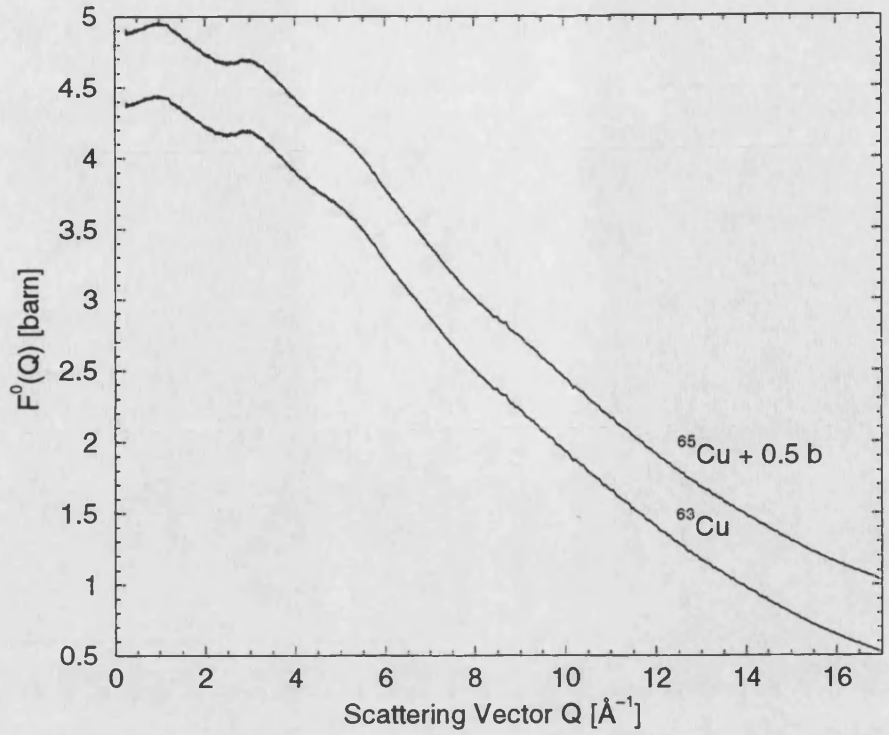

Figure 9.3: Measured total structure factors $^{65}F^0(Q)$ and $^{63}F^0(Q)$ for solutions of 2.22 molal $Cu(ClO_4)_2$ in hydrogenated perchloric acid.

The $F^0(Q)$ functions for the solutions of 2.22 molal $Cu(ClO_4)_2$ in hydrogenated perchloric acid are displayed in figure 9.3. The FSDP in these functions is concealed by the presence of the substantial incoherent scattering contribution of hydrogen.

9.4.2 First order difference functions

The first order difference function, $\Delta_{Cu}^{(D)}(Q)$, is obtained from equation 9.5 and is shown in the top graph of figure 9.4. It is found that $\Delta_{Cu}^{(D)}(Q)$ is affected by a slight downwards slope. The difference $[\Delta_{Cu}^{(D)}(Q) - \tilde{\Delta}_{Cu}^{(D)}(Q)]$ (bottom graph in figure 9.4), where $\tilde{\Delta}_{Cu}(Q)$ is the Fourier back transform of $\Delta G_{Cu}(r)$ after the unphysical low-r oscillations have been set to their theoretical limit, is largest at low-Q values and is of a similar shape to $F^0(Q)$ for the solutions in H_2O. This is an indication of a small hydrogen imbalance between the two solutions in heavy water used in the neutron diffraction experiment. The correction for the excess amount of hydrogen in the $^{63}Cu(ClO_4)_2$ solution in D_2O has been performed by subtracting a polynomial fit to the scaled $F^0(Q)$ for $^{63}Cu(ClO_4)_2$ in H_2O from the $^{63}F^0(Q)$ function in heavy

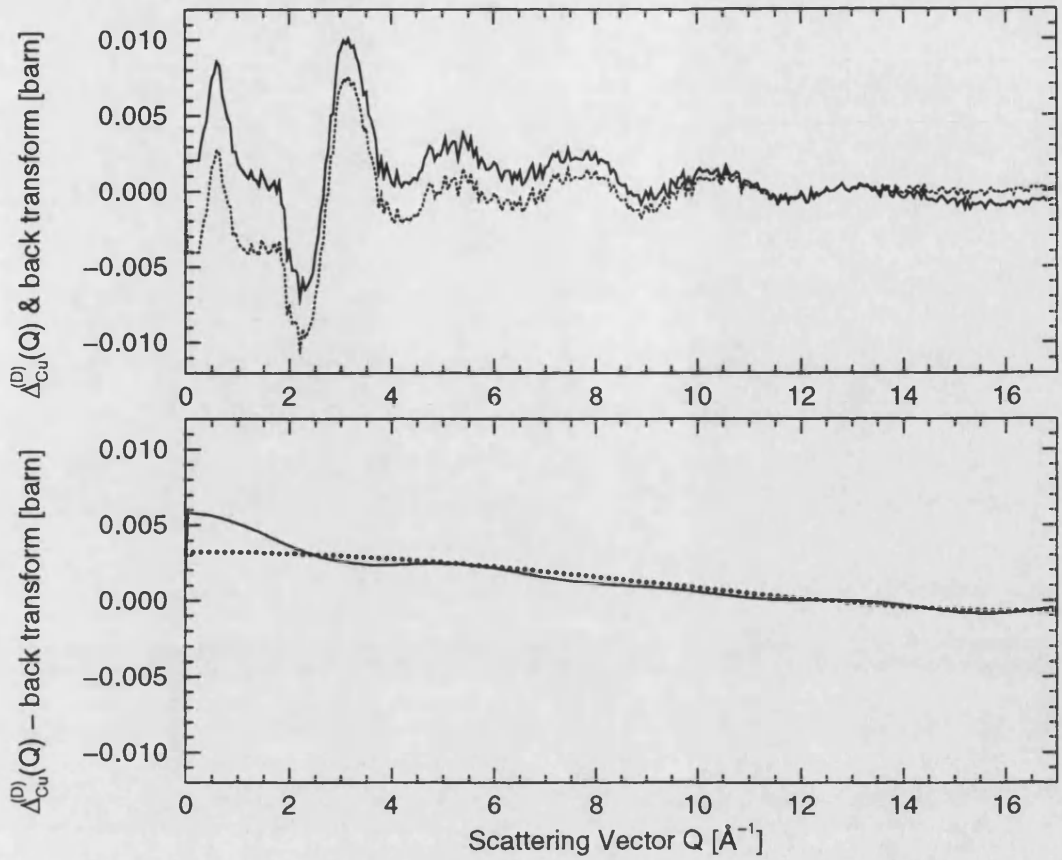

Figure 9.4: Top graph: First order difference function, $\Delta^{(D)}_{Cu}(Q)$, obtained by using equation 9.5 (solid curve), and the Fourier back transform, $\tilde{\Delta}^{(D)}_{Cu}(Q)$, of the corresponding real-space function after the unphysical low-r oscillations for $r \leq r_{min}$ have been set to their theoretical limit (dotted curve). Bottom graph: A comparison of $[\Delta^{(D)}_{Cu}(Q) - \tilde{\Delta}^{(D)}_{Cu}(Q)]$, given by the solid curve, and a polynomial fit to the scaled total structure factor of $^{63}Cu(ClO_4)_2$ in H_2O, given by the small circles.

water. The best agreement between $\Delta^{(D)}_{Cu}(Q)$ and $\tilde{\Delta}^{(D)}_{Cu}(Q)$ was achieved by using a scaling factor of 1.125×10^{-3}. The excess hydrogen in the solution of $^{63}Cu(ClO_4)_2$ in D_2O was estimated at 0.14 % from the level of $\Delta^{(D)}_{Cu}(Q)$ at high-Q.

The final $\Delta^{(D)}_{Cu}(Q)$ fulfills the sum-rule relations and is shown in figure 9.5. It exhibits a prominent FSDP at 0.60(3) Å^{-1} which shifts to 0.58(2) Å^{-1} on spline fitting.

The corresponding real-space function, $\Delta G^{(D)}_{Cu}(r)$, is displayed in figure 9.6. It comprises a sharp well defined first peak with a maximum at 1.95(2) Å. This peak is followed by a second, slightly broader peak with a maximum at 2.55(2) Å, which is also well defined and which has a shoulder on its high-r side. This is proceeded

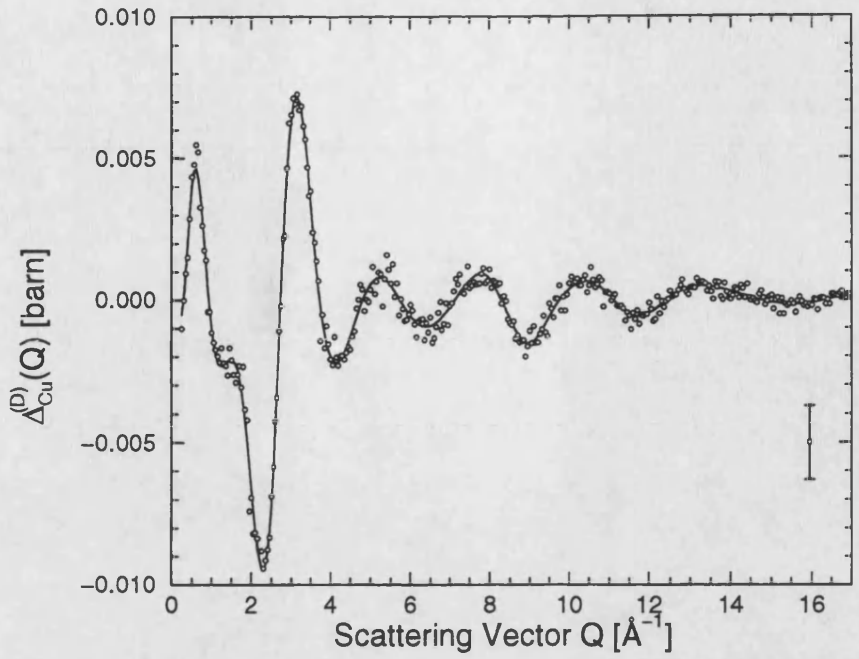

Figure 9.5: Final $\Delta^{(D)}_{Cu}(Q)$ obtained after correcting for the hydrogen imbalance. The small circles represent the first order difference function obtained by subtracting the measured data points and a representative error bar for these data points is shown in the lower right hand corner. The solid curve shows the cubic spline fit to the measured data points.

by a double peak with maxima at 4.2 Å and 4.6 Å. For approximately $r \geq 7.5$ Å, $\Delta G^{(D)}_{Cu}(r)$ does not exhibit any more pronounced structure. All of the peak positions and coordination numbers are summarised in table 9.5.

The first order difference function, $\Delta^{(H)}_{Cu}(Q)$, for the solutions of 2.22 molal $Cu(ClO_4)_2$ in H_2O is shown in figure 9.7. It is in very good agreement with its Fourier back transform $\tilde{\Delta}^{(H)}_{Cu}(Q)$, except in the region between about 5.5 Å^{-1} and 9.5 Å^{-1}. The $\Delta^{(H)}_{Cu}(Q)$ function exhibits a small negative going FSDP at $\approx 0.60(5)$ Å^{-1} which shifts to 0.54(3) Å^{-1} on spline fitting. Since the copper-hydrogen correlations are the only contributions with a negative weighting (see table 9.4), this negative FSDP indicates that the Cu-H correlations contribute to the intermediate range ordering (IRO) in the Cu^{2+} solutions.

The real-space function, $\Delta G^{(H)}_{Cu}(r)$, obtained from the two solutions in H_2O is shown in figure 9.8. $\Delta G^{(H)}_{Cu}(r)$ oscillates around the correct low-r limit, and it exhibits a sharp, well-defined first peak with a maximum at 1.96(2) Å. Since the second peak at 2.55(2) Å is negative, it can be concluded that it comprises

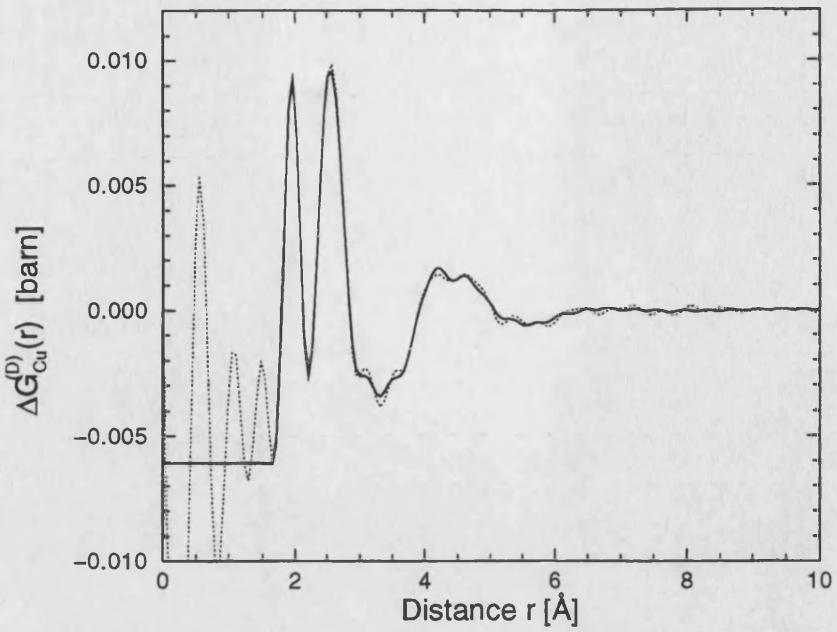

Figure 9.6: $\Delta G^{(D)}_{Cu}(r)$ for the solution of 2.00 molal $Cu(ClO_4)_2$ in deuterated perchloric acid. The dotted curve shows the result of Fourier transforming the first order difference function given by the open circles in figure 9.5. The solid curve corresponds to the Fourier transform of the spline fitted $\Delta^{(D)}_{Cu}(Q)$ with the unphysical oscillations for $r \leq 1.66$ Å set to the calculated $\Delta G^{(D)}_{Cu}(0)$ limit (table 9.4).

predominantly copper-hydrogen contributions. $\Delta G^{(H)}_{Cu}(r)$ also gives an indication that there is IRO in the solutions, since structure is visible up to $r \approx 10$ Å.

The peak positions in $\Delta G^{(D)}_{Cu}(r)$ and $\Delta G^{(H)}_{Cu}(r)$ and coordination numbers $\overline{n}^{\beta}_{Cu}$, assuming the first peak is attributed to $g_{CuO}(r)$ and assuming only copper-hydrogen or deuterium contributions to the second peak, are summarised in table 9.5.

	1st peak [Å]	$\overline{n}^{O}_{Cu}$	integration range [Å]	FWHM [Å]	2nd peak [Å]	$\overline{n}^{H/D}_{Cu}$	integration range [Å]
$\Delta G^{(D)}_{Cu}(r)$ [a])	1.95(2)	4.0(2)	1.66-2.24	0.29(1)	2.56(2)	9.1(3)	2.24-2.95
[b])	1.95(2)	4.0(2)	1.66-2.24	0.29(1)	2.55(2)	9.1(3)	2.24-2.95
$\Delta G^{(H)}_{Cu}(r)$ [a])	1.96(2)	3.5(3)	1.60-2.24	0.29(1)	2.59(2)	6.2(3)	2.24-2.95
[b])	1.96(2)	3.7(3)	1.60-2.24	0.34(1)	2.55(2)	6.9(3)	2.24-2.95

[a]) from data points; [b]) from spline fit

Table 9.5: Peak positions, coordination numbers, $\overline{n}^{O}_{Cu}$, assuming only Cu-O correlations under the first peak, and $\overline{n}^{H}_{Cu}$ and $\overline{n}^{D}_{Cu}$, assuming only Cu-H or Cu-D correlations under the second peak, integration ranges and the full width at half maximum (FWHM) of the first peak in $\Delta G_{Cu}(r)$.

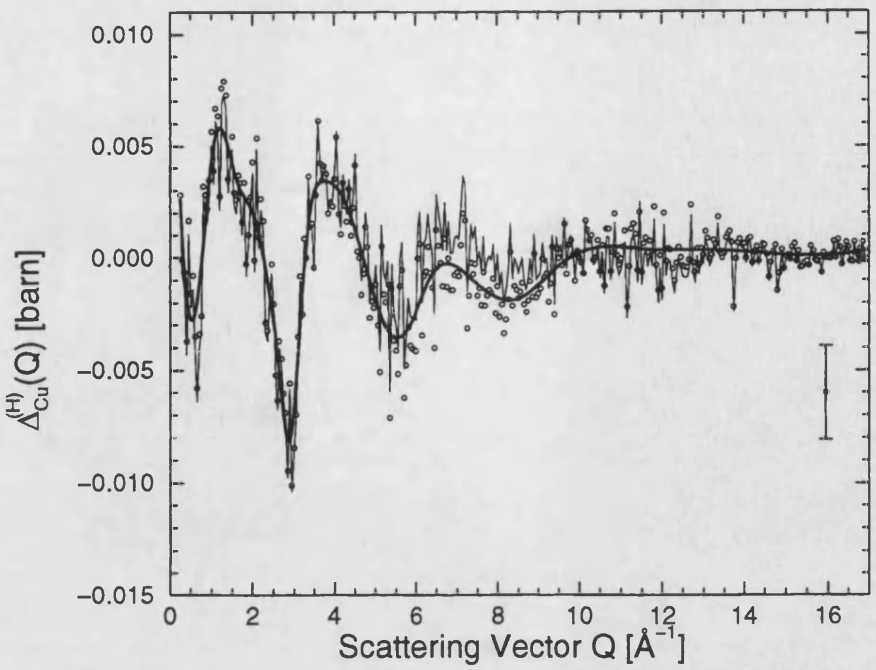

Figure 9.7: First order difference function, $\Delta^{(H)}_{Cu}(Q)$, for the solution of 2.22 molal $Cu(ClO_4)_2$ in hydrogenated perchloric acid. The circles represent the function obtained by subtracting the data points and a representative error bar is given. The Fourier back transform of the corresponding $\Delta G^{(H)}_{Cu}(r)$, after the unphysical low-r oscillations have been set to their calculated limiting $\Delta G^{(H)}_{Cu}(0)$ value, is shown by the thin solid curve, and the thick solid curve displays a cubic spline fit to the data points.

Our results for the next-nearest Cu-O correlations for the solutions in D_2O agree very well with the earlier experiments by Salmon et al.[3], which were also carried out using the D4 diffractometer on 2 molal solutions of $Cu(ClO_4)_2$ in D_2O. Salmon et al.[3] found a mean Cu-O distance of 1.96(3) Å, a coordination number $\overline{n}^{O}_{Cu} = 4.1(3)$, and a half width at half maximum of 0.15(2) Å. Like the experiments by Salmon et al.[3], our first order difference functions indicate that the second peak cannot be solely attributed to $g_{CuD}(r)$ since the coordination number found for the solutions in D_2O is much larger than the expected value of 8. Further, the coordination number for the solutions in H_2O is much smaller than 8, showing there are additional contributions with positive weightings, reducing the intensity of the negative going peak.

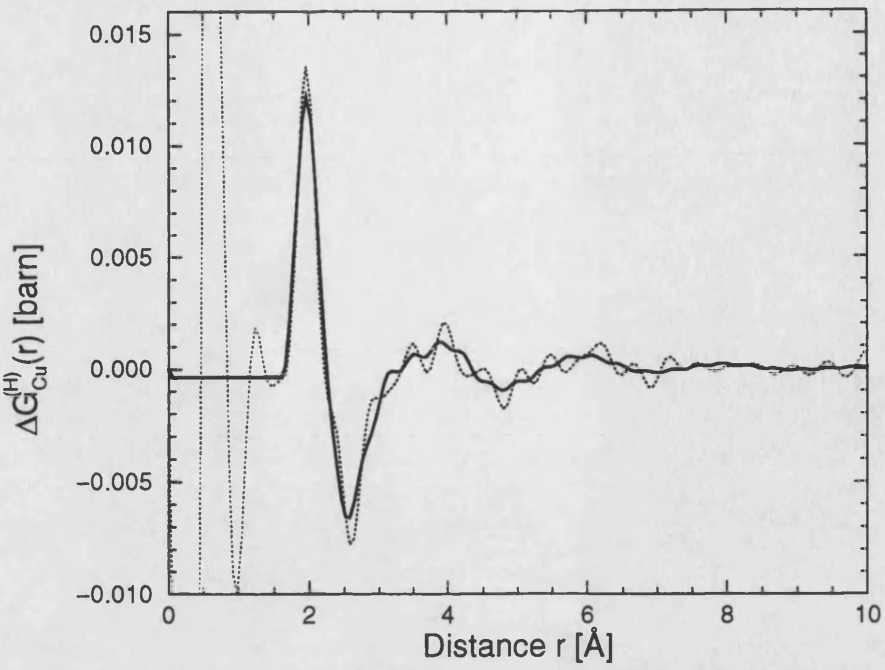

Figure 9.8: First order difference function for the solution of 2.22 molal $Cu(ClO_4)_2$ in hydrogenated perchloric acid in real-space. The dotted curve represents the Fourier transform of the data points given by the circles in figure 9.7, and the solid curve corresponds to the Fourier transform of the spline fitted $\Delta^{(H)}_{Cu}(Q)$, with the unphysical low-r oscillations for $r \leq 1.6$ Å set to their theoretical limit of $\Delta G^{(H)}_{Cu}(0)$, see table 9.4.

9.4.3 $S_{CuH}(Q)$ and $\Delta^{\Delta}_{Cu}(Q)$

The Cu-H partial structure factor, $S_{CuH}(Q)$, obtained from the data points by using equation 9.8 is shown in figure 9.9. It agrees well with the Fourier back transform of the corresponding $g_{CuH}(r)$, given in figure 9.11, after the unphysical low-r oscillations have been set to their theoretical limit.

Different methods have been applied in order to assess the effect that noise in $S_{CuH}(Q)$ has on the real-space function. The resulting $S_{CuH}(Q)$ are displayed in figure 9.10. The cubic spline fit to the data points for $S_{CuH}(Q)$ smoothes the noisy data well for $Q \leq 9$ Å^{-1}, but it does not reproduce the high-Q oscillations as well as the minimum information (MIN) method, described in section 3.5, which was also applied to the measured $S_{CuH}(Q)$. Additionally, in the range of $5.5 - 9.5$ Å^{-1} where the back Fourier transform is slightly lower than the measured data in figure 9.9, the MIN solution follows the Fourier back transform. The spline fit and MIN solution both give a FSDP in $S_{CuH}(Q)$ at $Q = 0.55(2)$ Å^{-1}. This confirms that an

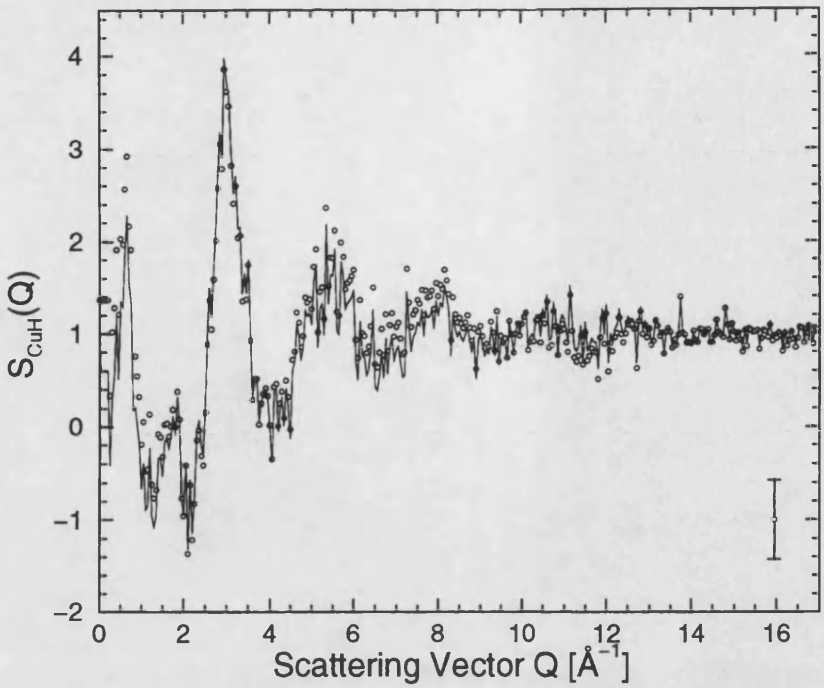

Figure 9.9: Partial structure factor, $S_{CuH}(Q)$, obtained from the data points (open circles) shown together with the Fourier back transform of the corresponding $g_{CuH}(r)$ (solid curve) after the unphysical low-r oscillations have been set to their theoretical value of $g_{CuH}(0) = 0$. The uncertainties on each data point are indicated by the error bar in the lower right hand corner.

IRO is associated, at least in part, with the copper-hydrogen correlations.

The first physical feature in $g_{CuH}(r)$ occurs at 2.58(2) Å in the Fourier transform of the measured data points and in the Fourier transform of the cubic spline fit, and at 2.54(3) Å in the MIN solution. The second peak is found at 4.57(2) Å and 4.63(3) Å in the spline fit and the MIN solution respectively, and there are high-r oscillations up to ≈ 12 Å. The profile of the high-r side of the first peak differs to some extent between the different $g_{CuH}(r)$ functions, see figure 9.11. Therefore, in order to characterise and compare the number of hydrogen atoms around Cu, the running coordination number, defined by

$$\overline{n}^{H}_{Cu}(r) = 4\pi n_0 c_H \int_{r=0}^{r} r^2 g_{CuH}(r) dr \tag{9.11}$$

has been calculated after setting the unphysical low-r oscillations to $g_{CuH}(0) = 0$.

Figure 9.12 shows that despite differences in the details of the $g_{CuH}(r)$ functions, the running coordination numbers for all the functions are in good agreement. They differ by a maximum of 0.4 for a given r. A hydration number $\overline{n}^{H}_{Cu}$ of 8.0 is obtained

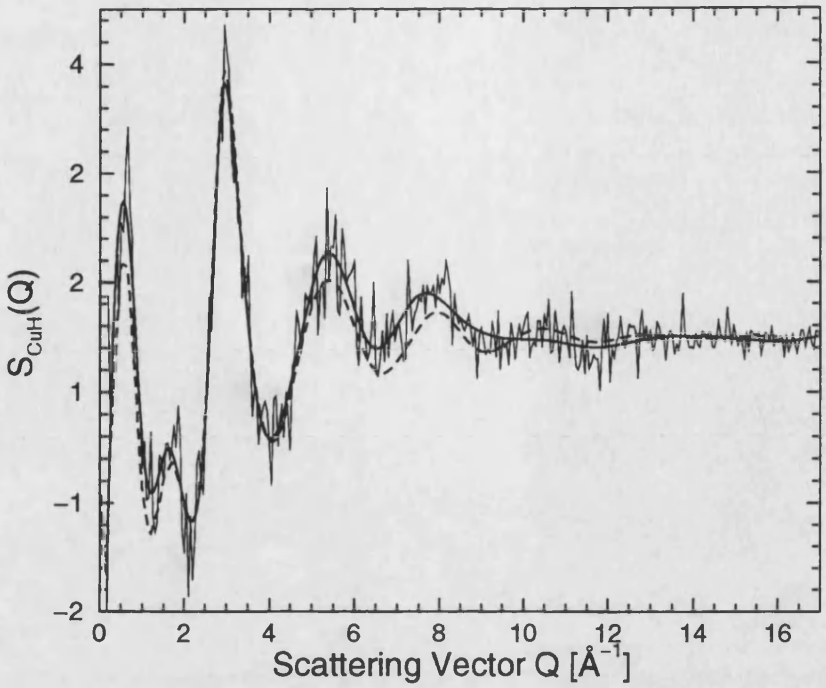

Figure 9.10: Measured data for $S_{CuH}(Q)$, shown by the small circles, displayed together with the different smoothed data sets. The thick solid curve shows a cubic spline fit to the raw data set, and the dashed curve represents the solution obtained from the minimum noise method, see section 3.5.

at a distance r = 2.9(2) Å for all of the functions, which corresponds to four water molecules close to the Cu^{2+} ion. This is consistent with the results from Salmon et al.[3] obtained on their first order difference function. However, our results show that the four further distant hydrogen atoms are not located at a distinct distance from the Cu^{2+} ion. Instead their contributions are distributed over a wide range (see the horizontal bar in figure 9.11), exceeding the position of the minimum following the first peak in $g_{CuH}(r)$. To be precise, at the position of the minimum of the measured data at 3.41(2) Å (marked by an arrow in figure 9.12) a running coordination number $\overline{n}^{H}_{Cu}(r)$ of 10.0(2) is measured.

$S_{CuO}(Q)$, to a first approximation, is obtained from $\Delta^{\Delta}_{Cu}(Q)$ by using equation 9.11. The latter is shown together with its Fourier back transform in figure 9.13. The agreement between the measured data and the back transform is very good, except for the Q-range between 5.5 Å^{-1} and 9.5 Å^{-1}, a range where discrepancies between $\Delta^{(H)}_{Cu}(Q)$ and $\tilde{\Delta}^{(H)}_{Cu}(Q)$ also occurred. The first peak in $\Delta^{\Delta}_{Cu}(Q)$

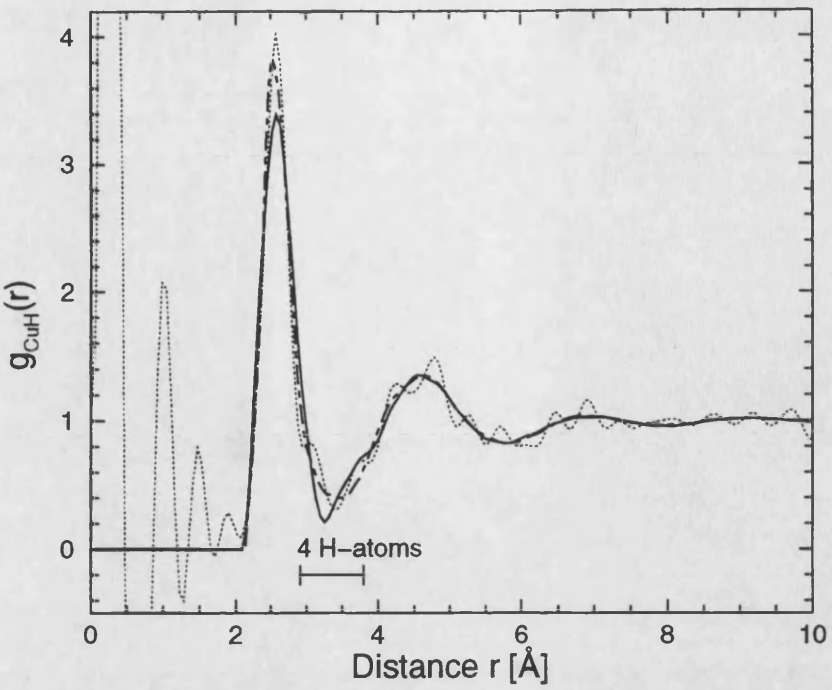

Figure 9.11: $g_{CuH}(r)$ for a 2 molal solution of $Cu(ClO_4)_2$ in perchloric acid. The dotted curve represents the Fourier transform of the measured data points, the solid curve shows the Fourier transform of the spline fit, and the chained curve shows the MIN solution. The region over which the four hydrogen atoms which lie beyond the nearest-neighbour 8 hydrogen atoms are distributed is displayed by the horizontal bar (see text).

is located at $1.31(2)\,\text{Å}^{-1}$.

In order to eliminate the noise on the measured data set, and therefore to obtain a smoother function in real-space, $\Delta G^{\Delta}_{Cu}(r)$, different methods were applied. A cubic spline fit to the data is shown in figure 9.14 together with the solution obtained from the minimum noise method. As for the Cu-H data the MIN solution mimics the Fourier back transform in the area between $5.5 - 9.5\,\text{Å}^{-1}$, and therefore differs slightly from the measured data.

The real-space function, $\Delta G^{\Delta}_{Cu}(r) = g_{CuO}(r) + 0.044\,g_{CuCu}(r) + 0.102\,g_{CuCl}(r)$, is displayed in figure 9.15. The first physical peak is found at $r = 1.96(2)$ Å for the direct Fourier transform of the data points, at $r = 1.95(2)$ Å for the spline fit, and at $r = 1.94(2)$ Å for the MIN solution. As for the Cu-H pair distribution function, all three solutions have a somewhat different profile in the region around the first minimum and the high-r side of the first peak (see inset in figure 9.15). Thus, for a better characterisation and comparison the running coordination number $\overline{n}^{O}_{Cu}(r)$

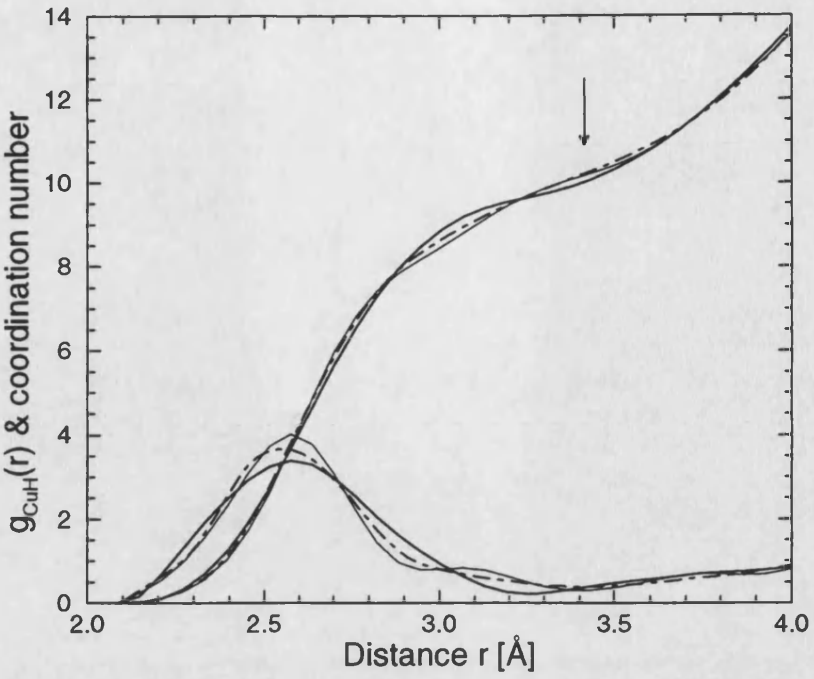

Figure 9.12: The $g_{CuH}(r)$ and running coordination numbers $\overline{n}^{H}_{Cu}(r)$ for the different functions. As in figure 9.11 the thick solid curves describe the Fourier transform of the spline fitted data set and the chained curves represent the MIN solution. The thin curves here correspond to the Fourier transform of the measured data points. The arrow at ≈ 3.41 Å marks the position of the minimum after the first peak for the measured data, and at this r-value a coordination number $\overline{n}^{H}_{Cu}$ of 10.0(2) is measured.

has been derived and is shown for all the data sets in figure 9.16.

Assuming there is no inner-sphere complexing of the perchlorate ion to the Cu^{2+}-ion, see section 9.1, a coordination number $\overline{n}^{O}_{Cu} = 4.0$ is obtained from the pair distribution functions at a distance of 2.34 Å (MIN solution) - 2.42 Å (measured data points). The results thus agree with the earlier measurements of Salmon et al.[3], who found four oxygen atoms bound to the Cu^{2+}-ion at a close distance of ≈ 1.96 Å, and with our findings for the copper-hydrogen correlations. Analogous to the results for $g_{CuH}(r)$, these nearest-neighbour O-atoms are *not* accompanied by further oxygen atoms at a particular single distance, but by a distribution of oxygen atoms over a broad distance range. The next two oxygen atoms can be found over the range from ≈ 2.4 Å to ≈ 3.4 Å (indicated by the horizontal bar in figure 9.15). At the position of the minimum after the first peak in the pair distribution function at ≈ 2.9 Å, a coordination number of 5.0(1) is obtained from all of the data sets.

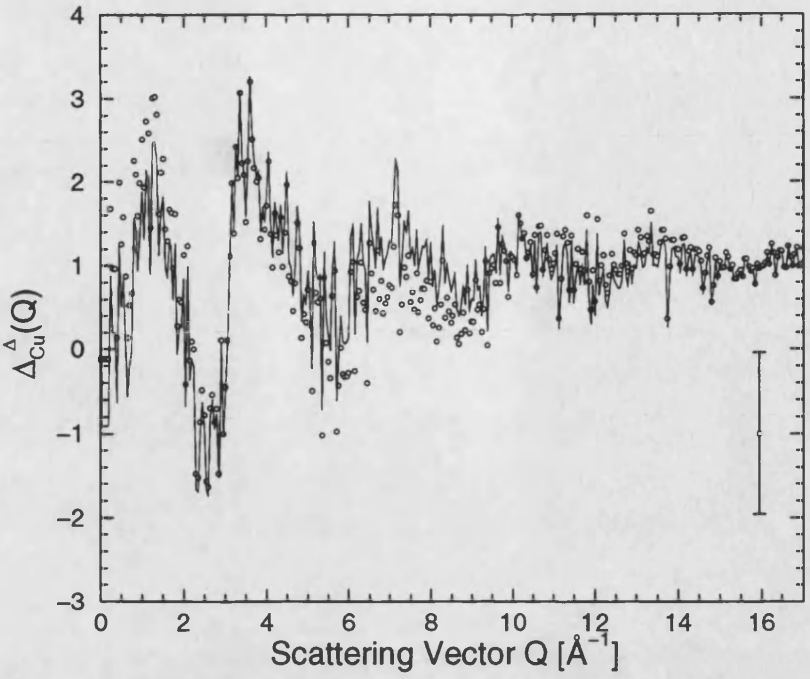

Figure 9.13: $\Delta^{\Delta}_{Cu}(Q)$ for a solution of 2 molal $Cu(ClO_4)_2$ in perchloric acid. The measured data is shown by the circles and the bar gives a representation of the uncertainty on each data point The thick solid curve represents the back Fourier transform of the corresponding $\Delta G^{\Delta}_{Cu}(r)$ after the unphysical low-r oscillations are set to the $\Delta G^{\Delta}_{Cu}(0)$ limit.

The second peak in $\Delta G^{\Delta}_{Cu}(r)$ for the MIN solution is positioned at 4.02(2) Å. This is in the region of the copper to perchlorate-oxygen distance in crystalline $Cu(ClO_4)_2 \cdot 6H_2O$ (Gallucci & Gerkin[7]).

In order to obtain a final pair distribution function for the Cu-O correlations that on the one hand reproduces the sharpness of the first peak obtained for the data points and on the other hand the smooth profile of the MIN solution, a combination of these two functions was generated by smoothly joining them in $r \cdot g(r)$. The so obtained $\Delta G^{\Delta}_{Cu}(r)$ function is shown in figure 9.17. To check the validity of our method, the back Fourier transform of this function is compared with the back Fourier transform of the measured data points, in figure 9.17. Good agreement is found over the entire measured Q-range.

As a self-consistency test for the partial structure factors, our measured first order difference functions in D_2O and H_2O are compared with their reconstructions made using the partial pair distribution functions, $g_{CuH}(r)$ and $\Delta G^{\Delta}_{Cu}(r)$, weighted

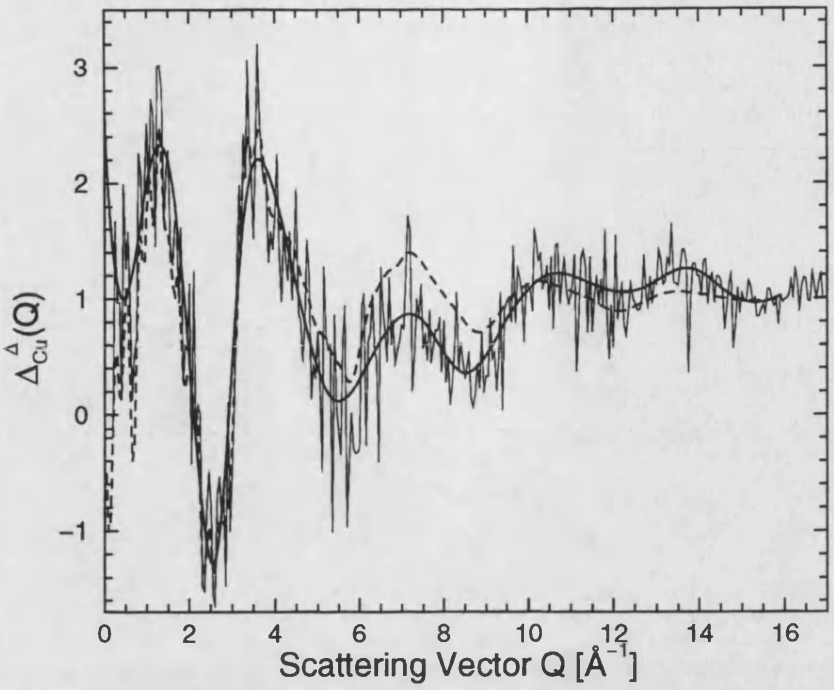

Figure 9.14: Measured data set for the function, $\Delta^{\Delta}_{Cu}(Q)$ (thin solid curve), in comparison with the smoothed data sets. The thick solid curve shows a cubic spline fit to the measured data and the dashed curve gives the MIN solution.

according to equation 9.4. They are displayed together in figures 9.18 and 9.19. The unsmoothed data sets reproduce the first order difference function for the solutions in H_2O perfectly. This is re-assuring as $\Delta G^{\Delta}_{Cu}(r)$ has actually been obtained using the first order difference function for the deuterated solutions, see equation 9.11. Also the reproduction of $\Delta G^{(D)}_{Cu}(r)$ only shows slight discrepancies at the second peak position.

Additionally the smoothed partial pair distribution functions, the MIN solution shown in figure 9.11 for $g_{CuH}(r)$ and the combined function in figure 9.17 for $\Delta G^{\Delta}_{Cu}(r)$, were neutron weighted and used to reproduce both first order difference functions. Again the agreement is good. The small discrepancies around the second peak arise from the slightly lower first peak in $g_{CuH}(r)$ obtained from the MIN solution compared to the measured data (see figure 9.11).

A further confirmation of our results has been obtained by a comparison of the coordination numbers under the first two peaks in $\Delta G^{(D)}_{Cu}(r)$ with the running coordination numbers measured from $g_{CuH}(r)$ and $\Delta G^{\Delta}_{Cu}(r)$. The coordination number for the first peak in $\Delta G^{(D)}_{Cu}(r)$ is 4.0(2), see table 9.5. Now if the integration range is

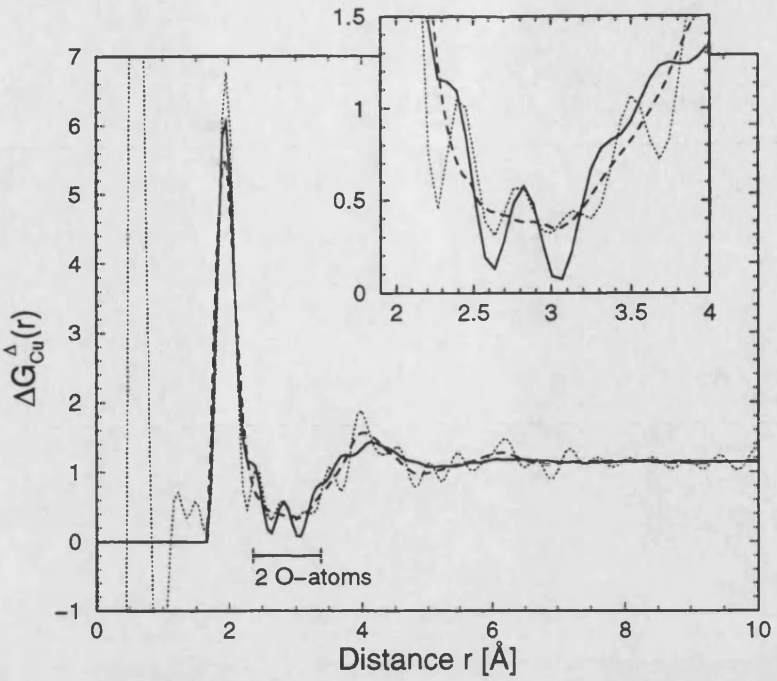

Figure 9.15: $\Delta G^{\Delta}_{Cu}(r) = g_{CuO}(r) + 0.044\, g_{CuCu}(r) + 0.102\, g_{CuCl}(r)$ for the solution of 2 molal $Cu(ClO_4)_2$ in perchloric acid. The Fourier transform of the measured data points is given by the dotted curve, the Fourier transform of the spline fit by the solid curve, and the MIN solution by the dashed curve. The horizontal bar indicates the area over which the contributions of two oxygen atoms, beyond the nearest-neighbour 4 oxygens, are measured. The inset shows the partial pair distribution functions in the region of the first minimum.

extended up to 2.95 Å, i.e. if it covers the first two peaks in $\Delta G^{(D)}_{Cu}(r)$ then the partial pair distribution functions yield coordination numbers of $\overline{n}^{O}_{Cu} = 5$ and $\overline{n}^{H}_{Cu} = 8$, see figures 9.12 and 9.16. Likewise, if the coordination number $\overline{n}^{O}_{Cu}$ is fixed at 5.0, a nearest neighbour coordination number of 8.2 hydrogen is obtained from the first order difference function. If the integration range in $\Delta G^{(D)}_{Cu}(r)$ is extended further to 3.37 Å to comprise the high-r shoulder in $\Delta G^{(D)}_{Cu}(r)$, then fixing $\overline{n}^{O}_{Cu}$ at 6.0, yields a Cu-H coordination number, $\overline{n}^{H}_{Cu}$, of 9.9(1) which agrees very well with the value of 10.0(2) found at this distance in $g_{CuH}(r)$. All of the coordination numbers referred to in this paragraph were calculated from the Fourier transforms of the measured data points.

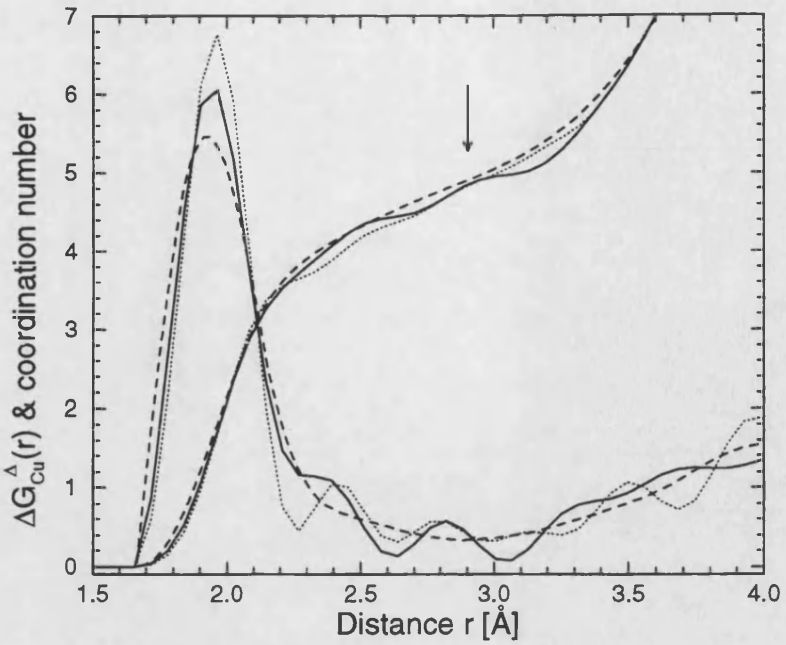

Figure 9.16: $\Delta G^{\Delta}_{Cu}(r)$ functions and running coordination numbers $\overline{n}^{O}_{Cu}(r)$. The Fourier transform of the measured data points is given by the dotted curve, the Fourier transform of the spline fit by the solid curve, and the MIN solution by the dashed curve. It can be seen that despite the differences in the shape of the pair distribution functions, the running coordination numbers differ only in small details.

9.5 Discussion

9.5.1 Intermediate range order (IRO)

The total structure factors for the solutions of 2.0 molal $Cu(ClO_4)_2$ in deuterated perchloric acid exhibit a weak FSDP at 0.58(2) $Å^{-1}$. In the first order difference functions, $\Delta^{(D)}_{Cu}(Q)$ and $\Delta^{(H)}_{Cu}(Q)$, the FSDPs become a notable feature and they can be traced to $S_{CuH}(Q)$. The position of the FSDPs in all the data sets are summarised in table 9.6.

data set	$\Delta^{(D)}_{Cu}(Q)$ [$Å^{-1}$]	$\Delta^{(H)}_{Cu}(Q)$ [$Å^{-1}$]	$S_{CuH}(Q)$ [$Å^{-1}$]	$\Delta^{\Delta}_{Cu}(Q)$ [$Å^{-1}$]
data points	0.60(3)	$\approx$0.60(5)	$\approx$0.60(5)	$\approx$1.30(3)
spline fit	0.58(2)	0.54(3)	0.55(2)	1.31(2)
MIN solution	-	-	0.55(2)	1.31(2)

Table 9.6: Position of the first sharp diffraction peaks.

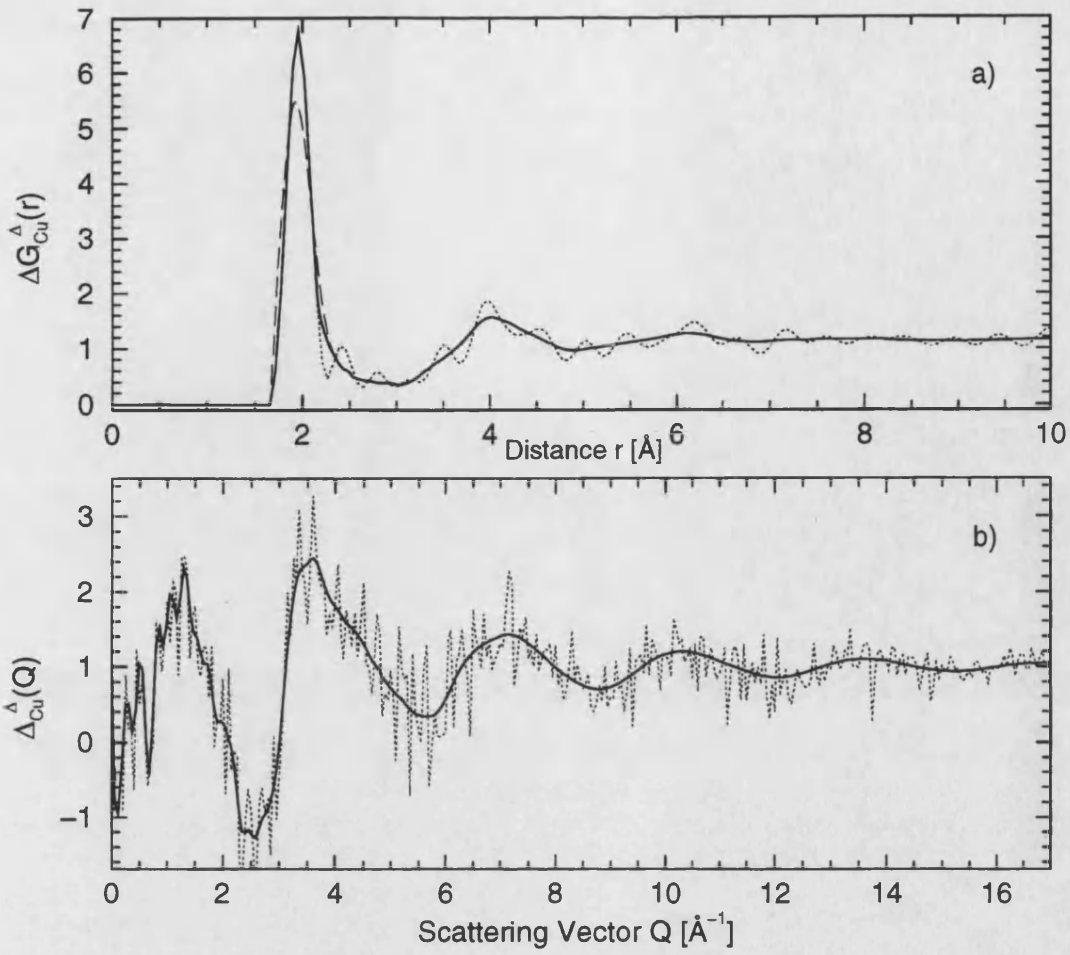

Figure 9.17: graph a): $\Delta G^{\Delta}_{Cu}(r)$ (solid curve) obtained by combining the Fourier transform of the measured data points (dotted curve) and the MIN solution (dashed curve) in the region around 2.25 Å, see text. graph b): Fourier back transform of the pair distribution function represented by the solid curve in graph a) (solid curve) in comparison with the Fourier back transform of the measured data points, given by the dotted curve.

The FSDP in $S_{CuH}(Q)$ is located at a position of $Q_1 = 0.55(2)$ Å^{-1} for the MIN solution and the spline fit. It follows from the properties of Fourier transforms that this peak is related to density fluctuations in real-space which have a periodicity of $2\pi/Q_1 \approx 11.4(4)$ Å and an amplitude which decays according to the peak shape (Salmon [17]). The first peak in $\Delta^{\Delta}_{Cu}(Q)$ occurs at the larger-Q value of 1.31(2) Å^{-1}. This leaves an open question about how the intermediate range ordering of the Cu-hydrogen correlations appears to take place on a different length scale to the intermediate range ordering of the Cu-oxygen correlations.

To investigate if there are strong contributions to the FSDP at 0.55 Å^{-1} from

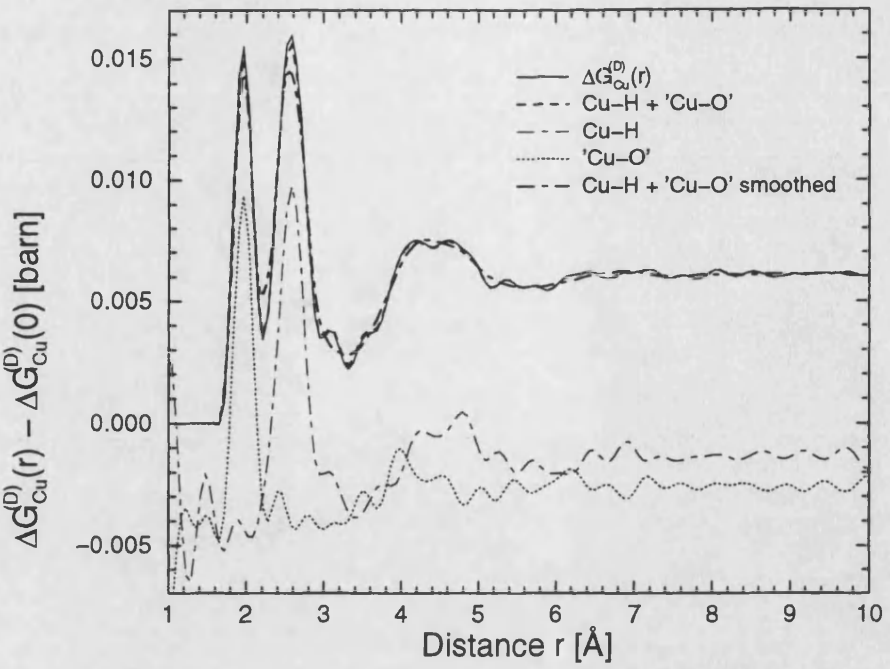

Figure 9.18: $\Delta G^{(D)}_{Cu}(r)$ shifted up by $-\Delta G^{(D)}_{Cu}(0)$ (solid curve) compared with the function built up from the neutron weighted $g_{CuH}(r)$ and $\Delta G^{\Delta}_{Cu}(r)$ functions (shifted down by -0.005 barn in the graph). The measured data points were used to give the thick dashed curve, which is almost indistinguishable from the measured $\Delta G^{(D)}_{Cu}(r)$ on the scale of the plot. The smoothed data sets, MIN solution in figure 9.11 for $g_{CuH}(r)$ and final $\Delta G^{\Delta}_{Cu}(r)$ function of figure 9.17, were used to give the thick chained curve.

any other correlations, $S_{CuH}(Q)$ in the Q-range of the FSDP was scaled according to its weighting in $\Delta^{(D)}_{Cu}(Q)$ and in $F^0(Q)$ for the deuterated solutions and it was found that within the errors it accounts for the full height of the FSDP in these functions. This is surprising since in aqueous $NiCl_2$ solutions a FSDP occurs in the Ni-Ni partial structure factor that arises from the intermediate range ordering of the Ni^{2+} aqua-ions i.e. from the centre-centre correlations (cf. the molecular liquid CCl_4 in Salmon[17]).

9.5.2 Comparison with *ab initio* molecular dynamics simulations

Ab initio molecular dynamics studies on Cu^{2+} in water were recently undertaken by Pasquarello[18] at the Institut Romand de Recherche Numérique en Physique des Matériaux in Lausanne, Switzerland. These simulations were carried out on a

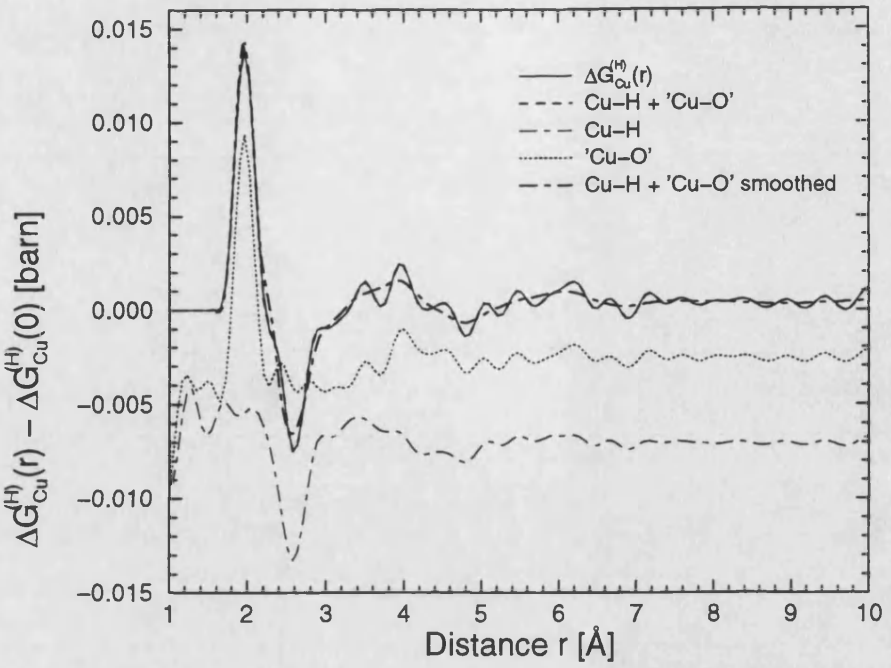

Figure 9.19: $\Delta G_{Cu}^{(H)}(r)$ shifted up by $-\Delta G_{Cu}^{(H)}(0)$ (solid curve) compared with the function built up by the neutron weighted $g_{CuH}(r)$ and $\Delta G_{Cu}^{\Delta}(r)$ (shifted down by -0.005 barn in the graph). The function obtained from the measured data points is given by the thick dashed curve, which is almost indistinguishable from the measured $\Delta G_{Cu}^{(H)}(r)$ on the scale of the plot. The function from the smoothed data sets is given by the thick chained curve.

system of 50 H_2O molecules and one Cu^{2+}-ion. The B-LYP (Becke - Lee, Yang and Parr) generalized-gradient approximation (GGA) within density functional theory was used (Pasquarello [18]). The so-far unpublished results from this study are compared in figures 9.20 and 9.21 with our experimental data.

In figure 9.20 it can be seen that although in the simulated data sets of the first order difference functions all of the peaks are notably narrower and sharper, the first and second peak positions agree with the experimental data within the errors. In $\Delta G_{Cu}^{(D)}(r)$ even the higher-r peaks at about $4-5$ Å are well represented.

In figure 9.21 $g_{CuH}(r)$ and $\Delta G_{Cu}^{\Delta}(r)$ from our experiments are compared with the $g_{CuH}(r)$ and $g_{CuO}(r)$ obtained in the simulation studies. The peak positions for both partial pair distribution functions agree within the errors, but again the simulated peaks are sharper, which means that the simulated system is more structured than the real one. It is anticipated (Pasquarello[18]) that this problem, which has already been encountered for pure water, could either be due to the intrinsic limitations of the theory or to the propagation of the effect of the periodic boundary

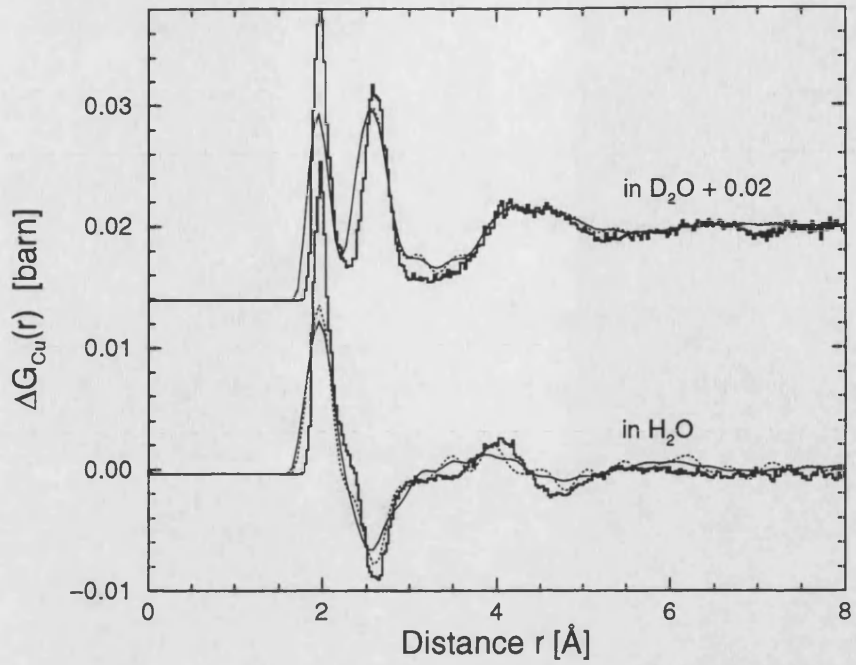

Figure 9.20: Comparison of the first order difference functions, $\Delta G_{Cu}(r)$, obtained from our experiments (the thin solid curve represents the spline fitted data sets, the dotted curve the measured data sets) with the results obtained from *ab initio* molecular dynamics studies, shown by the thick solid curves.

conditions. Although there are systematic differences in the running coordination numbers obtained from experiment and theory, arising from the sharper peaks in the simulation, their profiles are comparable. From the simulation a coordination number $\overline{n}^{H}_{Cu} = 8.0$ is found at a distance of 2.69(2) Å, $\overline{n}^{H}_{Cu} = 10.0$ at 3.24(2) Å, and $\overline{n}^{H}_{Cu} = 12.0$ at 3.69(2) Å, which is well within the start of the second peak in $g_{CuH}(r)$. Similarly for $g_{CuO}(r)$, a coordination number $\overline{n}^{O}_{Cu} = 4.0$ is obtained at 2.19(2) Å, and the two next-nearest neighbour oxygen atoms are distributed over a distance of about 1.5 Å.

These results from the molecular dynamics studies agree with our measured running coordination numbers, and with our conclusion that the Cu^{2+} hydration complex in copper-perchlorate solution cannot be described by a $4 + 2$ distortion with 4 nearest-neighbour water molecules and 2 next nearest-neighbour water molecules at set distances.

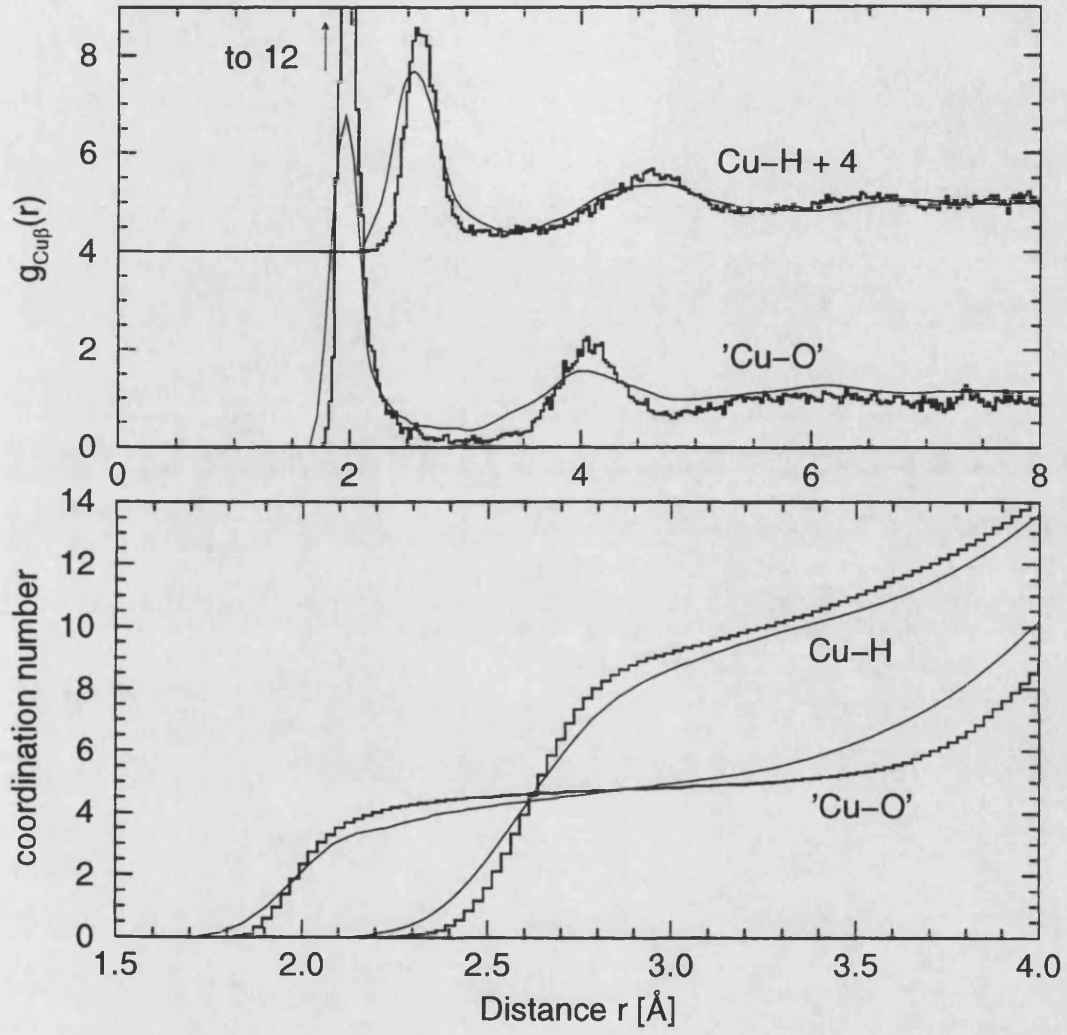

Figure 9.21: top graph: Comparison of the partial pair distribution functions, $g_{CuH}(r)$ and $\Delta G^{\Delta}_{Cu}(r)$, from our experiments, given by the thin curves, with the $g_{CuH}(r)$ and $g_{CuO}(r)$ obtained in the simulation studies, shown by the thick solid curves. (The experimental $g_{CuH}(r)$ is the MIN solution, shown in figure 9.11, and $\Delta G^{\Delta}_{Cu}(r)$ is the final function given in figure 9.17.) bottom graph: The corresponding running coordination numbers.

9.5.3 Jahn-Teller distortion in the Cu^{2+} hydration complex

Like earlier EXAFS, x-ray diffraction and neutron diffraction measurements on the Cu^{2+} aqua-ion (see a summary in table 9.7), our results show that the structure of the Cu^{2+} hydration complex is subject to a Jahn-Teller distortion, with four H_2O molecules bound to the Cu^{2+}-ion at a short distance. Our measured $r_{CuO}(eq)$ distance of 1.96(2) Å (measured data points, see section 9.4.3) agrees with the distances found in the literature, see table 9.7.

Conc. [mol/dm^3]	$r_{CuO}(eq)$ [Å]	$\overline{n}^{O}_{Cu}(eq)$	$r_{CuO}(ax)$ [Å]	$\overline{n}^{O}_{Cu}(ax)$	Method	Reference
1.0	1.96(1)	4	2.60(5)	2	EXAFS	Sham et al.[19]
1.019	2.00(1)	4	2.28(5)	2	EXAFS	Tajiri & Wakita[20]
1.90	1.96(2)	4.1(3)	-	-	Neutron	Salmon et al.[3]*)
1.90	1.99	3.9(2)	2.45	1.95(10)	Neutron	Okan & Salmon[21]**)
1.94	1.98(2)	4	2.34(2)	2	XRD	Magini[2]
2.48	1.96(2)	4	2.29(5)	2	EXAFS	Nomura & Yamaguchi[5]
2.92	1.98(2)	4	2.39(2)	2	XRD	Magini[2]
3.44	1.96(2)	4	2.27(5)	2	EXAFS	Nomura & Yamaguchi[5]
3.55	1.94(2)	4	2.43(3)	2	XRD	Ohtaki & Maeda[22]

Table 9.7 : The structure of the Cu^{2+} aqua-ion in aqueous solution as measured by the extended x-ray absorption fine structure (EXAFS) method, the x-ray diffraction (XRD) method, or the method of isotopic substitution in neutron diffraction. *) The $r_{CuO}(eq)$ value obtained from the neutron diffraction experiment corresponds to the first peak position in $\Delta G^{(D)}_{Cu}(r)$. **) The values for $r_{CuO}(eq)$ and $r_{CuO}(ax)$ were obtained from the same data set as *) by fitting the first two peaks of the function $r^2[\Delta G^{(D)}_{Cu}(r) - \Delta G^{(D)}_{Cu}(0)]$ by a sum of Gaussians, wherein the area of O_{eq} was fitted but the ratio of the area of O_{ax} to the area of O_{eq} was fixed. Magini[2] and Ohtaki & Maeda[22] obtained their results by fitting in $r^2\,g(r)$ (g(r) denotes the respective real-space functions), and the EXAFS results were obtained by fitting the EXAFS spectra in reciprocal-space.

However our measurements do not agree with the (4 + 2) coordination suggested by the results found in literature. By taking a closer look at the x-ray diffraction measurements in the literature, it is found that Ohtaki & Maeda[22] and Magini[2] had difficulties in separating the axial Cu-O interactions from the O-O interactions,

and that Ohtaki & Maeda[22] assumed a coordination number $\overline{n}^{O}_{Cu}(ax)$ of two. The EXAFS results on the other hand suffer from the difficulty in observing the peak that corresponds to the weak axial Cu-O bonds in the Fourier transform (Nomura & Yamaguchi[5]), and the results were all obtained by fitting the measured data to a model assuming a $(4+2)$ complex (Nomura & Yamaguchi[5], Tajiri & Wakita[20]). Additionally Sham et al.[19] state that two distinct metal-oxygen bond lengths are not clearly resolvable in the EXAFS Fourier transforms, and that the lengths and Debye Waller factors obtained suggest extremely weak axial bonds or solely static disorder due to non-bonding but highly polarised H_2O molecules in the axial direction. They also suggest that the complex might be essentially planar.

By contrast to the XRD, EXAFS, and former neutron diffraction experiments we can actually 'see' the axial Cu-O and axial Cu-H interactions. These show a $(4+1)$ coordination environment for the Cu^{2+} ion, in which the one long axial Cu-O bond can be found over a distance of about $2.37 \leq r_{CuO}(ax)\,[Å] \leq 3.0$. The corresponding axial hydrogen atoms are found over a distance of about $2.9 \leq r_{CuH}(ax)\,[Å] \leq 3.4$, see figures 9.16 and 9.12. We measure the next, even further distant oxygen atom over a distance of $3.0 \leq r_{CuO}\,[Å] \leq 3.4$, and the corresponding Cu-H distances are in the range of $3.4 - 3.8\,Å$. If we compare these distances with those found for $NiCl_2$ in aqueous solution, where the divalent cation is of about the same size as Cu^{2+} and where $g_{CuH}(r)$ was directly measured (Powell et al.[14]), the six H_2O molecules of the first hydration shell are found within a distance of $3.15\,Å$ from the Ni^{2+} ion. Then our sixth H_2O molecule is located outside the first hydration shell as defined for the Ni^{2+} aqua-ion, and might be too far distant from the Cu^{2+} ion for it to be considered as bound.

It is interesting to discuss our results with regard to the water exchange rate at $25\,°C$, $k^{Cu}_{ex} = 4.4(1) \times 10^9\,s^{-1}$ (or residence time $\tau_m = 2.3(1) \times 10^{-10}\,s$), and fast Jahn-Teller inversion time, $\tau_i = 5.1(6) \times 10^{-12}\,s$, measured for Cu^{2+} in water, and obtained by assuming a $4+2$ coordination model (Powell et al.[1]). The τ_i value suggests that the inversion occurs on average about 50 times, using an inversion mechanism as illustrated in figure 9.22, before a given water molecule exchanges (Powell et al.[23]).

This model for the inversion mechanism together with the measured timescales

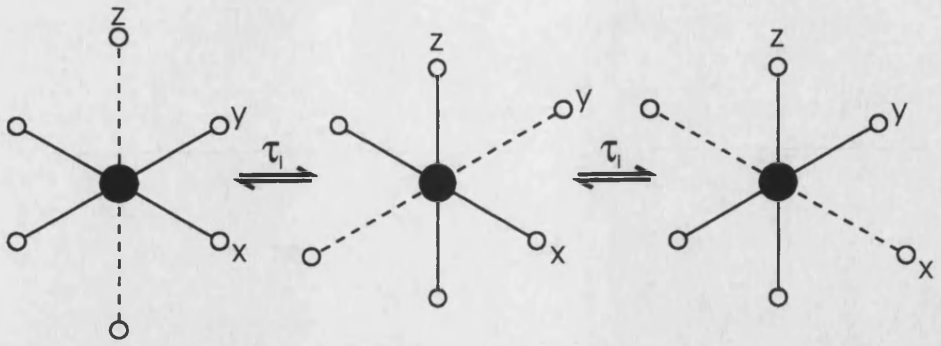

Figure 9.22: Illustration of the inversion mechanism of the Jahn-Teller distortion axis in an octahedral complex.

is expected to result in measuring a single axial Cu-O and a single axial Cu-H distance in our neutron diffraction experiments. Two relatively sharp peaks are therefore expected in the partial pair distribution functions, $g_{CuO}(r)$ and $g_{CuH}(r)$, at distinct axial distances with coordination numbers, $\overline{n}^{O}_{Cu}$ and $\overline{n}^{H}_{Cu}$ equal to two and four respectively. However our measured data suggests a model for the Cu^{2+} coordination complex wherein the four close H_2O molecules have a rather long mean residence time in the vicinity of the Cu^{2+} ion, and where the further distant H_2O molecules can 'come and go' and exchange rather rapidly with the bulk water.

The *ab initio* molecular dynamics study of Pasquarello confirms our results of a $4+1$ coordinated complex (Pasquarello[18] and section 9.5.2). Pasquarello has also shown that the inter-d absorption, using UV and visible light, is not selective between the $4+1$ and $4+2$ coordination complexes of Cu^{2+}. A further confirmation would be obtained if the ^{17}O NMR results of Powell et al.[1] can be interpreted following the $4+1$ coordination model, work which will hopefully be attempted in the near future (Powell & Merbach[24]). Additionally the question about how the inversion can take place in a $4+1$ coordination complex is still open. Hopefully our results will serve as a starting point for future work to answer this question.

9.6 Conclusions

- The method of first order difference functions in combination with H/D substitution was successfully applied to 2 molal $Cu(ClO_4)_2$ aqueous solutions, allowing for the separation of the Cu-H partial structure factor, $S_{CuH}(Q)$, and, to a first order approximation, of the Cu-O partial structure factor, $S_{CuO}(Q)$.

- The partial structure factors show, in agreement with the first order difference functions, that the hydration shell around the Cu^{2+} ion is *not* best described by a $4+2$ tetragonal distortion of the $[Cu(H_2O)_6]^{2+}$ octahedron. A $4+1$ distortion, where the four close oxygens atoms are found at a distance $r_{CuO} = 1.96(2)$ Å (measured data points) and the eight close hydrogen atoms are at a distance $r_{CuO} = 2.58(2)$ Å, is instead obtained. No distinct position is found for the single further distant H_2O molecule. Instead, a broad distribution of positions is observed.

- The $Cu(ClO_4)_2$ solutions exhibit intermediate range ordering as manifest by a FSDP that could be traced to the Cu-H correlations.

- Despite the problems inherent to both methods, the very recent *ab initio* molecular dynamics simulations of Pasquarello[18], which were carried out at a concentration of $1\,Cu : 50\,H_2O$, agree with our results obtained from the neutron first-order difference function method in combination with H/D substitution experiments. The molecular dynamics results confirm that the $4+1$ distortion is real and is *not* an artefact of the high concentration used in our experiment.

Bibliography

[1] Powell D H, Helm L and Merbach A E, *J. Chem. Phys.* **95** (1991) 9258.

[2] Magini M, *Inorg. Chem.* **21** (1982) 1535.

[3] Salmon P S, Neilson G W and Enderby J E, *J. Phys. C: Sol. State Phys.* **21** (1988) 1335.

[4] Salmon P S and Neilson G W, *J. Phys.: Cond. Mat.* **1** (1989) 5291.

[5] Nomura M and Yamaguchi T, *J. Phys. Chem.* **92** (1988) 6157.

[6] Wells A F, *Structural Inorganic Chemistry* (1984) Claredon Press: Oxford.

[7] Gallucci J C and Gerkin R E, *Acta Cryst.* **C45** (1989) 1279.

[8] Toth E, *Private Communication* (1999) .

[9] Sears V F, *Neutron News* **3** (1992) 26.

[10] Hughs D J and Harvey J A, *Neutron Cross Sections* in Brookhaven National Lab: **BNL 325** (1955).

[11] Garber D I and Kinsey R R, *Neutron Cross Sections* in Brookhaven National Lab: **BNL 325** 3rd Ed. (1976).

[12] Stehn J, Goldberg M D and Magurno B A, in Brookhaven National Lab: **BNL 325** 2nd Ed. Supplement No.2 (1964).

[13] Soper A K, Neilson G W, Enderby J E and Howe R A, *J. Phys. C* **10** (1977) 1793.

[14] Powell D H, Neilson G W and Enderby J E, *J. Phys.: Cond. Mat.* **5** (1993) 5723.

[15] Neilson G W, Howe R A and Enderby J E, *Chem. Phys. Lett.* **33** (1975) 284.

[16] Neilson G W and Enderby J E, *Proc. R. Soc. Lond. A* **390** (1983) 353.

[17] Salmon P S, *Proc. R. Soc. Lond. A* **445** (1994) 351.

[18] Pasquarello A, *Private Communication* (1999) .

[19] Sham T K, Hastings J B and Perlman M L, *Chem. Phys. Lett.* **83** (1981) 391.

[20] Tajiri Y and Wakita H, *Bull. Chem. Soc. Jap.* **59** (1986) 2285.

[21] Okan S E and Salmon P S, *Molec. Phys.* **85** (1995) 981.

[22] Ohtaki H and Maeda M, *Bull. Chem. Soc. Jap.* **47** (1974) 2197.

[23] Powell D H, Furrer P, Pittet P-A and Merbach A E, *J. Phys. Chem.* **99** (1995) 16622.

[24] Powell D H and Merbach A E, *Private Communication* (1999) .

[25] Salmon P S and Fischer H E, *Private Communication* (1997) .

Chapter 10

Summary and future work

In this final chapter the results from the work in all previous chapters will be summarised, and ideas of how this work could be extended in the future will be given.

10.1 Summary of results

The results presented in this thesis show the strength of the method of neutron diffraction for obtaining information on the structure of disordered materials. In particular, the isotopic substitution method has proven to be a valuable technique for the study of the binary GeSe and $GeSe_2$ systems and $Cu(ClO_4)_2$ solutions.

In chapter 4, the structure of the liquid semiconductor GeSe was investigated using the method of isotopic substitution in neutron diffraction. All three Faber-Ziman partial structure factors were successfully separated from the measured total structure factors, ${}^{N}_{N}F(Q)$, ${}^{70}_{N}F(Q)$ and ${}^{73}_{76}F(Q)$. Our measurements confirmed the nature of the previously reported solid state phase transition from a distorted to a normal NaCl-type structure with increasing temperature. The local ordering in liquid GeSe was found to be significantly different to that of either its high or low temperature crystalline forms, with Ge being fourfold coordinated to 3.2(2) Se and 0.8(1) Ge, and Se being coordinated to 3.2(2) Ge and 0.22(3) Se. Homopolar bonds occur as prominent features in the molten state.

Qualitative similarities with the structure of the molten semiconductor CuSe, for which structural information is also available at the partial structure factor

level, were observed. By comparison, although short A-A distances also occur in molten CuBr, albeit with a broader distribution, anion-anion homopolar bonds are not present. A comparison of the Bhatia Thornton partial structure factors of liquid GeSe with those for liquid $GeSe_2$ showed that the FSDP in $S_{NN}^{BT}(Q)$ for liquid GeSe is small compared to that for the network melt $GeSe_2$ and that there is no FSDP in the other Bhatia-Thornton partial structure factors.

In chapter 5, the total structure factor of liquid $GeSe_2$ was measured at 800 °C, 1000 °C and 1100 °C. Since the coherent neutron scattering lengths of Ge and Se are very similar, these total structure factors give, to a good approximation, the Bhatia Thornton partial structure factor $S_{NN}(Q)$. It was found that with increasing temperature a broadening in the distribution of nearest neighbours occurs, but their mean position at $r = 2.38(2) - 2.40(2)$ Å and coordination number $\overline{n} = 2.6(1) - 2.7(1)$ do not change at the level of the number-number partial pair distribution function. The increase in density and decrease in viscosity measured with increasing temperature were found to result from a destruction of the intermediate range ordering associated with the Ge-Ge correlations, in contrast to earlier deductions based on several physico-chemical properties of $GeSe_2$ (Ruska & Thurn[1]) which suggested that these changes are due to an increase in the coordination number from four to six. The measured changes in the profiles of $S_{NN}(Q)$ and $g_{NN}(r)$ with increasing temperature resemble those observed as the composition of molten $GeSe_2$ is altered to the GeSe stoichiometry by the addition of germanium. Finally, the comparison with recent simulations using the LDA and GGA schemes showed that the binary Ge-Se system can serve as a sensitive test-system for the methods used in current *ab initio* molecular dynamics simulations.

In chapter 6, the structure of the proto-typical network melt quenched glass $GeSe_2$ was studied using the method of isotopic substitution in neutron diffraction. All three partial structure factors, $S_{GeGe}(Q)$, $S_{GeSe}(Q)$ and $S_{SeSe}(Q)$ were extracted successfully from the measured total structure factors and were found to contribute to the intermediate range ordering (IRO). However, the IRO is dominated by the Ge-Ge correlations, i.e. by the real-space intermediate range ordering of Ge-centred structural motifs. The short range order in glassy $GeSe_2$ is similar to that in the HT crystalline phase, although a substantial number of defects are present. In the

glass 34(5) % of Ge are in edge sharing tetrahedra compared to 50 % in the crystal. The defects in the $GeSe_2$ glass have been identified for the first time by diffraction methods. An analysis of the defects yielded a maximum fraction of Ge in defected tetrahedra of 29(5) %, a minimum fraction of Ge in regular tetrahedra of 54(6) % and a fraction of Ge in Ge-Ge dimers of 25(5) %. The comparison with the structure of liquid $GeSe_2$ at 784 °C showed that the peaks in the partial structure factors at $Q > 1.5\,\text{Å}^{-1}$ for the glass are sharper than for the liquid. However, the FSDP in $S_{GeGe}(Q)$ and in $S_{NN}(Q)$ for the glass is of comparable height and at a comparable position to the FSDP in these functions measured for the liquid. By comparing the experimental results for glassy $GeSe_2$ with the molecular dynamics studies by Cobb et al.[2] it was shown that in reciprocal and real-space the simulated peaks are too low and too broad. Special problems in the molecular dynamics study were encountered in the region of the homopolar bonds for $g_{GeGe}(r)$, which are found at too large a distance compared with our experiment. Further, the FSDP in the Bhatia-Thornton concentration-concentration structure factor found in the experiment for $GeSe_2$ was not reproduced in the simulation.

In chapter 7, Ge_xSe_{1-x} ($0 \leq x \leq 0.4$) glasses were investigated by using differential scanning calorimetry (DSC) and neutron diffraction. The DSC measurements showed that the glass transition temperature, T_g, increases with the germanium content for $x \leq 0.33$ and decreases with higher germanium content. Also the glass transition in the investigated samples is a low enthalpy event, with the exception of pure Se.

The neutron diffraction experiments yielded, to a first order approximation, the Bhatia Thornton number-number partial structure factors and pair distribution functions. These showed that there are clear changes in the topology of Ge_xSe_{1-x} glasses in the range $0 \leq x \leq 0.4$, although the nearest neighbour bonding remains characterised by coordination numbers for Ge and Se of 4 and 2 respectively. However, the average coordination number $\overline{n}$ and the nearest neighbour distance r_1 increase with increasing x, giving rise to a slightly closer-packed structure. The compositions with $0.2 \leq x \leq 0.4$ were found to be characterised by a number-number partial structure factor $S_{NN}(Qr_1)$ that shows the typical three-peak structure for $0 \leq Qr_1 \leq 10$. The intermediate range ordering in these glasses, as manifest by a FSDP changes. The amplitude of the FSDP increases with in-

creasing Ge content up to x = 0.33 and decreases with a further increase of the Ge content up to x = 0.4. However the periodicity and coherence length of the corresponding real-space intermediate range ordering, as deduced from the FSDP, increase up to x = 0.4. In the $GeSe_4$, $GeSe_3$ $GeSe_{1.5}$ glasses heteropolar bonding is favoured and their structures, as measured at the total structure factor level, are in agreement with the chemically ordered continuous random network (COCRN) model. However since deviations from this model are found from the full partial structure factor analysis for $GeSe_2$, deviations for these other compositions might be expected.

In chapter 8, the structure of liquid lithium was studied. Neutron diffraction experiments were carried out at temperatures of 197 °C, 452 °C and 595 °C and at two different incident neutron wavelengths of $\lambda = 0.4962$ Å and $\lambda = 0.7011$ Å.

A careful treatment was made of the detector path integration problem and the inelasticity corrections and the total structure factors were corrected for the resolution function of the D4B diffractometer. It was found that at a short range scale, liquid lithium maintains a memory of the crystalline bcc-structure from which it melts. The comparison with classical molecular dynamics simulations and integral equation calculations showed that the static structure factor from our measurement yields an improvement to the Ashcroft empty core radius, and that the NPA pseudopotential does not give clearly better results for the static structure of lithium.

Finally, the valence electron form factor and ion-valence electron partial structure factor, $S_{IE}(Q)$, at 197 °C were obtained combining the measured static structure factor from our experiment with the x-ray structure factor measured by Olbrich et al.[3]. The results were found to agree better in intensity and shape with the results from Orbital free *ab initio* molecular dynamics simulations than any other experimentally derived $S_{IE}(Q)$ so far.

In chapter 9, the method of first order difference functions in combination with H/D substitution was successfully applied to 2 molal solutions of $Cu(ClO_4)_2$ in perchloric acid, allowing for the separation of the Cu-H partial structure factor, $S_{CuH}(Q)$, and, to a first order approximation, the Cu-O partial structure factor, $S_{CuO}(Q)$. These measured partial structure factors showed, in agreement with the first order difference functions, that the hydration shell around the Cu^{2+} ion is

not best described by a $(4+2)$ tetragonal distortion of the $[Cu(H_2O)_6]^{2+}$ octahedron. A $(4+1)$ distortion, where the four close oxygen atoms are found at a distance $r_{CuO} = 1.96(2)$ Å and the eight close hydrogen atoms are at a distance $r_{CuO} = 2.58(2)$ Å, was instead obtained. No distinct position was found for the single further distant H_2O molecule. Instead, a broad distribution of positions in the range of $2.37 \leq r_{CuO}$ [Å] ≤ 3.0 for the oxygen atom and of $2.9 \leq r_{CuH}$ [Å] ≤ 3.4 for the two hydrogen atoms, was observed. The $Cu(ClO_4)_2$ solutions exhibit intermediate range ordering as manifest by a FSDP that could be traced to the Cu-H correlations. Further, very recent *ab initio* molecular dynamics simulations, which were carried out at a concentration of $1\,Cu : 50\,H_2O$, were shown to agree with our results. The molecular dynamics results confirmed that the $(4+1)$ distortion is real and is *not* an artefact of the high concentration used in our experiment.

10.2 Future work

Since it has been shown in chapter 8 that for liquid lithium it is possible to obtain the ion-valence electron structure factor by the combination of structure factors measured using neutron diffraction and x-ray diffraction, it would be very interesting to carry out a new x-ray diffraction experiment on liquid lithium using synchrotron radiation. The static structure factor so obtained should, together with our measured neutron structure factor, yield an improvement to the valence electron form factor and ion-valence electron structure factor obtained so far.

Furthermore, an inelastic neutron scattering experiment to measure the dynamic structure factor $S(Q,\omega)$ in glassy $GeSe_2$ using three samples with different isotopic enrichments, i.e. the samples which were used in the isotopic substitution experiment on glassy $GeSe_2$ described in chapter 6, could be carried out to measure the vibrational density of states of the glass. Therefore it might be possible to associate the homopolar bonds and defects found from the structure work with individual vibrational modes.

Bibliography

[1] Ruska J and Thurn H, *J. Non-Cryst. Sol.* **22** (1976) 277.

[2] Cobb M, Drabold D A and Cappelletti R L, *Phys. Rev. B* **54** (1996) 12162.

[3] Olbrich H, Ruppersberg H and Steeb S, *Z. Naturforsch.* **38a** (1983) 1328.

Appendix A: Table of fitted Gaussians:

$t_{GeGe}(r)$:

position [Å]	coordination number	sigma [Å]
2.486	0.25	0.140
3.02	0.34	0.225
3.632	2.32	0.140
3.95	0.87	0.140

$t_{GeSe}(r)$:

position [Å]	coordination number	sigma [Å]
2.425	3.76	0.072
3.08	0.29	0.072
3.29	0.08	0.072
3.878	1.68	0.280
4.305	0.17	0.072
4.515	2.90	0.280
4.880	3.10	0.280

$t_{SeSe}(r)$:

position [Å]	coordination number	sigma [Å]
2.380	0.21	0.090
2.800	0.07	0.090

Appendix B: 'Moments method' of deconvolution (Howells[23])

The 'moments method' can be used for deconvoluting the structure factor of a liquid from the resolution function of the diffractometer. The measured intensity $I(2\theta_s)$ is expressed by

$$I(2\theta_s) = \int R(2\theta_s, \rho)\, S(2\theta_s + \rho)\, d\rho \tag{1}$$

where $2\theta_s$ is the scattering angle, ρ the angular displacement of the detector from $2\theta_s$, and $R(2\theta_s, \rho)$ the resolution function of the instrument. The aim is to use the moments procedure to calculate $S(2\theta_s)$ from the measured $I(2\theta_s)$ when the form of $R(2\theta_s, \rho)$ is known.

In Howells'[23] moments method the function $S(2\theta_s + \rho)$ is Taylor expanded about $2\theta_s$,

$$S(2\theta_s + \rho) = S(2\theta_s) + \rho S' + \frac{\rho^2}{2!} S'' + ... \tag{2}$$

where $S^n = d^n S(2\theta_s)/d(2\theta_s)^n$.

Equation 1) is then multiplied throughout by $R(2\theta_s, \rho)$ and integrated over ρ,

$$I(2\theta_s) = M_0 S(2\theta_s) + M_1 S' + M_2 S'' + M_3 S''' + ... \tag{3}$$

where M_n are the moments of the resolution function,

$$M_n = \frac{1}{n!} \int \rho^n\, R(2\theta_s, \rho)\, d\rho \tag{4}$$

and

$$M_n{}^n = d^n M_n(2\theta_s)/d(2\theta_s)^n\,. \tag{5}$$

Equation 3) is now differentiated with respect to $(2\theta_s)$, and with using $I^n = d^n I(2\theta_s)/d(2\theta_s)^n$ it can be written as,

$$\begin{bmatrix} I \\ I' \\ I'' \\ .. \end{bmatrix} = \begin{bmatrix} M_{00} & M_{01} & M_{02} & .. \\ M_{10} & M_{11} & .. & .. \\ M_{20} & .. & .. & .. \\ .. & .. & .. & .. \end{bmatrix} \begin{bmatrix} S \\ S' \\ S'' \\ .. \end{bmatrix} \tag{6}$$

where

$$
\begin{aligned}
M_{00} &= M_0 \\
M_{01} &= M_1 \\
M_{02} &= M_2 \\
M_{10} &= M_0' \\
M_{11} &= M_0 + M_1' \\
M_{12} &= M_1 + M_2' \\
M_{20} &= M_0^2 \\
M_{21} &= 2M_0' + M_1^2 \\
M_{22} &= M_0 + 2M_1' + M_2^2 \,. \qquad (7)
\end{aligned}
$$

The solution for the structure factor is given by [S] = [M]$^{-1}$ [I], where [M]$^{-1}$ can be written as

$$
[M]^{-1} = \begin{pmatrix} m_{00} & m_{01} & m_{02} \\ m_{10} & m_{11} & m_{12} \\ m_{20} & m_{21} & m_{22} \end{pmatrix} \qquad (8)
$$

If only the first two derivatives of I are taken, as in the case of our liquid lithium experiment, the deconvoluted structure factor $S(2\theta_s)$ is given by,

$$
S(2\theta_s) = m_{00} I(2\theta_s) + m_{01} \frac{d\, I(2\theta_s)}{d\,(2\theta_s)} + m_{02} \frac{d^2\, I(2\theta_s)}{d\,(2\theta_s)^2} \qquad (9)
$$

In the case of the first peak of $I(2\theta_s)$, it might be anticipated that the effect of the first correction, $m_{01}\, d\, I(2\theta_s)/d\,(2\theta_s)$, will be a shift of the peak position and the main effect of the second correction, $m_{02}\, d^2\, I(2\theta_s)/d\,(2\theta_s)^2$, will be a sharpening of the peak.

Additionally, if the area of the resolution function is normalised to unity at all $(2\theta_s)$ values then it follows from equation 4) that $M_0 = \int R(2\theta_s, \rho)\, d\rho = 1$ such that $M_0^n = 0$ and equation 7) simplifies to

$$
\begin{aligned}
M_{00} &= 1 \\
M_{01} &= M_1 \\
M_{02} &= M_2 \\
M_{10} &= 0 \\
M_{11} &= 1 + M_1'
\end{aligned}
$$

$$
\begin{aligned}
M_{12} &= M_1 + M_2' \\
M_{20} &= 0 \\
M_{21} &= M_1^2 \\
M_{22} &= 2M_1' + M_2^2 \,. \qquad (10)
\end{aligned}
$$

Appendix C: Preparation of $Cu(ClO_4)_2$ in aqueous solution

The Cu metal (99 % enrichment) was dissolved in HNO_3 (1:10 dilution of concentrated HNO_3). From this solution, $Cu(OH)_2$ / CuO was precipitated on addition of a Na_2CO_3 solution (final pH: 9.9 - 10.0). The precipitate was filtered and dried at 250 °C in an oven until its weight did not change any more (black solid). The dried CuO was dissolved in $DClO_4/D_2O$ and evaporated to dryness on a vacuum line. The solid $Cu(ClO_4)_2$ was dissolved in D_2O and evaporated on the vacuum line again. The final sample was prepared in a glove box by adding a sufficient amount of D_2O and $DClO_4$ (Toth[8]).

Appendix D: Optimisation of sample run-times (Salmon & Fischer[25]):

The run-times are optimised in a way such that for a given total counting time, $\tau = t_1 + t_2$, where the t_i are the counting times for samples i = 1 or 2, the error bars on the measured functions are as small as possible. Sample 1 and 2 can either be two different samples, for example in a first order difference experiment, or a sample in its container and the empty container.

In the small sample limit, i.e. when the attenuation and multiple scattering effects are neglected,

$$\frac{t_1}{t_2} = \sqrt{\frac{\Sigma_{S1}}{\eta_1} \cdot \frac{\eta_2}{\Sigma_{S2}}} \tag{11}$$

where Σ_{Si} is the total cross-section per atom of sample i and η_i the number of scatterers of sample i in the beam.

If the absorption in the samples is taken into consideration, Σ_S is replaced by $\Sigma_S A_{S,S}$, where $A_{S,S}$ is the Paalman & Pings attenuation factor, see section 3.3.1. For example, in the case of a sample in its container and the container, equation 11 is written as,

$$\frac{t_{SC}}{t_C} = \sqrt{\frac{\left[(A_{S,SC}\Sigma_S V_S n_{0,S}) + (A_{C,SC}\Sigma_C V_C n_{0,C})\right] A_{C,C}^2}{A_{C,C}\Sigma_C V_C n_{0,C} A_{C,SC}^2}} \tag{12}$$

where $V_S n_{0,S} = \eta_S$ with V_S, the volume of sample in the beam, and $n_{0,S}$, the number density of the sample.

Appendix E: Further study - Structure of disordered fast-ion conductors: the case of glassy $(CuI)_x(As_2Se_3)_{1-x}$

ISIS Experimental Report Rutherford Appleton Laboratory		RB Number: Date of Report:	9740 May 1999
Title of Experiment:	Structure of disordered fast-ion conductors: the case of glassy $(CuI)_x(As_2Se_3)_{1-x}$.	Local Contact:	Dr Chris Benmore
Principal Proposer: Affiliation:	Dr Philip S Salmon	Instrument:	SANDALS
Experimental Team:	Ingrid Petri	Date of Experiment:	Easter 1998

The object of this proposal was to study the evolution in the structure of the glassy fast-ion conductors $(CuI)_x(As_2Se_3)_{1-x}$ $(0 \le x \le 1)$ with increasing network modifier content. The modifier CuI is a fast-ion conductor in its high temperature crystalline phase (Boyce and Huberman 1979) and as it is added to the network former As_2Se_3, the ionic conductivity of the resultant glasses increases. It is therefore of interest to understand the concomitant change in the basic structure of these materials and thereby the reasons for the enhanced ionic motion. The absolute value of their ionic conductivity is orders of magnitude higher than in $(Cu_2Se)_x(As_2Se_3)_{1-x}$ glasses (Bychkov *et al* 1996) for which detailed information is now available at the partial structure factor level (Benmore and Salmon 1994).

The total structure factors for the glasses $(CuI)_{0.1}(As_2Se_3)_{0.9}$ and $(CuI)_{0.6}(As_2Se_3)_{0.4}$ are shown in figure 1. It is found that as the modifier content is increased, the first sharp diffraction peak moves from 1.26 $Å^{-1}$ for $x = 0.1$ to 0.99 $Å^{-1}$ for $x = 0.6$ and its intensity increases, indicating an enhancement of the intermediate range ordering. These changes are accompanied by an increase in the mean nearest-neighbour coordination number owing to the formation of Cu-Se and Cu-I bonds.

A full analysis of the data is being undertaken and the results will be compared with the structure of the corresponding sulphide glasses $(CuI)_x(As_2S_3)_{1-x}$ (Mamedov *et al* 1998a, 1998b) and with the structure of $(Cu_2Se)_x(As_2Se_3)_{1-x}$ glasses (Benmore and Salmon 1994).

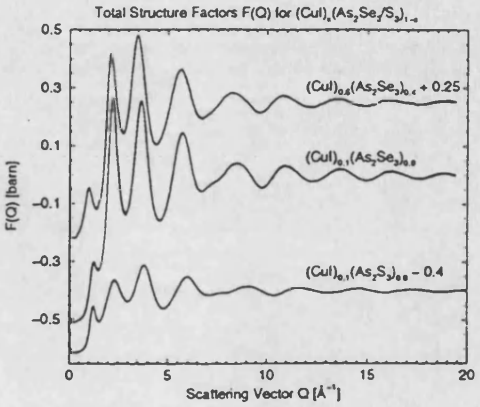

Figure 1. The measured total structure factors for the glasses $(CuI)_{0.1}(As_2Se_3)_{0.9}$ and $(CuI)_{0.6}(As_2Se_3)_{0.4}$ compared with the total structure factor for glassy $(CuI)_{0.1}(As_2S_3)_{0.9}$.

Benmore C J and Salmon P S 1994 *Phys. Rev. Lett.* **73** 264.

Boyce J B and Huberman B A 1979 *Phys. Rep.* **51** 189.

Bychkov E, Bolotov A, Grushko Yu, Vlasov Yu, Wortmann G 1996 *Solid State Ionics* **90** 289.

Mamedov S, Bolotov A, Brinker L, Kisliuk A and Soltwisch M 1998a *J. Non-Cryst. Sol.* **224** 89.

Mamedov, S, Bolotov A, Brinker L, Kisliuk A, Soltwisch M, Vlcek M and Sklenar A 1998b *Phys. Rev. B* **58** 8155.